Probing the Dynamic Universe with the Motions of Stars and Galaxies

by

Jennie Paine

B.S., Virginia Tech, 2016

M.S., University of Colorado, 2018

A thesis submitted to the

Faculty of the Graduate School of the

University of Colorado in partial fulfillment

of the requirements for the degree of

Doctor of Philosophy

Department of Astrophysical and Planetary Sciences

2023

Committee Members:

Jeremy Darling, Chair

Prof. Julia Comerford

Prof. Jason Dexter

Prof. Vanja Dukic

Prof. Meredith MacGregor

Paine, Jennie (Ph.D., Astrophysical and Planetary Sciences)

Probing the Dynamic Universe with the Motions of Stars and Galaxies

Thesis directed by Prof. Jeremy Darling

Observations of the motions of celestial objects have a variety of physical applications — from stellar dynamics to cosmology. This dissertation focuses on high precision measurements of proper motions and velocities of stars and galaxies and an exploration of their myriad applications. I first present a method for identifying extragalactic objects detected by *Gaia* astrometric mission, resulting in a catalog of over 500,000 active galactic nuclei. The proper motions of such an extragalactic astrometric catalog are sensitive to the galactocentric acceleration of the solar system and the isotropy of cosmic expansion, and I forecast the measurements of these effects with the *Gaia* catalog. Next, I use a nearby sample of galaxies to place limits on the magnitude of the proper motion signal caused by the linear velocity of the solar system, called secular parallax. I investigate the influence of peculiar velocities of nearby galaxies due to large scale structure on this measurement using simulated galaxy proper motions. Finally, I present a series of studies of stellar kinematics in the Galactic Center. I use radio observations of stellar SiO masers from the Very Large Array (VLA) and the Atacama Large Millimeter/submillimeter Array (ALMA) to measure high resolution astrometry and spectra of a sample of 28 stars. I present the resulting 3D velocities of the stars, and the first limits on their 3D accelerations. The stellar kinematics trace the gravitational potential around the central supermassive black hole, and thus I calculate limits on the mass distribution within the inner 2 pc using the maser measurements. I will discuss the influence that confounding factors such as maser variability and undetected binary stars may have on these measurements.

Acknowledgements

First of all, I want to thank my advisor, Jeremy Darling, for years of support and guidance. It has been a pleasure to work with and learn from you. Most of all, thank you for your understanding and flexibility whenever life got in the way of my academic plans.

Thank you to my coauthors, colleagues, and friends in the astronomy community who have helped me along the way. I would not have gotten to this point without a lot of assistance from the other graduate students in the APS department, from study sessions to coding tips. Most importantly, thank you to the friends I have made for uplifting and encouraging me.

Thanks to King Gizzard and the Lizard Wizard for their prolific discography and free high-quality concert recordings, which have been my soundtrack to many hundreds of hours of research and writing, especially *Polygondwanaland* and *Laminated Denim*. The various baristas who prepared delightful lavender oat milk lattes for me also deserve acknowledgement for keeping me caffeinated over the last few months especially.

Finally, I want to acknowledge and thank my little family who bring me so much joy and keep me going. To my kitties, Gemma and Henry, for their companionship and purrs. To my husband and best friend, Richard Melito, for unwavering support which made this work possible. Thank you for your encouragement and inspiration. And lastly, thank you to my daughter, Lily, whose curiosity is a reminder that it is a privilege to study the stars.

Contents

Chapter

Tables

Table

Figures

Figure

Chapter 1

Introduction

Preface

The body of work presented in this dissertation is a compilation of studies of the motions of stars, galaxies, and active galactic nuclei (AGN). The goals of these works are to investigate phenomena on a wide variety of scales using the common technique of leveraging high precision measurements of the proper motions and velocities of cosmic probes. This introduction is organized into two sections covering the motivation, scientific background, and observational techniques necessary for the study of extragalactic proper motions (Section 1.1) and of stellar maser kinematics in the Galactic Center (Section 1.2). Finally, I will summarize this dissertation work and how it connects to the topics introduced here (Section 1.3).

1.1 Extragalactic Proper Motions

Proper motions are the angular velocities of celestial objects. While an object's instantaneous velocity along the line of sight may be measured with spectroscopy as a Doppler shift, the two-dimensional (2D) tangential velocity requires repeated astrometry and knowledge of the object's distance to translate the proper motion to a velocity. For extragalactic objects, proper motions will reflect a combination of the object's motion with respect to an isotropic Hubble flow (called the peculiar velocity), cosmological effects, and observer induced effects. Due to their large distances, extragalactic objects generally have very small proper motions on scales of micro to milli arcseconds per year. However, these small motions are measurable with high precision astrometry. Further, by

measuring correlated proper motions among a large sample, one may detect proper motion signals smaller than the precision of individual proper motion measurements.

1.1.1 Vector Spherical Harmonic Modeling

The components of an object's total proper motion can be represented by a linear combination of vector spherical harmonics (Mignard, 2012), which are a vector extension of the typical spherical harmonics. Each degree, l, is composed of a pair of orthogonal basis functions, referred to as E-mode (curl-free, spheroidal) and B-mode (divergenceless, toroidal) for their analog to electric and magnetic fields. These functions can be expressed in terms of the spherical harmonic functions, Y_{lm}, as

$$\mathbf{S}_{lm} = \frac{1}{\sqrt{l(l+1)}} \nabla Y_{lm} = \mathbf{u} \times \mathbf{T}_{lm} \tag{1.1}$$

for the spheroidal functions and

$$\mathbf{T}_{lm} = \frac{1}{\sqrt{l(l+1)}} (-\mathbf{u} \times \nabla Y_{lm}) = -\mathbf{u} \times \mathbf{S}_{lm} \tag{1.2}$$

for the toroidal functions, where l and m are the degree and order, and $\mathbf{u}$ is the unit vector along the radial direction. More explicitly, in RA and Dec coordinates, the functions are

$$\mathbf{S}_{lm}(\alpha, \delta) = \frac{1}{\sqrt{l(l+1)}} \left[\frac{1}{\cos\delta} \frac{\partial Y_{lm}}{\partial \alpha} \mathbf{e}_\alpha + \frac{\partial Y_{lm}}{\partial \delta} \mathbf{e}_\delta \right] \tag{1.3}$$

and

$$\mathbf{T}_{lm}(\alpha, \delta) = \frac{1}{\sqrt{l(l+1)}} \left[\frac{\partial Y_{lm}}{\partial \delta} \mathbf{e}_\alpha - \frac{1}{\cos\delta} \frac{\partial Y_{lm}}{\partial \alpha} \mathbf{e}_\delta \right], \tag{1.4}$$

where $\mathbf{e}_\alpha$ and $\mathbf{e}_\delta$ are unit vectors in the RA and Dec coordinates, respectively. Any real-valued vector field on a sphere can be expressed as a linear combination of the vector spherical harmonics:

$$\mathbf{V}(\alpha, \delta) = \sum_{l=1}^{\infty} \left(t_{l0} \mathbf{T}_{l0} + s_{l0} \mathbf{S}_{l0} + 2 \sum_{m=1}^{l} \left(t_{lm}^{Re} \mathbf{T}_{lm}^{Re} - t_{lm}^{Im} \mathbf{T}_{lm}^{Im} + s_{lm}^{Re} \mathbf{S}_{lm}^{Re} - s_{lm}^{Im} \mathbf{S}_{lm}^{Im} \right) \right), \tag{1.5}$$

where the coefficients $t_{lm}^{Re,Im}$ and $s_{lm}^{Re,Im}$ are the real and imaginary parts of complex coefficients t_{lm} and s_{lm} found by projecting the vector field on the base functions $\mathbf{T}_{lm}$ and $\mathbf{S}_{lm}$. Figure 1.1 shows examples of dipoles ($l = 1$) and quadrupoles ($l = 2$) calculated with randomized coefficients

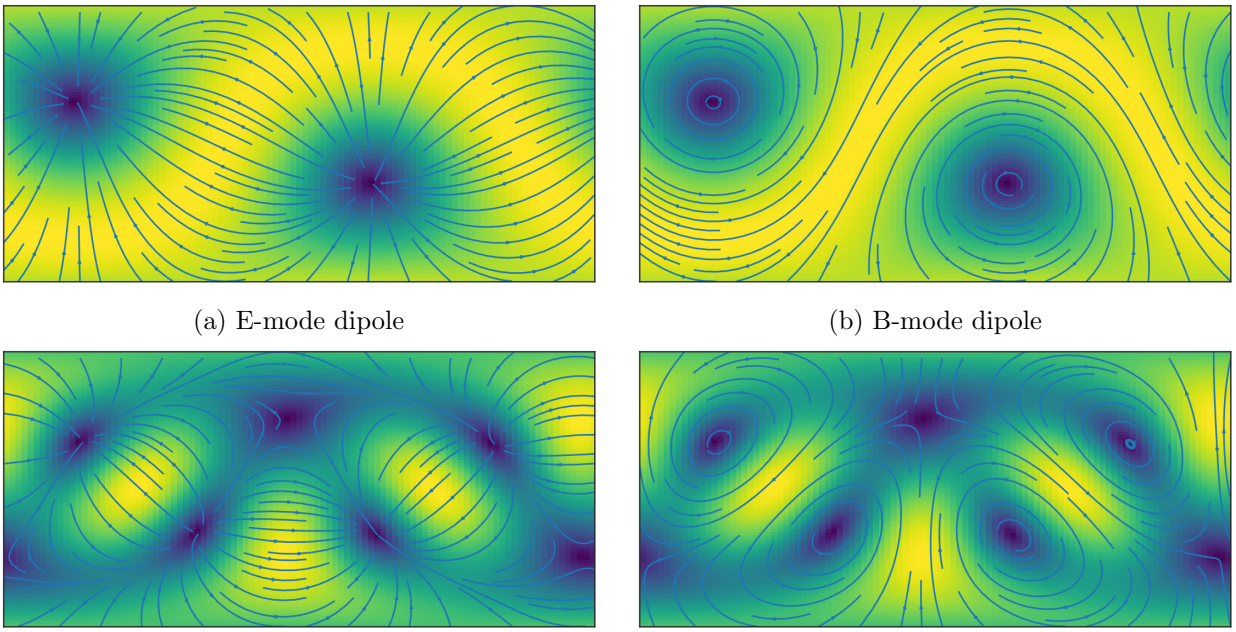

(a) E-mode dipole

(b) B-mode dipole

(c) E-mode quadrupole

(d) B-mode quadrupole

Figure 1.1: Example E and B-mode dipolar ($l = 1$) and quadrupolar ($l = 2$) vector fields using randomized coefficient values.

for demonstration. The power of a vector field of order l is defined as the squared field integrated over the unit sphere and is calculated from the $t_{lm}^{Re,Im}$ and $s_{lm}^{Re,Im}$ coefficients by

$$P_l = s_{l0}^2 + t_{l0}^2 + 2\sum_{m=1}^{l}\left((s_{lm}^{Re})^2 + (s_{lm}^{Im})^2 + (t_{lm}^{Re})^2 + (t_{lm}^{Im})^2\right). \tag{1.6}$$

The square root power can be interpreted as a characteristic vector length. The ratios of the coefficients will determine the orientation of the vector field.

There are several phenomena that induce correlated proper motions that may be represented with low-multipole (i.e. small l) vector spherical harmonics. Among these are observer-induced effects from the galactocentric acceleration of the solar system and the linear velocity of the solar system with respect to other galaxies, both of which create dipolar ($l = 1$) proper motion signals. Higher order modes ($l \geq 2$) may be induced by cosmological effects such as hypothetical anisotropic expansion of the universe and primordial gravitational waves. And finally, gravitational interactions between galaxies due to large scale structure (LSS) will create correlated proper motions on a variety of angular scales. The total proper motion power spectrum for an extragalactic sample is therefore a

linear combination of each of these effects. I discuss the multipoles most relevant to this dissertation and their underlying physical phenomena below.

E-mode dipoles: secular aberration drift and secular parallax. The explicit expression for an E-mode dipole is

$$\begin{aligned}\mathbf{V}_{E1}(\alpha,\delta) = &\left(s_{11}^{Re}\,\frac{1}{2}\sqrt{\frac{3}{\pi}}\,\sin\alpha + s_{11}^{Im}\,\frac{1}{2}\sqrt{\frac{3}{\pi}}\,\cos\alpha\right)\hat{\mathbf{e}}_\alpha \\ &+\left(s_{10}\,\frac{1}{2}\sqrt{\frac{3}{2\pi}}\,\cos\delta + s_{11}^{Re}\,\frac{1}{2}\sqrt{\frac{3}{\pi}}\,\cos\alpha\sin\delta - s_{11}^{Im}\,\frac{1}{2}\sqrt{\frac{3}{\pi}}\,\sin\alpha\sin\delta\right)\hat{\mathbf{e}}_\delta. \qquad (1.7)\end{aligned}$$

Conveniently, the power of a dipole relates directly to its amplitude (i.e. the maximum magnitude of the vector field) by

$$A_{E1} = \sqrt{\frac{3}{8\pi}P_{E1}}. \qquad (1.8)$$

The acceleration of the solar system toward the Galactic Center (GC) induces an E-mode dipole in extragalactic proper motions that points toward the GC, known as the secular aberration drift. The motion of the solar system barycenter produces a systematic deflection of the angular positions of all extragalactic objects known as secular aberration. As the velocity vector changes with time due to the galactocentric acceleration, the aberration pattern changes and results in the secular aberration drift dipole proper motion field. The amplitude of the secular aberration drift dipole is therefore related to the magnitude of the acceleration (Kovalevsky, 2003). For circular velocity about the GC of 255.2 km s^{-1} and radius of 8.34 kpc (Reid et al., 2014), the galactocentric acceleration is 0.80 ± 0.04 cm s^{-1} yr^{-1} and the expected dipole amplitude is 5.5 μas yr^{-1}. This expectation has been confirmed by several studies using quasar proper motions measured with radio interferometry (e.g. Xu et al. 2012; Titov & Lambert 2013; Truebenbach & Darling 2017a). Figure 1.2 shows the quasar proper motions and maximum likelihood dipole fit found by Truebenbach & Darling (2017a). While the proper motion field may appear random — especially since the radio proper motions of quasars are often dominated by randomly oriented relativistic jets — the various detections of the secular aberration drift demonstrate that extragalactic proper motions are in fact correlated and the underlying signals may be extracted.

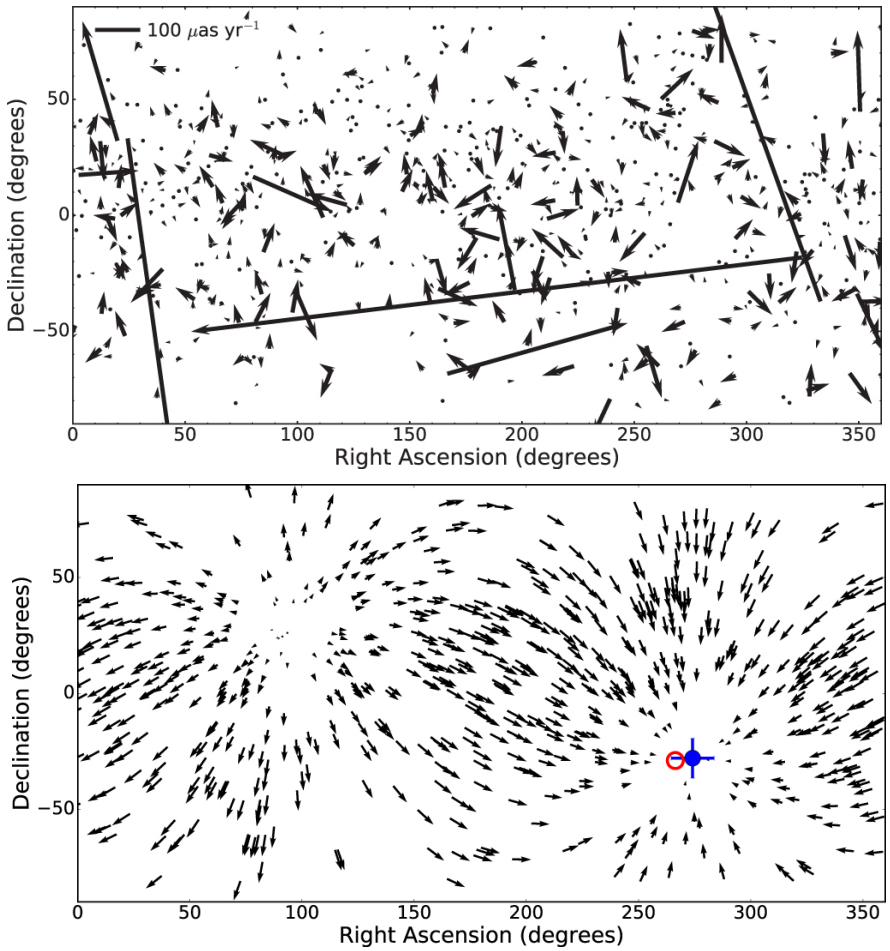

Figure 1.2: A demonstration of fitting a correlated signal to noisy proper motions from Truebenbach & Darling (2017a). Top: proper motions for a sample of 713 radio quasars measured using very long baseline interferometry. The largest proper motions are dominated by radio jets. Bottom: maximum likelihood dipole fit of the secular aberration drift. The red circle indicates the direction of the GC, which is the expected apex of the secular aberration drift dipole, and the blue point and error bar indicate the apex of the maximum likelihood dipole.

The solar system's motion with respect to the rest frame of nearby galaxies induces a second E-mode dipole signature in their proper motions. This motion will cause extragalactic objects to exhibit a parallax shift away from the direction motion (Ding & Croft, 2009), which is distinct from the annual parallax caused by the Earth's orbit around the Sun. The velocity of the solar system, $v_\odot$, expressed in units of AU yr^{-1} translates to the amplitude of the proper motion dipole in μas

yr^{-1} normalized to a distance of 1 Mpc:

$$|\mu| = \left(\frac{v_\odot}{1\ \mathrm{AU\ yr}^{-1}}\right)\left(\frac{1\ \mathrm{Mpc}}{D}\right)|\sin\beta|, \tag{1.9}$$

where β is the angle between a galaxy and the direction of motion, and D is the proper motion distance of the galaxy (which will be equal to the comoving distance in a flat cosmology; Hogg 1999).

Measurements of the cosmic microwave background (CMB) provide us an expectation for the relative velocity of the solar system under the assumption that the rest frame of nearby galaxies matches the rest frame of the CMB. The CMB exhibits a dominant temperature dipole which corresponds to a linear solar velocity of about 78 AU yr^{-1} towards the direction $(168°, -7°)$ in RA and Dec (Hinshaw et al., 2009). This velocity is a combination of the solar system's orbital velocity and the Galaxy's peculiar motion with respect to the CMB.

Secular extragalactic parallax has not yet been detected. However, the distance-dependence of the effect motivates further investigation. A statistical measurement of the secular parallax dipole as a function of redshift would essentially be an independent measurement of the Hubble parameter, H_0 (Bachchan et al., 2016), which is the rate of cosmic expansion in the local universe and relates the recession velocities of galaxies to their distances. The value of H_0 is in tension (see Di Valentino et al. 2021 for a review), and secular parallax would be an independent constraint which is not reliant on the extragalactic distance ladder. Further, the individual proper motions of galaxies with respect to the statistical measurement, whether made as function of distance or redshift, would indicate the galaxy's geometric distance and peculiar velocity.

E-mode quadrupole: triaxial anisotropic expansion. The isotropy of the universe and of dark energy is a basic assumption of the standard model of cosmology. However, a hypothetical anisotropic expansion would cause a shearing signal in extragalactic proper motions where galaxies appear to stream towards the directions of faster expansion and away from directions of slower expansion. The isotropy of the early universe is well constrained by measurements of the CMB (Planck Collaboration et al., 2020), but a proper motion measurement probes isotropy in

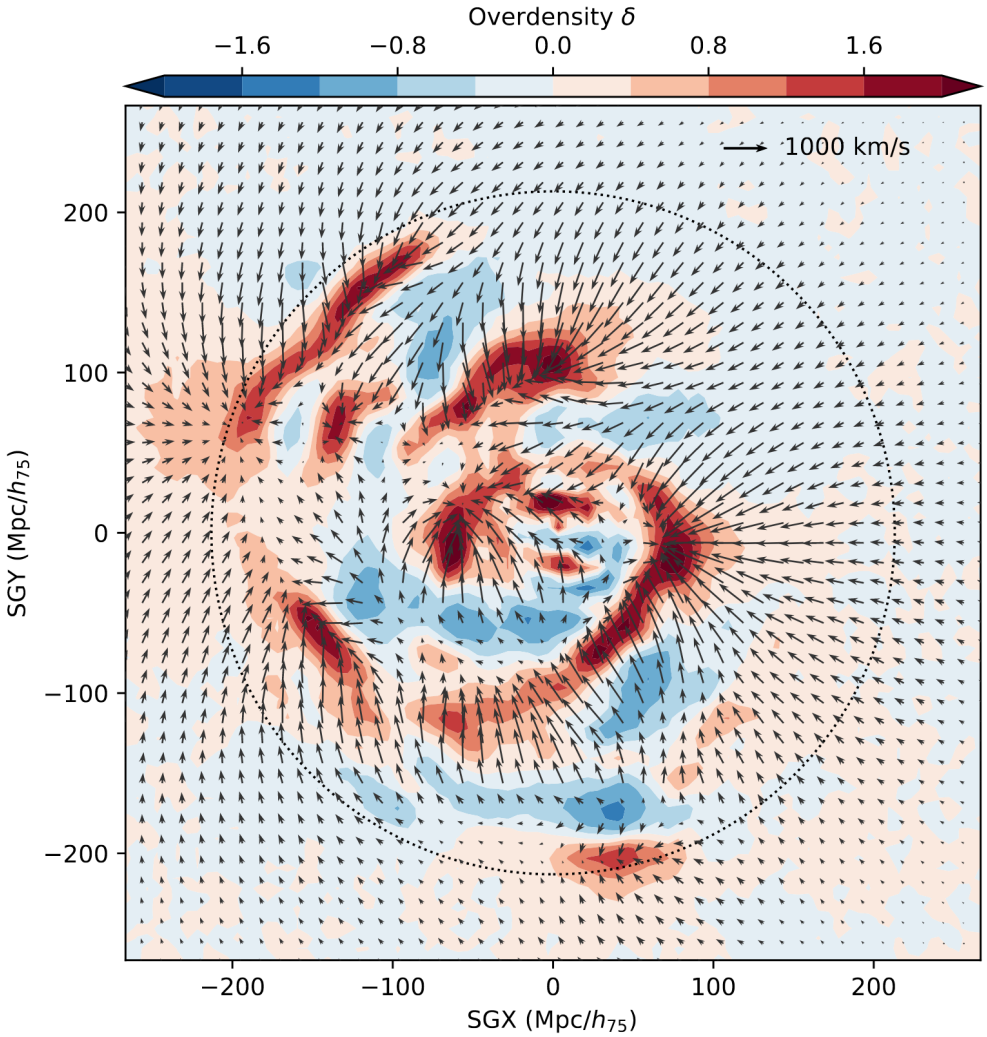

Figure 1.3: A slice of the Cosmicflows-3 peculiar velocity field (arrows) and over-density field (color scale) from Graziani et al. (2019).

the more local universe where the expansion is dominated by dark energy. The simplest form of anisotropic expansion to write down is triaxial expansion, characterized by a fractional departure from isotropic Hubble flow along three axes of expansion. Darling (2014) showed that triaxial expansion with arbitrary orientation can be expressed as a curl-free quadrupolar proper motion field. Using the a catalog of 429 extragalactic radio proper motions (Titov & Lambert, 2013), Darling (2014) found that the expansion is isotropic to within 7%.

***l* ≥ 1 E-modes: peculiar velocity field.** LSS in the universe grows hierarchically through gravitational interactions, leading to the observation of galaxy peculiar velocities induced

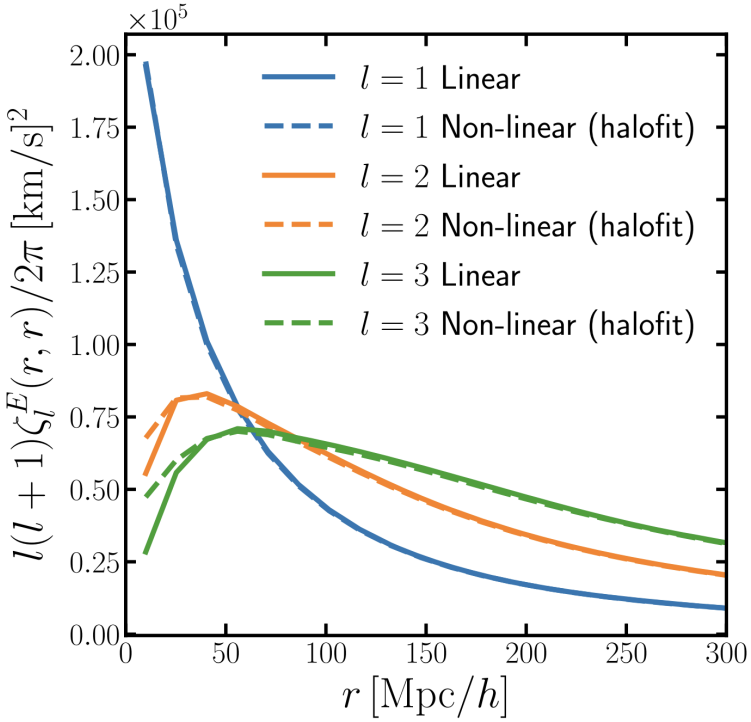

Figure 1.4: The first three multipoles of the peculiar velocity power spectrum from Hall (2019). For each multipole, the power spectrum has been computed from linear theory (solid) and and with a non-linear correction (dashed).

by over-densities. For example, Figure 1.3 shows the peculiar velocity field of the Cosmicflows-3 sample of galaxies mapped onto the reconstructed density field (Graziani et al., 2019), demonstrating velocity infalls onto over-dense regions. The peculiar velocity power spectrum is expected to be curl-free (Percival & White, 2009), with the dominant order increasing as a function of distance. Figure 1.4 shows the $l = 1, 2, 3$ multipoles of the LSS power spectrum as a function of distance from Hall (2019). Most of the power is in $l = 1$ at small distances. As the distance increases, the power shifts to higher l (smaller angular scales), with the total power integrated over all l remaining constant.

The peculiar velocity field translates to an E-mode proper motion vector field that will be dependent on distance. Thus, the peculiar velocity field is a confounding signal for the detection of secular parallax. However, on smaller angular scales the peculiar proper motions are separable from secular parallax. Methods to measure the peculiar velocity field using proper motions have been

proposed (e.g. Nusser et al. 2012; Darling & Truebenbach 2018; Truebenbach & Darling 2018; Hall 2019), and the benefit of a peculiar proper motion measurement is the ability to probe the density power spectrum without precise knowledge of the distances of the sample. By comparison, measurements of the radial component of peculiar velocity (such as Cosmicflows) require precise distance measurements to separate the peculiar velocity from the recession velocity due to expansion.

$l \geq 2$ E and B-modes: primordial gravitational waves. Primordial gravitational waves are predicted by inflation in the early universe. One much sought-after observational signature of the primordial gravitational wave background is B-mode polarization of the CMB, the detection of which would constrain models of inflation (see Baumann et al. 2009 for a discussion). However, foreground dust in our own Galaxy imparts a B-mode polarization as well, which obscures the gravitational wave signal. Pulsar timing arrays are sensitive to very low frequency gravitational waves, and a stochastic gravitational wave background at these frequencies is expected to be dominated by supermassive black hole binaries. However, current constraints from pulsar timing arrays do not detect the background signal (Arzoumanian et al., 2020). Meanwhile, gravitational wave detectors such as LIGO and VIRGO detect an astrophysical foreground from compact binaries which mask the stochastic gravitational wave background (e.g. Abbott et al. 2016, 2021; Biscoveanu et al. 2020).

Another avenue to constrain primordial gravitational waves is through extragalactic proper motions. Gravitational waves will deflect light from distant sources, creating an apparent proper motion (Braginsky et al., 1990). The proper motions will be correlated on a variety of angular scales ($l \geq 2$) and with equal power in the E and B-modes. The energy density of the primordial gravitational wave background, Ω_{GW}, is related to the scale of the imparted proper motion (Gwinn et al., 1997; Book & Flanagan, 2011), and since the quadrupole contributes 5/6 of the total signal, Ω_{GW} may be estimated by

$$\Omega_{GW} = \frac{6}{5}\frac{1}{4\pi}\frac{P_2}{H_0^2}, \tag{1.10}$$

where P_2 is the total quadrupole power (Eq. 1.6). Darling et al. (2018) found 95% confidence

upper limits on the gravitational wave background of $\Omega_{GW} < 0.0064$ using 711 radio sources, and $\Omega_{GW} < 0.011$ using proper motions of 508 radio sources with one epoch of astrometry from the *Gaia* mission. We additionally used the catalog of *Gaia* extragalactic objects presented in Chapter 2 to predict that *Gaia* astrometry alone will limit the gravitational wave background to $\Omega_{GW} < 0.006$.

1.1.2 Measuring Astrometry for Extragalactic Objects

Much of the work studying extragalactic proper motions has utilized high precision astrometry of radio quasars from Very Long Baseline Interferometry (VLBI). Astrometry of extragalctic radio sources has been ongoing since the 1970's to form the International Celestial Reference Frame (ICRF; Charlot et al. 2020). Previously thought to be stationary on the sky, the decades of radio observations have revealed that these sources are in fact not stationary. Relativistic jets cause intrinsic proper motions that often dominate the individual motions and are a source of uncorrelated noise in the proper motion vector fields. Additionally, Titov et al. (2011) first detected the correlated secular aberration drift in the quasar proper motion field, which was unaccounted for in previous iterations of the ICRF.

The European Space Agency's *Gaia* mission is an optical astrometric survey that provides an all-sky catalog complete down to a magnitude of $G \sim 21$. While the *Gaia* mission was designed for and predominately measures astrometry of stars in the Galaxy, the telescope also detects a sample of the brightest extragalactic objects, including active galactic nuclei (AGN), quasars, and resolved galaxies. The onboard source selection algorithms are optimized for stars, so most extragalactic sources will be point-like. AGN and quasars are therefore typically better fit than resolved galaxies, and often multiple peaks will be detected in an individual resolved galaxy which can degrade the astrometry (Lindegren et al., 2021).

The *Gaia* sample of extragalactic objects will not reach the same astrometric precision achieved with VLBI. The expected end-of-mission errors for extragalactic objects are on the order of a few 100 μas yr^{-1}. However, *Gaia* has detected several million extragalactic sources (Gaia Collaboration et al., 2022a), and sensitivity to correlated proper motions scales with sample size as $N^{-1/2}$

in amplitude and as N^{-1} in power. Additionally, *Gaia* detects galaxies which are more nearby compared to the radio quasar sample, making the *Gaia* sample uniquely suited to constraining secular parallax and low-multipole peculiar velocity fields.

The first challenge in using the *Gaia* extragalactic proper motions is finding them. The *Gaia* mission has measured proper motions for 1.5 billion objects, the vast majority of which are stars in our Galaxy. Stars will have generally much larger, more significant proper motions than extragalactic sources, so too much stellar contamination will dominate the proper motion field. Several methods to identify extragalactic objects in the *Gaia* catalog have been implemented, including machine-learning using only *Gaia* data (Gaia Collaboration et al., 2022a), and cross-matches with external catalogs of AGN and quasars (Gaia Collaboration et al., 2018a, 2022b).

The selection method will depend on the proper motion signal of interest. For low-multipole signals, all-sky coverage is desired to sample the vector field on large angular scales. If the signal is distance-independent, such as the secular aberration drift or anisotropy, then a selection method that maximizes sample size while targeting point-like sources such as AGN will be ideal. By contrast, if the signal is stronger at low distances, such as secular parallax and the low-mulitpole modes of the peculiar velocity field, then selecting for the less numerous nearby galaxy sample will be advantageous despite the larger astrometric errors.

In Section 1.3, I will summarize my work identifying, analyzing, and simulating *Gaia* extragalactic proper motions.

1.2 Galactic Center Stellar Kinematics

1.2.1 Stars as Probes of Gravity

Broadly, stellar kinematics probe the gravity profile in which the stars reside, which in the centers of galaxies will be dominated by a supermassive black hole, stars, and dark matter. The dark matter profiles in galactic centers are particularly of interest due to the discrepancy between simulations, which predict steep profiles (cusps), and observations, which find flat profiles (cores).

This difference is known as the core-cusp problem (see de Blok 2010 for a review). Dark matter profiles on scales of several parsec and smaller are additionally poorly constrained by both simulations and observations.

The question of the distribution of dark matter in galactic centers is also tied to the presence and growth of the central black hole. If the supermassive black hole grows adiabatically, then the dark matter profile will steepen within the sphere of influence of the black hole (Gondolo & Silk, 1999), known as a dark matter spike. Stars respond similarly to the presence of a black hole, so one may expect to find stellar and dark matter spikes in the same galaxies. However, gravitational scattering of dark matter particles off of stars in the central stellar cluster will soften the dark matter spike (Gnedin & Primack, 2004; Merritt, 2004; Shapiro & Heggie, 2022). The stellar cusp in our galaxy is shallower than predicted by theory (Schödel et al., 2018; Habibi et al., 2019), suggesting the absence of a dark matter spike, but the two profiles are not necessarily coupled if the stellar cluster formed after the growth of the black hole.

Sgr A* is the supermassive black hole at the center of our galaxy and a strong, compact radio source. The first strong evidence for the existence of the black hole was provided by near-infrared (near-IR) observations of stars on short period orbits around Sgr A* (Ghez et al., 2000, 2005; Schödel et al., 2002; Eisenhauer et al., 2005). The orbits of these "S" stars suggest a black hole mass of $4.15 \times 10^6\ M_\odot$ and a distance to the GC of 8.2 kpc Ghez et al. (2008); Genzel et al. (2010). Additionally, following the pericenter passage of S2 — a star on a highly eccentric orbit with pericenter at 120 AU from Sgr A* (approximately 1400 times the black hole's event horizon) — IR stellar orbits were able to test General Relativity. Namely, gravitational redshift (GRAVITY Collaboration et al., 2018; Do et al., 2019) and Schwarzschild precession (GRAVITY Collaboration et al., 2020) were detected from the orbit of S2.

Since there is no obvious, bright near-IR counterpart source to Sgr A* from which to reference the positions of S stars, the IR stellar orbit measurements rely on the definition of an astrometric reference frame. The first method used was to define a cluster-rest frame, where a set of reference stars in the central stellar cluster were assumed to have zero net motion. However, the accuracy of

this reference frame is limited by the intrinsic dispersion of the proper motions of reference stars and the number of reference stars, and therefore the cluster-rest frame does not improve over time (Yelda et al., 2010).

More recently, the reference frame has been defined using the proper motions of SiO maser-emitting stars in the vicinity of Sgr A*. Stellar SiO masers are high brightness temperature sources observed in radio frequencies where the Sgr A* radio source is also detected (see more discussion of the origins and observations of SiO masers below in Section 1.2.2). Observations of the GC over the past several decades have identified at least 28 stellar SiO masers within a few parsecs of Sgr A* (e.g. Menten et al. 1997; Reid et al. 2007; Li et al. 2010; Borkar et al. 2020), and a subset of these maser-emitting stars are bright IR sources used for the reference frame. Menten et al. (1997) first proposed measuring the SiO proper motions relative to the Sgr A* radio continuum and matching the radio positions to the IR counterparts to determine the location of Sgr A* in IR images and establish a reference frame where Sgr A* is at rest. Since then, several iterations of the reference frame have been determined using SiO maser proper motions (e.g. Menten et al. 1997; Reid et al. 2007; Yelda et al. 2010; Sakai et al. 2019). Figure 1.5 shows an IR image from Reid et al. (2007) of stars in the GC with the proper motions of SiO masers used for the reference frame over-plotted. The advantage of the radio reference frame is that as proper motion uncertainties decrease in time by $t^{-3/2}$, so does the reference frame improve. However, projecting the maser proper motions forward in time is a large source of uncertainty in the reference frame and resulting IR orbital measurement, so continuous monitoring of the SiO masers is required to improve the precision of IR measurements.

1.2.2 Stellar SiO Masers

Here I will introduce some of the maser physics background necessary to understand the observed properties of stellar SiO masers and their impact on the accuracy of maser measurements for tracing stellar kinematics (see Elitzur 1992 for a comprehensive review of astrophysical masers). Masers are defined based on the original acronym: microwave amplification by stimulated emission

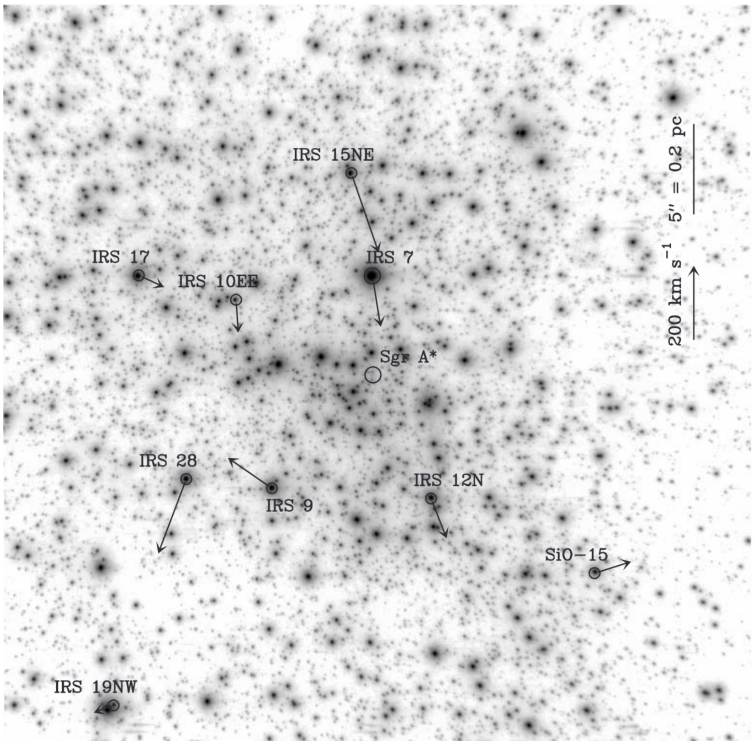

Figure 1.5: An IR (K-band) image of the central ±20" of the GC from Reid et al. (2007), with east towards the left and north towards the top. SiO maser emitting stars are circle and their proper motions with respect to Sgr A* are indicated with arrows. The scales in the upper right assume a distance to the GC of 8.0 kpc.

of radiation (MASER). In order to have maser action, several conditions must be met. First, a population inversion of the maser energy levels is required, i.e. $N_2 > N_1$, where N_1 and N_2 are the populations of molecules in the lower and higher energy levels of the maser transition, respectively. Such a population inversion must be sustained by a "pumping" mechanism involving at least a third level, wherein molecules are excited to a higher energy level and quickly decay to the metastable upper state of the maser transition. The pump may be a radiative, collisional, or chemical process. Second, the maser must be stimulated by some external radiation, which may be continuum or spontaneous emission of the same energy as the maser transition.

In thermodynamic equilibrium, the energy level populations will follow a Boltzmann distribution:

$$\frac{N_2}{N_1} = \exp\left(\frac{-\Delta E}{kT_x}\right), \tag{1.11}$$

where ΔE is the energy of the transition, T_x is the excitation temperature, and k is the Boltzmann constant. Thus, for a population inversion where $N_2 > N_1$, the inferred excitation temperature is negative and the system is necessarily not in thermodynamic equilibrium. Masers must therefore occur in low density environments, otherwise a high density medium will cause the populations to thermalize.

Stimulated emission occurs when a transition from higher to lower energy is induced by an incoming photon with frequency matching that of the transition. The outgoing photon is coherent with the initial photon to conserve energy and momentum (i.e. matching in energy and direction). In a population inversion, the rate of stimulated emission will be higher than absorption, and thus radiation is no longer attenuated by the medium following $\exp(-\tau_\nu)$, where τ_ν is the optical depth, but amplified by $\exp|\tau_\nu|$. Thus, the absolute value of the optical depth is known as the maser gain.

The maser gain is related to the path length for radiation, l, and the populations by

$$|\tau_\nu| \propto \int (N_2 - N_1) dl. \tag{1.12}$$

In order to produce large gain while maintaining the requirement of low density, significant maser amplification requires a long path length, or large column density. The large spatial extent and low densities (compared to terrestrial densities) of astrophysical environments such as circumstellar envelopes make them ideal environments for maser action. However, velocity coherence is required along the line of sight in order to have significant maser amplification, since transitions will not be stimulated by maser photons if they are Doppler shifted. Therefore masers are formed along paths of velocity coherence, and result in beamed emission with very narrow line widths. Maser sources are generally comprised of numerous component sources with their own well-defined velocities.

Stellar masers typically occur in the extended atmospheres and circumstellar envelopes of red giants and asymptotic giant branch (AGB) stars. The AGB is a post main-sequence phase of stellar evolution reached by stars with masses of less than about 6 $M_\odot$. During the AGB phase, the star has high luminosity ($\geq 3000 L_\odot$), low temperature (< 3000 K), and begins to lose mass at rates of around 10^{-7} – 10^{-4} $M_\odot$ yr^{-1} via low velocity winds (Habing, 1996). This mass-loss

leads to the formation of a circumstellar envelope. Radiation pressure on dust grains which form at around two stellar radii drive a stellar wind, accelerating the dust and the rest of the circumstellar envelope outward.

In oxygen-rich AGB stars, molecular maser emission is frequently observed from SiO, H_2O, and OH molecules. The maser emission originates from different radii about the star depending on the molecule, with SiO emitting closest to the star in the extended atmosphere, followed by H_2O in the envelope, and OH at the largest radii in the outer envelope. A schematic from Reid (2002) of the stellar environment and the locations of the different species of masers is shown in Figure 1.6. The layered structure of the maser molecules is predicted by excitation arguments (Elitzur, 1992): SiO masers are generated in excited vibrational states with high excitation energies, whereas H_2O and OH masers are generated by transitions within the ground vibration state. The temperatures required to pump the SiO, H_2O, and OH masers are $\sim$ 1800, 643, and 120 K, respectively, with decreasing temperature corresponding to larger radii where the maser may be found.

The SiO maser lines observed are rotational transitions in typically excited vibrational states. Several SiO lines are observed at frequencies around 43 GHz ($J = 1 - 0$) and 86 GHz ($J = 2 - 1$). They typically emit at radii of $\sim$ a few AU, above the photosphere and below the dust formation point (Kemball, 2007). Dust grains deplete SiO gas, so dust formation puts an upper limit on the radius where SiO masers may operate.

VLBI observations of stellar SiO masers typically resolve the emission into discrete spots in a ring-like structure around the star. An example of the 43 GHz masers towards TX Cam observed over several months by Gonidakis et al. (2013) are shown in Figure 1.7. The results of this monitoring campaign also demonstrate the variability of SiO maser emission over relatively short timescales. Individual maser spots track the local motion of material around the star, which is not always symmetric, and components may turn on or off between observations. The variability of the maser components may be caused by changes in the dominant pumping mechanism or acceleration of the maser medium with respect to the star disrupting the requirement of velocity coherence. The result for lower resolution observations which detect the aggregate maser emission

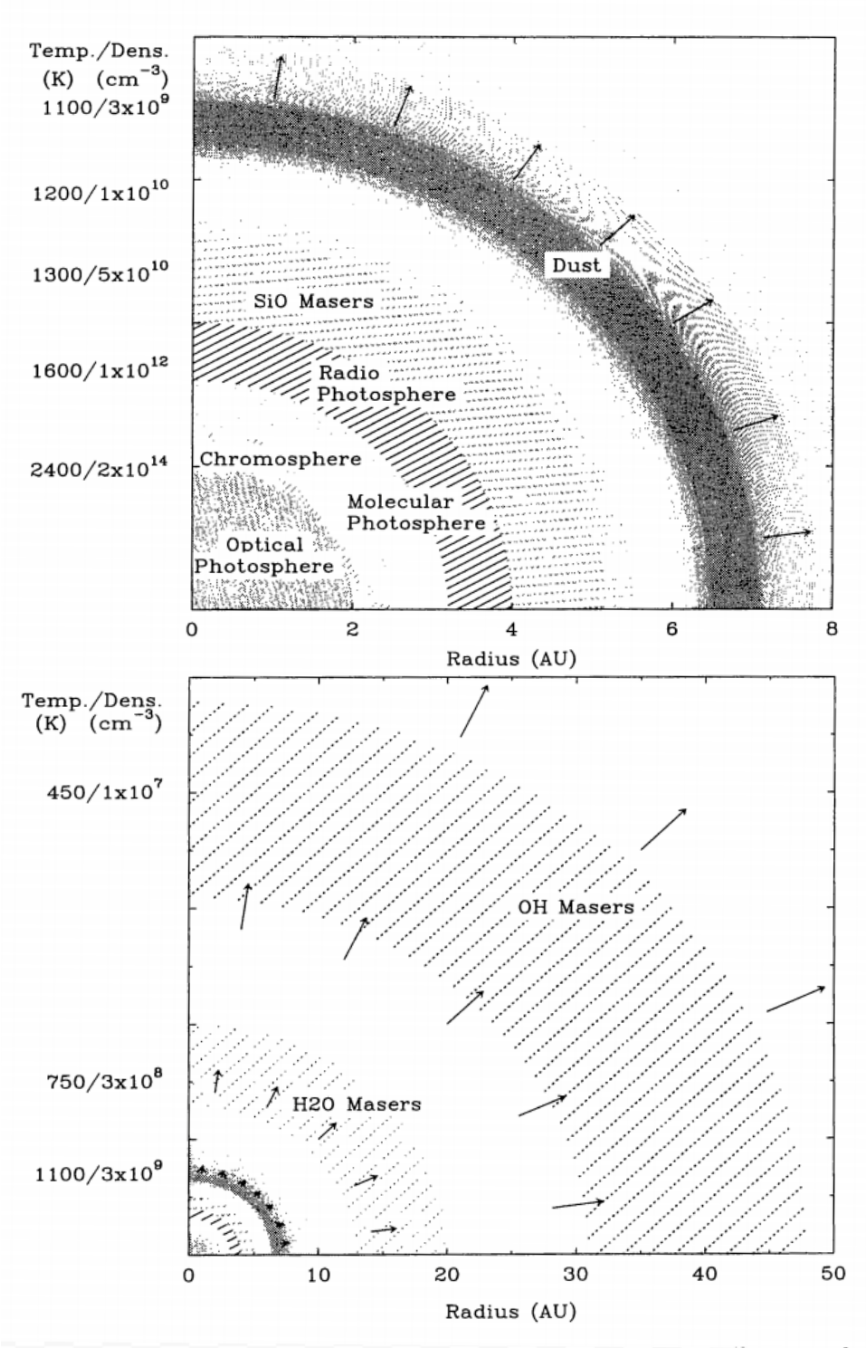

Figure 1.6: A schematic of a star and circumstellar envelope of a maser-emitting star from Reid (2002). The upper panel shows the structure up to the dust formation point, and the lower panel shows the outer envelope. The vertical axes indicate characteristic temperatures and densities at each radius.

of many components is that SiO maser spectra often show multiple peaks distributed over a velocity range of $\sim$ 10 km s^{-1} relative to the systemic stellar velocity (Jewell et al., 1991), and which may

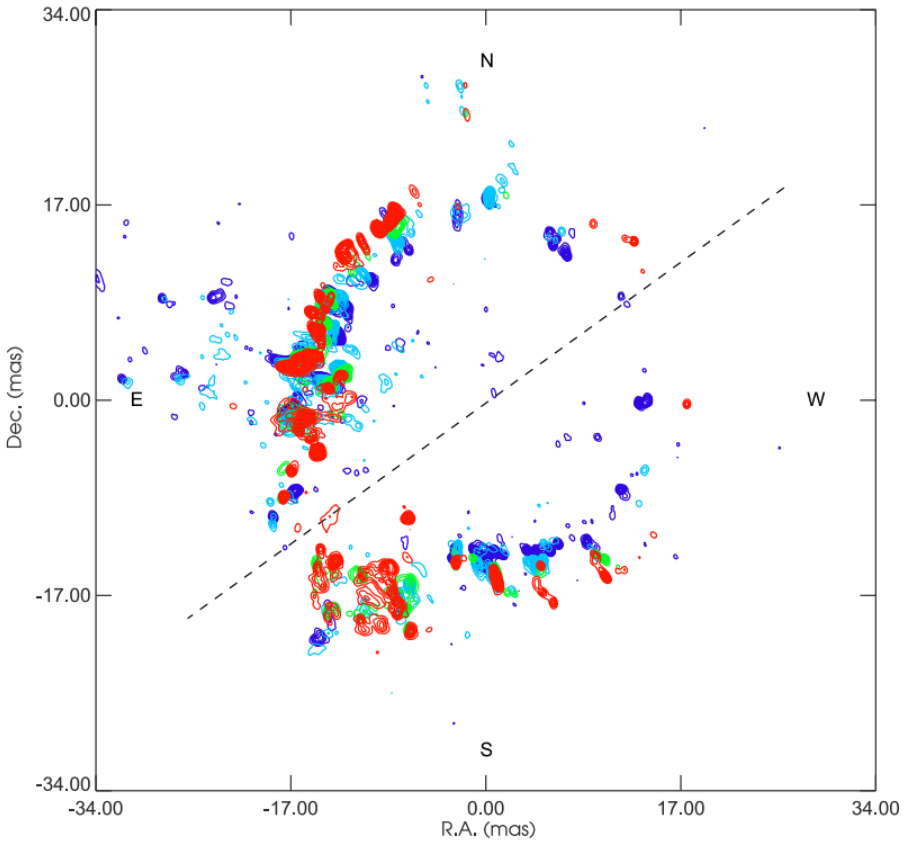

Figure 1.7: Contour maps of the $v = 1$, $J = 1 - 0$ SiO masers towards the Mira variable star TX Cam from Gonidakis et al. (2013). Several epochs are overplotted to show the expansion of the star: 1997 May 24 (purple), 1997 June 19 (blue), 1997 October 9 (green), 1997 December 17 (red). The emission shows asymmetrical expansion along the NE-SW and SE-NW axes, with faster flow along the later axis.

vary in time. Different maser transitions observed simultaneously may not match in the location of spectral peaks since the transitions are not necessarily coincident around the star.

1.2.3 Radio Interferometry

Radio interferometers are telescopes comprised of an array of antennae. The angular resolution of most telescopes is diffraction limited, meaning that the smallest angular scale resolved will be $\sim \lambda/D$, where λ is the observed wavelength and D is diameter of a telescope. Thus for low frequency, long wavelength radio observations, exceedingly large dishes would be required to achieve high angular resolution with single-dish observations. Radio interferometers resolve this

issue by combining signals from many dishes to simulate the aperture of a telescope the size of the largest separation between antennae.

Rather than directly measuring the brightness of the sky, $I(x, y)$, interferometers sample the Fourier transform of the brightness, known as the complex visibility, $V(u, v)$. Creating an image from the observations is thus a process of computing the inverse Fourier transform of the visibilities and recovering the intensity distribution of the original image of the sky (Thompson et al., 2017). In practice, the synthesized beam of the instrument, which is analogous to the point spread function of a single-dish telescope, must be deconvolved from the inverse Fourier transform of the visibilities to obtain a model of $I(x, y)$. The resulting image is not unique; in fact there are infinite possible solutions compatible with the sampled visibilities. Therefore, image-plane analysis of interferometric data, for example fitting astrometry, is a process of fitting models to models.

In cases where the observed source can be represented with a simple model (or a linear combination of simple models as in the case of a sample of point sources), one may forgo the imaging step and instead fit to the visibilities (e.g. Martí-Vidal et al. 2012; see also Pearson 1995 for a discussion of visibility model fitting and its applications). Visibility fitting is often employed in analysis of data from sparse arrays where there are too few visibilities to create an image (e.g. Doeleman et al. 2008). Even for arrays such as VLA and ALMA with a large number of antennas, there are benefits to direct analysis of the visibilities. When comparing source properties between different observations, differences between epochs and telescopes used may be compounded by the imaging process. The visibilities have uncorrelated Gaussian noise, unlike images where the noise is correlated between pixels, hence the parameters of simple models can often best be obtained with visibility analysis. Additionally, the smallest resolvable angular size is smaller than the diffraction limit of the interferometer for high signal-to-noise sources (Martí-Vidal et al., 2012), and thus avoiding the imaging process and fitting directly to the visibilities maximizes the resolution of the observations.

In the following section, I will summarize my work presented in this dissertation using radio observations of SiO masers in the GC to study stellar kinematics.

1.3 Summary of This Dissertation

In Section 1.1, I presented several applications of correlated extragalactic proper motions. These include the secular aberration drift, secular parallax, aniostropic expansion, and the peculiar velocity field due to LSS. The *Gaia* mission offers a rich data set of extragalactic proper motions, but the extragalactic sample must be identified and methods to extract the various signals developed. In Section 1.2, I discussed how stellar kinematics measured from proper motions and Doppler shifts trace the gravity profile in the GC, including the influence of the supermassive black hole Sgr A*, and distributed stars and dark matter. The precise profiles of dark matter on small scales in the centers of galaxies, including our own, remains an open question. Stellar SiO masers trace the kinematics of a sample of GC stars with very high precision. However, maximizing the sensitivity of maser measurements to the gravity profile requires continual monitoring of their positions and velocities, as well as the development of methods to account for the intrinsic noise introduced by the complex and variable maser structure. The primary goals of this dissertation are to progress the science of high precision proper motion and velocity measurements and to explore their applications to various fundamental properties of our universe — from the nature of dark matter in galactic centers to expansion of the local universe.

In Chapter 2, I present a catalog of mid-IR selected AGN in the first *Gaia* data release. As discussed in Section 1.1.2, the method of separating the extragalactic sources from the vast majority of stars in the *Gaia* survey dictates the proper motion signals which may be sampled. At the time of the first data release, the *Gaia* catalog did not contain ancillary data products with in-house-developed methods to identify the extragalactic sample. Therefore, I use a well-established method to identify AGN in the *WISE* survey — an all-sky mid-IR survey — to identify over 500,000 likely AGN in the first *Gaia* catalog, and assess the completeness and stellar contamination of the sample. By simulating the end-of-mission proper motions of these AGN candidates, I predict the sensitivity of this sample to the secular aberration drift and anisotropic expansion.

The *Gaia-WISE* sample of AGN will not be sensitive to the secular parallax dipole due to

their typically high redshifts and the $1/D$ dependence of the secular parallax amplitude. Therefore, in Chapter 3, I find a distinct sample of nearby galaxies with redshift-independent distance measurements from the Cosmicflows survey, and develop methods to measure the secular parallax dipole. I present two measurements of the dipole using the second and third *Gaia* data releases, which result in the first limits on the secular parallax amplitude. The influence of the low-mulitpole modes of the peculiar velocity field are explored using simulated end-of-mission proper motions of the galaxy sample. I show that the peculiar velocities offset the expected secular parallax dipole direction and amplitude such that a distance-dependent dipole measurement probes the combination of Galaxy's linear velocity and the correlated motions of nearby galaxies unless the CMB-derived velocity is assumed as a prior.

In Chapter 4, I shift focus closer to home and present 3D stellar kinematics in the GC using radio observations of SiO masers. I analyze five epochs of observations using visibility fitting to extract astrometry and spectra, which is a novel approach for the SiO maser sample. The resulting kinematics are the most precise published velocities for this sample of stars, and a first attempt to measure their accelerations. I discuss how the intrinsic variability of maser measurements and the unknown distances of the stars may result in the observation of several stars with very large velocities or accelerations. Lastly, I demonstrate how these stellar kinematics probe the mass distribution in the GC and assess the precision required to detect a hypothetical dark matter spike.

I build upon this maser work in Chapter 5 using two new epochs of observations. I present updated methods to measure the maser velocities and accelerations. These include a more conservative approach to the acceleration limits calculated from proper accelerations and a more realistic estimation of the systematic errors introduced by maser variability. I assess the updated kinematics in terms of the GC mass distribution. Additionally, I confirm several anomalous velocity and acceleration measurements first identified in the previous chapter, suggesting that these measurements cannot be simply disregarded as spurious. Therefore, I explore the possibility that orbits due to unseen binary stars are enhancing the measured stellar kinematics. Finally, I discuss future work which will address the maser measurement errors and maximize the physical applications of the

maser kinematics.

In Chaper 6, I conclude with a summary of the findings of these works and a discussion of future prospects for measurements of cosmic probes.

Chapter 2

The Gaia-WISE extragalactic astrometric catalog

Abstract

The *Gaia* mission has detected a large number of active galactic nuclei (AGN) and galaxies, but these objects must be identified among the thousandfold more numerous stars. Extant astrometric AGN catalogs do not have the uniform sky coverage required to detect and characterize the all-sky, low-multipole proper motion signals produced by the barycenter motion, gravitational waves, and cosmological effects. To remedy this, we present an all-sky sample of 567,721 AGN in *Gaia* Data Release 1, selected using *WISE* two-color criteria. The catalog has fairly uniform sky coverage beyond the Galactic plane, with a mean density of 12.8 AGN per square degree. The objects have magnitudes ranging from $G = 8.8$ down to *Gaia's* magnitude limit, $G = 20.7$. The catalog is approximately 50% complete but suffers from low stellar contamination, roughly 0.2%. We predict that the end-of-mission *Gaia* proper motions for this catalog will enable detection of the secular aberration drift to high significance (23σ) and will place an upper limit on the anisotropy of the Hubble expansion of about 2%.

This Chapter was published as Paine et al. 2018, ApJS, 236, 37, and is reproduced here.

2.1 Introduction

The *Gaia* mission will provide astrometric and proper motion measurements for a large number of bright active galactic nuclei (AGN), but separating the $\sim 10^6$ extragalactic objects from the $\sim 10^9$ stars remains challenging (Gaia Collaboration et al., 2016a). Current catalogs include the

Large Quasar Astrometric Catalog (LQAC; Souchay et al. 2015), the Véron Catalog of Quasars and AGN (Véron-Cetty & Véron, 2010), the Secrest et al. (2015) catalog of mid-infrared AGN, and the *Gaia* Universe Model Snapshot (GUMS), a simulated catalog (Robin et al., 2012). Many of these catalogs are dominated by the Sloan Digital Sky Survey (SDSS) footprint that covers 35% of the sky (Ahn et al., 2012), which is problematic for all-sky proper motion studies that attempt to detect low-multipole correlated proper motion signals such as the secular aberration drift dipole (Titov & Lambert, 2013; Xu et al., 2012; Truebenbach & Darling, 2017b), the stochastic gravitational wave background quadrupole (Gwinn et al., 1997; Titov et al., 2011; Book & Flanagan, 2011; Darling et al., 2018), or the isotropy of the Hubble expansion (Darling, 2014; Chang & Lin, 2015; Bengaly, 2016).

Desirable features of extragalactic proper motion catalogs are all-sky, uniform selection, and low stellar contamination. Completeness is not very important: it impacts the signal-to-noise of correlated global proper motions, which scales with the square root of the number of objects. In this work, we consider only low-multipole proper motion signals, but completeness will ultimately determine the maximum multipole that can be studied due to the limiting sky density of sources. Stellar contamination is the largest concern for detecting global signals of a few μarcsec yr^{-1} because stellar proper motions can be large and significant and therefore dominate the individually insignificant extragalactic proper motions. What stellar contamination remains in any given extragalactic catalog may be addressed using a non-Gaussian permissive likelihood function as described in Darling et al. (2018).

This paper presents the *Gaia-WISE* extragalactic astrometric catalog, a catalog designed to have low stellar contamination and fairly uniform sky coverage outside of the Galactic Plane. Section 2.2 presents the *WISE* color-color selection used to identify AGN and exclude stars, and Section 2.3 explores the sky distribution of the catalog, its optical and mid-IR properties, its redshift distribution, and the expected end-of-mission proper motion uncertainties. Section 2.4 predicts the performance of this catalog in detecting the secular aberration drift caused by the barycenter acceleration about the Galactic Center. Section 2.4 also predicts the expected *Gaia*

sensitivity to anisotropy in the Hubble expansion. We discuss the ramifications of this work and the future prospects for extragalactic proper motion studies in Sections 2.5 and 2.6. We assume a Hubble constant of $H_0 = 72$ km s^{-1} Mpc^{-1} and a flat cosmology (other cosmological assumptions are not required).

2.2 Catalog Selection Method

The *WISE* survey is an all-sky mid-infrared (MIR) survey in the 3.4, 4.6, 12 and 22 μm bandpasses ($W1$, $W2$, $W3$, and $W4$, respectively; Wright et al. 2010). The ALLWISE data release, used in this work, combines data from the cryogenic and post-cryogenic (Mainzer et al., 2011) survey phases, and provides better sensitivity and accuracy over previous *WISE* data releases. *WISE* colors have been shown to cleanly separate AGN from stars and normal galaxies, and several methods exist in the literature for selecting AGN with *WISE* (e.g. Stern et al. 2005, 2012; Mateos et al. 2012; Assef et al. 2013; Truebenbach & Darling 2017a). To create our catalog of *Gaia* AGN, we did not consider selection methods using only a $W1 - W2$ color cut in order to avoid contamination from brown dwarfs at low Galactic latitudes, which can reside in the color space selected by single-color cuts (Kirkpatrick et al., 2011).

We employed the ALLWISE catalog of MIR AGN described in Secrest et al. (2015). The catalog is based on the *WISE* two-color selection technique of Mateos et al. (2012) which has cuts in the $W1 - W2$ and $W2 - W3$ color space, referred to as the color wedge. This AGN color wedge was defined based on the Bright Ultrahard *XMM-Newton* survey (BUXS), one of the largest flux-limited samples of 'ultrahard' X-ray-selected AGN, but the method does not employ X-ray selection directly. BUXS is comprised of 258 objects, of which 56.2% are type 1 AGN and nearly the rest are type 2. BUXS type 2 AGN are intrinsically less luminous than type 1 AGN. Since the completeness of the MIR wedge has a strong dependence on luminosity, the wedge preferentially selects type 1 AGN. Secrest et al. (2015) selected 1.4 million MIR AGN using ALLWISE profile-fitting magnitudes with S/N ≥ 5 and the color wedge criteria of Mateos et al. (2012). They included an additional constraint of limiting their selections to ALLWISE sources with `cc_flags` = "0000"

to avoid sources contaminated by image artifacts.

We cross-matched the Secrest et al. (2015) catalog of MIR AGN with *Gaia* Data Release 1 using *allWISE_best_neighbour*, the precomputed *WISE* cross-match table provided in the *Gaia* archive (Marrese et al., 2017). The table includes only the most likely matches between the *WISE* and *Gaia* catalogs, called "best neighbours." Since *Gaia* is used as the leading catalog in cross-matching, a *Gaia* source may be matched to multiple sources from an external catalog. Marrese et al. (2017) then determined the best match to the *Gaia* source using the angular distance, position errors, epoch difference, and density of sources in the external catalog. A small number of *Gaia* sources have $G > 21$, fainter than *Gaia's* nominal magnitude limit of 20.7, which are likely incorrectly determined magnitudes (Gaia Collaboration et al., 2016a). Such objects were excluded from the cross-match. Additionally, all stars from the Tycho 2 survey were removed to avoid stellar contamination, which excluded 65 objects. We discuss possible further stellar contamination in Section 2.2.2. The resulting catalog of *Gaia* MIR AGN contains 567,721 objects. The first 10 objects are given in Appendix A, and the full catalog is available online.

2.2.1 Completeness

The completeness of the *WISE* color wedge selection is dependent on the ratio of the AGN luminosity to the host luminosity because host galaxy light can contaminate the MIR emission (Mateos et al., 2012; Padovani et al., 2017). Thus, lower luminosity AGN will have the colors of normal galaxies and will be excluded by the color wedge. To assess the completeness of our catalog, we compared the catalog to the sample of SDSS DR9 QSOs (Ahn et al., 2012) in *Gaia*. SDSS QSOs were identified in the *Gaia* source catalog via the cross-matching algorithm provided in the *Gaia* archive with a matching radius of 1 arcsecond. Of these *Gaia*-SDSS QSOs, 44.6% were also identified by the *WISE* color wedge, suggesting that our sample is missing more than half of all AGN in the *Gaia* catalog. Only 49.3% of *Gaia*-SDSS QSOs have S/N > 5 detections and zero contamination and confusion flags in all three *WISE* bands; most of the incompleteness of the *Gaia-WISE* catalog is therefore due to non-detections in the least-sensitive *WISE* W3 band. Among the

WISE-detected Gaia-SDSS QSOs, 90.2% lie in the *WISE* MIR color wedge. The remaining quasars generally have bluer $W1 - W2$ colors than the color wedge, likely due to contamination by host galaxy starlight.

2.2.2 Stellar Contamination

Mateos et al. (2012) found that contamination by normal galaxies in the MIR wedge is minimal. For astrometric purposes, however, objects need only be extragalactic, so unresolved galaxies are acceptable. Contamination by Galactic stars is of much greater concern due to their large proper motions.

To assess any remaining stellar contamination after omitting the Tycho stars, we cross-matched our sample with the SDSS DR12 catalog (Alam et al., 2015). In our sample, 229,073 AGN reside within the SDSS footprint, and 65,575 have a spectroscopic classification from SDSS. Of those, only 104 objects (0.16%) are identified by their spectroscopic classification as stars. Extrapolating to the whole sky gives approximately 910 total stars in our sample, suggesting negligible contamination from stars. We also consider contamination from dusty stars that would not be found in our SDSS cross-match. Nikutta et al. (2014) find that a majority of objects brighter than $W1 = 11$ are Galactic stars. Our sample contains 1836 objects with $W1 < 11$, which indicates a maximum of 0.32% contamination from dusty stars.

2.3 Results

2.3.1 Sky Distribution

Figure 2.1 illustrates the distribution of *Gaia*-*WISE* AGN on the sky. The lower density of AGN at low Galactic latitudes is due to a combination of dust along the Galactic plane and the effectiveness of the MIR color wedge at excluding stars. Additionally, *WISE* photometry is limited by confusion near the Galactic plane due to high source density (Wright et al., 2010). The higher densities near the ecliptic poles are due to increased coverage by both *WISE* and *Gaia*. The

Table 2.1: Catalog Statistics

	G (mag)	$W1$ (mag)	$W2$ (mag)	$W3$ (mag)	$W1-W2$ (mag)	$W2-W3$ (mag)	Redshift	$\sigma^a_{\mu,RA}$ (μas yr^{-1})	$\sigma^a_{\mu,Dec}$ (μas yr^{-1})
Mean	19.3	15.2	14.0	10.9	1.2	3.0	1.3	236	218
Median	19.4	15.3	14.1	11.1	1.2	3.0	1.2	205	191
Minimum	8.8	4.8	3.7	0.2	0.5	2.0	0.0	2	3
Maximum	21.0	18.8	17.1	12.9	2.2	5.8	7.0	1062	797

[a] *Gaia* expected end-of-mission proper motion uncertainty (see Section 2.3.5).

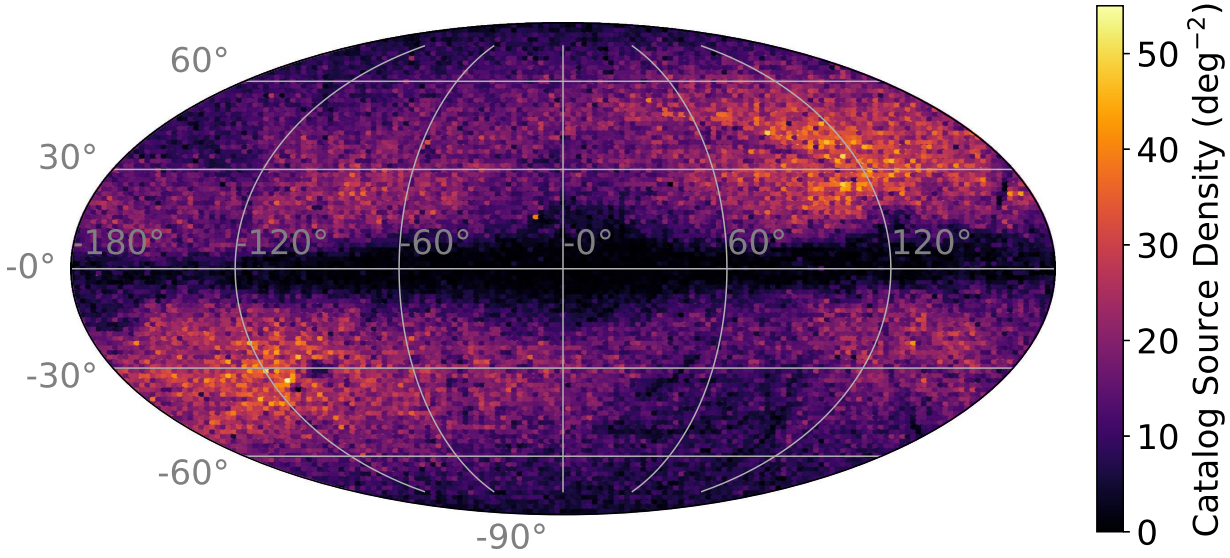

Figure 2.1: *Gaia*-*WISE* extragalactic astrometric catalog density plot in Galactic coordinates. The colorbar indicates the number of objects per deg^2.

mean and median densities above the Galactic plane ($b > 15°$) are 12.8 and 12.0 objects per deg^2, respectively, and the maximum density is 55 objects per deg^2.

2.3.2 Optical Properties

Gaia surveys the sky down to $G = 20.7$, with a small fraction of objects at $G > 21$ (Gaia Collaboration et al., 2016a). As illustrated in Figure 2.2, the majority of *WISE* AGN lie at the fainter end of *Gaia's* magnitude distribution. Statistics for the distribution of G magnitudes are listed in Table 2.1.

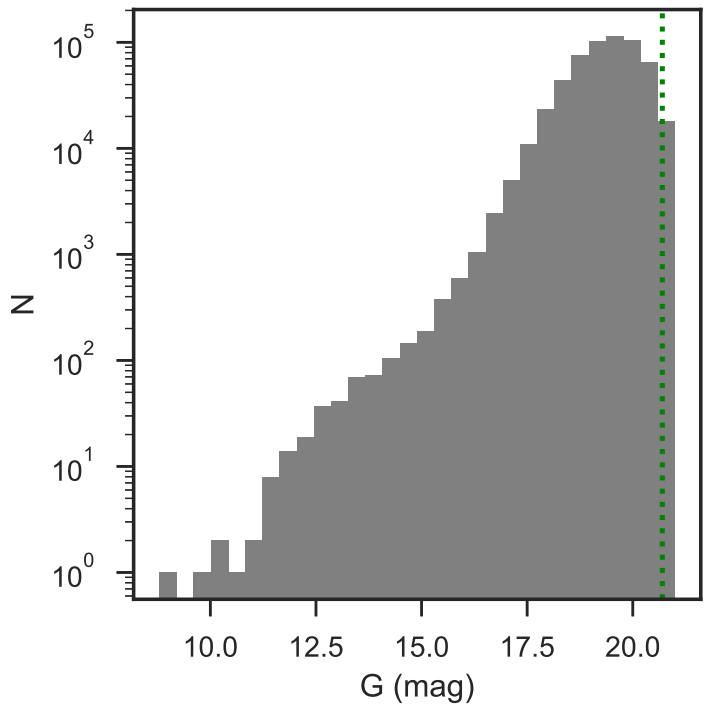

Figure 2.2: Distribution of *Gaia* G-band magnitudes in the *Gaia-WISE* extragalactic astrometric catalog. The green dotted line indicates *Gaia's* nominal magnitude limit, $G = 20.7$.

2.3.3 Mid-IR Properties

The *WISE* two color distribution for our catalog is shown in Figure 2.3, along with the Mateos et al. (2012) wedge. The majority of objects reside in a locus near the bluer end of the color wedge, with a small number of outliers with redder colors. The distribution around the locus tapers before the color cuts, suggesting that the color wedge captures most of the AGN population, except for the bottom right cut where AGN colors begin to overlap with the color space occupied by normal galaxies. The distributions of *WISE* $W1$, $W2$, and $W3$ magnitudes, and $W1 - W2$ and $W2 - W3$ colors are shown in Figure 2.4; statistics for these distributions are given in Table 2.1.

2.3.4 Redshifts

Redshifts were obtained for objects with spectroscopic redshifts from SDSS. Redshifts with nonzero warning flags or negative errors were discarded, since a negative redshift error indicates

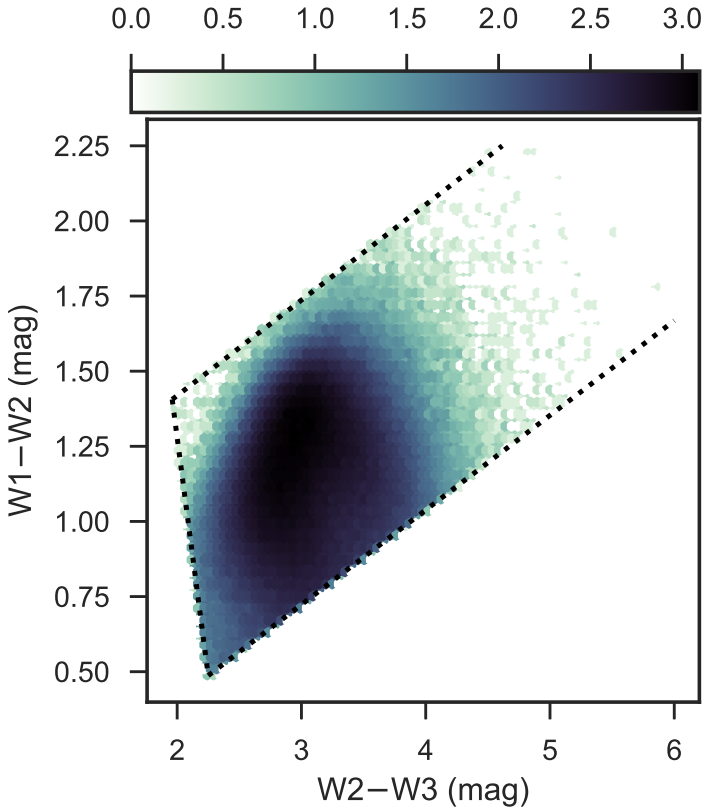

Figure 2.3: *WISE* colors for *Gaia* MIR AGN. The dashed lines indicate the color wedge of Mateos et al. (2012). The color bar indicates the logarithm of the number of objects per hexagonal bin.

a poor fit even if the warning flag is zero. This yielded redshifts for 90,365 objects ($\sim$ 15%). The redshift distribution is shown in Figure 2.5. Note that this distribution is incomplete and subject to selection bias due to targeted quasar surveys by SDSS and thus the corresponding redshift sensitivity biases. The catalog contains 202 redshifts above $z = 4$, which is unexpectedly high considering *Gaia's* magnitude limit. However, a majority of these are confirmed quasars in the SDSS Baryon Oscillation Spectroscopic Survey (BOSS) quasar catalog, of which many were selected for the survey using *WISE* colors (Pâris et al., 2017).

2.3.5 Proper Motion Uncertainties

Gaia DR2 will include positions, proper motions, and parallaxes — or limits on these quantities — for all objects. Predicted proper motion standard errors can be calculated ahead of the

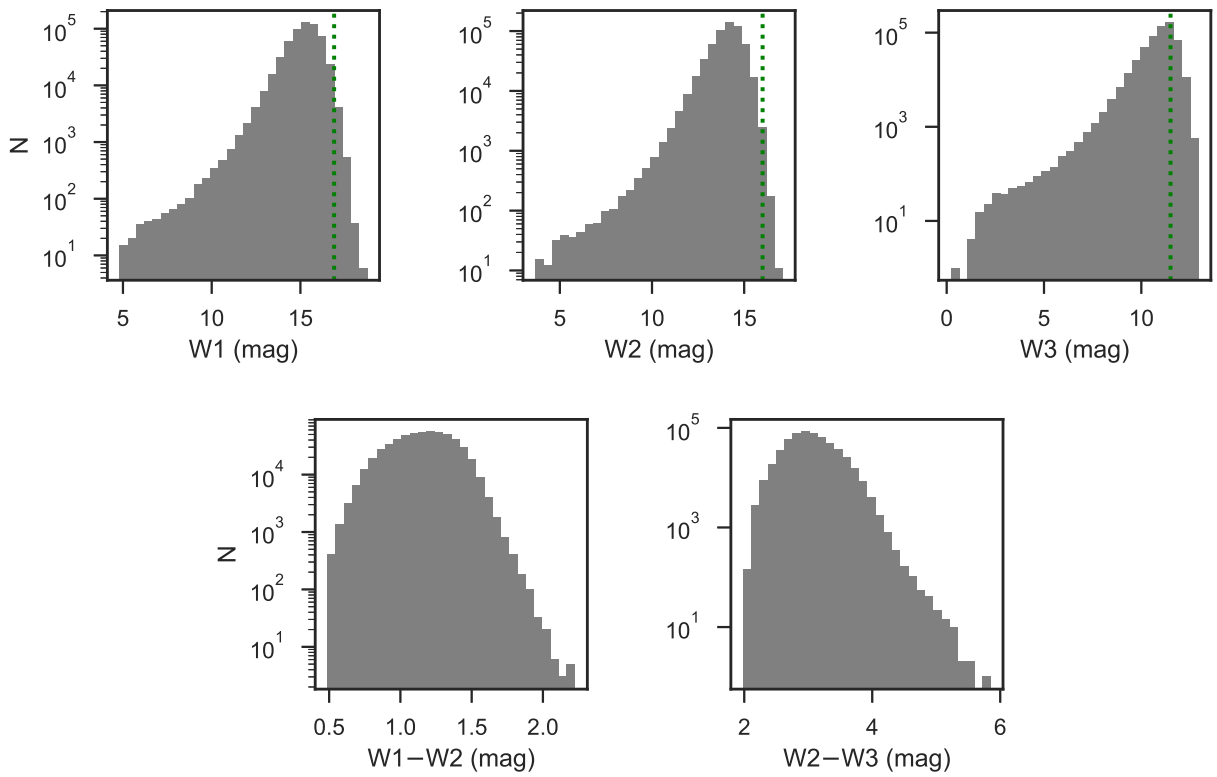

Figure 2.4: Distribution of $W1$, $W2$, and $W3$ band magnitudes, and $W1-W2$ and $W2-W3$ colors in the *Gaia-WISE* extragalactic astrometric catalog. Green dotted lines show the nominal S/N = 5 magnitudes for each band (16.9, 16.0, and 11.5 for $W1$, $W2$, and $W3$, respectively).

release using Gaia performance characteristics.[1] The PyGaia Python toolkit is an implementation of Gaia performance models that can be used for basic simulation and analysis of Gaia data, including calculation of proper motion uncertainties. We utilized the PyGaia Python toolkit to calculate predicted proper motion uncertainties for each AGN, shown in Figure 2.6. This calculation relies on each object's G magnitude, $V-I_C$ color, and ecliptic latitude. For objects where the $V-I_C$ color was not available, this value was set to zero, which has a negligible impact on the predicted proper motion uncertainty. The reported uncertainties include known instrumental effects. Statistics for the distributions of predicted uncertainties are given in Table 2.1. The uncertainties in R.A. proper motion are generally larger than those in decl., which is a consequence of the *Gaia's* scanning law.

[1] `www.cosmos.esa.int/web/gaia/science-performance`

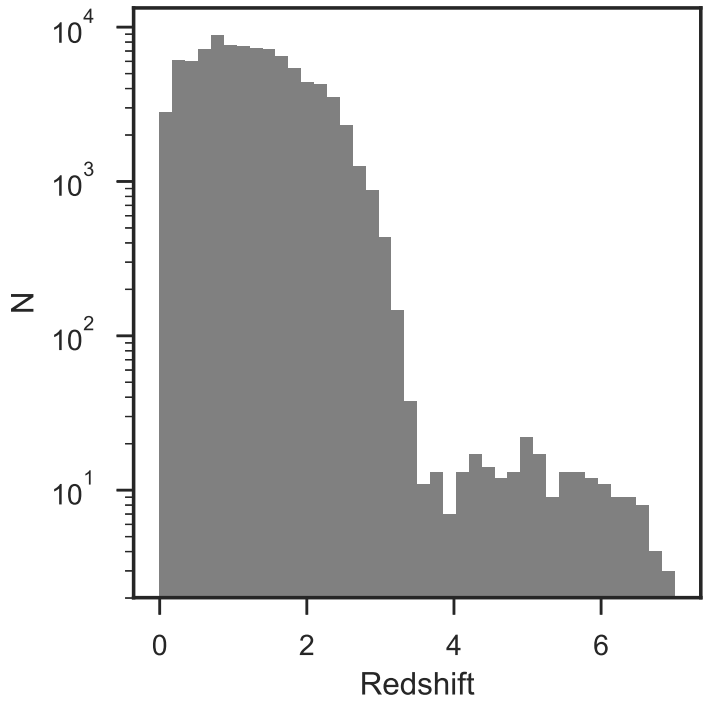

Figure 2.5: Distribution of redshifts in the *Gaia-WISE* extragalactic astrometric catalog, where available (Section 2.3.4).

2.4 Applications

Although proper motions for *Gaia* AGN will not be available until DR2, we can use the predicted uncertainties to test *Gaia's* potential capability to detect or constrain select proper motion signals. For this purpose, we generate a null proper motion catalog by randomly selecting proper motions consistent with zero based on each object's expected errors and assuming Gaussian-distributed errors. One can then add proper motion signals to the noisy null catalog to study the expected sensitivity of the *Gaia-WISE* catalog to various correlated proper motions. These include the secular aberration drift (Section 2.4.1), an anisotropic Hubble expansion (Section 2.4.2), and a stochastic long-period gravitational wave background (Darling et al., 2018).

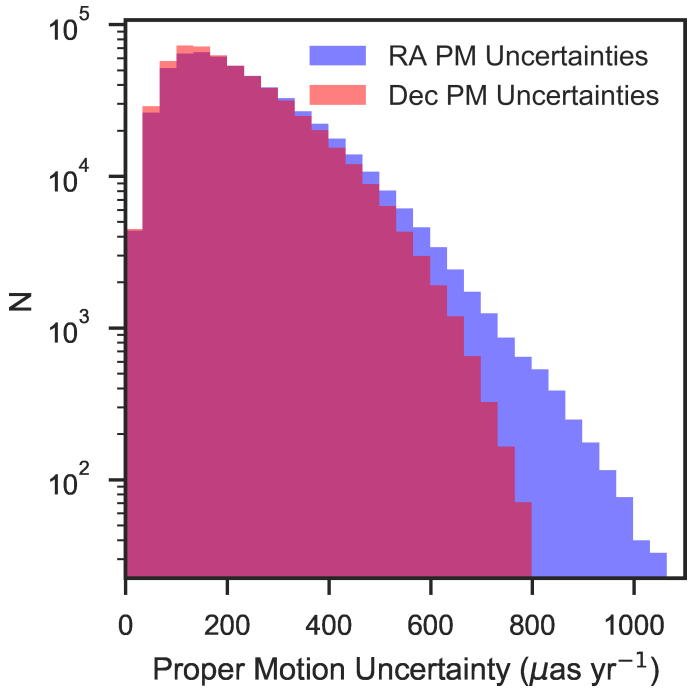

Figure 2.6: Predicted proper motion uncertainties in both right ascension (blue) and declination (pink), with overlapping values shown in magenta.

2.4.1 Secular Aberration Drift

The aberration of light is an apparent angular deflection of light rays caused by an observer's velocity across the rays and the finite speed of light. Aberration can be caused by the Earth's annual motion or the secular solar motion in the Galaxy or with respect to the cosmic microwave background rest-frame. If the observer experiences a constant acceleration then the aberration will exhibit a secular drift that manifests as an apparent proper motion of objects in a dipole pattern converging toward the acceleration vector direction.

The secular aberration drift caused by the solar system's acceleration toward the Galactic Center (a consequence of its orbit) is detectable in extragalactic proper motions as a dipole vector field that resembles an electric field and converges on the Galactic Center (e.g. Xu et al. 2012; Titov & Lambert 2013; Truebenbach & Darling 2017b). The expected solar acceleration and corresponding secular aberration drift dipole amplitude can be predicted using the distance to the

Galactic center (R_0) and the orbital speed of the Sun ($\Theta_0 + V_\odot$), which includes solar motion $V_\odot$ in the direction of Galactic rotation Θ_0: $a = (\Theta_0 + V_\odot)^2/R_0$ and $|\vec{\mu}| = a/c$. Reid et al. (2014) measured $R_0 = 8.34 \pm 0.16$ kpc and $\Theta_0 + V_\odot = 255.2 \pm 5.1$ km s^{-1} from the trigonometric parallaxes and proper motions of masers associated with young massive stars. These yield an acceleration of $a = 0.80 \pm 0.04$ cm s^{-1} yr^{-1} and a dipole amplitude of $|\vec{\mu}| = 5.5 \pm 0.2$ μas yr^{-1}.

An E-mode vector field dipole painted on the sky, $\tilde{\mathbf{V}}_{E1}(\alpha, \delta)$, can be expressed as a $\ell = 1$ vector spherical harmonic following the notation of Mignard (2012):

$$\begin{aligned}\tilde{\mathbf{V}}_{E1}(\alpha,\delta) = &\left(s_{11}^{Re}\,\frac{1}{2}\sqrt{\frac{3}{\pi}}\,\sin\alpha + s_{11}^{Im}\,\frac{1}{2}\sqrt{\frac{3}{\pi}}\,\cos\alpha \right)\hat{\mathbf{e}}_\alpha \\ &+ \left(s_{10}\,\frac{1}{2}\sqrt{\frac{3}{2\pi}}\,\cos\delta + s_{11}^{Re}\,\frac{1}{2}\sqrt{\frac{3}{\pi}}\,\cos\alpha\sin\delta - s_{11}^{Im}\,\frac{1}{2}\sqrt{\frac{3}{\pi}}\,\sin\alpha\sin\delta \right)\hat{\mathbf{e}}_\delta \end{aligned} \tag{2.1}$$

where the coefficients $s_{\ell m}^{Re,Im}$ determine the direction and amplitude of the dipole, α and δ are the R.A. and decl. coordinates, and $\hat{\mathbf{e}}_\alpha$ and $\hat{\mathbf{e}}_\delta$ are the unit vectors in those directions. In this formalism, the expected E-mode dipole caused by the solar orbit about the Galactic Center (266.4°, −29.0°) is $(s_{10}, s_{11}^{Re}, s_{11}^{Im}) = (-7.71 \pm 0.34, 0.615 \pm 0.027, -9.82 \pm 0.44)$ μas yr^{-1}.

In order to predict the *Gaia* sensitivity to the secular aberration drift signal, we assigned a proper motion to each object that is consistent with no proper motion by randomly sampling its predicted Gaussian proper motion error distribution (Section 2.3.5). Over 1000 random trials, we added the expected secular aberration drift signal to the noisy null proper motions, omitting the uncertainties in the input dipole, and used a least-squares minimization to fit a dipole to the data. The resulting mean of the best-fit parameters is $(s_{10}, s_{11}^{Re}, s_{11}^{Im}) = (-7.73 \pm 0.48, 0.606 \pm 0.337, -9.79 \pm 0.36)$ μas yr^{-1}, consistent with the original input dipole, with a mean Z-score of 23. We therefore predict that *Gaia* will produce the best determination of the secular aberration drift to date.

2.4.2 Anisotropic Cosmic Expansion

Extragalactic proper motions can test the isotropy of the Hubble expansion in the current epoch. If we neglect the peculiar motions of galaxies caused by density inhomogeneities, an isotropic

Hubble expansion produces no extragalactic proper motions. In contrast, anisotropic expansion will cause extragalactic objects to stream toward directions of faster expansion and away from directions with slower expansion. All-sky proper motion observations can therefore measure the expansion isotropy and constrain cosmological models that attempt to explain accelerating expansion without invoking dark energy, such as Lemaitre-Tolman-Bondi models and Bianchi universes (e.g. Amendola et al. 2013).

Quercellini et al. (2009) and Fontanini et al. (2009) showed that a triaxial expansion can be described using a Bianchi I model, which has the metric

$$ds^2 = -dt^2 + a^2(t)\,dx^2 + b^2(t)\,dy^2 + c^2(t)\,dz^2. \tag{2.2}$$

This metric permits different expansion rates along the three axes: $H_x = \dot{a}/a$, $H_y = \dot{b}/b$, and $H_z = \dot{c}/c$. The observed Hubble parameter would be $H = \frac{d}{dt}(abc)^{1/3}/(abc)^{1/3}$, and the Friedmann-Robertson-Walker metric is recovered for $a(t) = b(t) = c(t)$. The expansion can therefore be characterized by the fractional departure from the isotropic Hubble expansion along the coordinate i using a unitless shear parameter:

$$\Sigma_i = \frac{H_{i,0}}{H_0} - 1. \tag{2.3}$$

The principal shearing axes can be arbitrarily oriented on the sky, and Darling (2014) showed that the proper motion induced by this anisotropy model can be completely described by a quadrupolar E-mode vector field.

To test the catalog's potential to constrain anisotropy, we performed 1000 trials of adding a randomly generated anisotropy signal to the noisy null proper motions and fitting the anisotropy model to attempt to recreate the original input signal. We used the shear equation (Equation A1) of Darling (2014) to form these artificial anisotropy signals. For each trial, shear terms Σ_x, Σ_y, and Σ_z were drawn from Gaussian distributions with a mean of zero and a random standard deviation sampled from a uniform distribution between 0 and 0.1. The rotation angles were randomly selected from a uniform distribution between 0 and 2π, assuming that there is no preferred direction for anisotropy. After the signal is added to the null proper motions, we use a least-squares minimization

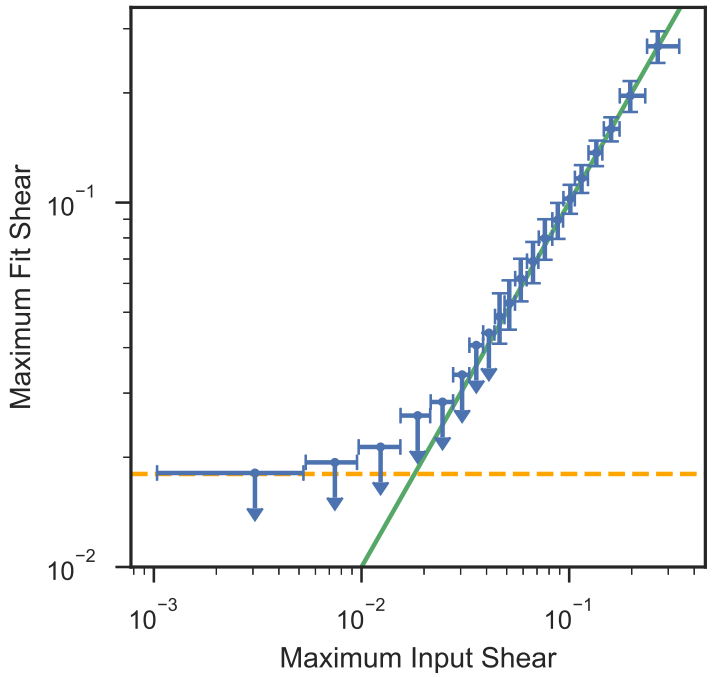

Figure 2.7: Maximum absolute value of the fit shear vs. the input shear for Hubble expansion anisotropies added to the synthetic *Gaia-WISE* AGN catalog proper motions. Non-significant fits are displayed as upper limits.

to fit the shear equation to the data in an attempt to recover the original signal.

The shear equation parameters are degenerate due to the rotation degeneracy of the principal axes (no particular axis is required to be the direction of maximum or minimum expansion), and therefore individual fit parameters do not necessarily match the original input parameters. Instead, we compare the maximum input shear to the maximum fit shear, as shown in Figure 2.7. There is a roughly one-to-one correlation for large input values; however, for maximum input shear below $\sim 3 \times 10^{-2}$, noise dominates and the fit parameters tend toward a noise floor of 0.018 (a 1.8% departure from isotropy). The fit, however, is not significant for such low input anisotropy. For larger inputs where the fits are significant, we recover the input anisotropy with uncertainty of about $\pm$ 0.01.

2.5 Discussion

Prior to the first *Gaia* data release, the *Gaia* Universe model snapshot (GUMS) simulated a synthetic catalog of objects that *Gaia* could have potentially observed (Robin et al., 2012). GUMS simulated that nearly one million quasars would be observed by *Gaia*. Our sample roughly agrees with that number, given that it is about 50% incomplete. However, unlike GUMS, our sample consists of real objects actually detected by *Gaia*.

The Large Quasar Astrometric Catalog (LQAC3; Souchay et al. 2015), is a collection of 321,957 objects and represents the complete set of already identified quasars as of 2015. While the LQAC3 reliably contains extragalactic objects, the LQAC3-*Gaia* cross-match is dominated by the SDSS footprint. Our catalog has a more uniform sky distribution, and is therefore preferable for the study of low-multipole proper motion signals.

We expect *Gaia-WISE* AGN to be able to measure the secular aberration drift with 23σ significance. Mignard & Klioner (2012) predicted that *Gaia* would detect the secular aberration drift with about 10σ accuracy, assuming 10^4 – 10^5 quasars observed by *Gaia* with proper motion errors lower than predicted here. Titov et al. (2011) predicted *Gaia* to measure the dipole parameters with about 10% relative precision. We find that the catalog should be able to measure the dipole parameters with higher precision, with the exception of the s_{11}^{Re} component.

While isotropy is a fundamental pillar of cosmology and is well constrained by the cosmic microwave background (Planck Collaboration et al., 2016), *Gaia-WISE* AGN will be able to probe the isotropy of expansion for the relatively local universe since the majority are at redshift below 2.5 (95th percentile value). We predict that *Gaia-WISE* AGN will place an upper limit on the anisotropy of the Hubble expansion of about 2%. If the anisotropy is larger than about 3%, then a significant measurement may be possible. Darling (2014) showed that the expansion is isotropic to within 7% in the most constrained direction using a catalog of 429 radio sources. Local anisotropy has been previously measured using the Hubble parameters derived from SNe Ia. Chang & Lin (2015) found that the maximum anisotropy of the Hubble parameter is $3\% \pm 1\%$

for a set of supernovae in the redshift range $z < 1.4$. Bengaly (2016) find that the maximum variance of the Hubble parameter is (2.30 ± 0.86) km s^{-1} Mpc^{-1} for $z < 0.1$, which corresponds to a maximum departure from isotropy of $3.3\% \pm 1.2\%$. The *Gaia* isotropy measurement will therefore be competitive with and orthogonal to other more traditional methods.

Our analysis of the astrometric signals that may be detected using *Gaia-WISE* AGN has assumed that the proper motions of all objects will be determined with the same precision as point sources. In reality, some galaxies may appear extended to *Gaia*, in which case the precision of the image centroid position will be diminished. The intrinsic variability of AGN will be an additional proper motion noise source, since variable AGN flux can cause the image centroid to move by up to a few mas for nearby AGN (Popović et al., 2012). Microlensing of quasars may also cause the image centroid to shift due to the appearance or disappearance of microimages (Williams & Saha, 1995; Lewis & Ibata, 1998). The effect on the centroid position may be as large as tens of μas due to stellar mass objects in the lensing galaxy (Treyer & Wambsganss, 2004) or a few mas due to stellar clusters (Popović & Simić, 2013). The effects of both AGN variability and microlensing will add uncorrelated noise to the proper motions. They will therefore be averaged out in the determination of correlated signals such as the secular aberration drift and anisotropic expansion, despite adding to the overall noise in the signals.

2.6 Conclusions

We presented a catalog of *Gaia* AGN selected using the *WISE* two-color method of Mateos et al. (2012). The catalog contains 567,721 objects, and we estimate that this sample is roughly 50% complete. We find that the *WISE* wedge reliably selects extragalactic objects, with only a negligible portion (0.2%) of our sample likely contaminated by stars. We demonstrated two potential applications of the catalog, a precise measurement of the secular aberration drift and strong constraints on the isotropy of the Hubble expansion. Based on the expected end-of-mission proper motion uncertainty for each object in the *Gaia-WISE* catalog, we predict a measurement of the secular aberration drift with $\sim 23\sigma$ significance and an upper limit on the anisotropy of the

Hubble flow of $\sim 2\%$.

Acknowledgments

The authors thank the anonymous referee for helpful feedback.

The authors acknowledge support from the NSF grant AST-1411605 and the NASA grant 14-ATP14-0086.

This work has made use of data from the European Space Agency (ESA) mission *Gaia* (`https://www.cosmos.esa.int/gaia`), processed by the *Gaia* Data Processing and Analysis Consortium (DPAC, `https://www.cosmos.esa.int/web/gaia/dpac/consortium`). Funding for the DPAC has been provided by national institutions, in particular the institutions participating in the *Gaia* Multilateral Agreement.

This publication makes use of data products from the Wide-field Infrared Survey Explorer, which is a joint project of the University of California, Los Angeles, and the Jet Propulsion Laboratory/California Institute of Technology, funded by the National Aeronautics and Space Administration.

Funding for SDSS-III has been provided by the Alfred P. Sloan Foundation, the Participating Institutions, the National Science Foundation, and the U.S. Department of Energy Office of Science. The SDSS-III web site is `http://www.sdss3.org/`. SDSS-III is managed by the Astrophysical Research Consortium for the Participating Institutions of the SDSS-III Collaboration including the University of Arizona, the Brazilian Participation Group, Brookhaven National Laboratory, Carnegie Mellon University, University of Florida, the French Participation Group, the German Participation Group, Harvard University, the Instituto de Astrofisica de Canarias, the Michigan State/Notre Dame/JINA Participation Group, Johns Hopkins University, Lawrence Berkeley National Laboratory, Max Planck Institute for Astrophysics, Max Planck Institute for Extraterrestrial Physics, New Mexico State University, New York University, Ohio State University, Pennsylvania State University, University of Portsmouth, Princeton University, the Spanish Participation Group, University of Tokyo, University of Utah, Vanderbilt University, University of Virginia, University

of Washington, and Yale University.

This research has made use of the NASA/IPAC Extragalactic Database (NED) which is operated by the Jet Propulsion Laboratory, California Institute of Technology, under contract with the National Aeronautics and Space Administration.

Software used in this research: Astropy (Astropy Collaboration et al., 2013, 2018, 2022), pyGaia, STILTS (Taylor, 2006), TOPCAT (Taylor, 2005).

Chapter 3

Secular Extragalactic Parallax: Measurement Methods and Predictions for Gaia

Abstract

Secular extragalactic parallax caused by the solar system's velocity relative to the cosmic microwave background rest frame may be observable as a dipole proper motion field with amplitude 78 μas yr^{-1} Mpc. Nearby galaxies also exhibit proper motions caused by their transverse peculiar velocities that prevent detection of secular parallax for any single galaxy, although a statistical detection may be made instead. Such a detection could constrain the local Hubble parameter. We present methods to measure secular parallax using correlated extragalactic proper motions. From *Gaia* Data Release 2 and Data Release 3, we find limits on the secular parallax amplitude using the proper motions of nearby galaxies. The current measurement is an insignificant dipole with an upper limit amplitude of 980 μas yr^{-1} Mpc. This measurement will be improved by larger sample size and reduced proper motion uncertainties in future data releases. Using the local peculiar velocity field derived from Cosmicflows-3, we simulate galaxy proper motions and predict that a significant detection ($5 - 10\sigma$) of the secular parallax amplitude will be possible by *Gaia*'s end of mission. The detection is contingent on proper motions of nearby (< 5 Mpc), bright ($G < 15$ mag) galaxies, and corresponds to an insignificant upper limit on the Hubble parameter. We further investigate the implications of our simulations for the study of transverse peculiar velocities, which we find to be consistent with large scale structure theory. The peculiar velocity field additionally results in low-multipole correlated proper motions on the order of 0.3 μas yr^{-1} that may be confounded

with other cosmological proper motion measurements, such as limits on the gravitational wave background and the anisotropy of the Hubble expansion.

The majority of this chapter was published as Paine et al. 2020, ApJ, 890, 146. Section 3.4 is an unpublished result using the latest *Gaia* data release, and will be submitted as a research note in 2023. Sections 3.1 - 3.3 and 3.5 - 3.7 are reproduced from the published paper with some additional context and discussion for the new result.

3.1 Introduction

A galaxy's proper motion reflects a combination of its peculiar velocity, cosmological effects, and observer induced apparent motions. One such observer induced motion is the secular extragalactic parallax caused by the solar system's velocity with respect to the cosmic microwave background (CMB) rest frame (Kardashev, 1986; Ding & Croft, 2009; Bachchan et al., 2016). The CMB temperature dipole has an amplitude of about 369 km s^{-1} toward the direction $(l, b) = (264°, 48°)$, $(168°, -7°)$ in RA and Dec., and corresponds to a linear solar velocity of about 78 AU yr^{-1} (Hinshaw et al., 2009). This velocity is a combination of the solar system's orbit in the Galaxy and the Galactic peculiar motion and will therefore cause a parallax shift away from the direction of motion for extragalactic objects that is distinct from the annual parallax caused by the Earth's orbit in the solar system. The resulting secular parallax may be observed as a proper motion of amplitude 78 μas $yr^{-1}(\frac{1\text{Mpc}}{\text{D}})|\sin\beta|$, where D is the proper motion distance of the galaxy, which is equivalent to the comoving distance for a flat universe (Hogg, 1999), and β is the angle between the position of the galaxy and the CMB apex. The global signal is therefore a proper motion dipole that diminishes with distance.

Detection of secular parallax for any individual galaxy is complicated by confounding proper motions. The largest expected contributions to the proper motion are the peculiar velocities caused by gravitational interactions with large-scale structure (LSS) and the secular aberration drift caused by the solar system barycenter acceleration about the Galactic center. Secular aberration drift is observed as a distance-independent dipole with amplitude of ~ 5 μas yr^{-1} (Titov & Lambert, 2013;

Truebenbach & Darling, 2017b), which should be separable from a distance dependent dipole. LSS, however, induces distance-dependent proper motions at all angular scales with amplitudes comparable to secular parallax (Hall, 2019). For individual galaxies, separating the peculiar and secular parallax components of the proper motion is not possible without independent estimates of the peculiar velocity and distance of the galaxy, though the inferred secular parallax distance would not provide an independent distance estimate in this case. However, a statistical detection of secular parallax may be possible for large sample of galaxy proper motions, which may be used to calibrate existing extragalactic distance measures and to constrain the Hubble parameter (Ding & Croft, 2009; Hall, 2019).

To detect the global secular parallax dipole, one needs a large sample of nearby galaxies with proper motion measurements. The *Gaia* mission has measured proper motions for at least a half million extragalactic objects identified as mid-infrared active galactic nuclei (AGN; Lindegren et al. 2018). Most *Gaia* AGN are either too distant to be useful for secular parallax or may not have distance measures, so in this work we target a new sample of more local galaxies dectected by *Gaia* using the Cosmicflows-3 catalog (Tully et al., 2016). Individual galaxies should not have significant proper motion measurements from *Gaia*, but with large sample size and even sky distribution, we may constrain correlated proper motions with smaller amplitudes than the individual uncertainties. Future data releases should increase the number of extragalactic objects with measured proper motions and should have substantially lower uncertainties.

The expected secular parallax, peculiar proper motions, and higher multipole signals are detailed in Section 3.2. We present a first secular parallax limit using *Gaia* DR2 proper motions for a sample of nearby Cosmicflows-3 galaxies in Section 3.3, and an updated limit using *Gaia* DR3 proper motions in Section 3.4. In Section 3.5, we utilize the Cosmicflows peculiar velocity field to simulate galaxy proper motions consistent with *Gaia's* end-of-mission performance and predict the detection of secular parallax. We analyze the peculiar proper motions in detail in Section 3.6. Discussion and main conclusions are given in Section 3.7. We assume a flat cosmology and a Hubble constant of $H_0 = 70$ km s^{-1} Mpc^{-1}, which is $H_0 = 15$ μas yr^{-1} in proper motion units.

3.2 Characterizing the Proper Motion Vector Field

The term "secular parallax" may have two definitions. The first usage refers to the phenomenon of an apparent distance-dependent dipolar proper motion field caused by the observer's velocity relative to the bulk motion of a sample of objects. In this work, we use "secular parallax" to describe the proper motion dipole predicted from the solar system's velocity measured with respect to the CMB reference frame, which may be leveraged to constrain galaxy distances. The former definition includes the dipole correlated components of galaxy velocities with respect to the CMB frame. We distinguish such peculiar proper motions from secular parallax proper motions, although the net dipole one measures is the sum of the two effects. Secular parallax detection as a method to measure galaxy distances or the Hubble constant is contingent on knowing the underlying velocity as a prior, and therefore one must separate the secular parallax from the peculiar transverse motions that are not as well constrained. In this section, we describe the expected secular parallax and other relevant proper motion components.

The global secular parallax field is modeled as a distance-dependent E-mode (curl-free) dipole where galaxies appear to stream away from the direction of motion (Ding & Croft, 2009). For example, a galaxy at 1 Mpc and 90° from the CMB apex will have a secular parallax, observed as a proper motion, of 78 μas yr^{-1} oriented away from the direction of the CMB dipole apex. The magnitude of the proper motion is modulated by the angle between the galaxy and the direction of the apex, β (Ding & Croft, 2009), given by the following expression:

$$|\mu| = \left(78\ \mu\text{as yr}^{-1}\ \text{Mpc}\right)\left(\frac{1}{D}\right)|\sin\beta|. \tag{3.1}$$

Figure 3.1 shows the expected parallax dipole proper motions for a sample of *Gaia* galaxies described in Section 3.3.1 which we use to limit the secular parallax signal.

Following the notation of Mignard (2012), an E-mode dipole vector field may be expressed

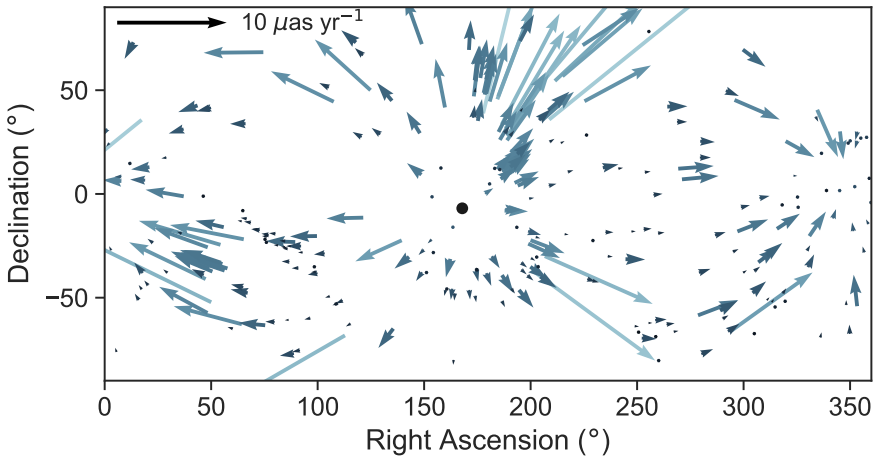

Figure 3.1: The expected secular parallax proper motions for 232 nearby *Gaia* galaxies, which are described in Section 3.3.1. The colors of the arrows scale with distance, which range from $3-410$ Mpc. The direction of the solar system motion with respect to the CMB is indicated by the black dot.

as an $\ell = 1$ vector spherical harmonic:

$$\begin{aligned}\tilde{\mathbf{V}}_{E1}(\alpha,\delta) =& \sqrt{\frac{3}{4\pi}}\left(s_{11}^{Re}\sin\alpha + s_{11}^{Im}\cos\alpha\right)\hat{\mathbf{e}}_{\alpha} \\ &+ \sqrt{\frac{3}{4\pi}}\left(s_{10}\sqrt{\frac{1}{2}}\cos\delta + s_{11}^{Re}\cos\alpha\sin\delta - s_{11}^{Im}\sin\alpha\sin\delta\right)\hat{\mathbf{e}}_{\delta}\end{aligned} \tag{3.2}$$

where the coefficients s_{10} and $s_{11}^{Re,Im}$ determine the direction and amplitude of the vector field, and α and δ are the coordinates in RA and Dec. The vectors $\hat{\mathbf{e}}_{\alpha}$ and $\hat{\mathbf{e}}_{\delta}$ are unit vectors in RA and Dec. The power of the vector field is the integral of the squared field over the unit sphere and is calculated from the coefficients by

$$P_{E1} = s_{10}^2 + 2\left((s_{11}^{Re})^2 + (s_{11}^{Im})^2\right). \tag{3.3}$$

The power is related to the dipole amplitude by

$$A_{E1} = \sqrt{\frac{3}{8\pi}P_{E1}}, \tag{3.4}$$

where the factor of $\sqrt{3/8\pi}$ comes from integrating over 4π sr.

The distance dependence of secular parallax may be incorporated by expressing the coefficients in units of μas yr^{-1} Mpc (velocity units). The solar system's velocity with respect to the CMB

is 369 ± 0.9 km s^{-1} in the direction $(l, b) = (264°, 48°)$ (Hinshaw et al., 2009), which causes an observed proper motion dipole with coefficients $(s_{10}, s_{11}^{Re}, s_{11}^{Im}) = (27.2, -155.0, -33.1)$ μas yr^{-1} Mpc. The secular parallax dipole root power is $\sqrt{P_{E1}} = 226$ μas yr^{-1} Mpc and the amplitude is 78 μas yr^{-1} Mpc, as given by Equation 3.1.

Two other E-mode dipolar proper motions of interest in this work are the secular aberration drift and the peculiar proper motion dipole caused by LSS. The former is a distance-independent dipole that has been previously detected using quasar proper motions from very long baseline interferometry (Titov & Lambert, 2013; Truebenbach & Darling, 2017b). The secular aberration drift amplitude is $\sim 5\mu$as yr^{-1}, which will dominate dipolar proper motions for galaxies at distances of approximately 16 Mpc or greater. We expect that the secular aberration drift will be detected with *Gaia* using high redshift AGN (Paine et al., 2018), enabling the study of distance-dependent dipoles after the distance-independent signal is subtracted.

Peculiar velocities induce distance-dependent proper motions at all angular scales, including a dominant dipole for local galaxies. Hall (2019) presented predictions for the LSS transverse velocity power spectrum and its correlation to the secular parallax dipole. The transverse peculiar velocity dipole causes proper motions of similar amplitude to secular parallax for galaxies within $\sim$ 100 Mpc. Hall (2019) therefore predict transverse peculiar velocities dominate the error on secular parallax measurements for local galaxies. The predicted peculiar velocity dipole decreases in power as a function of distance, which causes the observed peculiar proper motion dipole amplitude to decrease faster than $1/D$. The distance dependence of peculiar proper motions means that the peculiar dipole may not be fit separately and subtracted prior to fitting for secular parallax, unlike the secular aberration drift.

In Section 3.6, we investigate higher multipole vector fields associated with peculiar proper motions. Expressions for $\ell = 2, 3$ vector fields may be found in Mignard (2012). The power for any general ℓ is

$$P_l = s_{\ell 0}^2 + t_{\ell 0}^2 + 2 \sum_{m=1}^{\ell} \left((s_{\ell m}^{Re})^2 + (s_{\ell m}^{Im})^2 + (t_{\ell m}^{Re})^2 + (t_{\ell m}^{Im})^2 \right), \tag{3.5}$$

where s and t denote the spheroidal (E-mode) and toroidal (B-mode) components of the vector field, respectively.

The total proper motion field is then the vector sum of distance-dependent and distance-independent components:

$$\tilde{\mu}(D) = \tilde{\mathbf{V}}_{E1,SP}\ D^{-1} + \tilde{\mathbf{V}}_{E1,PV}\ D^{-1} + \sum_{\ell=2}^{\infty} \left(\tilde{\mathbf{V}}_{E\ell,PV}\ D^{-1} + \tilde{\mathbf{V}}_{\ell} \right), \tag{3.6}$$

where $\tilde{\mathbf{V}}_{E1,SP}$ denotes the dipole induced by the solar system velocity with respect to the CMB. $\tilde{\mathbf{V}}_{E1,PV}$ and $\tilde{\mathbf{V}}_{E\ell,PV}$ denote the dipole and higher order E-modes induced by peculiar velocities. The secular aberration drift and higher order distance-independent modes are represented by $\tilde{\mathbf{V}}_{\ell}$. Note that the secular parallax and peculiar components have units of velocity, μas yr^{-1} Mpc, whereas the distance-independent multipoles are given in units of proper motion, μas yr^{-1}.

3.3 A First Secular Parallax Limit

3.3.1 Sample Selection

Making a statistical detection of extragalactic parallax will require a large sample of nearby galaxies with both proper motion and distance measurements. For this purpose, we selected galaxies from Cosmicflows-3 (Tully et al., 2016), a catalog of 17,669 redshift-independent galaxy distances. The majority of distances were measured using either the relation between galaxy rotation and luminosity (the Tully-Fisher relation; Tully & Fisher 1977) or the relations between the velocity dispersion, radius, and luminosity of elliptical galaxies (the fundamental plane; Djorgovski & Davis 1987; Dressler et al. 1987). Redshift based distance estimates are more widely available for galaxies detected by *Gaia*. However, the accuracy of redshift based distance estimates is diminished for relatively small distances because the recession velocity predicted by the Hubble flow is comparable to typical radial peculiar velocities. Such estimates are therefore inappropriate for very nearby galaxies (< 10 Mpc) that will show the largest observer induced proper motions. Additionally, the Cosmicflows-3 catalog includes line-of-sight peculiar velocity measurements, which Graziani et al. (2019) used to derive the local peculiar velocity field and matter distribution. In Section 3.5, we

employ these peculiar velocities to forecast the detection of secular parallax in future *Gaia* data releases

We cross-matched Cosmicflows-3 with *Gaia* DR2 using a 3 arcsecond matching radius, which resulted in 9,823 objects. We performed cuts of the sample in order to mitigate contamination from Galactic stars, which will typically have larger, more significant proper motions than those expected for galaxies. We excluded any sources within 10 degrees of the Galactic plane ($|b| \leq 10°$), and any remaining sources with significant annual parallaxes measured by *Gaia* ($|p| \geq 5\sigma_p$). Finally, we removed galaxies within 1.5 Mpc, approximately the radius of the Local Group. The resulting catalog contains 9,699 galaxies, of which only 429 have a full 5-parameter astrometric solution (measured position, parallax, and proper motion) in *Gaia* DR2. We use only these 429 galaxies with proper motion measurements below. In Section 3.5, we utilize the larger sample, including sources without proper motion measurements, to simulate end-of-mission proper motions and predict detection of the secular parallax dipole.

3.3.1.1 Visual Inspection

Parallax induces the largest proper motions in nearby galaxies, but nearby galaxies are not point-like. However, extended objects did not receive special treatment in the data processing for *Gaia* DR2 and were treated as single stars in the astrometric solution (Gaia Collaboration et al., 2018b). To ensure that the *Gaia* positions and proper motions are reasonable, we visually inspected all 429 galaxies using Sloan Digital Sky Survey (SDSS) g-band imaging where available, or images from the Digitized Sky Survey II (DSS-II). Each image was examined for potentially problematic features, including extended galaxies without a clear centroid or off-center *Gaia* positions. Examples of such galaxies are shown in Figure 3.2. In cases where SDSS imaging was not available and the *Gaia* position appeared marginal from DSS-II images, other images from the literature were examined. Nearby galaxies (< 50 Mpc) received more scrutiny than more distant ones, since the proper motions of nearby objects provide a larger contribution to the secular parallax signal. The majority of the galaxies in our initial cross-match are extended, however only 119 were identified as

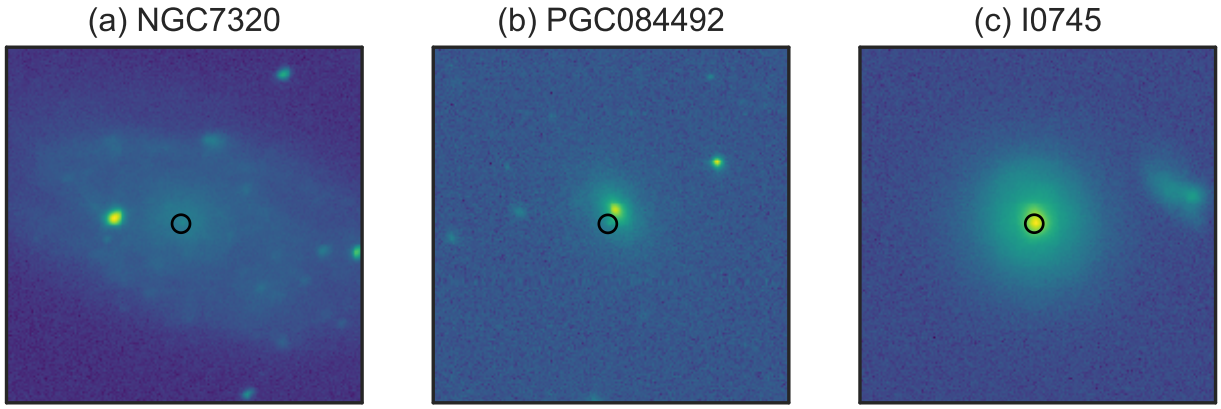

Figure 3.2: SDSS g-band images of three extended galaxies demonstrating examples of the visual criteria used to verify *Gaia* positions. Circles indicate the *Gaia* position for each galaxy and are each 2 arcsec in radius (typical position errors for objects in our sample are 0.5 mas). (a) A galaxy with no core. (b) A galaxy where the *Gaia* position is off-center. (c) An example of an extended galaxy with an acceptable *Gaia* postion.

extended with a poor *Gaia* position and were removed from the sample. We identified an additional 6 *Gaia* positions where there were no visible sources as well as one foreground star, which were removed from the sample. The resulting catalog contains 303 galaxies which pass visual inspection.

3.3.1.2 Proper Motion and Distance Clipping

Out of the 303 remaining objects, 242 have proper motion amplitudes greater than 1 mas yr^{-1}, at least an order of magnitude larger than the expected proper motions caused by either secular parallax or a galaxy's peculiar motions. 71 of these galaxies have $> 5\sigma$ proper motions in RA and/or Dec. As a result, an initial error-weighted fit of the parallax dipole (Equation 3.2) to the sample has a non-significant amplitude (defined by Equation 3.4) of 32 ± 8 mas yr^{-1} Mpc. Significant proper motions of galaxies are most likely either spurious measurements or foreground stars that were missed during visual inspection, so we remove any sources with $> 5\sigma$ proper motions in either RA or Dec. The proper motions and positions of the remaining 232 galaxies are shown in Figure 3.3, and their distances and G magnitudes are shown in Figure 3.4.

To understand the sensitivity of our fitting technique to the remaining large, but insignificant

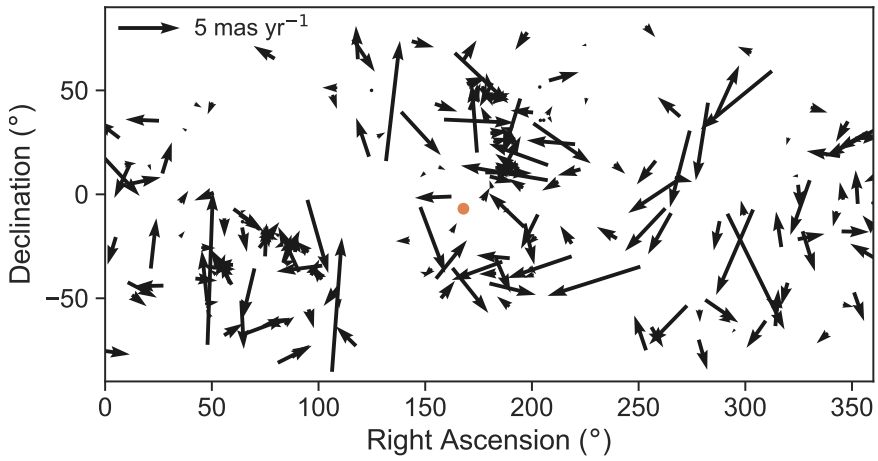

Figure 3.3: Proper motions and sky distribution of our sample of 232 *Gaia*-Cosmicflows galaxies. Note that none of the proper motions shown are significant. The coordinates are located at the midpoint of each arrow. The direction of the solar system motion with respect to the CMB is indicated by the orange dot. Apparent clustering of arrows is due to the exclusion of objects within 10 degrees of the Galactic plane.

proper motions, we tested the parallax model on the sample with a range of maximum proper motion vector amplitude[1] cutoffs between 0.1 and 5 mas yr^{-1}. For each proper motion cutoff, we fit a distance dependent E-mode dipole using least-squares minimization. None of the fits are significant and the coefficients are generally consistent with zero. For each cut we find the 95% confidence interval upper limit for the dipole amplitude via Monte Carlo sampling of the fit coefficients. The top plot of Figure 3.5 shows the amplitude upper limit vs. maximum proper motion amplitude in the fit sample. Note that the fit amplitudes are expressed in mas yr^{-1}, so the fits are at least an order of magnitude larger than the expectation. The variability below the 1 mas yr^{-1} cut off may be attributed to small sample sizes. The amplitude upper limit for the fit to the sample with no maximum proper motion cutoff is ~ 3.5 mas yr^{-1} Mpc, and we find only a marginal reduction in the limit for proper motion cutoffs around 1-4 mas yr^{-1}.

Our galaxy sample includes objects at distances up to 410 Mpc, most of which have expected secular parallax proper motions smaller than a few μas yr^{-1} and should not contribute greatly to the global parallax signal relative to the more numerous nearby galaxies. However, the systematics

[1] Proper motion amplitudes are calculated by $|\mu| = \sqrt{\mu_{\alpha*}^2 + \mu_\delta^2}$, where $\mu_{\alpha*} = \mu_\alpha \cos\delta$, and μ_α and μ_δ are the proper motion in the RA and Dec directions, respectively.

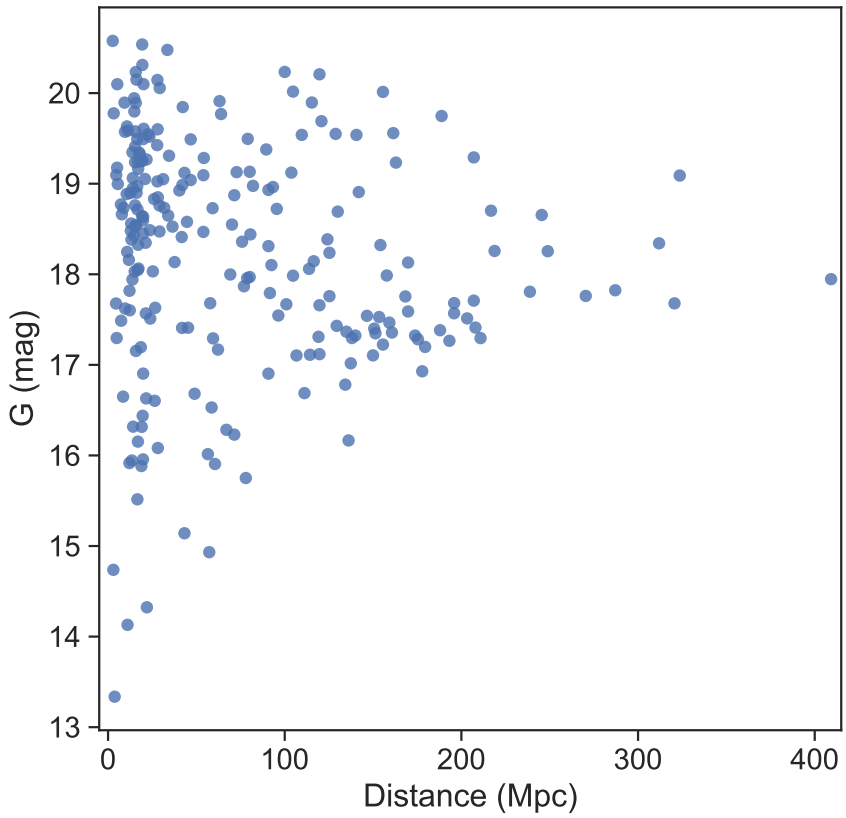

Figure 3.4: G magnitudes vs. distance for our sample of 232 *Gaia*-Cosmicflows galaxies. *Gaia* proper motion uncertainties scale with magnitude.

that dominate the Gaia DR2 proper motions for this sample are distance-independent, so fits of the distance-dependent dipole may be sensitive to distance binning. In particular, we want to test whether the inclusion of galaxies at large distances may bias the best-fit amplitudes to larger values due to the dominant systematic errors. The bottom plot of Figure 3.5 shows the same varying maximum proper motion fits described above for three choices of maximum distance: 20, 50, and 100 Mpc. Again we find only small differences between cuts, except for low distance and proper motion cuts where the sample size is small. Conversely, increasing the minimum distance of the sample consistently increases the best-fit amplitudes and uncertainties. The fits are therefore most sensitive to the proper motions of the nearest galaxies in the sample, with little to no improvement on the limit from increasing the sample size by including distant galaxies.

We next consider the impact that cluster member galaxies may have on these fits, as galaxies

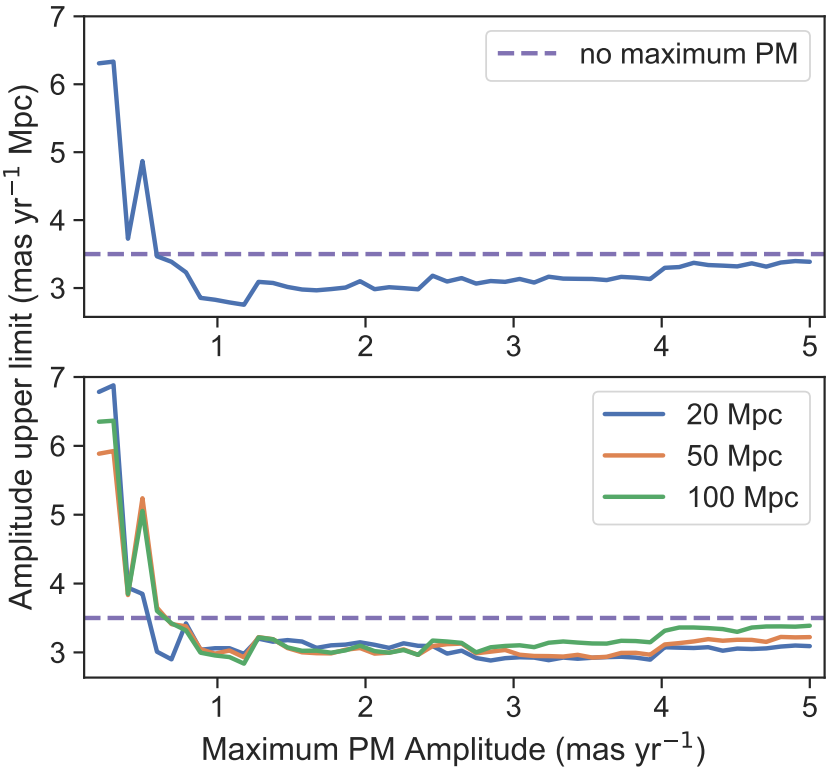

Figure 3.5: Top: dipole amplitude upper limits vs. maximum proper motion amplitude for the sample within 410 Mpc. The purple dashed line is the upper limit for the sample with no maximum proper motion cut off. The sample size for the maximum cut off is 213 objects, whereas the sample size for cut offs < 0.8 mas yr^{-1} is between 6 and 44 objects. Bottom: Same as top for maximum distance cutoffs of 20, 50, and 100 Mpc. The purple dashed line is the upper limit for the sample with no maximum proper motion or distance cut offs.

in clusters can have peculiar velocities on the order of 1000 km s^{-1} and may result in proper motions that are correlated with other members of the same cluster. Three nearby clusters are represented in our sample: Virgo (14 galaxies), Ursa Major (6 galaxies), and Fornax (12 galaxies). At approximately the distance of the Virgo cluster, a peculiar transverse velocity of 1000 km s^{-1} would correspond to a $\sim$ 15 μas yr^{-1} proper motion, well below the statistical and systematic errors in the sample. If we exclude all cluster members from the sample, we find a dipole amplitude upper limit of ~ 3.5 μas yr^{-1} Mpc, confirming that cluster members are not the source of the large amplitudes discussed previously.

We therefore conclude that further cuts on the catalog do not significantly improve the secular

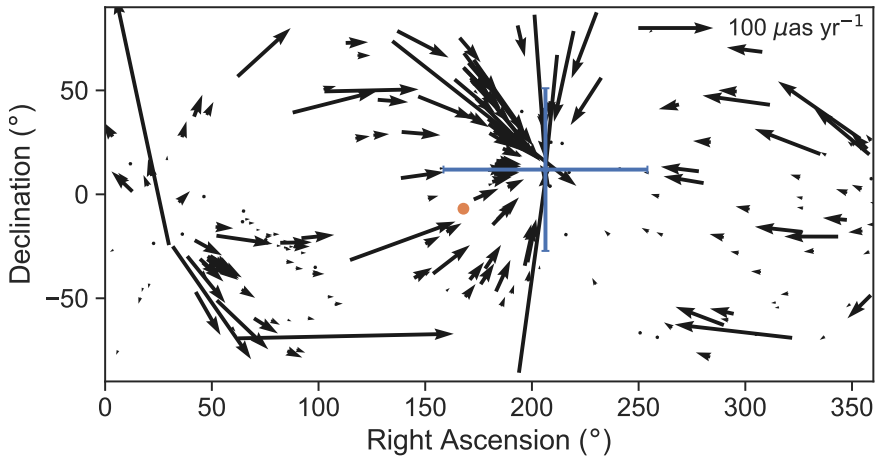

Figure 3.6: Best fit distance dependent dipole to the proper motions of our sample of 232 nearby galaxies (Figure 3.3). Note that this dipole is not significant. The blue cross shows the location and uncertainty of best fit antapex. The direction of the solar system motion with respect to the CMB is indicated by the orange dot.

parallax limit. In Section 3.3.2, we present details on this limit using the proper motions displayed in Figure 3.3.

3.3.2 Results

We fit a distance dependent E-mode dipole to the proper motions of our sample of 232 galaxies using least-squares fitting. The best fit dipole is $(s_{10}, s_{11}^{Re}, s_{11}^{Im}) = (800 \pm 3300, 2400 \pm 2100, -1200 \pm 1800)$ μas yr^{-1} Mpc, which results in a 95% confidence interval upper limit on the dipole amplitude of ~ 3500 μas yr^{-1} Mpc. The best fit proper motions are shown in Figure 3.6. The dipole is not significant, but it is coincidentally nearly anti-aligned with the expected dipole.

The limit is about an order of magnitude larger than either the expectation from the solar system's velocity or the peculiar velocities of nearby galaxies. It therefore represents an insignificant upper limit on the velocity of the solar system with respect to the bulk peculiar flow. For an estimate of H_0, one needs only the component of of the proper motion caused the by the velocity with respect to the CMB, which may be estimated by fixing the dipole direction to the CMB dipole apex. The unfixed dipole is nearly anti-aligned with the CMB dipole, so the fixed-direction fit has zero amplitude. The uncertainties on dipole coefficients $(s_{10}, s_{11}^{Re}, s_{11}^{Im})$ are $(270, 1500, 320)$ μas yr^{-1} Mpc,

and the 95% confidence upper limit on the amplitude is $\sim$ 1500 μas yr^{-1} Mpc. The fractional uncertainty of the amplitude may be translated to H_0, which implies an H_0 limit of 1400 km s^{-1} Mpc^{-1}. We note that we do not measure an H_0 limit; rather it is an estimate of the limit that may be achieved using current *Gaia* data.

The large scale systematics in *Gaia* DR2 proper motions are of the order 40 μas yr^{-1} for angular scales $\gtrsim 18^\circ$ (Lindegren et al., 2018; Gaia Collaboration et al., 2018a). Further, Gaia Collaboration et al. (2018a) find that the dipole systematic proper motion effects are of the order of 10 μas yr^{-1} for their *Gaia* celestial reference frame quasar sample. To assess the large scale systematics present in our sample of 232 galaxies, we fit a distance-independent E1 dipole to the sample. We find an insignificant dipole of $(s_{10}, s_{11}^{Re}, s_{11}^{Im}) = (280\pm210, 360\pm170, -80\pm160)$ μas yr^{-1}, which corresponds to 200 ± 80 μas yr^{-1} amplitude. The apex directions of the distance-dependent and independent fits are consistent, indicating that both fits probe the same underlying systematics. Additionally, the distance-dependent dipole amplitude normalized to the median distance of the sample, 43 Mpc, is ~ 30 μas yr^{-1}, which is consistent with the known *Gaia* systematics.

Either an improvement of the statistical and systematic errors or a larger sample size will therefore be required to reduce the uncertainty of the secular parallax limit. The uncertainty on the coefficients and amplitude of the global signal scales with the sample size as $N^{-1/2}$, so to achieve uncertainty on the signal at 1 Mpc of about 10 μas yr^{-1} without any reduction on the individual proper motion uncertainties would require a larger sample size by a factor of 10,000, assuming identical distance and sky distributions. However, proper motion uncertainties scale as $t^{-3/2}$, so the longer time baseline of future *Gaia* data releases will decrease the individual uncertainties. The average per-object uncertainties will decrease by about an order of magnitude by *Gaia*'s nominal end of mission. For the sample used to make the above limit, the mean expected uncertainties are $\sim$ 120 and 110 μas yr^{-1} in RA and Dec.

3.4 An Updated Secular Parallax Measurement with Gaia DR3

The third *Gaia* data release (*Gaia* DR3) was released on 13 June 2022 (Gaia Collaboration et al., 2022c), and includes the astrometric solution of the early-DR3 release 3 December 2022 (Gaia Collaboration et al., 2021a). In comparison to DR2, overall proper motion precision is increased by a factor of 2 and systematic errors are reduced by a factor of 2.5. The new data release also includes a 5-parameter astrometric solution for a larger portion of the *Gaia*-Cosmicflows crossmatch, as described below. In this section, we find a new limit on the secular parallax dipole using the improved astrometry available with *Gaia* DR3.

3.4.1 Sample Selection

The sample selection for DR3 was conducted in a similar fashion to DR2 (Section 3.3.1). We cross-matched the Cosmicflows-3 catalog with *Gaia* DR3 using a 3 arcsecond matching radius, which resulted in 2668 objects with at least a 5-parameter solution. Additional cuts to minimize contamination by foreground stars were to exclude sources near the Galactic plane ($|b| \leq 10^\circ$), sources with $> 5\sigma$ annual parallax measurements, and sources with $> 5\sigma$ proper motion measurements in either RA or Dec. Finally, we remove galaxies within 1.5 Mpc to exclude the Local Group. The resulting sample contains 2408 sources, which is a factor of ~ 10 larger than the DR2 galaxy sample. Due to the substantially larger sample size, we did not visually inspect each source.

The mean proper motion uncertainties are 0.62 mas yr^{-1} in RA and 0.60 mas yr^{-1} in Dec. The distances and G magnitudes of the sample are shown in Figure 3.7. In comparison to the DR2 sample, the proportion of the sample at moderately large distances is substantially increased, with 77% at $D > 50$ Mpc.

3.4.2 Results

We perform a least-squares fit of the distance-dependent dipole to the proper motions of the 2408 objects sample. The resulting best fit dipole is $(s_{10}, s_{11}^{Re}, s_{11}^{Im}) = (420 \pm 650, 1070 \pm 380, -630 \pm$

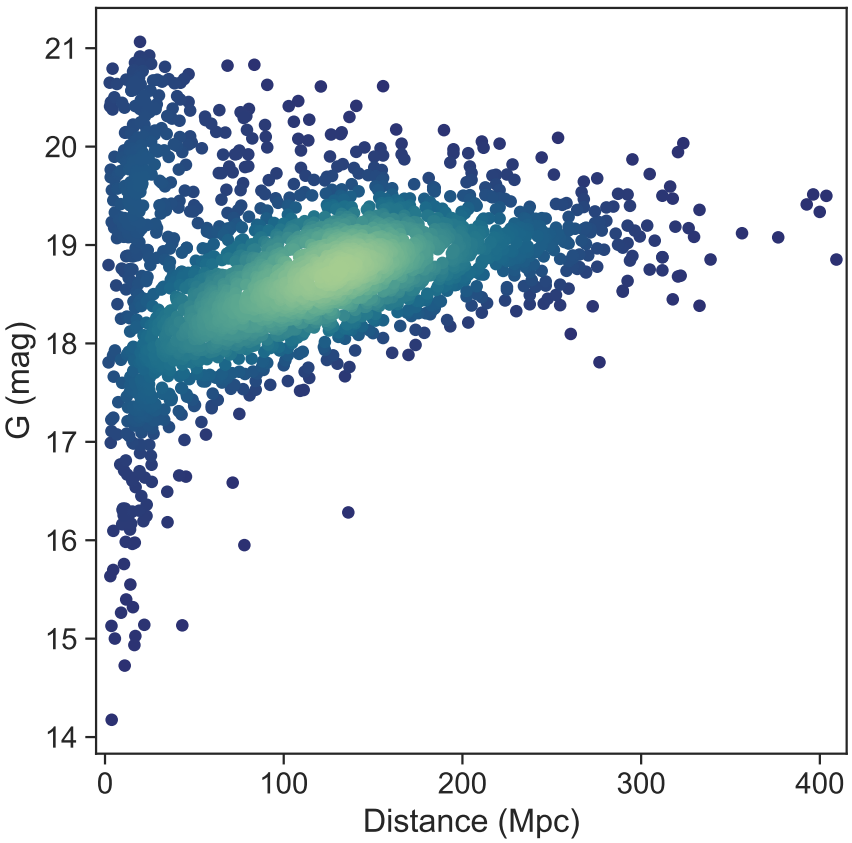

Figure 3.7: G band magnitudes vs. distance for the *Gaia* DR3-Cosmicflows sample of galaxies. Color scales with the density of over-plotted points.

330) μas yr^{-1} Mpc, which corresponds to an amplitude of 630 ± 180 μas yr^{-1} Mpc with an apex towards $(30 \pm 16°, -13 \pm 20°)$ in RA and Dec. The best fit dipole is shown in Figure 3.8. The Z-score of the fit was 2.2, so the dipole is not significant, but the direction of the dipole is consistent with the result from DR2. The 95% confidence interval upper limit on the amplitude is ~ 980 μas yr^{-1} Mpc.

We also fit a distance-independent dipole to the DR3 sample, which resulted in best fit coefficients of $(s_{10}, s_{11}^{Re}, s_{11}^{Im}) = (78 \pm 41, 68 \pm 30, -44 \pm 28)$ μas yr^{-1}, corresponding to an amplitude of 48 ± 14 μas yr^{-1} with an apex towards $(33 \pm 20°, -34 \pm 17°)$. The fact that the direction of the distance-dependent and independent dipoles are consistent indicates that the DR3 result is still sensitive to large scale systematics in the *Gaia* astrometric solution.

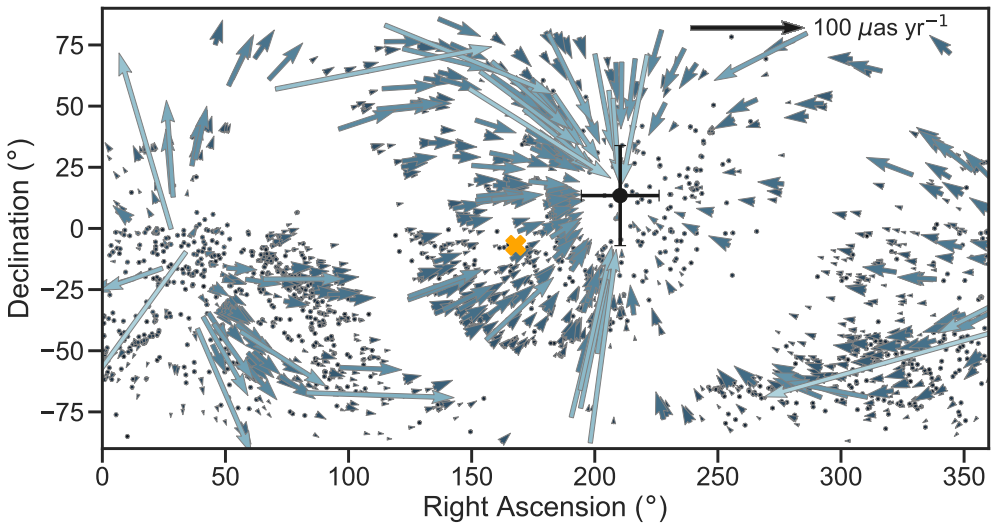

Figure 3.8: Best fit distance-dependent dipole for the *Gaia* DR3-Cosmicflows sample. The colors of arrows scale with distance. The error bars show the location of the dipole antapex, and the orange X indicates the direction of the solar system motion with respect to the CMB.

The uncertainties of the dipole coefficients are reduced from the DR2 measurement to DR3 by about a factor of 5 each. Statistical proper motion uncertainties scale with time by $t^{-3/2}$, and the fit uncertainties scale with sample size by $N^{-1/2}$. *Gaia* DR2 included astrometry from the first 22 months of the mission, and DR3 includes 34 months, so we would expect reduction in uncertainties around a factor of $(\frac{232}{2408})^{-1/2}(\frac{22}{34})^{-3/2} \approx 6$. The slight discrepancy between this expectation and the factor of 5 reduction in the fit uncertainties is most likely attributable to differences in the distribution of distances (the new result includes many objects at larger distances which have less impact on the fit), and the fact that we did not do visual inspection so the sample is not as clean.

3.5 Secular Parallax Predictions

As demonstrated in the previous sections, the systematics present in *Gaia* DR2 and DR3 act as a noise floor below which we may not analyze low multipole proper motions. Future *Gaia* data releases, however, will likely contain larger numbers of extragalacitic proper motion measurements with lower per object statistical uncertainties and systematics. We can expect that the majority of the 9,823 objects in our initial *Gaia*-Cosmicflows crossmatch will have proper motion measurements

by the final data release. In this section, we therefore forecast the detectability of secular parallax for *Gaia* end-of-mission astrometry and explore the ideal sample selection to be used for future data releases.

3.5.1 Simulated Proper Motion Catalog

We calculate proper motions consistent with *Gaia's* expected end-of-mission performance for objects in the *Gaia*-Cosmicflows crossmatch described in Section 3.3.1. We exclude any galaxies closer than 1.5 Mpc, with galactic latitude below 10 degrees, or with significant annual parallax detected by *Gaia*. The later two requirements mitigate contamination by foreground stars. One additional object was identified as a foreground star by visual inspection. The catalog contains 9,698 objects, most of which do not have measured proper motions as of *Gaia* DR2. For each galaxy, we simulate a *Gaia* end-of-mission proper motion based on three components: the source's predicted proper motion errors, the expected secular parallax, and predicted peculiar velocity based on the Cosmicflows-3 peculiar velocity field.

End-of-mission proper motion errors are calculated using the PyGaia Python toolkit.[2] The predicted uncertainties assume a five year mission, although *Gaia*'s total mission lifetime has already passed its nominal five years (Gaia Collaboration et al., 2016b). The calculation depends on the source's G magnitude, ecliptic latitude, and $V - I_C$ color. We set the latter to zero for all sources as the color has negligible impact on the predicted uncertainty and is not available for all sources. The mean expected uncertainties are 77 μas yr^{-1} for proper motion in R.A. and 68 μas yr^{-1} in Dec. Note that the predicted uncertainties do not include potential systematic errors. We generate proper motion noise for each object by randomly sampling from a Gaussian distribution with standard deviation set to the object's predicted proper motion uncertainty in R.A. and Dec.

Peculiar proper motions are calculated from the local peculiar velocity field described in detail in Graziani et al. (2019). The velocity field was reconstructed from the Cosmicflows-3 catalog, utilizing the observed distance moduli and redshifts of Cosmicflows galaxies to infer both the matter

[2] `www.cosmos.esa.int/web/gaia/science-performance`

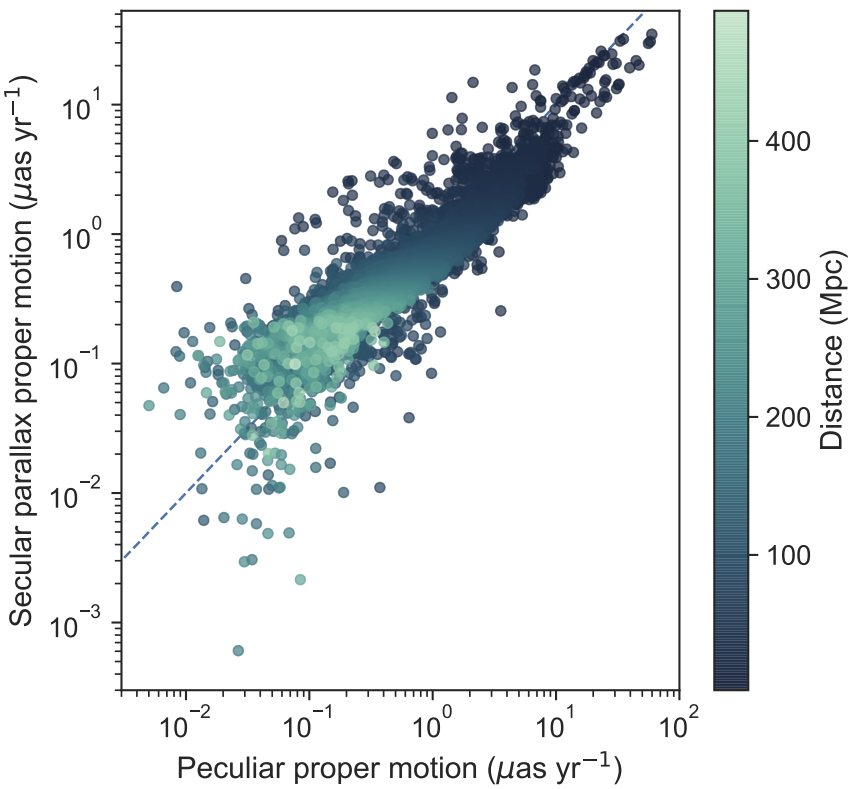

Figure 3.9: Simulated secular parallax vs. peculiar proper motion components for individual objects. Colors scale with the distance of each galaxy. For reference, the dashed line denotes a one-to-one correspondence where peculiar proper motions show the same amplitude (but not necessarily direction) as the secular parallax.

over-density field and the three-dimensional peculiar velocity field. We find peculiar proper motions then by converting the transverse velocities to angular motions. The transverse velocities are on the order of a few hundred km s^{-1} in the CMB frame, with a maximum of $\sim$ 1000 km s^{-1}. The resulting peculiar proper motions range from 0.005 to 60 μas yr^{-1} and the mean is $\sim$ 1 μas yr^{-1}.

In Figure 3.9, we plot the peculiar vs. secular parallax proper motions (calculated from Equation 3.2) for each galaxy. The peculiar proper motion amplitude is larger than the expected secular parallax for 58% of galaxies in the sample. While the transverse velocity amplitudes of individual galaxies do not depend on distance, the corresponding peculiar angular motions depend on distance as $1/D$, which complicates the measurement of secular parallax. Additionally, the transverse velocity angular power spectrum varies with distance, with more power in $\ell = 1$ at

Table 3.1: Dipole properties for the expected secular parallax dipole, the best-fit dipole to simulated peculiar proper motions, and the best-fit dipole to the full simulation including secular parallax, peculiar, and random noise proper motion components.

	s_{10} (μas yr^{-1} Mpc)	s_{11}^{Re} (μas yr^{-1} Mpc)	s_{11}^{Im} (μas yr^{-1} Mpc)	Amplitude (μas yr^{-1} Mpc)	Apex coordinates RA, Dec
Secular Parallax	27.2	-155	-33.1	78	167.9°, $-6.9°$
Peculiar	$-139(38)$	$-38.9(24.0)$	86.9(20.3)	69.1(11.6)	245.9°, 46.1°
Full simulation	$-112(38)$	$-194(24)$	53.8(20.3)	107(12)	195.5°, 21.6°

smaller distances (Hall 2019; Section 3.6.1).

To create the simulated proper motion catalog, we first sample each object's end-of-mission uncertainties to generate a noise term, and then add the predicted parallax and peculiar proper motions. We note that the largest contribution to real extragalactic proper motions is typically the secular aberration drift, which we do not include in our simulations in this work. However, the secular aberration drift is expected to be measured with high significance using the sample of $> 5 \times 10^5$ AGN detected by *Gaia* (Paine et al., 2018). The following predictions are therefore made with the assumption that the secular aberration drift dipole can be constrained or subtracted prior to fitting for secular parallax. We also do not include the effects of possible contaminating foreground stars; the proper motion is calculated assuming that each *Gaia* source is the Cosmicflows galaxy.

3.5.2 Gaia End of Mission Simulations

To simulate secular parallax detection, we perform error weighted least squares fits of the distance-dependent dipole model to the simulated proper motion catalog. We perform 1,000 fits, where for each trial we generate random noise for each object by sampling the end-of-mission uncertainties. The average resulting fit is a 107 ± 12 μas yr^{-1} Mpc dipole with apex of ($195 \pm 6°$, $22 \pm 7°$) in RA and Dec, and mean Z-score of 7.8. The mean dipole coefficients are listed in Table 3.1. The average best-fit dipole is significantly offset from the secular parallax expectation

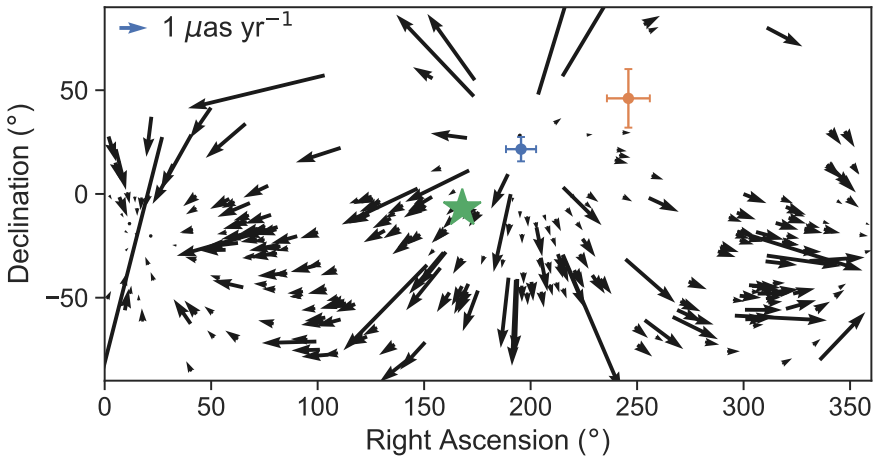

Figure 3.10: Arrows show the simulated best fit dipole for the proper motions including secular parallax, peculiar motions, and noise consistent with *Gaia* end-of-mission uncertainties. The midpoint of the arrows represent the coordinates of 300 objects randomly selected from the simulated catalog to illustrate the proper motion vector field. The blue cross shows the location of the apex of the fit, whereas the orange cross shows the location of the apex when fitting to the peculiar proper motions alone, and the green star is the location of the CMB apex and the apex of the secular parallax dipole. The offset of the best fit dipole from the CMB apex demonstrates the mixing of the peculiar and parallax dipoles.

from the CMB, which is due to dipole correlations of the peculiar proper motions in our sample. For each trial, we also perform fits to the catalog excluding the predicted secular parallax proper motions, in order to demonstrate the impact of peculiar motions on secular parallax detection. The mean dipole coefficients for the noisy peculiar proper motions are also listed in Table 3.1 and correspond to a 69.1 ± 11.6 μas yr^{-1} Mpc dipole toward $(246 \pm 14°, 46 \pm 10°)$. The dipole detected in the full simulation reflects the combination of the expected secular parallax and peculiar proper motions. In fact, the best-fit dipole parameters are consistent with the sum of the separate parallax and peculiar dipole parameters, and the amplitude is consistent with the parallax and peculiar dipole amplitudes summed in quadrature. The mixing of the two dipoles is further demonstrated in Figure 3.10, which shows the locations of the best-fit dipole apex for the full simulation, for the peculiar proper motions, and the expected secular parallax apex (CMB apex).

From Equation 3.2, one can demonstrate that the vector field produced by addition of two dipoles is simply another dipole. It is therefore not possible to separate the parallax and peculiar

dipoles observationally without prior knowledge of either component. However, the CMB dipole has a well measured direction, so we may fix the location of the dipole apex in order to recover the secular parallax amplitude. This is achieved by constraining the ratios of s_{10} to s_{11}^{Re} and s_{11}^{Im} while fitting (the signs and relative absolute values of the coefficients determine the direction of the dipole, whereas the sum of squares gives the amplitude as in Equations 3.3-3.4). We perform 1,000 trials fitting the fixed-direction distance-dependent dipole, again randomly generating noise for each trial. The resulting average fit has amplitude ~ 74 μas yr^{-1} Mpc detected with mean Z-score of 9.5. This represents a significant detection of the secular parallax amplitude. We note that the peculiar proper motion dipole is nearly orthogonal to the expected secular parallax dipole and therefore contributes almost zero amplitude to the fixed-direction fits. The orthogonality of the two components is a fortunate coincidence due to the solar system's phase in its Galactic orbit and the Galaxy's peculiar motion.

Finally, we test the possibility of constraining both the parallax and peculiar dipoles. We perform 1,000 trials simultaneously fitting two distance-dependent dipoles, one with direction fixed to the CMB apex and one with variable direction and amplitude. Neither dipole is recovered when simultaneously fitting, so it will be necessary to account for the secular parallax dipole prior to studying the peculiar proper motions from LSS. This may be achieved by either fitting for the parallax dipole independently as described above and subtracting the detected field, or assuming the secular parallax proper motion field from the CMB.

3.5.2.1 Predicted Dependence on Sample Selection

The 9 σ detection prediction is made for nearly the full *Gaia*-Cosmicflows sample, only employing cuts on the sample to mitigate stellar contamination and poor centroid fits. However, the predicted detection is very sensitive sample selection. Below, we consider several variables that may impact the detection: the minimum and maximum distances, D_{min} and D_{max}; maximum individual proper motion amplitude; and minimum G magnitude.

The choice of D_{min} should impact the relative contribution of the peculiar proper motions to

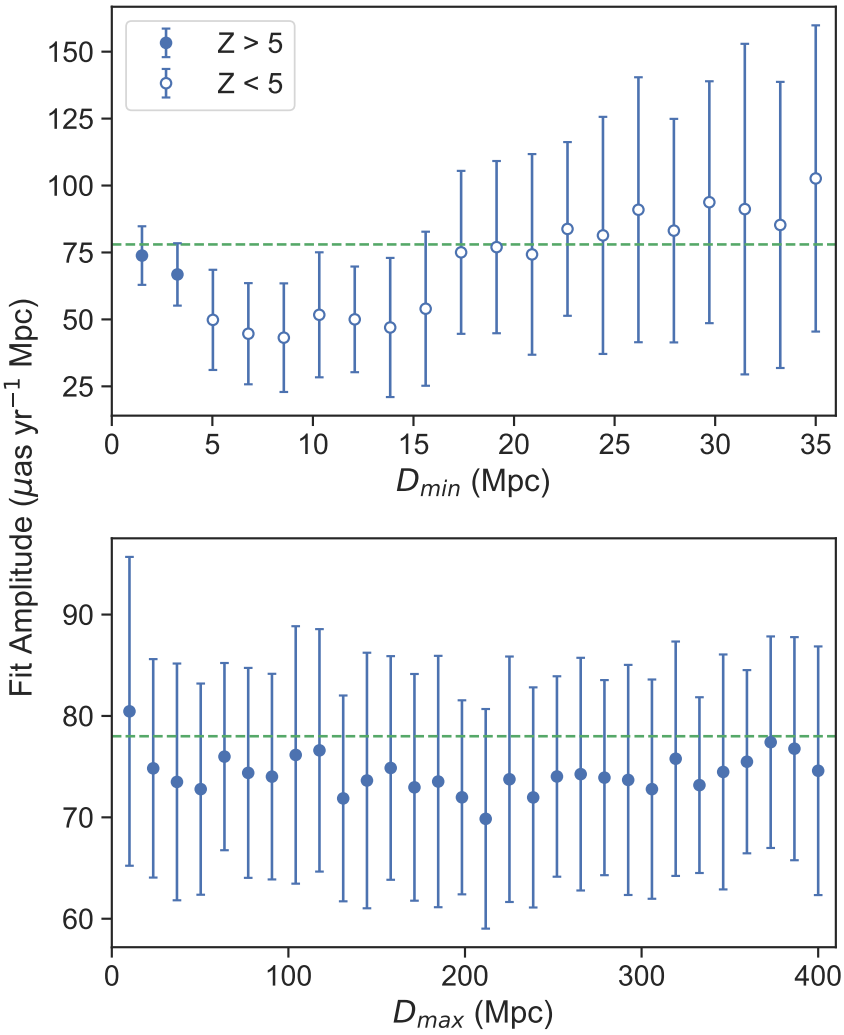

Figure 3.11: Simulated fixed-direction, distance-dependent dipole fits for minimum distance cuts between 1.5 and 35 Mpc (top) and for maximum distance cuts between 10 and 400 Mpc (bottom). Fits are made to the simulated proper motions including expected secular parallax, model predicted peculiar motions, and noise components. The green dashed lines indicate the input secular parallax amplitude of 78 μas yr^{-1}. Top: the first point indicates a $\sim 10\sigma$ detection of the secular parallax amplitude. Note that only the first two distance cuts result in significant fits. Bottom: all fits are significant regardless of maximum distance cut. The uncertainties are similar to the first two points in the top plot (note that the axes scales are not the same).

the detected dipole since the peculiar velocity dipole decreases in power for larger distances (Hall 2019, see also Section 3.6.1). The peculiar dipole is approximately orthogonal to the expected secular parallax in all distance bins, and should therefore have nearly zero component in the fixed-direction fits. In Figure 3.11, we show the fixed-direction best-fit dipole amplitudes for D_{min} cuts

between 1.5 and 35 Mpc, where we performed 50 trials per distance cut. Only $D_{min} < 5$ Mpc cuts result in significant detection of the secular parallax amplitude on average. The mean Z-scores of the fits for the two smallest D_{min} cuts are 9.5 and 8.0, respectively. For D_{min} cuts between 20 and 35 Mpc, typical Z-scores are 2. The prediction is therefore very sensitive to the inclusion of very nearby galaxies which have predicted parallaxes between 8 - 35 μas yr^{-1}. By comparison, D_{max} has little impact on the detection. Figure 3.11 also shows the best-fit dipole amplitudes for D_{max} cuts between 10 and 400 Mpc. We find that the best-fit dipole amplitude and Z-score are fairly constant for all D_{max}. The significance of the fits drops to $\sim 7\sigma$ for distance cuts < 20 Mpc, where the sample size is < 500 objects. Distant galaxies with large uncertainties compared to their expected parallax therefore have little impact on the detection as long as nearby objects with the most signal are included.

The G magnitude of each object impacts the simulated proper motions due to the dependence of the end-of-mission proper motion uncertainties on G. Magnitude vs. distance for each object are plotted in Figure 3.12, showing a tail of nearby, bright galaxies with $G < 15$. These objects will have the largest predicted proper motions and smallest uncertainties, provided that good astrometric solutions can be obtained for nearby, extended galaxies. The error-weighted fits are therefore highly sensitive to proper motions of these galaxies. We test this by varying the minimum G magnitude in the sample between 13 and 16 mag, and for each cut we perform 50 fits with resampled noise components. The best-fit dipole amplitudes are shown in Figure 3.12. We find that all fits including galaxies brighter than 15 mag are significant and consistent with secular parallax within 1 σ. Relatively bright and nearby galaxies will most likely require closer individual inspection when real *Gaia* data is available in order to cull objects that may throw off the total fits due to spurious proper motions or larger than expected peculiar motions. The the fact that some fits for G cuts < 15 are significant indicates that secular parallax may be detectable only if the majority of bright galaxies need not be culled. Nearby, diffuse galaxies will also require individual inspection, but they do not contribute to the measured signal as much as the brightest galaxies.

The mean noise-free proper motion is ~ 1 μas yr^{-1} and the maximum is 65 μas yr^{-1}, whereas

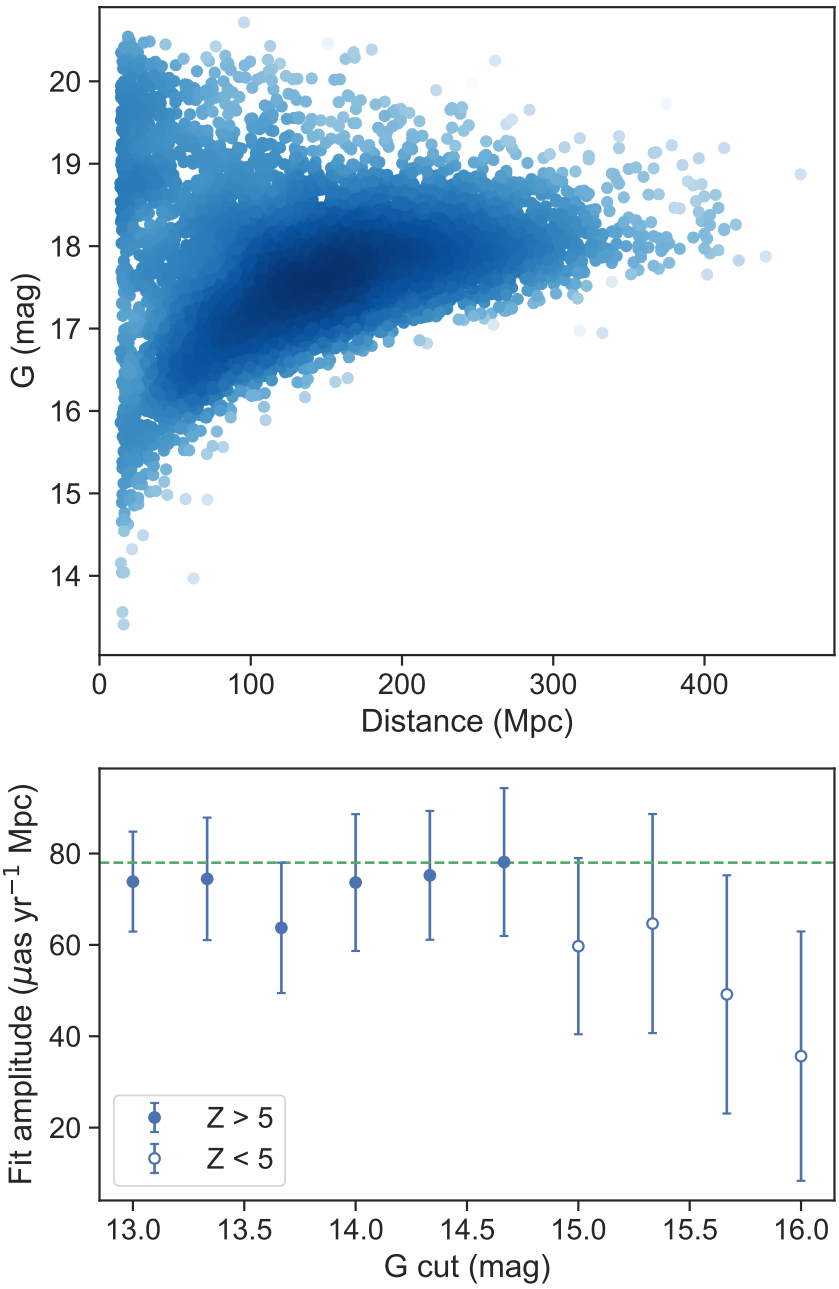

Figure 3.12: Top: G magnitudes vs. distance for *Gaia*-Cosmicflows galaxies. Predicted *Gaia* end-of-mission proper motion uncertainties scale with G. Bottom: simulated fixed-direction, distance-dependent dipole fits for minimum G magnitude cuts between 13 and 16 mag. The green dashed line indicates the input secular parallax amplitude of 78 μas yr^{-1}. The first 6 cuts (minimum $G < 15$) result in significant average fits.

the mean expected uncertainty is about 80 μas yr^{-1}. The majority of simulated proper motions are then dominated by noise and vary greatly between trials. Controlling the maximum individual

proper motion can therefore probe the dependence of the fits on noisy, insignificant proper motions. In Figure 3.13, we plot the best-fit fixed-direction dipole amplitudes and Z-scores for maximum individual proper motion amplitude cuts up to 300 μas yr^{-1}, where we have performed 50 trials per proper motion cut. New noise components are randomly generated for each trial, so the specific objects that are cut vary per trial. The best-fit dipole amplitude only depends on proper motion cut if the maximum proper motion is small enough so as to exclude nearby galaxies with the largest secular parallaxes. However, the significance of the fits is increased for cuts between 50-150 μas yr^{-1}. Picking a proper motion cut in this range does not impact the previously established dependence on distance and magnitude cuts: the fits are still only significant if relatively bright galaxies within 5 Mpc are included, but are insensitive to D_{max}.

3.6 Low Multipole Analysis of Peculiar Proper Motions

In this section, we study the predicted peculiar proper motions of Cosmicflows galaxies and compare to LSS theory. We also assess the impact that peculiar proper motions may have on quadrupole ($\ell = 2$) proper motion measurements, including gravitational waves and anisotropic expansion. In the following subsections, we utilize the simulated catalog described in Section 3.5.1 including only the peculiar velocity component of each galaxy's proper motion.

3.6.1 Comparison to LSS Theory

Peculiar velocities arise from gravitational interactions with large-scale matter density fluctuations, causing transverse velocities, and therefore proper motions, of galaxies to deviate from a perfectly isotropic Hubble flow. Previous works (e.g. Darling & Truebenbach 2018 and Hall 2019) have demonstrated that extragalactic proper motions may probe these peculiar transverse velocities and therefore the matter power spectrum. Hall (2019) derive the peculiar velocity power spectrum for low redshift based on the matter power spectrum computed with the CAMB cosmology code. The peculiar velocity field is expected to be nearly curl-free and corresponds to an E-mode transverse velocity power spectrum where the dominant mode is distance dependent. Dipole cor-

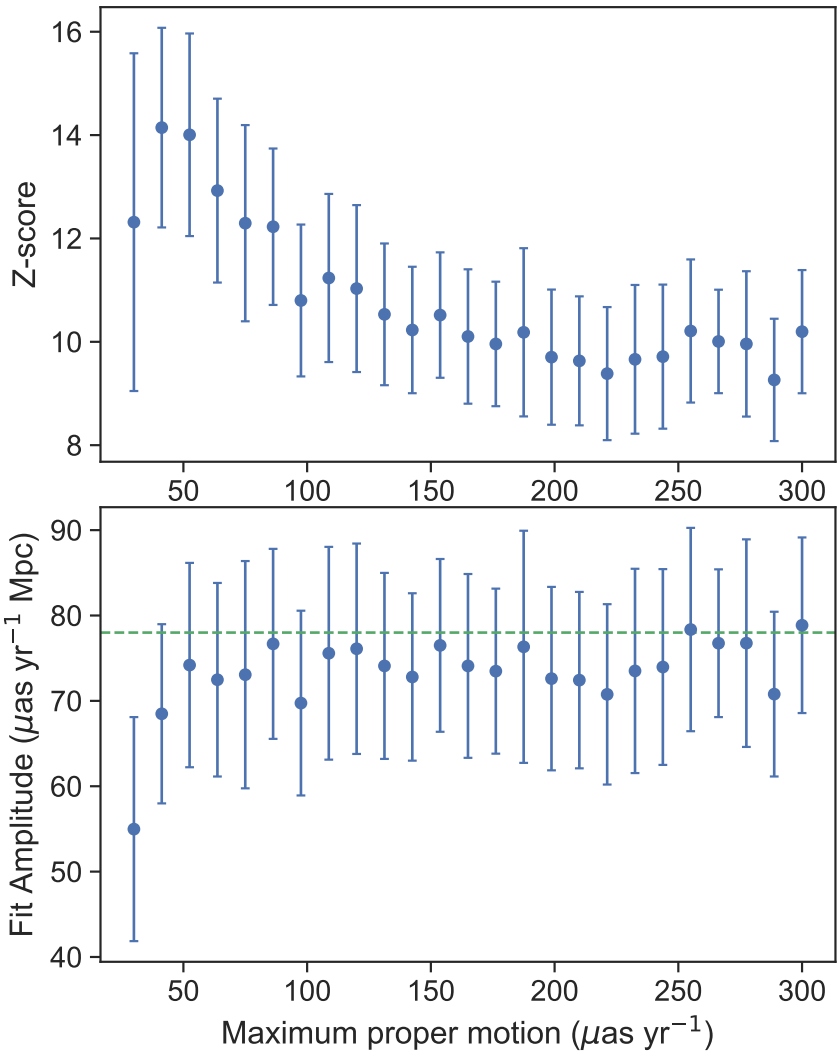

Figure 3.13: Z-scores (top) and best-fit amplitudes (bottom) of fixed-direction, distance-dependent dipole fits for maximum proper motion cuts up to 300 μas yr^{-1}. The green dashed line indicates the input secular parallax amplitude of 78 μas yr^{-1}.

relations dominate for small distances, and the power transfers to higher ℓ (smaller angular scales) with increasing distance.

For comparison, in Figure 3.14 we show the E-mode dipole, quadrupole, and octopole square root powers ($\sqrt{P_\ell}$) fit to the noise-free model-predicted peculiar proper motions for 10 Mpc distance bins up to 300 Mpc, which gives an estimate of the power as a function of distance. The proper motion powers are normalized to 1 Mpc and can therefore be related to a transverse peculiar

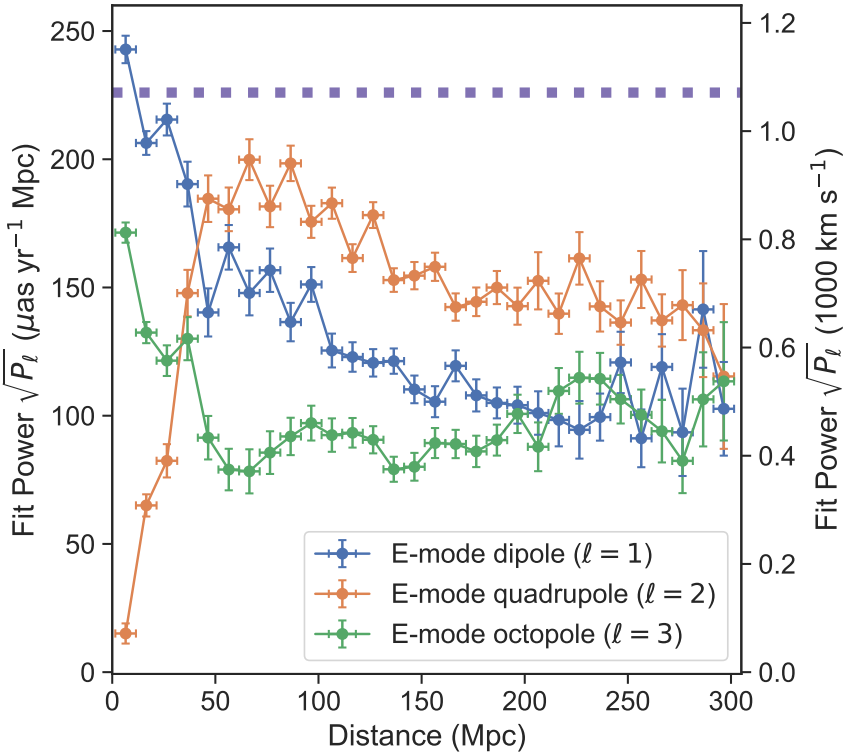

Figure 3.14: E-mode distance-dependent dipoles (blue), quadrupoles (orange), and octopoles (green) fit to the peculiar proper motions for objects in 10 Mpc distance bins up to 300 Mpc. The secular parallax power is indicated by the purple dashed line. The right vertical axis shows the same powers converted to distance independent velocities. Error bars represent the width of distance bins (horizonal) and the uncertainties of the fits (vertical), The fits were performed for noise-free modeled proper motions, so the fits and uncertainties are not indicative of expected *Gaia* end-of-mission results.

velocity, where a 1 μas yr^{-1} proper motion at 1 Mpc is equivalent to a 1 AU yr^{-1} $\approx$ 4.74 km s^{-1} velocity. This method is equivalent to fitting distance-independent vector fields to the transverse velocities. The total velocity power in $\ell = 1$, 2, and 3 is on the order of 1000 km s^{-1} at all distances. Square root powers should not be interpreted as representative proper motions or velocities. The amplitudes of the fits, however, represent the maximum magnitude of the vector field. For a dipole, the amplitude is simply proportional to the power, as given by Equation 3.4, but the amplitude for higher ℓ is not. We find the amplitude of each $\ell = 2, 3$ fit by solving numerically for the maximum of the best fit vector field magnitudes. The amplitudes of the highest power bins are 84, 88, and 80 μas yr^{-1} Mpc, corresponding to velocities of 398, 417, and 380 km s^{-1} for ℓ = 1, 2, and 3,

respectively, roughly as expected for peculiar velocities induced by LSS.

As expected, the dipole power decreases with distance as the power shifts to the quadrupole, which peaks between 50-100 Mpc. The octopole power, however, does not match the theory predictions, since we see more power in the octopole than the quadrupole at small distances. This discrepancy may be due to uneven sky coverage of the galaxy sample. Alternatively, the octopole power may reflect real deviations of local matter density fluctuations, and therefore the peculiar velocity field, from universe-averaged models. We note, however, that the distance dependence of the peculiar proper motion power spectrum will not be detected using the *Gaia*-Cosmicflows sample. When *Gaia*-like noise is added to the proper motions, the power per distance bin is not significantly detected.

The secular parallax dipole power is $\sqrt{P_{E1}} = 226$ μas yr^{-1} Mpc. While secular parallax decreases as $1/D$, the normalized power (which is a proxy for the solar system's linear velocity) is not a function of distance. Secular parallax is therefore dominant for distances $\gtrsim 40$ Mpc compared to the peculiar dipole. However, *Gaia* will not be sensitive enough to significantly detect secular parallax at that distance.

3.6.2 Impact on Distance-Independent Measurements

Cosmological effects such as the isotropy of the Hubble expansion and primordial gravitational waves induce distance-indepedent proper motion signals at low ℓ. Here we assess the impact that peculiar velocities will have on distance-independent proper motion quadrupole measurements. In comparison to the sample of local galaxies selected for this work, distance independent measures may be made for quasars at generally higher redshift. It is thus most relevant to compare the quadrupole powers recovered for large distance cuts, where we expect the LSS power spectrum to be dominated by higher ℓ. Figure 3.15 shows the results of simultaneously fitting an E-mode dipole and both E and B-mode quadrupoles to the noise-free peculiar proper motions for varying D_{min}. Note that these are distance-independent fits, so the square root powers are 1-2 orders of magnitude lower than those in Figure 3.14 and cannot be simply scaled to a relative velocity. The

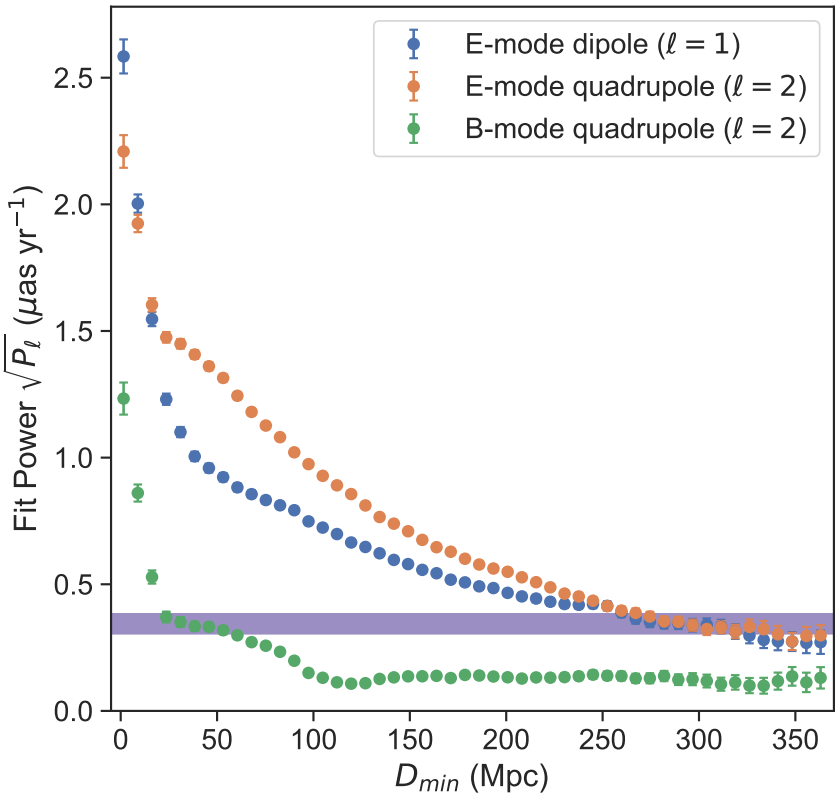

Figure 3.15: Distance-independent E-mode dipole (blue) and quadrupole (orange), and B-mode quadrupole (green) fits to the peculiar proper motions for varying minimum distances. The purple bar at 0.34 μas yr^{-1} represents the approximate total $\sqrt{P_2}$ (E2+B2) for $D_{min} > 300$ Mpc cuts.

powers in each mode approach minimum values $\sqrt{P_\ell} < 0.4$ μas yr^{-1} for large distance cuts. Below, we describe the implications of these fit powers for measurements of the isotropy of the Hubble expansion and gravitational waves.

3.6.2.1 Anisotropic Expansion

Triaxial anisotropic expansion would be observable as an E-mode proper motion quadrupole, where galaxies appear to stream towards the directions of faster expansion (Darling, 2014). The anisotropy is characterized by the fractional departure from the Hubble expansion in a given direction:

$$\Sigma_i = \frac{H_{i,0}}{H_0} - 1,$$

where i denotes the triaxial expansion axes x, y, and z. From Equations A1 and A2 of Darling (2014), we derive an expression to relate the total anisotropy to a proper motion quadrupole power by

$$\sqrt{P_{E_2}} = H_0 \sqrt{\frac{4\pi}{5}\left(\Sigma_x^2 + \Sigma_y^2 + \Sigma_z^2\right)}, \tag{3.7}$$

where H_0 is the Hubble constant expressed in units of proper motion, which we assume to be $H_0 \approx 70$ km s^{-1} Mpc^{-1} $= 15$ μas yr^{-1}.

The mean peculiar E-mode $\ell = 2$ power for $D_{min} > 300$ Mpc is $\sqrt{P_{E_2}} = 0.3$ μas yr^{-1}, or 0.014 in units of $H_0\sqrt{4\pi/5}$. For each fit, we also solve for Σ_i using the relations to the quadrupole coefficients derived in Darling (2014). The average maximum anisotropy inferred from the quadrupole fits for $D_{min} > 300$ is $\Sigma_{max} \approx 0.01$. Anisotropic expansion would therefore be indistinguishable from LSS proper motions for anisotropy $< 1\%$. The predicted end-of-mission anisotropy noise floor for *Gaia* quasars is about 2% (roughly $\sqrt{P_{E2}} = 1$ μas yr^{-1}; Paine et al. 2018), so the anticipated limit on anisotropy from *Gaia* is unaffected by LSS. However, improved astrometric precision from a next generation Very Large Array (ngVLA) or future space based astrometry mission may enable quadrupole measurements with quasars that will approach or be limited by the LSS power.

3.6.2.2 Gravitational Waves

The primordial gravitational wave background will cause angular deflection of light rays with equal power in the E and B-modes for $\ell \geq 2$ (Gwinn et al., 1997; Book & Flanagan, 2011), which may be observable as extragalactic proper motions. The power in $\ell = 2$ contributes 5/6 of the total gravitational wave signal, so the gravitational wave energy density may be estimated by

$$\Omega_{GW} = \frac{6}{5}\frac{1}{4\pi}\frac{P_2}{H_0^2}, \tag{3.8}$$

where P_2 is the total quadrupole power (E and B-modes). Darling et al. (2018) found astrometric limits on the gravitational wave energy density of $\Omega_{GW} < 0.0064$ for proper motions of 711 radio sources and $\Omega_{GW} < 0.011$ for proper motions of 508 radio sources combined with one epoch of

Gaia data from the first data release. Additionally, they predicted a $\Omega_{GW} = 4 \times 10^{-4}$ noise floor for *Gaia* end-of-mission AGN proper motions.

For $D_{min} > 300$ the total quadrupole square root power approaches $\sqrt{P_2} = 0.34$ μas yr^{-1}, which corresponds to $\Omega_{GW} = 5 \times 10^{-4}$, similar to the predicted *Gaia* noise floor. However, the power in B2 is significantly lower than that in E2 for the peculiar proper motions, whereas gravitational waves produce equal power in E and B-modes. With improved astrometric precision, one may differentiate between the LSS quadrupole and gravitational waves by comparing the powers detected in the E and B-modes.

3.7 Discussion and Conclusions

3.7.1 Gaia DR2 Result

The systematic errors of *Gaia* DR2 proper motions impose a noise floor that limits the amplitude of proper motion signals that may be studied with vector spherical harmonic decomposition. The large-scale systematics have been studied in detail by Lindegren et al. (2018) and Gaia Collaboration et al. (2018a), and correspond to ~ 40 μas yr^{-1} for large angular scales. We find that the addition of distance data utilized in the secular parallax measurement, which one would not expect to be spatially correlated, does not allow us to probe signals below the systematic noise floor. We therefore find a 3500 μas yr^{-1} Mpc upper limit on the extragalactic secular parallax amplitude. Increased sample size would improve the sensitivity of the measurement since uncertainties scale as $N^{-1/2}$. However, achieving the statistical uncertainty to detect the 80 μas yr^{-1} Mpc signal of secular parallax using *Gaia* DR2 would require a sample size of $\sim 10^6$, which is more than the number of galaxies in the local volume.

3.7.2 Gaia DR3 Result

Improved astrometry and increased sample size from *Gaia* DR2 to DR3 result in reduction in the uncertainties of best fit dipole by about a factor of 5. However, we find that the secular

parallax measurement is still sensitive to the large-scale systematics in the astrometric solution. The resulting upper limit on the secular parallax amplitude using DR3 is 980 μas yr^{-1} Mpc.

A catalog of extragalactic objects was released as part of *Gaia* DR3, including a subset with estimated redshifts (Gaia Collaboration et al., 2022a). The "pure" galaxy subset (estimated to be 94% pure of stellar contamination by Gaia Collaboration et al. 2022a) contains 230,000 objects with estimated redshifts. The mean proper motion uncertainties of this sample are about 1 mas yr^{-1}, suggesting that this sample may be sensitive to correlated proper motions down to about (1 mas yr^{-1}) $/\sqrt{230000} = 2$ μas yr^{-1}. The redshift-based distances of the sample are > 100 Mpc and the majority are > 500 Mpc, while the secular parallax amplitude normalized to 100 Mpc is 0.78 μas yr^{-1}. We therefore conclude that this sample is unlikely to provide a better limit on the secular parallax amplitude using current data.

3.7.3 Predicted Proper Motion Measurements

Using the expected improvements to the sample size and proper motion uncertainties of *Gaia*-Cosmicflows galaxies in future data releases, we predict a significant (5-10σ) detection of the secular parallax amplitude. This prediction is dependent on the assumption that the systematic errors in *Gaia* DR2 and DR3 will be resolved. The detection is also highly sensitive to sample selection: relatively bright, local galaxies must be included to significantly detect secular parallax. We find that the secular parallax is only detected for simulations with D_{min} cuts < 5 Mpc and G magnitude cuts < 15. The significance of the detection may also be improved by employing a proper motion amplitude cut < 150 μas yr^{-1}, which limits the portion of the sample with highly noise-dominated proper motions. Very distant galaxies with expected secular parallaxes well below *Gaia*'s expected proper motion precision may be included in the sample, but have little to no effect on the detected dipole as long as the signal is detected for local galaxies. *Gaia* data release 3 is expected to include results for extended objects and quasars, which may have implications for the secular parallax measurement.

The ultimate goal of a secular parallax measurement would be extragalactic distance esti-

mates. However, the secular parallax may only be measured if a prior is assumed for the peculiar motion and distance, such as those provided by Cosmicflows-3, and therefore an independent distance estimate from secular parallax is most likely not possible for individual galaxies. Regardless, a statistical measurement of the secular parallax amplitude would lead to a constraint on the Hubble constant. If redshift is used as proxy for distance in Equation 3.1, then the amplitude of the fit is a product of the secular parallax proper motion amplitude and the local value of the Hubble parameter, H_0. One therefore needs to either constrain the secular parallax amplitude or assume the value from the CMB to infer the Hubble parameter. Our prediction does not directly translate to a redshift based fit because the galaxies closer than 5 Mpc that dominate the simulated fits most likely have large peculiar velocities relative to the recessional velocities predicted by the Hubble flow. However, the fit for nearby galaxies will be useful to assess the mixing of the secular parallax and peculiar dipole signals. From the results in Figure 3.11, we predict $\sim 2\sigma$ amplitude fits for D_{min} cuts > 20 Mpc, and thus a $\sim 2\sigma$ upper limit on H_0 if the secular parallax amplitude is assumed from the CMB dipole.

The primary limitation of the predicted detection and any resulting constraint on the Hubble constant is the dependence on very nearby galaxy proper motions, and thus the mixing of the secular parallax signal with the peculiar dipole. A potential method to improve the signal to noise at larger distances is to search for galaxy cluster members detected by *Gaia*. Individual proper motions could be averaged to determine the bulk motion of the cluster. Though cluster peculiar velocities are ~ 500 km s^{-1}(Planck Collaboration et al., 2018), the peculiar dipole would be lower in amplitude than the secular parallax for clusters at distances $\gtrsim 40$. After *Gaia*, astrometry from ngVLA or a future space based mission with lower per object uncertainties would improve the signal measured from more distant galaxies. Though an ngVLA quasar survey would miss many local galaxies observed by *Gaia*, the diminished peculiar dipole signal at the distances of relatively low redshift quasars may result in an improved constraint on the direction and amplitude of the secular parallax dipole.

Previous works have also made predictions of the secular parallax measurement with *Gaia*,

namely, Ding & Croft (2009) and Hall (2019). Contrary to our results, neither work predicts a significant detection of the secular parallax. The discrepancy with our results are most likely due to differences in the samples used for predictions. Both Ding & Croft (2009) and Hall (2019) assume larger samples of more distant objects, whereas we find that significant secular parallax detection with *Gaia* is contingent on galaxies closer than ~ 5 Mpc. Our simulations excluding galaxies closer than at least 20 Mpc are consistent with previous works.

Our analysis of the Cosmicflows peculiar velocities are largely consistent with the LSS predictions of Hall (2019) though our methods of simulating the peculiar velocities are independent. The noise-free, Cosmicflows-based peculiar proper motions show a dominant dipole for low distances bins and power generally shifting to higher ℓ modes with increasing distance. We find that the peculiar proper motion dipole may be significantly detected with *Gaia* if one first detects or assumes the secular parallax dipole from the CMB. However, the distance dependence of the peculiar proper motion power spectrum will not be detectable with *Gaia*.

We demonstrated that the peculiar velocities also produce low multipole correlated proper motions that are distance independent, and therefore may impact other cosmological proper motion measurements made with quasars for signals of ~ 0.3 μas yr^{-1}. This would be indistinguishable from $\sim 1\%$ anisotropic expansion and would dominate the E-mode fields caused by a gravitational wave background. However, the gravitational wave energy density could still be constrained by studying the corresponding B-modes.

Acknowledgments

We thank the anonymous referee for very helpful comments and corrections. The authors acknowledge support from the NSF Graduate Research Fellowship Program under grant DGE-1650115, the NSF grant AST-1411605, and the NASA grant 14-ATP14-0086. RG acknowledges support from the European Research Council (ERC) under the European Union's Horizon 2020 research and innovation programme (grant agreement no759194 - USNAC). This work has made use of data from the European Space Agency (ESA) mission *Gaia* (`https://www.cosmos.esa.`

int/gaia), processed by the *Gaia* Data Processing and Analysis Consortium (DPAC, https://www.cosmos.esa.int/web/gaia/dpac/consortium). Funding for the DPAC has been provided by national institutions, in particular the institutions participating in the *Gaia* Multilateral Agreement.

Software used in this research: Astropy (Astropy Collaboration et al., 2013, 2018, 2022), pyGaia, TOPCAT (Taylor, 2005).

Chapter 4

3D Kinematics of Stellar SiO Masers in the Galactic Center

Abstract

We present 3D velocity measurements and acceleration limits for stars within a few parsec of the Galactic Center (GC) black hole, Sgr A*, based on observations of 43 and 86 GHz circumstellar maser emission. Observations were taken with the Very Large Array (VLA) in 2013, 2014, and 2020 and with the Atacama Large Millimeter/submillimeter Array (ALMA) in 2015 and 2017. We detect 28 masers in total, of which four are new detections. Combining these data with extant maser astrometry, we calculate stellar proper motions and accelerations with uncertainties as low as ~ 10 μas yr^{-1} and 0.5 μas yr^{-2}, respectively, corresponding to approximately 0.5 km s^{-1} and 0.04 km s^{-1} yr^{-1} at a distance of 8 kpc. We measure radial velocities from maser spectra with ~ 0.5 km s^{-1} uncertainties, though the precision and accuracy of such measurements for deducing the underlying stellar velocities are limited by the complex spectral profiles of some masers. We therefore measure radial acceleration limits with typical uncertainties of ~ 0.1 km s^{-1} yr^{-1}. We analyze the resulting 3D velocities and accelerations with respect to expected motions resulting from models of the mass distribution in the GC.

This Chapter was published as Paine & Darling, 2022, ApJ, 927, 181, and is reproduced here.

4.1 Introduction

Observations of Galactic Center (GC) over the past several decades have identified stellar SiO masers within a few parsecs of the central galactic black hole Sgr A*. The SiO maser emission

originates in the extended envelopes of late type stars and provides high brightness temperature sources for astrometry and narrow spectral profiles for Doppler velocity tracking. Thus, stellar masers are useful as high spatial and spectral resolution tracers of 3D stellar kinematics in the GC.

Circumstellar SiO masers are associated with asymptotic giant branch (AGB) stars, which are late-type red giant stars (see Kemball 2007 for review). Several lines are observed at frequencies around 43 and 86 GHz, which are rotational transitions in predominantly excited vibrational states, though a smaller number in ground vibrational states have been observed. Stellar SiO masers have been resolved with Very Long Baseline Interferometry (VLBI) observations, showing that the maser emission originates from discrete regions typically within about a few AU around the star (e.g. Gonidakis et al. 2010). When the emission is not resolved, SiO masers can be treated as point sources which track the stellar position. The cumulative spectrum typically shows maser emission in a range around 10 km s^{-1} relative to the systemic stellar velocity and may have multiple distinct peaks.

Astrometry and velocity tracking of SiO masers in the GC has been ongoing for several decades (e.g. Menten et al. 1997; Reid et al. 2003, 2007; Li et al. 2010; Borkar et al. 2020). Several masers associated with infrared-bright stars have also been utilized to construct an astrometric reference frame to improve measurements of infrared (IR) stars on short-period orbits around Sgr A* (Yelda et al. 2010; Plewa et al. 2015; Boehle et al. 2016; Sakai et al. 2019). The orbits of these IR stars provided some of the first evidence for the existence of black holes and revealed the presence of a 4.15×10^6 $M_\odot$ mass black hole (Ghez et al., 2008; Genzel et al., 2010). The recent pericentre passage of the star S2 showed a detectable gravitational redshift (GRAVITY Collaboration et al., 2018) and Schwarzschild precession (GRAVITY Collaboration et al., 2020). Such precision measurements depend on improvements to the astrometric reference frame derived from SiO masers.

SiO maser stars may also directly probe Sgr A* and the surrounding environment. Stellar kinematics trace the underlying mass distribution, and therefore enable mapping of the total stellar and dark matter mass profiles at various radii in the GC. Additionally, if high velocity stellar masers

with short orbital periods are identified, masers may enable measurements of the metric around Sgr A*. The required accuracy assumed for most general relativistic spectroscopic tests of stars near the central black hole is 10 km s^{-1} (Angélil & Saha, 2011), but the spectral resolution for SiO masers is at least two orders of magnitude better, with statistical uncertainties $\sim$ 10 - 100 m s^{-1}. Accurately tracking the systemic stellar velocity using the maser spectra is often a challenge as we demonstrate in this work. However, if the systematics can be quantified, general relativistic tests may be possible with SiO maser orbit measurements, such as tests of the equivalence principle or "no hair" theorem.

We present new observations from the Karl G. Jansky Very Large Array [1] (VLA) and Atacama Large Millimeter/submillimeter Array (ALMA) of stellar SiO masers within $\sim$ 2 pc of Sgr A*. Observations of the 43 and 86 GHz masers and data reduction methods are detailed in Section 4.2. Results are presented in Section 4.3, including stellar proper motions, proper accelerations, radial velocities, and radial accelerations. Analysis of the 3D stellar kinematics is given in Section 4.4. Finally, we discuss the implications of the stellar motions in Section 4.5 and give conclusions in Section 4.6.

4.2 Observations and Data Reduction

Observations of the inner few parsec of the GC around Sgr A* were carried out over the course of seven years with VLA and ALMA. Three VLA sessions were used to observe the $v = 1$ and $v = 2$, $J = 1 - 0$ lines at 43.12203 and 42.82048 GHz, and two ALMA sessions were used to observe the $v = 1$, $J = 2 - 1$ line at 86.24337 GHz. The ground state transitions $v = 0$, $J = 1 - 0$ and $v = 0$, $J = 2 - 1$ were also covered in our observations, but no ground state masers were observed in any VLA or ALMA sessions. Initial observations with both VLA and ALMA were intended for high velocity maser searches and therefore have lower angular and spectral resolution than followup observations. We detail the observations, calibration, and data reduction in the

[1] The National Radio Astronomy Observatory is a facility of the National Science Foundation operated under cooperative agreement by Associated Universities, Inc.

Table 4.1: VLA and ALMA observations

Telescope	Date	MJD	Lines observed	Beam (" × ")	Channel width (km s^{-1})
VLA	2013 Feb 14	2013.13	$J = 1 - 0$, $v = 1$ and $v = 2$	3.398×1.444	1.0
VLA	2014 Mar 7	2014.18	$J = 1 - 0$, $v = 1$ and $v = 2$	0.1894×0.1032	1.0
ALMA	2015 Apr 10	2015.27	$J = 2 - 1$, $v = 1$	4.112×2.512	1.75
ALMA	2017 Sep 19	2017.72	$J = 2 - 1$, $v = 1$	0.625×0.3125	0.25
VLA	2020 Dec 27	2020.99	$J = 1 - 0$, $v = 1$ and $v = 2$	0.1230×0.0483	0.5

following subsections. A summary of the observing sessions is given in Table 4.1.

4.2.1 VLA Observations

We observed the GC with the VLA in the D configuration on 2013 February 14 (13A-071), and in the A configuration on 2014 March 7 (14A-440) and 2020 December 27 (19A-310). The phase center for all observations was Sgr A*. During the 2013 observation, the VLA had 26 antennas in operation with baselines ranging from ∼40 to 1486 m, resulting in a 3.398" × 1.444" synthesized beam. The spectral setup consisted of 32 contiguous spectral windows, each with 1024 channels with 125 kHz channel width in dual polarization. The spectral windows covered frequencies from 42.1121 to 44.1276 GHz. During calibration, channels between frequencies 43.1171 and 43.1235 GHz had to be discarded due to bandpass edge roll-off, which corresponds to velocities of about -13 - $+34$ km s^{-1} for $v = 1$, $J = 1 - 0$ (43.12203 GHz) masers.

The 2014 observation was conducted with 27 antennas in operation and baselines ranging from 793 to 36623 m. The synthesized beam was 0.1894" × 0.1032". The spectral setup was similar to that of 2013, but covered a smaller range of frequencies. The observation had 16 contiguous spectral windows in dual polarization mode, each with 1024 channels with 125 kHz channel width, and covered frequencies from 42.6307 to 43.685 GHz.

The 2020 observation was conducted with 26 antennas in operation and baselines ranging from 793 to 36623 m. The synthesized beam was 0.1230" × 0.0483". The spectral configuration

included four spectral windows, each with 62.5 kHz wide channels in dual polarization mode. Three spectral windows contained 2048 channels and were centered on 42.612, 43.124, and 43.380 GHz with 128 MHz bandwidth each. A fourth smaller spectral window contained 1024 channels and was centered on 42.836 GHz with 64 MHz bandwidth.

We performed standard calibration using the Common Astronomy Software Application (CASA; McMullin et al. 2007). For all observations, 1733-1304 was used for bandpass and initial phase calibration and 1331+305 (3C286) for the flux density scale. Phases and amplitudes were self-calibrated with the Sgr A* continuum emission. The continuum emission was then subtracted in the *uv*-plane by fitting to the line-free channels. Initial spectral maps were made using the CLEAN algorithm, and these images were used to identify masers by eye. The measurement sets were regridded to the LSRK frame and channel widths of 1.0 km s^{-1} for the 2013 and 2014 data, and 0.5 km s^{-1} for the 2020 data. We then fit maser positions and spectra to the calibrated, continuum subtracted visibility data directly using the package *uvmultifit* (Martí-Vidal et al., 2014). Positions are measured as offsets from the phase center, which is the Sgr A* continuum. Visibility fitting, rather than image fitting, was done in order to mitigate any systematics introduced between different telescopes, frequencies, and epochs.

4.2.2 ALMA Observations

We observed the 86 GHz masers in the GC with ALMA on 2015 April 10 (2013.1.00834) and 2017 September 19 (2016.1.00940). The 2015 observation was conducted in the C34-1/(2) configuration, with 35 antennas in operation and baselines ranging from 15 to 348 m. The resulting synthesized beam was 4.112" × 2.512". The spectral configuration consisted of four contiguous spectral windows in dual linear polarization, each with 1920 channels with 488.281 kHz channel width. The spectral windows covered frequencies from 84.842 to 88.5688 GHz.

The 2017 observation was conducted in the more extended C40-8/9 configuration, with 44 antennas in operation and baselines ranging from 41 to 12145 m. The resulting synthesized beam was 0.625"×0.3125". The spectral setup contained four spectral windows in dual linear polarization

which were intended for higher spectral resolution than the previous ALMA setup. One window contained 3840 channels with 61.035 kHz width and was centered on 86.355026 GHz. The other three windows each contained 1920 channels with 122.07 kHz width and were centered on 85.752122, 86.958551, and 85.980837 GHz.

Calibrations for both observations were performed initially using the standard ALMA pipeline in CASA. Further self-calibration was done using the Sgr A* continuum emission. The remaining data reduction followed in a similar manner to that described above for the VLA observations. The Sgr A* continuum emission was subtracted from the visibility data by fitting to the line-free channels. Masers were initially identified by eye from spectral line maps created using the CLEAN algorithm to determine initial positions for visibility fitting. The measurement sets were regridded to the LSRK frame and channel widths of 1.75 km s^{-1} for the 2015 data and 0.25 km s^{-1} for the 2017 data. We then fit maser offset positions and spectra to the visibility data using the *uvmultifit* package.

4.3 Results

We required a 5σ significance flux measurement reported by *uvmultifit* in at least one channel for detection. A subset of the masers within 1 pc projected distance from Sgr A* detected by ALMA in 2017 are shown in Figure 4.1. Maser positions where then determined by finding the error-weighted mean position for all channels with $> 3\sigma$ measurements. The maser spectra, which are shown in Appendix C, were used to determine radial velocities by calculating the centroid of the $> 3\sigma$ channels. Offset positions referenced to the Sgr A* continuum centroid and radial velocities of each maser are given in Table 4.2.

Two new masers were detected in the VLA data: we name these SiO-28 and SiO-31. Three new masers were detected in the ALMA data: SiO-28, SiO-29, and SiO-30. New masers were named using the convention of Reid et al. (2007), Li et al. (2010), and Borkar et al. (2020). All new sources were detected in at least two epochs, except for SiO-31 which was only detected at 5σ-significance in two channels in the 2020 VLA data (see Figure C.1). Further observations will

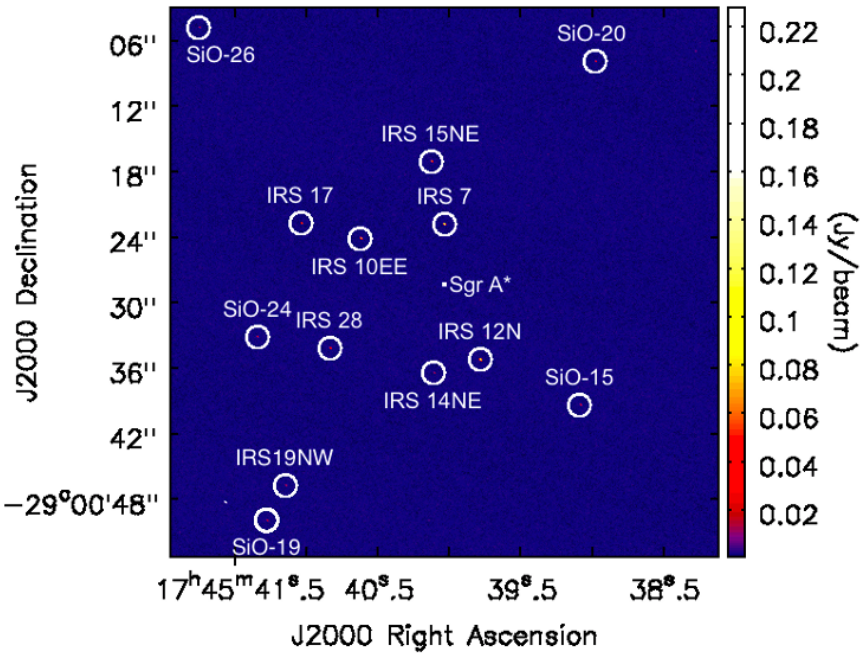

Figure 4.1: A subset of the 86 GHz SiO masers near Sgr A* detected by ALMA in 2017. The field of view spans ±1 pc. The beam is 0.1617×0.1176 arcsec ($\sim 6.4 \times 4.7$ mpc) and is shown in the lower left.

Table 4.2: Maser positions and velocities

Star	Epoch (year)	Line	R.A. offset (arcsec)	Dec. offset (arcsec)	Radial velocity (km s^{-1})
IRS9	2013.13	$J = 1 - 0$, $v = 1$	5.69 ± 0.04	-6.2 ± 0.1	-342.7 ± 0.2
	2014.18	$J = 1 - 0$, $v = 1$	5.6986 ± 0.0002	-6.3157 ± 0.0006	-339.26 ± 0.07
	2014.18	$J = 1 - 0$, $v = 2$	5.6983 ± 0.0003	-6.3155 ± 0.0006	-337.82 ± 0.07
	2015.27	$J = 2 - 1$, $v = 1$	5.98 ± 0.05	-6.30 ± 0.03	-342.0 ± 0.1
	2017.72	$J = 2 - 1$, $v = 1$	5.7111 ± 0.0002	-6.3056 ± 0.0002	-341.36 ± 0.01
	2020.99	$J = 1 - 0$, $v = 1$	5.7188 ± 0.0003	-6.3009 ± 0.0006	-341.57 ± 0.04
IRS7	2014.18	$J = 1 - 0$, $v = 1$	0.0323 ± 0.0007	5.487 ± 0.002	-106.8 ± 0.2
	2014.18	$J = 1 - 0$, $v = 2$	0.0334 ± 0.0007	5.487 ± 0.002	-104.96 ± 0.08
	2015.27	$J = 2 - 1$, $v = 1$	0.034 ± 0.003	5.526 ± 0.002	-119.50 ± 0.03
	2017.72	$J = 2 - 1$, $v = 1$	0.03304 ± 0.00009	5.47053 ± 0.00009	-120.28 ± 0.03

Continuation of Table 4.2

Star	Epoch (year)	Line	R.A. offset (arcsec)	Dec. offset (arcsec)	Radial velocity (km s^{-1})
	2020.99	$J = 1 - 0$, $v = 1$	0.038 ± 0.001	5.459 ± 0.003	-108.4 ± 0.1
SiO-14	2013.13	$J = 1 - 0$, $v = 1$	-7.57 ± 0.04	-28.2 ± 0.1	-112.2 ± 0.2
	2013.13	$J = 1 - 0$, $v = 2$	-7.56 ± 0.03	-28.39 ± 0.08	-109.5 ± 0.2
	2014.18	$J = 1 - 0$, $v = 2$	-7.6321 ± 0.0004	-28.4614 ± 0.0008	-112.42 ± 0.07
	2014.18	$J = 1 - 0$, $v = 1$	-7.6312 ± 0.0003	-28.4612 ± 0.0008	-111.96 ± 0.06
	2015.27	$J = 2 - 1$, $v = 1$	-7.552 ± 0.007	-28.413 ± 0.004	-112.76 ± 0.02
	2017.72	$J = 2 - 1$, $v = 1$	-7.6247 ± 0.0002	-28.4698 ± 0.0002	-113.06 ± 0.02
	2020.99	$J = 1 - 0$, $v = 2$	-7.6185 ± 0.0005	-28.467 ± 0.001	-115.92 ± 0.08
	2020.99	$J = 1 - 0$, $v = 1$	-7.6185 ± 0.0005	-28.468 ± 0.001	-115.55 ± 0.07
SiO-28[a]	2014.18	$J = 1 - 0$, $v = 2$	-1.113 ± 0.002	-42.555 ± 0.005	-103.8 ± 0.2
	2014.18	$J = 1 - 0$, $v = 1$	-1.112 ± 0.002	-42.559 ± 0.004	-103.11 ± 0.08
	2015.27	$J = 2 - 1$, $v = 1$	-0.98 ± 0.08	-42.54 ± 0.05	-104.5 ± 0.1
	2017.72	$J = 2 - 1$, $v = 1$	-1.114 ± 0.002	-42.568 ± 0.002	-105.48 ± 0.03
	2020.99	$J = 1 - 0$, $v = 2$	-1.117 ± 0.002	-42.544 ± 0.005	-103.67 ± 0.06
	2020.99	$J = 1 - 0$, $v = 1$	-1.117 ± 0.002	-42.545 ± 0.004	-102.83 ± 0.06
SiO-29[a]	2015.27	$J = 2 - 1$, $v = 1$	-26.7 ± 0.1	23.57 ± 0.07	-93.0 ± 0.2
	2017.72	$J = 2 - 1$, $v = 1$	-26.836 ± 0.002	23.604 ± 0.002	-90.20 ± 0.07
SiO-31[a]	2020.99	$J = 1 - 0$, $v = 1$	9.359 ± 0.002	-18.338 ± 0.004	-81.1 ± 0.1
SiO-18	2014.18	$J = 1 - 0$, $v = 1$	-18.684 ± 0.001	-26.095 ± 0.003	-78.5 ± 0.1
	2015.27	$J = 2 - 1$, $v = 1$	-18.48 ± 0.03	-25.98 ± 0.02	-79.02 ± 0.08
	2017.72	$J = 2 - 1$, $v = 1$	-18.625 ± 0.002	-26.077 ± 0.002	-74.57 ± 0.07
	2020.99	$J = 1 - 0$, $v = 1$	-18.715 ± 0.003	-26.094 ± 0.007	-76.9 ± 0.2
	2020.99	$J = 1 - 0$, $v = 2$	-18.710 ± 0.002	-26.096 ± 0.004	-76.49 ± 0.07
SiO-26	2015.27	$J = 2 - 1$, $v = 1$	22.31 ± 0.05	23.49 ± 0.03	-72.5 ± 0.1
	2017.72	$J = 2 - 1$, $v = 1$	22.499 ± 0.001	23.477 ± 0.001	-72.23 ± 0.05
IRS12N	2013.13	$J = 1 - 0$, $v = 2$	-3.23 ± 0.03	-6.86 ± 0.07	-64.6 ± 0.1

Continuation of Table 4.2

Star	Epoch (year)	Line	R.A. offset (arcsec)	Dec. offset (arcsec)	Radial velocity (km s^{-1})
	2013.13	$J = 1 - 0$, $v = 1$	-3.27 ± 0.03	-6.91 ± 0.09	-64.6 ± 0.1
	2014.18	$J = 1 - 0$, $v = 2$	-3.2714 ± 0.0004	-6.931 ± 0.001	-66.02 ± 0.08
	2014.18	$J = 1 - 0$, $v = 1$	-3.2702 ± 0.0004	-6.9318 ± 0.0008	-65.41 ± 0.07
	2015.27	$J = 2 - 1$, $v = 1$	-3.254 ± 0.007	-6.898 ± 0.005	-64.78 ± 0.03
	2017.72	$J = 2 - 1$, $v = 1$	-3.2755 ± 0.0001	-6.9412 ± 0.0001	-62.64 ± 0.01
	2020.99	$J = 1 - 0$, $v = 1$	-3.2796 ± 0.0002	-6.9494 ± 0.0005	-63.87 ± 0.04
	2020.99	$J = 1 - 0$, $v = 2$	-3.2793 ± 0.0002	-6.9491 ± 0.0004	-63.86 ± 0.04
IRS28	2013.13	$J = 1 - 0$, $v = 2$	10.50 ± 0.05	-5.9 ± 0.1	-53.8 ± 0.1
	2014.18	$J = 1 - 0$, $v = 2$	10.4919 ± 0.0002	-5.8675 ± 0.0004	-53.84 ± 0.03
	2014.18	$J = 1 - 0$, $v = 1$	10.4916 ± 0.0002	-5.8673 ± 0.0004	-53.41 ± 0.03
	2015.27	$J = 2 - 1$, $v = 1$	10.48 ± 0.01	-5.829 ± 0.008	-53.89 ± 0.04
	2017.72	$J = 2 - 1$, $v = 1$	10.4965 ± 0.0003	-5.8875 ± 0.0003	-52.53 ± 0.02
	2020.99	$J = 1 - 0$, $v = 2$	10.502 ± 0.002	-5.911 ± 0.004	-55.37 ± 0.08
	2020.99	$J = 1 - 0$, $v = 1$	10.5029 ± 0.0009	-5.914 ± 0.002	-52.91 ± 0.08
SiO-27	2014.18	$J = 1 - 0$, $v = 1$	-19.930 ± 0.002	33.672 ± 0.005	-44.0 ± 0.2
	2015.27	$J = 2 - 1$, $v = 1$	-19.82 ± 0.04	33.68 ± 0.03	-43.67 ± 0.07
	2017.72	$J = 2 - 1$, $v = 1$	-19.9361 ± 0.0005	33.6805 ± 0.0005	-43.50 ± 0.03
	2020.99	$J = 1 - 0$, $v = 2$	-19.940 ± 0.002	33.697 ± 0.005	-44.3 ± 0.4
	2020.99	$J = 1 - 0$, $v = 1$	-19.940 ± 0.002	33.695 ± 0.004	-42.9 ± 0.2
SiO-30[a]	2015.27	$J = 2 - 1$, $v = 1$	-23.13 ± 0.08	21.38 ± 0.05	-38.6 ± 0.1
	2017.72	$J = 2 - 1$, $v = 1$	-23.024 ± 0.002	21.314 ± 0.002	-37.34 ± 0.04
SiO-15	2014.18	$J = 1 - 0$, $v = 2$	-12.4597 ± 0.0003	-11.0673 ± 0.0008	-35.35 ± 0.05
	2014.18	$J = 1 - 0$, $v = 1$	-12.4593 ± 0.0007	-11.067 ± 0.002	-35.2 ± 0.1
	2015.27	$J = 2 - 1$, $v = 1$	-12.42 ± 0.03	-11.01 ± 0.02	-36.45 ± 0.06
	2017.72	$J = 2 - 1$, $v = 1$	-12.4667 ± 0.0008	-11.0682 ± 0.0008	-33.91 ± 0.04
	2020.99	$J = 1 - 0$, $v = 2$	-12.474 ± 0.001	-11.070 ± 0.002	-36.1 ± 0.1

Continuation of Table 4.2

Star	Epoch (year)	Line	R.A. offset (arcsec)	Dec. offset (arcsec)	Radial velocity (km s^{-1})
	2020.99	$J = 1 - 0$, $v = 1$	-12.475 ± 0.001	-11.070 ± 0.003	-35.8 ± 0.2
SiO-19	2013.13	$J = 1 - 0$, $v = 2$	16.22 ± 0.06	-21.6 ± 0.2	-28.8 ± 0.1
	2014.18	$J = 1 - 0$, $v = 2$	16.2447 ± 0.0003	-21.6647 ± 0.0007	-28.71 ± 0.07
	2014.18	$J = 1 - 0$, $v = 1$	16.2442 ± 0.0004	-21.664 ± 0.001	-27.80 ± 0.08
	2015.27	$J = 2 - 1$, $v = 1$	16.25 ± 0.01	-21.605 ± 0.009	-28.58 ± 0.04
	2017.72	$J = 2 - 1$, $v = 1$	16.2549 ± 0.0008	-21.6745 ± 0.0008	-31.29 ± 0.04
	2020.99	$J = 1 - 0$, $v = 1$	16.2626 ± 0.0008	-21.659 ± 0.002	-26.18 ± 0.08
	2020.99	$J = 1 - 0$, $v = 2$	16.261 ± 0.001	-21.651 ± 0.003	-25.80 ± 0.07
IRS10EE	2013.13	$J = 1 - 0$, $v = 2$	7.68 ± 0.01	4.19 ± 0.04	-27.26 ± 0.07
	2014.18	$J = 1 - 0$, $v = 2$	7.6838 ± 0.0002	4.1846 ± 0.0004	-27.48 ± 0.02
	2014.18	$J = 1 - 0$, $v = 1$	7.6839 ± 0.0003	4.1843 ± 0.0006	-26.98 ± 0.03
	2015.27	$J = 2 - 1$, $v = 1$	7.68 ± 0.02	4.22 ± 0.01	-28.00 ± 0.05
	2017.72	$J = 2 - 1$, $v = 1$	7.6844 ± 0.0002	4.1767 ± 0.0002	-28.56 ± 0.01
	2020.99	$J = 1 - 0$, $v = 1$	7.68504 ± 0.00009	4.1701 ± 0.0002	-27.68 ± 0.02
	2020.99	$J = 1 - 0$, $v = 2$	7.68490 ± 0.00008	4.1702 ± 0.0002	-27.59 ± 0.01
SiO-20	2014.18	$J = 1 - 0$, $v = 1$	-13.8629 ± 0.0004	20.3643 ± 0.0009	-17.11 ± 0.07
	2014.18	$J = 1 - 0$, $v = 2$	-13.8625 ± 0.0006	20.362 ± 0.001	-16.9 ± 0.1
	2015.27	$J = 2 - 1$, $v = 1$	-13.84 ± 0.03	20.41 ± 0.02	-17.13 ± 0.08
	2017.72	$J = 2 - 1$, $v = 1$	-13.8604 ± 0.0006	20.3502 ± 0.0006	-16.87 ± 0.02
	2020.99	$J = 1 - 0$, $v = 1$	-13.858 ± 0.002	20.343 ± 0.005	-20.8 ± 0.1
	2020.99	$J = 1 - 0$, $v = 2$	-13.857 ± 0.003	20.344 ± 0.006	-19.55 ± 0.05
IRS15NE	2014.18	$J = 1 - 0$, $v = 2$	1.1968 ± 0.0003	11.2295 ± 0.0007	-11.81 ± 0.05
	2014.18	$J = 1 - 0$, $v = 1$	1.1970 ± 0.0003	11.2293 ± 0.0006	-11.04 ± 0.07
	2015.27	$J = 2 - 1$, $v = 1$	1.24 ± 0.03	11.25 ± 0.02	-11.02 ± 0.05
	2017.72	$J = 2 - 1$, $v = 1$	1.1903 ± 0.0004	11.2097 ± 0.0004	-11.78 ± 0.03
	2020.99	$J = 1 - 0$, $v = 2$	1.1847 ± 0.0005	11.193 ± 0.001	-14.56 ± 0.09

Continuation of Table 4.2

Star	Epoch (year)	Line	R.A. offset (arcsec)	Dec. offset (arcsec)	Radial velocity (km s^{-1})
	2020.99	$J = 1 - 0$, $v = 1$	1.1855 ± 0.0008	11.196 ± 0.002	-12.4 ± 0.1
IRS14NE	2014.18	$J = 1 - 0$, $v = 1$	0.935 ± 0.002	-8.159 ± 0.004	-9.4 ± 0.1
	2015.27	$J = 2 - 1$, $v = 1$	0.91 ± 0.05	-8.31 ± 0.03	-12.2 ± 0.1
	2017.72	$J = 2 - 1$, $v = 1$	0.9468 ± 0.0009	-8.1701 ± 0.0009	-11.63 ± 0.05
	2020.99	$J = 1 - 0$, $v = 2$	0.965 ± 0.002	-8.182 ± 0.005	-12.4 ± 0.2
SiO-16	2015.27	$J = 2 - 1$, $v = 1$	-26.33 ± 0.03	-34.39 ± 0.02	7.90 ± 0.08
	2017.72	$J = 2 - 1$, $v = 1$	-26.4178 ± 0.0009	-34.4788 ± 0.0009	6.36 ± 0.03
SiO-21	2015.27	$J = 2 - 1$, $v = 1$	40.88 ± 0.03	-21.98 ± 0.02	13.46 ± 0.06
	2017.72	$J = 2 - 1$, $v = 1$	40.911 ± 0.001	-22.043 ± 0.001	13.44 ± 0.03
SiO-24	2015.27	$J = 2 - 1$, $v = 1$	17.16 ± 0.04	-4.71 ± 0.03	18.10 ± 0.08
	2017.72	$J = 2 - 1$, $v = 1$	17.1976 ± 0.0008	-4.8225 ± 0.0008	17.95 ± 0.03
	2020.99	$J = 1 - 0$, $v = 1$	17.214 ± 0.001	-4.831 ± 0.003	19.0 ± 0.1
	2020.99	$J = 1 - 0$, $v = 2$	17.213 ± 0.001	-4.828 ± 0.003	19.5 ± 0.1
SiO-22	2015.27	$J = 2 - 1$, $v = 1$	41.44 ± 0.03	15.21 ± 0.02	32.79 ± 0.06
	2017.72	$J = 2 - 1$, $v = 1$	41.4088 ± 0.0007	15.1811 ± 0.0007	35.41 ± 0.03
SiO-6	2015.27	$J = 2 - 1$, $v = 1$	35.15 ± 0.02	30.72 ± 0.01	51.58 ± 0.09
	2017.72	$J = 2 - 1$, $v = 1$	35.2719 ± 0.0005	30.7032 ± 0.0005	52.17 ± 0.05
SiO-17	2013.13	$J = 1 - 0$, $v = 2$	8.111 ± 0.009	-27.47 ± 0.02	53.17 ± 0.03
	2013.13	$J = 1 - 0$, $v = 1$	8.10 ± 0.02	-27.51 ± 0.04	53.59 ± 0.05
	2014.18	$J = 1 - 0$, $v = 2$	8.0811 ± 0.0001	-27.6578 ± 0.0002	53.37 ± 0.02
	2014.18	$J = 1 - 0$, $v = 1$	8.0811 ± 0.0001	-27.6585 ± 0.0003	53.73 ± 0.02
	2015.27	$J = 2 - 1$, $v = 1$	8.07 ± 0.02	-27.64 ± 0.02	53.45 ± 0.03
	2017.72	$J = 2 - 1$, $v = 1$	8.0900 ± 0.0005	-27.6538 ± 0.0004	53.40 ± 0.02
	2020.99	$J = 1 - 0$, $v = 2$	8.0978 ± 0.0005	-27.641 ± 0.001	54.20 ± 0.04
	2020.99	$J = 1 - 0$, $v = 1$	8.0991 ± 0.0007	-27.641 ± 0.002	54.48 ± 0.06
SiO-11	2015.27	$J = 2 - 1$, $v = 1$	1.87 ± 0.08	40.36 ± 0.05	70.5 ± 0.1

Continuation of Table 4.2

Star	Epoch (year)	Line	R.A. offset (arcsec)	Dec. offset (arcsec)	Radial velocity (km s^{-1})
	2017.72	$J = 2 - 1$, $v = 1$	1.764 ± 0.001	40.316 ± 0.001	70.94 ± 0.05
	2020.99	$J = 1 - 0$, $v = 2$	1.7714 ± 0.0001	40.3245 ± 0.0003	70.84 ± 0.02
	2020.99	$J = 1 - 0$, $v = 1$	1.7717 ± 0.0002	40.3241 ± 0.0004	71.85 ± 0.02
IRS17	2014.18	$J = 1 - 0$, $v = 2$	13.133 ± 0.001	5.550 ± 0.002	74.5 ± 0.2
	2014.18	$J = 1 - 0$, $v = 1$	13.132 ± 0.002	5.546 ± 0.004	75.6 ± 0.3
	2015.27	$J = 2 - 1$, $v = 1$	13.13 ± 0.02	5.61 ± 0.01	74.13 ± 0.05
	2017.72	$J = 2 - 1$, $v = 1$	13.1310 ± 0.0003	5.5480 ± 0.0003	71.81 ± 0.02
	2020.99	$J = 1 - 0$, $v = 2$	13.126 ± 0.001	5.543 ± 0.003	72.31 ± 0.06
	2020.99	$J = 1 - 0$, $v = 1$	13.126 ± 0.001	5.543 ± 0.003	72.90 ± 0.08
IRS19NW	2013.13	$J = 1 - 0$, $v = 1$	14.57 ± 0.05	-18.3 ± 0.1	84.4 ± 0.1
	2013.13	$J = 1 - 0$, $v = 2$	14.46 ± 0.05	-18.4 ± 0.1	84.4 ± 0.1
	2014.18	$J = 1 - 0$, $v = 2$	14.5695 ± 0.0003	-18.4681 ± 0.0007	84.06 ± 0.05
	2014.18	$J = 1 - 0$, $v = 1$	14.5694 ± 0.0003	-18.4683 ± 0.0006	84.23 ± 0.05
	2015.27	$J = 2 - 1$, $v = 1$	14.53 ± 0.02	-18.44 ± 0.01	84.08 ± 0.05
	2017.72	$J = 2 - 1$, $v = 1$	14.5735 ± 0.0008	-18.4727 ± 0.0008	82.85 ± 0.04
	2020.99	$J = 1 - 0$, $v = 2$	14.5772 ± 0.0002	-18.4724 ± 0.0005	82.60 ± 0.02
	2020.99	$J = 1 - 0$, $v = 1$	14.5774 ± 0.0003	-18.4728 ± 0.0006	83.68 ± 0.04
SiO-25	2013.13	$J = 1 - 0$, $v = 2$	-33.07 ± 0.03	-17.81 ± 0.08	118.19 ± 0.07
	2013.13	$J = 1 - 0$, $v = 1$	-33.05 ± 0.03	-17.71 ± 0.08	118.80 ± 0.05
	2014.18	$J = 1 - 0$, $v = 2$	-33.056 ± 0.002	-17.716 ± 0.005	117.60 ± 0.06
	2014.18	$J = 1 - 0$, $v = 1$	-33.061 ± 0.002	-17.728 ± 0.005	118.62 ± 0.06
	2015.27	$J = 2 - 1$, $v = 1$	-32.96 ± 0.02	-17.88 ± 0.02	118.01 ± 0.06
	2017.72	$J = 2 - 1$, $v = 1$	-33.105 ± 0.002	-17.917 ± 0.002	117.63 ± 0.03

[a] New detection

be required to confirm if SiO-31 is a genuine SiO maser source.

Maser positions are measured with typical uncertainties < 1 mas for the higher resolution epochs (2014.18, 2017.72, and 2020.99) and around 10 mas for the lower resolution epochs (2013.13 and 2015.27). These offset uncertainties are dominated by the maser position fit since the position of Sgr A* is well-measured in all epochs. Extended continuum emission from the GC mini-spiral was detected in both of the lower resolution epochs which was resolved out in the higher resolution data. We note that this emission may impact the resulting astrometry, but these epochs do not strongly affect the proper motion fits described in the next section since the statistical uncertainties of the offset positions are relatively large.

The majority of our spectra show variability in time and between different lines (see Appendix C). The most notable example is IRS 7, where the peak of maser emission from the 43 and 87 GHz spectra are significantly offset by more than 10 km s^{-1}, with strong SiO maser emission spread over ~ 30 km s^{-1} in the 87 GHz spectra. Since the VLA and ALMA spectra appear to be self-consistent over time, the variability of the IRS 7 spectra seems to be due to differences in the excitation conditions between the 43 and 87 GHz masers. Generally, however, SiO maser flux is known to be variable on timescales of ~ 1 year or longer following the underlying stellar pulsations (e.g. Pardo et al. 2004). Since the time interval between VLA and ALMA observations is > 1 year, it is unclear if the smaller differences between 43 and 86 GHz spectra seen in the other stars in the sample are due to time-dependent variability in the star or differences in the excitation conditions. We also note that the peak and centroid velocities of the $J = 1 - 0$, $v = 1$ and $v - 2$ spectra among stars with simultaneous detections of both lines often disagree, and we address this further in Section 4.3.3.

The spectral variability of IRS 7 also indicates that its astrometry may not be as accurate as that of other stars in the sample. As noted by Reid et al. (2003), the broad velocity range of the SiO emissions suggests that IRS 7 has a large maser shell that may span 10 mas. The maser position therefore may not match the stellar position to better than $\sim$5 mas. However, we report only the statistical uncertainties on the maser positions in Table 4.2.

4.3.1 Proper motions and proper accelerations

We combined our five epochs with extant maser astrometry of Reid et al. (2007) and Li et al. (2010) to calculate stellar proper motions and accelerations. For the majority of masers, we included only our three higher resolution epochs (VLA 2014, ALMA 2017, and VLA 2020) and the Reid et al. (2007) astrometry to perform fits. However, for masers fewer than three high resolution epochs to fit, we also included our lower resolution data (VLA 2013 and ALMA 2015) and the Li et al. (2010) astrometry. Li et al. (2010) include observations of the 86 GHz masers from the Australia Telescope Compact Array (ATCA), which has lower resolution than VLA or ALMA astrometry and often showed large offsets from the trends in the masers' positions. 17 masers were fit with only the high resolution data, 7 masers included the lower resolution data, and 4 masers did not have enough epochs of observations for a fit.

All maser positions, including those from literature, are referenced to the in-beam Sgr A* continuum position. The resulting proper motions are therefore referenced to Sgr A* and should be independent of systematic differences in absolute astrometry between epochs. We first find proper motions by fitting a straight line to the maser positions over time, following the equation

$$\Delta x = \Delta x_0 + \mu_x \left(t - t_0\right), \tag{4.1}$$

where x denotes either the R.A. or Dec. coordinate directions, α and δ, respectively. Δx is the offset position from Sgr A*, μ_x is the proper motion, and Δx_0 and t_0 are the first position measurement and date used in the fit, which varies per maser depending on the earliest detection.

Proper accelerations were then measured by fitting the residuals of the proper motion fit, following the equation

$$r_{\Delta x} = r_{\Delta x_0} + \frac{1}{2} a_x \left(t - t_0\right)^2, \tag{4.2}$$

where $r_{\Delta x}$ and $r_{\Delta x_0}$ are the residuals of the offset positions and initial positions, and a_x is the proper acceleration. We measure proper motions and accelerations for 24 masers with at least three epochs of observations. Figures showing the proper motion fits are given in Appendix D and the results are given in Table 4.3. We do not significantly measure proper accelerations for any

star in our sample using the residual fitting method. As shown in Table 4.3, all measurements are consistent with zero transverse acceleration in each coordinate and in magnitude. We also checked for acceleration by simultaneously fitting proper motion and acceleration to the position time series for masers with at least four epochs, however the results gave unrealistically large accelerations for some masers given their projected distance from Sgr A*.

4.3.2 Transverse velocities and accelerations

We converted the proper motions and proper accelerations to velocities and accelerations using an assumed distance of 8 kpc since the precise distances of the stars in our sample are not known. More precise stellar distances may be constrained with future measurements if 3D acceleration is measured, and therefore the distance from the star to Sgr A* can be calculated. The resulting velocities and accelerations are listed in Table 4.4.

4.3.3 Doppler velocities and accelerations

As described previously, we find radial velocities by calculating the centroid of each maser spectrum. However, very long baseline interferometry (VLBI) observations of stellar SiO masers shows that the maser emission is distributed in patches around the star and the velocity inferred from the cumulative spectrum may not match the true stellar velocity (e.g. Gonidakis et al. 2010). As can be seen in the spectra shown in Appendix C, many of the masers in our sample have complicated spectral profiles and the inferred velocities can differ between two line profiles taken during the same observation. We therefore estimated an additional systematic uncertainty on the stellar velocities. First, in cases where two lines were detected in a single epoch, we calculated the weighted mean of the two independent velocity measurements so we have one velocity per epoch. We then performed a linear fit to the velocities, and calculated a systematic uncertainty from standard deviation of the residuals of the linear fit. The systematic was added in quadrature to the statistical uncertainties.

Radial accelerations were calculated by fitting a slope to the velocity measurements for stars

Table 4.3: Offsets, proper motions and proper accelerations of stellar masers

Star	t_0 (year)	$\Delta\alpha_0$ (arcsec)	μ_α (mas yr^{-1})	a_α (mas yr^{-2})	$\Delta\delta_0$ (arcsec)	μ_δ (mas yr^{-1})	a_δ (mas yr^{-2})
IRS9	1998.39	5.65051 ± 0.00064	3.057 ± 0.042	-0.0003 ± 0.0036	-6.3517 ± 0.0011	2.303 ± 0.068	-0.0001 ± 0.0057
IRS7	1995.49	0.0344 ± 0.0050 [a]	-0.04 ± 0.11	0.0037 ± 0.0076	5.5659 ± 0.0050 [a]	-4.25 ± 0.15	-0.002 ± 0.011
SiO-14	1998.41	-7.66448 ± 0.00034	2.054 ± 0.021	-0.0007 ± 0.0017	-28.4517 ± 0.0020	-0.75 ± 0.12	-0.000 ± 0.010
SiO-28	2014.18	-1.11207 ± 0.00037	-0.712 ± 0.080	-0.006 ± 0.023	-42.5651 ± 0.0087	1.8 ± 2.0	0.31 ± 0.54
SiO-29	...	...	...	...	...	...	...
SiO-31	...	...	...	...	...	...	...
SiO-18	2014.18	-18.670 ± 0.031	-2.9 ± 7.4	-0.7 ± 2.1	-26.088 ± 0.010	1.0 ± 2.7	-0.43 ± 0.77
SiO-26	...	...	...	...	...	...	...
IRS12N	1996.41	-3.25154 ± 0.00038	-1.120 ± 0.023	-0.0007 ± 0.0018	-6.88149 ± 0.00039	-2.778 ± 0.023	0.0004 ± 0.0018
IRS28	1998.41	10.4674 ± 0.0010	1.541 ± 0.063	-0.0005 ± 0.0050	-5.7813 ± 0.0029	-5.54 ± 0.18	-0.007 ± 0.014
SiO-27	2014.18	-19.93043 ± 0.00061	-1.52 ± 0.13	0.015 ± 0.031	33.6670 ± 0.0028	3.94 ± 0.70	0.08 ± 0.15
SiO-30	...	...	...	...	...	...	...
SiO-15	2000.85	-12.42632 ± 0.00099	-2.426 ± 0.065	0.0026 ± 0.0053	-11.0754 ± 0.0031	0.45 ± 0.21	-0.009 ± 0.017
SiO-19	2014.18	16.24461 ± 0.00047	2.63 ± 0.12	-0.011 ± 0.035	-21.6666 ± 0.0045	0.2 ± 1.4	0.22 ± 0.42
IRS10EE	1995.49	7.68371 ± 0.00024	0.036 ± 0.014	0.0003 ± 0.0010	4.22082 ± 0.00044	-1.979 ± 0.026	-0.0001 ± 0.0019
SiO-20	2014.18	-13.86276 ± 0.00018	0.717 ± 0.062	0.005 ± 0.020	20.36321 ± 0.00093	-3.47 ± 0.35	0.07 ± 0.13
IRS15NE	1995.49	1.23178 ± 0.00039	-1.852 ± 0.023	0.0006 ± 0.0017	11.33613 ± 0.00079	-5.661 ± 0.048	0.0013 ± 0.0037
IRS14NE	2014.18	0.9334 ± 0.0033	4.29 ± 0.85	0.09 ± 0.23	-8.15823 ± 0.00068	-3.38 ± 0.19	-0.024 ± 0.049
SiO-16	2008.42	-26.44 ± 0.13	2 ± 14	-0.9 ± 2.4	-34.087 ± 0.075	-42.1 ± 8.1	0.2 ± 1.0
SiO-21	2008.42	40.754 ± 0.022	17.0 ± 2.4	-0.11 ± 0.40	-21.795 ± 0.018	-26.7 ± 1.9	-0.02 ± 0.24
SiO-24	2015.27	17.1853 ± 0.0011	4.99 ± 0.26	-0.002 ± 0.063	-4.8159 ± 0.0084	-2.5 ± 2.4	0.04 ± 0.59
SiO-22	2008.42	41.319 ± 0.073	9.7 ± 7.8	-0.5 ± 1.4	15.38 ± 0.12	-22 ± 13	0.4 ± 1.6
SiO-6	2008.42	34.98 ± 0.12	32 ± 13	0.7 ± 1.9	30.792 ± 0.092	-9.6 ± 9.9	0.1 ± 1.2
SiO-17	1998.41	8.04279 ± 0.00044	2.450 ± 0.026	0.0003 ± 0.0022	-27.7040 ± 0.0027	2.78 ± 0.17	-0.001 ± 0.014
SiO-11	2008.42	1.7424 ± 0.0083	2.32 ± 0.69	-0.002 ± 0.064	40.296 ± 0.019	2.3 ± 1.5	0.01 ± 0.14
IRS17	2000.85	13.1477 ± 0.0012	-1.052 ± 0.078	0.0018 ± 0.0066	5.5657 ± 0.0015	-1.083 ± 0.097	-0.0002 ± 0.0093
IRS19NW	1998.41	14.55147 ± 0.00028	1.143 ± 0.017	-0.0000 ± 0.0013	-18.4621 ± 0.0012	-0.460 ± 0.067	-0.0011 ± 0.0052
SiO-25	2013.13	-33.0445 ± 0.0054	-13.2 ± 1.8	-0.02 ± 0.64	-17.669 ± 0.015	-54.1 ± 3.9	0.1 ± 1.4

[a] Position uncertainties for IRS 7 have been manually increased to 5 mas to reflect the fact that this star may have an extended maser shell as discussed in Section 4.3.

Table 4.4: 3D velocities and accelerations of stellar masers

Star	v_α (km s^{-1})	a_α (km s^{-1} yr^{-1})	v_δ (km s^{-1})	a_δ (km s^{-1} yr^{-1})	v_{LSR} (km s^{-1})	a_{LSR} (km s^{-1} yr^{-1})	$\|v\|$ (km s^{-1})	$\|a\|$ (km s^{-1} yr^{-1})
IRS9	115.9 ± 1.6	-0.01 ± 0.14	87.3 ± 2.6	-0.00 ± 0.22	-341.1 ± 1.2	-0.05 ± 0.29	370.7 ± 1.4	0.05 ± 0.29
IRS7[a]	-1.4 ± 4.3	0.14 ± 0.29	-161.2 ± 5.5	-0.08 ± 0.41	-113.6 ± 7.0	0.1 ± 1.8	197.2 ± 6.1	0.19 ± 0.90
SiO-14[b]	77.91 ± 0.81	-0.027 ± 0.065	-28.6 ± 4.6	-0.01 ± 0.38	-111.02 ± 0.43	-0.58 ± 0.10	138.6 ± 1.1	0.58 ± 0.10
SiO-28	-27.0 ± 3.0	-0.23 ± 0.87	69 ± 77	12 ± 20	-104.16 ± 0.98	0.02 ± 0.25	128 ± 41	12 ± 20
SiO-29	...	...	...	...	-91.58 ± 0.98	...	...	...
SiO-31	...	...	...	...	-81.10 ± 0.13	...	...	...
SiO-18	-110 ± 280	-28 ± 80	40 ± 100	-16 ± 29	-78.4 ± 1.5	0.42 ± 0.38	140 ± 220	33 ± 71
SiO-26	...	...	...	...	-72.36 ± 0.11	...	...	...
IRS12N	-42.47 ± 0.85	-0.026 ± 0.066	-105.35 ± 0.88	0.015 ± 0.069	-65.01 ± 0.69	0.22 ± 0.16	130.88 ± 0.83	0.22 ± 0.16
IRS28	58.5 ± 2.4	-0.02 ± 0.19	-209.9 ± 6.9	-0.25 ± 0.52	-53.60 ± 0.50	-0.01 ± 0.12	224.4 ± 6.5	0.25 ± 0.52
SiO-27	-57.5 ± 5.1	0.6 ± 1.2	150 ± 27	2.9 ± 5.8	-43.846 ± 0.080	0.099 ± 0.025	166 ± 24	3.0 ± 5.7
SiO-30	...	...	...	...	-37.96 ± 0.45	...	...	...
SiO-15	-92.0 ± 2.5	0.10 ± 0.20	17.3 ± 8.0	-0.33 ± 0.65	-35.4 ± 1.0	0.01 ± 0.26	100.1 ± 2.7	0.34 ± 0.62
SiO-19	99.7 ± 4.5	-0.4 ± 1.3	8 ± 53	9 ± 16	-29.3 ± 1.4	0.21 ± 0.32	104.2 ± 6.0	9 ± 16
IRS10EE	1.36 ± 0.53	0.010 ± 0.039	-75.07 ± 0.98	-0.005 ± 0.072	-27.53 ± 0.38	-0.070 ± 0.091	79.97 ± 0.93	0.071 ± 0.090
SiO-20	27.2 ± 2.3	0.20 ± 0.75	-132 ± 13	2.7 ± 5.0	-16.62 ± 0.67	-0.37 ± 0.17	136 ± 13	2.8 ± 5.0
IRS15NE[b]	-70.25 ± 0.86	0.021 ± 0.063	-214.7 ± 1.8	0.05 ± 0.14	-10.99 ± 0.41	-0.34 ± 0.11	226.2 ± 1.7	0.35 ± 0.11
IRS14NE	163 ± 32	3.4 ± 8.7	-128.1 ± 7.0	-0.9 ± 1.8	-10.50 ± 0.95	-0.32 ± 0.25	207 ± 26	3.5 ± 8.4
SiO-16	90 ± 520	-33 ± 91	-1600 ± 310	8 ± 39	7.13 ± 0.55	...	1600 ± 310	...
SiO-21	643 ± 91	-4 ± 15	-1012 ± 72	-0.8 ± 9.0	13.447 ± 0.033	...	1199 ± 78	...
SiO-24	189.3 ± 9.8	-0.1 ± 2.4	-96 ± 91	2 ± 22	17.84 ± 0.47	0.22 ± 0.13	213 ± 42	2 ± 22
SiO-22	370 ± 300	-18 ± 53	-820 ± 480	15 ± 62	34.10 ± 0.93	...	900 ± 450	...
SiO-6	1200 ± 490	27 ± 72	-360 ± 370	5 ± 47	51.87 ± 0.21	...	1250 ± 480	...
SiO-17	92.9 ± 1.0	0.011 ± 0.083	105.3 ± 6.4	-0.06 ± 0.52	53.27 ± 0.17	0.105 ± 0.040	150.2 ± 4.5	0.12 ± 0.24
SiO-11[b]	88 ± 26	-0.1 ± 2.4	86 ± 59	0.5 ± 5.4	70.60 ± 0.12	0.105 ± 0.029	142 ± 39	0.5 ± 5.2
IRS17	-39.9 ± 3.0	0.07 ± 0.25	-41.1 ± 3.7	-0.01 ± 0.35	74.36 ± 0.80	-0.36 ± 0.21	93.8 ± 2.1	0.37 ± 0.21
IRS19NW	43.34 ± 0.63	-0.001 ± 0.049	-17.4 ± 2.5	-0.04 ± 0.20	84.37 ± 0.22	-0.226 ± 0.052	96.44 ± 0.57	0.230 ± 0.063
SiO-25[b]	-501 ± 68	-1 ± 24	-2050 ± 150	3 ± 52	118.48 ± 0.10	-0.196 ± 0.038	2120 ± 140	3 ± 50

[a] The velocity centroids of the VLA and ALMA spectra for IRS 7 are offset by $\sim$15 km s^{-1}. The radial velocity and acceleration measurements therefore may not accurately track the motion of the star.

[b] Stars with $> 3\sigma$ radial acceleration measurements, which may be impacted by maser spectral variability.

with at least three epochs of observations. Velocity and acceleration fit results are given in Table 4.4, and figures showing the fits are given in Appendix C. For stars with too few measurements to fit an acceleration, we report the error weighted mean velocity in Table 4.4. Radial velocities and accelerations are expressed in the local standard of rest (LSR) frame. Note that radial velocity and acceleration measurements are only based on the observations detailed in this work and did not include any measurements from literature, unlike the proper motion analysis.

The majority of stars have insignificant radial acceleration limits, with uncertainties ranging from ~ 0.02–1 km s^{-1} yr^{-1}. However radial acceleration was measured at the $> 3\sigma$ level for SiO-14 (-0.58 ± 0.10 km s^{-1} yr^{-1}), SiO-27 (0.099 ± 0.025 km s^{-1} yr^{-1}), IRS15NE (-0.34 ± 0.11 km s^{-1} yr^{-1}), SiO-11 (0.105 ± 0.029 km s^{-1} yr^{-1}), IRS19NW (-0.226 ± 0.052 km s^{-1} yr^{-1}), and SiO-25 (-0.196 ± 0.038 km s^{-1} yr^{-1}). We note that maser variability over time and between lines may introduce a systematic acceleration that does not match the true acceleration of the star.

Velocities from the 2017 ALMA data are often but not always the largest outliers from the fit compared other epochs, with average residuals around ± 1.2 km s^{-1}. We verified that there is no systematic velocity shift being introduced by our reduction or spectra fitting methods by comparing the Sgr A* absorption spectrum observed with two ALMA epochs. By cross-correlating the two spectra, we found that the cross-correlation is maximized at -0.4 km s^{-1}. It is therefore unlikely that the 2017 ALMA velocities are being offset by a significant systematic error.

We also attempted to measure radial accelerations by simultaneously fitting spectral profiles to all spectra for a given star following a method detailed in Pesce et al. (2020) and Reid et al. (2013), who measured accelerations of extragalactic water megamasers. Per star, we performed 100 fits with varying number of Gaussian components and randomized initial values for the velocities of each component. However, we found that the spectra were poorly fit unless we allowed each Gaussian component to have an independent acceleration measurement, which is not useful for determining the underlying systemic acceleration. This is likely due to the variable nature of stellar SiO masers and the fact that we include spectra from multiple maser transitions, which complicates tracking maser peaks between epochs. This method may have better utility for future

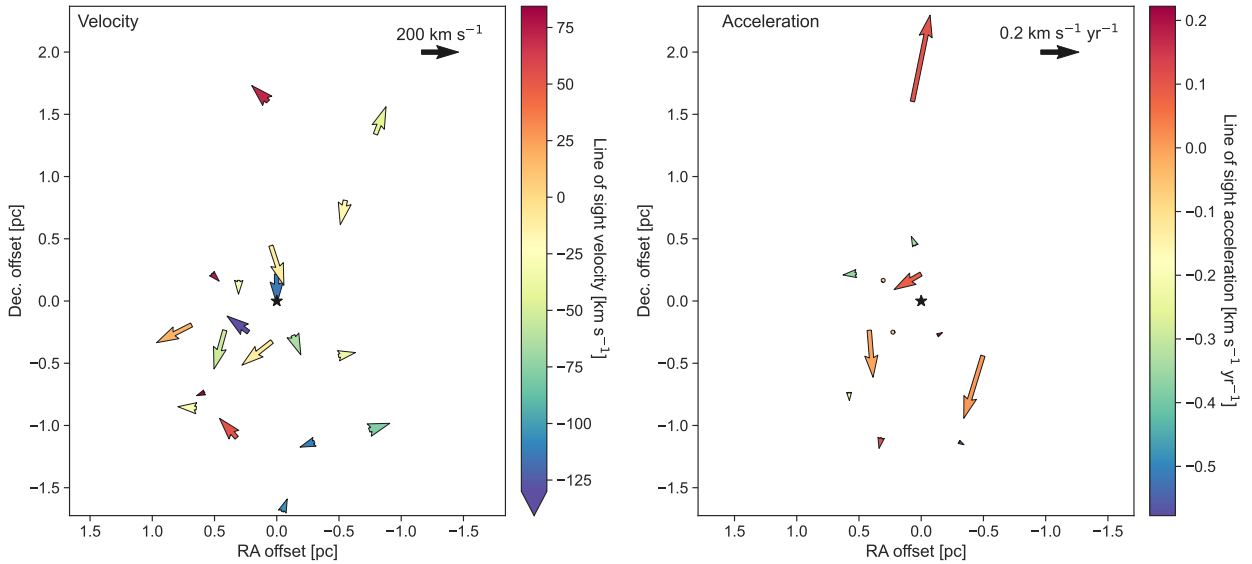

Figure 4.2: Stellar velocities (left) and accelerations (right) assuming a distance of 8 kpc to convert proper motions to physical velocities and accelerations. Masers with proper velocities > 900 km s^{-1} or proper accelerations > 0.5 km s^{-1} yr^{-1} are not shown. The majority of 2D velocities shown are significant, with the exception of SiO-11, SiO-18, and SiO-28, but all of the radial velocities are significant. Note that none of the accelerations in the plane of the sky are significant, and only SiO-14 has a radial acceleration measured with $> 5\sigma$ significance. Positions are indicated by the arrow tails. The star IRS 9 at $(\Delta x, \Delta y) = (0.22$ pc, -0.25 pc) has a radial velocity of -340 km s^{-1}, which is below the range of the velocity color bar on the left.

works with a higher number of spectra of the same transition.

4.4 Stellar kinematics

The 3D stellar velocities and accelerations are shown in Figure 4.2. Masers with proper velocities > 900 km s^{-1} or proper accelerations > 0.5 km s^{-1} yr^{-1} are not shown in the figure. Note that transverse motions are referenced to the Sgr A* continuum, whereas radial motions are in the LSR frame and do not account for any radial velocity of Sgr A*.

4.4.1 Enclosed mass limits

Stellar kinematics may be utilized to constrain the stellar and dark matter mass distribution in the GC. We estimate enclosed mass limits using the 3D velocities for each maser with a $> 5\sigma$ significance 3D velocity measurement. Reid et al. (2003) derived a strict lower limit on the enclosed

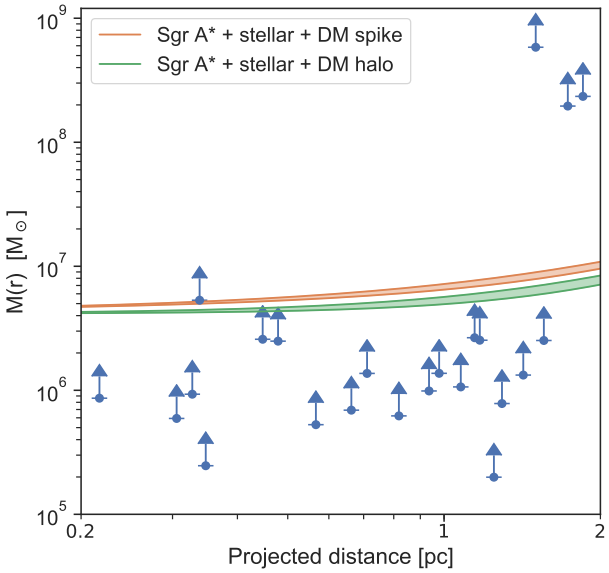

Figure 4.3: Enclosed mass lower limits based on the stellar 3D velocities as a function of projected distance. The dark matter halo model (green region) is a generalized NFW profile (McMillan, 2017), and the maximal dark matter spike model (orange region) includes an additional sharp spike in the dark matter density profile (Lacroix, 2018).

mass for a star given its total velocity magnitude, v, and projected distance from Sgr A*, r_{proj}:

$$M_{encl} \geq \frac{v^2 r_{proj}}{2G}. \tag{4.3}$$

The lower limit approaches an equality as r_{proj} approaches the true distance, when the star is near pericenter, and if the eccentricity of the orbit is close to 1. Following Reid et al. (2003), we subtract 2σ from the stellar velocity to obtain a conservatively small velocity allowed by the measurement uncertainties prior to calculating the enclosed mass limit.

Figure 4.3 shows the mass limits calculated for each star compared to two models of the dark matter distribution in the Galactic Center. The first is a dark matter halo based on a generalized Navarro-Frenk-White (NFW) profile, using the main model parameters of McMillan (2017): a slope index of $\gamma = 1$, scale radius of $r_s = 18.8$ kpc, local dark matter density of $\rho_\odot = 0.0101$ $M_\odot$ pc^{-3}, and distance to the GC of $R_0 = 8.2$ kpc. The second model includes a sharp spike in the dark matter density profile scaling as $r^{-7/3}$ within the spike scale radius of $R_{sp} = 100$ pc, which is the maximal dark matter spike obtained by Lacroix (2018). Both models include a central black hole

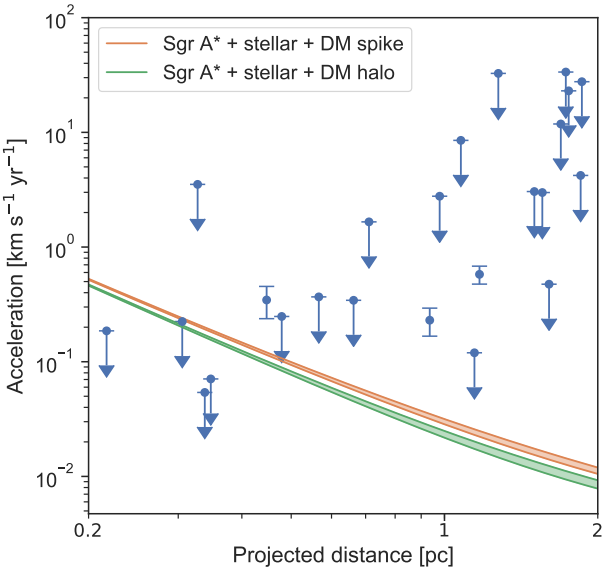

Figure 4.4: 3D stellar acceleration magnitude limits as a function of projected distance. Shaded regions show expected accelerations due to models of the interior stellar and dark matter mass. The dark matter halo model (green) is a generalized NFW profile (McMillan, 2017), and the maximal dark matter spike model (orange) includes an additional sharp spike in the dark matter density profile (Lacroix, 2018).

mass of 4.15×10^6 $M_\odot$ (GRAVITY Collaboration et al., 2019) and stellar density profiles following r^γ. We display a range of stellar profiles with γ values between 1.1 to 1.5 and stellar mass density normalizations between 1.2 to 1.8×10^5 $M_\odot$ pc^{-3} at 1 pc (Schödel et al., 2018). All but four of the stars have M_{encl} lower limits consistent with the expected values: IRS 9, SiO-25, SiO-16, and SiO-21, in order of projected distance. We discuss possible reasons that the enclosed mass may be over estimated for these stars in Section 4.5.1.

4.4.2 Accelerations

Figure 4.4 shows the acceleration estimates for our masers as a function of projected distance from Sgr A* compared to expected accelerations for the two mass models described in Section 4.4.1, assuming circular orbits. Approximately 0.04 km s^{-1} yr^{-1} precision would be required to differentiate between the two dark matter models in the range of radii where our sample of masers are found.

The upper limit accelerations for the majority of masers are at least an order of magnitude higher than the expected acceleration and the difference tends to be larger for masers at larger projected distance. This is due the fact that masers closer to Sgr A* are more likely to have more position measurements and therefore lower acceleration uncertainties than masers farther from Sgr A*. Three masers, SiO-14, IRS15 and IRS19NW, have at least 3σ-significance acceleration magnitudes, indicated by error bars rather than upper limits in Figure 4.4, which disagree with the model accelerations. These accelerations are dominated by the radial acceleration and may be affected by intrinsic spectral variation as discussed in Section 4.3.3 (see also Figure C.1).

4.5 Discussion

4.5.1 High velocity stars

From Figure 4.3, we identified four stars with velocities that exceed the expectation for stars within their projected distance from Sgr A*. The first is IRS 9, which has a 3D velocity of 370 km s^{-1}. This result is consistent with that of Reid et al. (2007), who discussed several possible explanations for the star's high velocity. However, Trippe et al. (2008) found that this velocity is not excessively high compared to the global distribution of 3D stellar velocities in the GC, the tail end of which extends up to about 500 km s^{-1}.

SiO-25, SiO-16, and SiO-21 each have significantly higher velocity measurements than predicted for stars in orbit in the GC: approximately 2100, 1600, and 1200 km s^{-1}, respectively. In the case of these three masers, however, the total velocity is dominated by the 2D velocity inferred from the proper motion. Observational limitations may be causing spurious large proper motion measurements since these masers have a relative paucity of observations compared to other masers in our sample. In fact, SiO-16 and SiO-21 are outside of the VLA field of view and therefore only detected in the 86 GHz line by ALMA.

However, if the proper motions for these stars are accurate but the stars are closer than the assumed 8 kpc distance to the GC, we may have overestimated the 2D velocity. To estimate

the likelihood that three foreground stars would contaminate our sample of masers, we used the model for the distribution of AGB stars in the Galaxy from Jackson et al. (2002). We integrated their number density model over the volume observed in our ALMA observations towards the GC, resulting in ~ 0.1 foreground AGB stars expected in our observations. We therefore conclude it is unlikely that all three masers are actually foreground stars.

4.5.2 GC reference frame

Proper motions of SiO masers associated with bright IR stars have been used to derive the GC astrometric reference frame (Yelda et al. 2010; Plewa et al. 2015; Boehle et al. 2016; Sakai et al. 2019), which is necessary to mitigate systematic uncertainties in precision measurements of the orbits of IR stars. Sakai et al. (2019) constructed the astrometric reference frame using maser astrometry from 2005 – 2017 and reported uncertainties on the SiO-based proper motions ranging from about 0.02 – 0.6 mas yr^{-1} for seven stars: IRS 9, IRS 7, IRS 12N, IRS 28, IRS 10EE, IRS 15NE, and IRS 17.

Our proper motion analysis incorporates several more epochs of observations and a longer time baseline of about 25 years from 1995 – 2020. For the seven reference frame stars, we measure proper motions with similar or better precision than those reported in Sakai et al. (2019), with uncertainties ranging from about 0.01 – 0.2 mas yr^{-1}. The astrometry reported in this work could be used to further improve the GC reference frame since the proper motion fit parameters in Table 4.3 may be used with Equation 4.1 to predict the stellar position at any future epoch.

4.6 Conclusions

We presented five epochs of SiO maser astrometry for stars in the GC from 2013 to 2020. Masers were observed at 43 GHz with the VLA in 2013, 2014, and 2020, and at 86 GHz with ALMA in 2015 and 2017. We observed 28 masers total, of which four are new detections. These masers act as high brightness temperature probes of the underlying stellar kinematics within a few parsec of Sgr A*. By incorporating archival data since 1995 in our maser position time series, we calculated

proper motions and proper accelerations with $\sim$ 0.1 mas yr^{-1} and 0.01 mas yr^{-2} precision, respectively. The proper motions have similar or better precision than those used to derived the GC astrometric reference frame for IR stellar orbits, and may therefore be used to further improve the precision of the reference frame.

The proper motions and proper accelerations correspond to 2D velocities and accelerations with uncertainties of about 4 km s^{-1} and 0.4 km s^{-1} yr^{-1}, though we note that accurate determination of the stellar velocities and accelerations depend on the radial distances to these stars which are currently unknown and assumed to be 8 kpc for all masers. From spectra, we measure radial velocities and accelerations with $\sim$0.5 km s^{-1} and 0.1 km s^{-1} yr^{-1} precision, respectively.

We also studied the stellar kinematics in the context of expected stellar velocities and accelerations in the GC based on models of the combined mass of Sgr A*, the stellar population, and the dark matter distribution. Lower limits on the enclosed mass were calculated for each maser based on their 3D velocities and projected distances. Several stars were found to yield enclosed mass limits 1–2 orders of magnitude higher than those predicted due to particularly high transverse velocity measurements. These may caused by inaccurate proper motion measurements due to a paucity of observations or by incorrectly translating proper motions to velocities if the stars are closer than the assumed 8 kpc.

The primary limitation on the analysis presented here is the variability of SiO masers. The majority of our masers show spectral variability in time and between lines, which may degrade the accuracy of measuring the systemic radial velocities and accelerations of the stars themselves. Further high resolution observations will improve the statistical uncertainties in proper motion and radial measurements, as well as potentially help resolve any systematics introduced by maser variability. Higher precision measurements will enable improved mapping of the stellar and dark matter mass distributions, as well as probes of the metric around Sgr A* and general relativistic tests, which we intend to pursue in future work.

Acknowledgements

We thank the anonymous referee for very helpful comments. The authors acknowledge support from the NSF Graduate Research Fellowship Program under grant DGE-1650115 and the NSF grant AST-1908122. This paper makes use of the following ALMA data: ADS/JAO.ALMA #2013.1.00834.S, ADS/JAO.ALMA#2016.1.00940.S. ALMA is a partnership of ESO (representing its member states), NSF (USA) and NINS (Japan), together with NRC (Canada), MOST and ASIAA (Taiwan), and KASI (Republic of Korea), in cooperation with the Republic of Chile. The Joint ALMA Observatory is operated by ESO, AUI/NRAO and NAOJ.

Software used in this research: Astropy (Astropy Collaboration et al., 2013, 2018, 2022), CASA (McMullin et al., 2007), numpy (Harris et al., 2020), matplotlib (Hunter, 2007), scipy (Virtanen et al., 2020), uvmultifit (Martí-Vidal et al., 2014)

Chapter 5

Updated Observations and Kinematics of Stellar SiO Masers in the Galactic Center

Abstract

Since the publication of Paine & Darling (2022), which has been reproduced in Chapter 4, we obtained two epochs of observations of the GC stellar SiO masers from ALMA and VLA. In this chapter, we present these observations along with new methods for analysing the position and velocity time series for the masers. The updated measurements track the stellar proper motions and proper accelerations with typical uncertainties around 0.3 mas yr^{-1} and 0.03 mas yr^{-2}, respectively. For masers with several decades of astrometry, uncertainties are as low as 16 μas yr^{-1} and 0.55 μas yr^{-2}, corresponding to 0.65 km s^{-1} and 0.021 km s^{-1} yr^{-1} at a distance of 8.2 kpc. The radial velocities and accelerations are measured with about 0.5 km s^{-1} and 0.1 km s^{-1} yr^{-1} precision, respectively. Using additional VLA maser observations, we analyze the spectral variability observed over the course of several weeks in our sample, and find that this effect corresponds to a 0.7 km s^{-1} systematic uncertainty in the stellar velocities inferred from individual maser spectra. We compare the maser kinematics to various models of the dark matter and stellar mass density profiles in the GC. Several stars are identified with anomalously large acceleration measurements, and we assess the possibility that these measurements are caused by undetected binary orbits. Finally, we discuss future work and observations to address current limitations of the SiO maser kinematics and analysis thereof.

This chapter is in preparation and will be submitted for publication in ApJ in 2023.

5.1 Introduction

As demonstrated in the previous chapter, stellar SiO masers are high resolution tracers of stellar kinematics in the GC. Since the masers are found in a region of the GC where stellar observations at shorter wavelengths are affected by dust obscuration and stellar crowding, radio observations offer a unique window into the gravity profile within a few parsecs of Sgr A*. However, achieving the resolution and accuracy necessary to constrain the stellar and dark matter mass distributions, and to potentially probe the metric around Sgr A*, requires continual observations of the SiO masers. Additionally, the reference frame for IR observations based on the SiO maser proper motions degrades with time as the uncertainty of the predicted maser positions grows.

In Chapter 4, we measured 2D velocities and accelerations with about 4 km s^{-1} and 0.4 km s^{-1} yr^{-1} precision, and radial velocities and accelerations with about 0.5 km s^{-1} and 0.1 km s^{-1} yr^{-1} precision, respectively. We identified several stars with exceptionally large proper motions (SiO-25, SiO-16, and SiO-21) and large radial accelerations (SiO-14, IRS 15, and IRS 19NW) which cannot be explained by orbits gravitationally bound to the GC. However, the accuracy of these measurements is greatly dependent on the intrinsic maser variability, which is difficult to estimate per star without resolved observations of the maser emission. Additional measurements are required to confirm or reject these anomalous kinematics, as well as improve the sensitivity of the entire maser sample to the small scale details of the gravity profile in the GC.

In this chapter we present two new epochs of observations of the SiO masers with ALMA in 2021 and VLA in 2022, and updated stellar kinematics using new methods for measuring stellar velocities and accelerations. The observations and data reduction are detailed in Section 5.2. The analysis of the maser astrometry and spectra are described in Sections 5.3 and 5.4. The resulting 3D stellar kinematics and mass profile constraints are given in Section 5.5. We discuss the impact that unseen binary companions may have on our results and prospects for addressing limitations of the SiO maser observations for studying stellar kinematics in Section 5.6

5.2 Observations and Data Reduction

We observed the GC masers around 86 GHz with ALMA on 2021 August 19 (ALMA 2019.1.00292.S), and around 43 GHz with VLA on 2022 March 7 (VLA 22A-202). In both cases, the observations, calibration, and reduction were conducted in a manner consistent with previous observations, namely ALMA 2016.1.00940 and VLA 19A-310. Calibrations were done using the Common Astronomy Software Applications (CASA) package (McMullin et al., 2007).

The ALMA 2021 observation was done with band 3 and the array in the C43-8 configuration, which has baselines between 110 – 8500 m. The spectral configuration consisted of four spectral windows covering the SiO $J = 2 - 1$ $v = 0$, $v = 1$, and $v = 2$ transitions and the ^{29}SiO $J = 2 - 1$ $v = 1$, each with 234.375 MHz bandwidth and consisting of 122.07 kHz (0.42 km s^{-1}) channels in dual linear polarization. Calibrations were conducted using the ALMA pipeline, with further self-calibration using the Sgr A* continuum.

The VLA 2022 observations used the A configuration. The spectral configuration consisted of four spectral windows covering the SiO $J = 1 - 0$ $v = 0$, $v = 1$, and $v = 2$ transitions and the ^{29}SiO $J = 1 - 0$ $v = 1$ transition, each consisting of 62.5 kHz (0.44 km s^{-1}) channels in dual polarization. The bandwidths were 128 MHz, except for the spectral window covering the $v = 2$ transition, which was 64 MHz (a smaller bandwidth was chosen to ease scheduling constraints since the maximum number of baseline boards is not always available). Bandpass calibration and initial phase calibration were done using 1733−1304, and the flux calibration was done using 1331+305 (3C286). Phases and amplitudes were self-calibrated with the Sgr A* continuum.

5.2.1 Visibility Fitting

After calibration, the reduction and u-v plane fitting for the ALMA and VLA observations proceeded in a similar fashion to each other. For each spectral window, the Sgr A* continuum was subtracted in the u-v plane by fitting to the line-free channels using the CASA task *uvcontsub*. Maser sources were then identified by eye from continuum-subtracted image cubes created using the

CLEAN algorithm, however these images were not primarily used in the astrometry and spectral analysis. Channels containing maser emission were then regridded to the kinematic local standard of rest (LSRK) frame with 0.25 km s^{-1} channel widths for the ALMA 2021 data and 0.5 km s^{-1} channels for the VLA 2022 data.

The positions and spectra for each maser were fit in the u-v plane using the package *uvmultifit* (Martí-Vidal et al., 2014). Using a by-eye determination of the channels containing emission for each source, we identified groups of masers with overlap in frequency space. For each group, we then fit the visibilities simultaneously for all masers in the group. We require a $> 5\sigma$ measurement of the maser emission in at least one channel to report a detection of a source. There are several previously detected masers that were identified by eye and where faint emission was found with *uvmultifit*, but that did not pass the 5σ threshold for detection: SiO-16, SiO-25, SiO-29, and SiO-30 in ALMA 2021; and IRS 14NE ($v = 1$ and $v = 2$ lines), SiO-28 ($v = 1$ line), SiO-31 ($v = 1$ line) in VLA 2022.

The detected masers are listed in Table 5.1. Note that IRS 9 was not observed in the $v = 2$, $J = 1 - 0$ line due to smaller bandwidth of that spectral window in VLA 2022. Several masers which were reported in Chapter 4 do not have any new detections in ALMA 2021 or VLA 2022: SiO-16, SiO-25, SiO-29, and SiO-30. *uvmultifit* reports an offset of each source in each channel from the phase center, which is Sgr A* due to the self-calibration of the phases on the continuum. We then determine an offset position for each detected maser by taking the error-weighted mean of the best fit coordinates in each channel with $> 5\sigma$ measurement of the maser emission. These mean offsets are presented in Table 5.1. In cases where both the $v = 1$ and $v = 2$ $J = 1 - 0$ line were detected in the VLA epoch, we report both positions. Radial velocities were determined by calculating the centroid of each maser spectrum, and are reported in Table 5.1. The statistical uncertainties on the velocity centroid are typically ~ 0.05 km s^{-1}. In Section 5.4, we calculate an additional systematic uncertainty on the stellar velocity inferred from the maser spectra.

Table 5.1: Maser positions and velocities

Star	Epoch (year)	Line	R.A. offset (arcsec)	Dec. offset (arcsec)	Radial velocity (km s^{-1})
IRS9	2021.63	$J = 2-1,\ v = 1$	5.7174 ± 0.0007	-6.2972 ± 0.0005	-342.32 ± 0.03
	2022.18	$J = 1-0,\ v = 1$	5.7231 ± 0.0003	-6.2957 ± 0.0006	-341.50 ± 0.05
IRS7	2021.63	$J = 2-1,\ v = 1$	0.0320 ± 0.0003	5.4524 ± 0.0002	-118.05 ± 0.04
	2022.18	$J = 1-0,\ v = 1$	0.030 ± 0.001	5.450 ± 0.002	-101.6 ± 0.3
SiO-14	2021.63	$J = 2-1,\ v = 1$	-7.6121 ± 0.0006	-28.4714 ± 0.0004	-115.61 ± 0.03
	2022.18	$J = 1-0,\ v = 1$	-7.6157 ± 0.0004	-28.4673 ± 0.0008	-115.44 ± 0.05
	2022.18	$J = 1-0,\ v = 2$	-7.6152 ± 0.0004	-28.4665 ± 0.0008	-114.74 ± 0.07
SiO-28	2021.63	$J = 2-1,\ v = 1$	-1.113 ± 0.003	-42.549 ± 0.002	-103.51 ± 0.07
	2022.18	$J = 1-0,\ v = 2$	-1.118 ± 0.002	-42.548 ± 0.003	-103.6 ± 0.1
SiO-31	2021.63	$J = 2-1,\ v = 1$	9.360 ± 0.001	-18.3295 ± 0.0009	-77.72 ± 0.09
SiO-18	2021.63	$J = 2-1,\ v = 1$	-18.712 ± 0.002	-26.093 ± 0.002	-77.13 ± 0.07
	2022.18	$J = 1-0,\ v = 1$	-18.7175 ± 0.0006	-26.090 ± 0.001	-77.01 ± 0.05
	2022.18	$J = 1-0,\ v = 2$	-18.7173 ± 0.0004	-26.0877 ± 0.0009	-77.55 ± 0.03
SiO-26	2021.63	$J = 2-1,\ v = 1$	22.495 ± 0.003	23.471 ± 0.002	-72.4 ± 0.1
IRS12N	2021.63	$J = 2-1,\ v = 1$	-3.2796 ± 0.0005	-6.9520 ± 0.0003	-63.84 ± 0.03
	2022.18	$J = 1-0,\ v = 1$	-3.2802 ± 0.0002	-6.9536 ± 0.0004	-64.05 ± 0.03
	2022.18	$J = 1-0,\ v = 2$	-3.2799 ± 0.0002	-6.9531 ± 0.0005	-65.16 ± 0.04
IRS28	2021.63	$J = 2-1,\ v = 1$	10.503 ± 0.001	-5.9107 ± 0.0007	-52.39 ± 0.05
	2022.18	$J = 1-0,\ v = 1$	10.5026 ± 0.0006	-5.911 ± 0.001	-52.10 ± 0.06
	2022.18	$J = 1-0,\ v = 2$	10.5033 ± 0.0006	-5.911 ± 0.001	-52.16 ± 0.04
SiO-27	2021.63	$J = 2-1,\ v = 1$	-19.937 ± 0.003	33.688 ± 0.002	-44.2 ± 0.1
	2022.18	$J = 1-0,\ v = 1$	-19.940 ± 0.002	33.699 ± 0.004	-43.8 ± 0.1
	2022.18	$J = 1-0,\ v = 2$	-19.941 ± 0.002	33.698 ± 0.005	-43.3 ± 0.1
SiO-15	2021.63	$J = 2-1,\ v = 1$	-12.475 ± 0.002	-11.061 ± 0.002	-35.66 ± 0.06
	2022.18	$J = 1-0,\ v = 1$	-12.4797 ± 0.0008	-11.067 ± 0.002	-38.12 ± 0.07
	2022.18	$J = 1-0,\ v = 2$	-12.4803 ± 0.0005	-11.061 ± 0.001	-36.79 ± 0.06
SiO-19	2021.63	$J = 2-1,\ v = 1$	16.268 ± 0.001	-21.6604 ± 0.0008	-27.57 ± 0.05
	2022.18	$J = 1-0,\ v = 1$	16.269 ± 0.001	-21.659 ± 0.002	-27.2 ± 0.1
	2022.18	$J = 1-0,\ v = 2$	16.267 ± 0.001	-21.655 ± 0.002	-29.09 ± 0.09
IRS10EE	2021.63	$J = 2-1,\ v = 1$	7.6847 ± 0.0005	4.1688 ± 0.0003	-29.01 ± 0.02
	2022.18	$J = 1-0,\ v = 1$	7.6849 ± 0.0003	4.1675 ± 0.0005	-27.28 ± 0.04
	2022.18	$J = 1-0,\ v = 2$	7.6847 ± 0.0002	4.1691 ± 0.0004	-27.37 ± 0.03
SiO-20	2021.63	$J = 2-1,\ v = 1$	-13.860 ± 0.002	20.345 ± 0.001	-18.59 ± 0.06
	2022.18	$J = 1-0,\ v = 1$	-13.860 ± 0.001	20.344 ± 0.003	-17.56 ± 0.09
	2022.18	$J = 1-0,\ v = 2$	-13.860 ± 0.002	20.342 ± 0.004	-17.9 ± 0.1
IRS15NE	2021.63	$J = 2-1,\ v = 1$	1.1820 ± 0.0007	11.1848 ± 0.0005	-12.88 ± 0.03
	2022.18	$J = 1-0,\ v = 1$	1.1809 ± 0.0004	11.1821 ± 0.0009	-13.52 ± 0.04
	2022.18	$J = 1-0,\ v = 2$	1.1815 ± 0.0005	11.183 ± 0.001	-13.30 ± 0.06
IRS14NE	2021.63	$J = 2-1,\ v = 1$	0.969 ± 0.004	-8.180 ± 0.002	-12.9 ± 0.1

Continuation of Table 5.1

Star	Epoch (year)	Line	R.A. offset (arcsec)	Dec. offset (arcsec)	Radial velocity (km s^{-1})
SiO-21	2021.63	$J = 2 - 1$, $v = 1$	40.984 ± 0.006	-22.130 ± 0.004	12.96 ± 0.05
SiO-24	2021.63	$J = 2 - 1$, $v = 1$	17.212 ± 0.004	-4.833 ± 0.002	18.93 ± 0.06
	2022.18	$J = 1 - 0$, $v = 1$	17.219 ± 0.002	-4.831 ± 0.004	21.5 ± 0.2
	2022.18	$J = 1 - 0$, $v = 2$	17.217 ± 0.001	-4.832 ± 0.003	20.5 ± 0.1
SiO-22	2021.63	$J = 2 - 1$, $v = 1$	41.416 ± 0.002	15.186 ± 0.001	34.20 ± 0.05
SiO-6	2021.63	$J = 2 - 1$, $v = 1$	35.2932 ± 0.0009	30.7091 ± 0.0006	52.65 ± 0.06
SiO-17	2021.63	$J = 2 - 1$, $v = 1$	8.101 ± 0.002	-27.643 ± 0.001	53.92 ± 0.04
	2022.18	$J = 1 - 0$, $v = 1$	8.1003 ± 0.0002	-27.6356 ± 0.0005	54.48 ± 0.03
	2022.18	$J = 1 - 0$, $v = 2$	8.1000 ± 0.0003	-27.6354 ± 0.0006	54.17 ± 0.04
SiO-11	2021.63	$J = 2 - 1$, $v = 1$	1.775 ± 0.001	40.3209 ± 0.0007	70.93 ± 0.03
	2022.18	$J = 1 - 0$, $v = 1$	1.7725 ± 0.0006	40.329 ± 0.001	71.54 ± 0.05
	2022.18	$J = 1 - 0$, $v = 2$	1.7737 ± 0.0003	40.3271 ± 0.0007	71.10 ± 0.03
IRS17	2021.63	$J = 2 - 1$, $v = 1$	13.1288 ± 0.0007	5.5437 ± 0.0005	73.56 ± 0.05
	2022.18	$J = 1 - 0$, $v = 1$	13.129 ± 0.001	5.544 ± 0.003	75.11 ± 0.06
	2022.18	$J = 1 - 0$, $v = 2$	13.129 ± 0.002	5.541 ± 0.005	74.0 ± 0.1
IRS19NW	2021.63	$J = 2 - 1$, $v = 1$	14.580 ± 0.002	-18.474 ± 0.001	84.38 ± 0.07
	2022.18	$J = 1 - 0$, $v = 1$	14.5797 ± 0.0002	-18.4720 ± 0.0005	82.12 ± 0.04
	2022.18	$J = 1 - 0$, $v = 2$	14.5796 ± 0.0003	-18.4725 ± 0.0006	81.78 ± 0.05

Radial velocities are reported in the LSRK frame.

5.3 Astrometric Analysis

We measure proper motions and proper accelerations from the position time series for each maser in Tables 4.2 and 5.1, and including astrometry from Reid et al. (2007) and Li et al. (2010). The lower resolution data from VLA 2013, ALMA 2015 and Li et al. (2010) were only included in the fits if a star had fewer than three remaining high resolution epochs of observations. 19 stars were fit with only the high resolution data, 6 included the lower resolution data, and 3 did not have enough observations to fit a proper motion at all.

Prior to fitting, we take the error-weighted mean position of the v=1 and v=2 lines per epoch if both were detected simultaneously. We then calculate a reference epoch, t_{ref}, for each maser from the coordinate error-weighted mean time in the position time series. We find proper motions

by fitting a slope to the positions over time:

$$\Delta x = \Delta x_{ref} + \mu_x (t - t_{ref}), \tag{5.1}$$

where x denotes either the RA or Dec. coordinates, α or δ, respectively. Δx is the offset position from Sgr A* in either coordinate, Δx_{ref} is the position at the reference epoch, and μ_x is the proper motion.

We then find proper accelerations by fitting to the residuals of the proper motion fits:

$$r_{\Delta x} = r_{\Delta x_{ref}} + \frac{1}{2} a_x \left(t - t_{ref}\right)^2, \tag{5.2}$$

where $r_{\Delta x}$ and $r_{\Delta x_{ref}}$ are the residuals of the offset positions and reference epoch positions, and a_x is the proper acceleration. The results of the proper motion and proper acceleration fits are given in Table 5.2, and figures showing the fits are given in Appendix F. We caution that most of the proper acceleration upper limits for masers with shorter time baselines may be unrealistically large due to fitting curvature to the noise in the position time series, especially in cases where the the position measured closest to t_{ref} is a large outlier from the linear proper motion fit. In Table 5.2, we note proper accelerations measured from masers with < 15 year time baselines, effectively all those without astrometry from Reid et al. (2007).

Offset positions, proper motions, and proper accelerations were converted to physical coordinates, velocities, and accelerations assuming a distance to the GC of $R_0 = 8.2$ kpc, which are given in Table 5.3. 2D accelerations of masers with < 15 years of observations are excluded from Table 5.3. In the conversion from angular to physical units, we treat R_0 as a constant for error propagation. However, various measurements of R_0 range from about $8.0 - 8.3$ kpc (Do et al. 2019; Reid et al. 2019; GRAVITY Collaboration et al. 2021; Leung et al. 2023 and references therein), so one may consider the impact of the uncertainty in R_0. Using the small angle approximation, the uncertainty in the velocity in either RA or Dec is $\sigma_v^2 \approx v^2 \left[\left(\frac{\sigma_{R_0}}{R_0} \right)^2 + \left(\frac{\sigma_\mu}{\mu} \right)^2 \right]$. Assuming an approximate uncertainty in R_0 of 0.1 kpc, then $\frac{\sigma_{R_0}}{R_0} \approx 0.01$. Fractional uncertainties in the proper motions in either coordinate direction range from about $0.006 - 6$. For most of the stars, the

Table 5.2: Updated offsets, proper motions and proper accelerations of stellar masers

Star	t_0 (year)	$\Delta\alpha_0$ (arcsec)	μ_α (mas yr^{-1})	a_α (mas yr^{-2})	$\Delta\delta_0$ (arcsec)	μ_δ (mas yr^{-1})	a_δ (mas yr^{-2})
IRS9	2016.94	5.6509 ± 0.0014	3.040 ± 0.072	-0.0006 ± 0.0025	-6.3517 ± 0.0016	2.354 ± 0.082	-0.0004 ± 0.0028
IRS7	2018.12	0.035 ± 0.005^b	-0.103 ± 0.076	-0.0003 ± 0.002	5.570 ± 0.005^b	-4.47 ± 0.09	-0.0012 ± 0.0022
SiO-14	2016.37	-7.6650 ± 0.0012	2.097 ± 0.068	0.0003 ± 0.0025	-28.4524 ± 0.0029	-0.85 ± 0.15	0.0016 ± 0.0055
SiO-28	2019.50	-1.1123 ± 0.0013	-0.63 ± 0.22	-0.004 ± 0.026^a	-42.5713 ± 0.0093	2.8 ± 1.5	0.06 ± 0.16^a
SiO-29	...	...	...	...	...	...	...
SiO-31	...	...	...	...	...	...	...
SiO-18	2020.87	-18.671 ± 0.023	-5.6 ± 3.2	-0.09 ± 0.38^a	-26.0854 ± 0.0087	-0.4 ± 1.2	-0.04 ± 0.13^a
SiO-26	2018.23	22.50 ± 0.01	-1.0 ± 3.4	-0.01 ± 0.39^a	23.48092 ± 0.00081	-1.56 ± 0.23	0.001 ± 0.027^a
IRS12N	2016.72	-3.25176 ± 0.00039	-1.113 ± 0.018	-0.00001 ± 0.00066	-6.88163 ± 0.00034	-2.79 ± 0.016	0.00019 ± 0.00064
IRS28	2015.48	10.46867 ± 0.00097	1.464 ± 0.057	-0.0007 ± 0.0019	-5.7810 ± 0.0017	-5.516 ± 0.089	-0.0011 ± 0.0028
SiO-27	2018.06	-19.9321 ± 0.0012	-1.06 ± 0.28	0.01 ± 0.028^a	33.6712 ± 0.0025	2.62 ± 0.62	0.002 ± 0.058^a
SiO-30	...	...	...	...	...	...	...
SiO-15	2015.56	-12.4266 ± 0.0014	-2.454 ± 0.095	0.0007 ± 0.0034	-11.0768 ± 0.0034	0.58 ± 0.21	-0.0013 ± 0.0079
SiO-19	2016.39	16.24467 ± 0.00045	2.82 ± 0.13	0.0 ± 0.018^a	-21.6680 ± 0.0047	0.7 ± 1.0	0.06 ± 0.13^a
IRS10EE	2017.28	7.6834 ± 0.0004	0.056 ± 0.017	0.00025 ± 0.00054	4.22093 ± 0.00045	-1.986 ± 0.021	0.0001 ± 0.0007
SiO-20	2016.28	-13.86277 ± 0.00029	0.53 ± 0.10	-0.008 ± 0.015^a	20.3619 ± 0.0023	-2.69 ± 0.56	0.043 ± 0.067^a
IRS15NE	2012.41	1.23210 ± 0.00038	-1.892 ± 0.020	-0.00003 ± 0.00068	11.33699 ± 0.00069	-5.765 ± 0.036	-0.0004 ± 0.0013
IRS14NE	2017.81	0.9327 ± 0.0026	4.39 ± 0.66	0.050 ± 0.084^a	-8.1601 ± 0.0013	-2.79 ± 0.32	0.008 ± 0.033^a
SiO-16	2017.71	-26.44 ± 0.13	2.0 ± 14.0	-0.4 ± 1.2^a	-34.087 ± 0.075	-42.1 ± 8.1	0.10 ± 0.51^a
SiO-21	2018.00	40.7388 ± 0.0038	18.56 ± 0.40	0.001 ± 0.018^a	-21.8359 ± 0.0038	-22.31 ± 0.39	0.001 ± 0.017^a
SiO-24	2018.86	17.19772 ± 0.00092	4.56 ± 0.38	-0.018 ± 0.091^a	-4.82254 ± 0.00025	-2.42 ± 0.15	0.005 ± 0.036^a
SiO-22	2018.74	41.3916 ± 0.0061	1.85 ± 0.61	-0.001 ± 0.027^a	15.1699 ± 0.0078	1.21 ± 0.72	0.001 ± 0.032^a
SiO-6	2019.04	35.2205 ± 0.0088	5.52 ± 0.85	-0.001 ± 0.038^a	30.6896 ± 0.0043	1.47 ± 0.39	0.0 ± 0.017^a
SiO-17	2014.75	8.04318 ± 0.00038	2.405 ± 0.022	-0.00027 ± 0.00077	-27.7024 ± 0.0046	2.74 ± 0.26	-0.0010 ± 0.0084
SiO-11	2021.11	1.7645 ± 0.0012	2.12 ± 0.34	-0.006 ± 0.055^a	40.3171 ± 0.0047	2.1 ± 1.3	-0.04 ± 0.27^a
IRS17	2018.03	13.1461 ± 0.0018	-0.89 ± 0.11	0.0017 ± 0.0040	5.56602 ± 0.00068	-1.071 ± 0.038	-0.0002 ± 0.0014
IRS19NW	2017.78	14.55133 ± 0.00066	1.161 ± 0.032	0.0002 ± 0.0011	-18.4621 ± 0.0012	-0.456 ± 0.059	-0.0001 ± 0.0021
SiO-25	2016.66	-33.0410 ± 0.0088	-14.0 ± 2.5	-0.01 ± 0.44^a	-17.666 ± 0.030	-54.7 ± 6.9	0.1 ± 1.2^a

[a] Acceleration measurements from < 15 years of observations, which may be inaccurate.

[b] Position uncertainties for IRS 7 have been manually increased to 5 mas to reflect the fact that this star may have an extended maser shell as discussed in Section 4.3.

uncertainty of the tangential velocity would be dominated by the proper motion measurement uncertainty. However, for the best measured proper motions, the fractional uncertainty of the proper motion is similar to that of R_0, so the uncertainties in Table 5.3 may be an underestimate.

5.4 Spectral Analysis

The velocity of the maser spectrum centroid may not accurately match the systemic stellar velocity which we are interested in measuring, as discussed in Chapter 4. To account for this, we estimate an additional systematic uncertainty on the centroid velocities using additional observations of the 43 GHz masers. Coincidentally, a separate, but similar, observing program of the 43 GHz masers was conducted with the VLA on 2022 March 21, 24, and 28 (VLA 22A-328). While these observations did not have as high spectral resolution as 22A-202, the additional spectra enable us to estimate the variation in the maser spectra over the course of 2 – 3 weeks.

For 22A-328, the $J = 1-0$, $v = 1$ and $v = 2$ lines were observed in dual polarization with 100 kHz channels covering a 128 MHz bandwidth each. Prior to calibration, the channels were averaged to 200 kHz (1.4 km s^{-1}). 22A-328 was calibrated similarly to 22A-202, except the source 1924-2914 was used for bandpass calibration. The Sgr A* continuum was subtracted in the u-v plane by fitting to the line-free channels, and the continuum subtracted data was regridded to the LSRK frame with 1.5 km s^{-1} channels. We fit the maser spectra for each day of observations independently using *uvmultifit*, resulting in three measurements of the spectrum for each maser line. Every maser detected in 22A-202 was also detected in 22A-328. We then calculated the velocity centroid of each spectrum.

A few examples of the 22A-202 and 22A-328 maser spectra are shown in Figure 5.1. To estimate the variability of the velocity inferred from our maser spectra, we calculated the standard deviation of all velocity measurements from 22A-202 and 22A-328 for each maser. IRS 7 had an anomalously large standard deviation of 1.9 km s^{-1}, but we would expect greater variance in the velocity measurements for this star as it is a super giant with maser emission spread over a larger velocity range than the other masers in our sample. Thus, the minimum, maximum, and mean

Table 5.3: Updated 3D velocities and accelerations of stellar masers

Star	v_α (km s^{-1})	a_α (km s^{-1} yr^{-1})	v_δ (km s^{-1})	a_δ (km s^{-1} yr^{-1})	v_{LSR} (km s^{-1})	a_{LSR} (km s^{-1} yr^{-1})
IRS9	115.3 ± 2.7	-0.023 ± 0.094	89.3 ± 3.1	-0.02 ± 0.11	-340.28 ± 0.93	-0.18 ± 0.17
IRS7	-3.9 ± 2.9	-0.009 ± 0.078	-169.7 ± 3.4	-0.045 ± 0.084	-118.2 ± 5.0	0.24 ± 0.21
SiO-14	79.5 ± 2.6	0.012 ± 0.096	-32.2 ± 5.7	0.06 ± 0.21	-111.32 ± 0.42	-0.483 ± 0.070
SiO-28	-23.8 ± 8.2	···	108 ± 58	···	-104.06 ± 0.51	0.061 ± 0.096
SiO-29	···	···	···	···	-91.58 ± 0.51	···
SiO-31	···	···	···	···	-79.41 ± 0.50	···
SiO-18	-210.0 ± 120.0	···	-14 ± 47	···	-77.96 ± 0.96	0.16 ± 0.16
SiO-26	-40.0 ± 130.0	···	-59.3 ± 8.9	···	-72.40 ± 0.15	0.012 ± 0.039
IRS12N	-42.21 ± 0.69	0.0 ± 0.025	-105.82 ± 0.62	0.007 ± 0.024	-64.94 ± 0.43	0.108 ± 0.072
IRS28	55.5 ± 2.2	-0.028 ± 0.072	-209.2 ± 3.4	-0.04 ± 0.11	-53.83 ± 0.55	0.116 ± 0.088
SiO-27	-40 ± 11	···	100 ± 23	···	-43.78 ± 0.35	0.015 ± 0.058
SiO-30	···	···	···	···	-37.96 ± 0.50	···
SiO-15	-93.1 ± 3.6	0.03 ± 0.13	22.1 ± 8.1	-0.05 ± 0.30	-35.15 ± 0.62	-0.17 ± 0.11
SiO-19	106.8 ± 5.0	···	26 ± 38	···	-28.94 ± 0.86	0.16 ± 0.14
IRS10EE	2.13 ± 0.66	0.010 ± 0.021	-75.30 ± 0.78	0.002 ± 0.027	-27.48 ± 0.36	-0.047 ± 0.058
SiO-20	20.3 ± 4.0	···	-102 ± 21	···	-16.94 ± 0.66	-0.24 ± 0.12
IRS15NE	-71.76 ± 0.74	-0.001 ± 0.026	-218.6 ± 1.4	-0.014 ± 0.050	-11.16 ± 0.41	-0.284 ± 0.073
IRS14NE	166 ± 25	···	-106 ± 12	···	-10.49 ± 0.76	-0.33 ± 0.16
SiO-16	90 ± 520	···	-1600 ± 310	···	7.13 ± 0.50	···
SiO-21	704 ± 15	···	-846 ± 15	···	13.53 ± 0.12	-0.083 ± 0.031
SiO-24	173 ± 14	···	-91.6 ± 5.6	···	17.55 ± 0.74	0.37 ± 0.14
SiO-22	70 ± 23	···	46 ± 27	···	33.6 ± 1.5	0.17 ± 0.37
SiO-6	209 ± 32	···	56 ± 15	···	51.65 ± 0.12	0.164 ± 0.031
SiO-17	91.21 ± 0.85	-0.010 ± 0.029	103.9 ± 9.9	-0.04 ± 0.32	53.34 ± 0.13	0.102 ± 0.021
SiO-11	81 ± 13	···	78 ± 51	···	70.61 ± 0.34	0.103 ± 0.062
IRS17	-33.8 ± 4.0	0.06 ± 0.15	-40.6 ± 1.4	-0.009 ± 0.052	74.23 ± 0.75	-0.11 ± 0.13
IRS19NW	44.0 ± 1.2	0.007 ± 0.040	-17.3 ± 2.2	-0.003 ± 0.080	84.36 ± 0.36	-0.182 ± 0.060
SiO-25	-531 ± 94	···	-2080 ± 260	···	118.41 ± 0.24	-0.18 ± 0.11

of the standard deviations excluding IRS 7 are 0.05, 0.7, and 0.3 km s^{-1}, respectively. We take the maximum value of 0.7 km s^{-1} as a conservative estimate of the systematic uncertainty in the stellar velocities measured from maser spectra.

We find radial accelerations by adding the 0.7 km s^{-1} uncertainty in quadrature to the statistical uncertainties reported in Tables 4.2 and 5.1, and then fitting a slope to the velocity time series for each star with at least three epochs of observations. For stars with fewer than three epochs, we calculate only the error weighted mean velocity. The results are given in Table 5.3, and the spectra and fits are displayed in Appendix E.

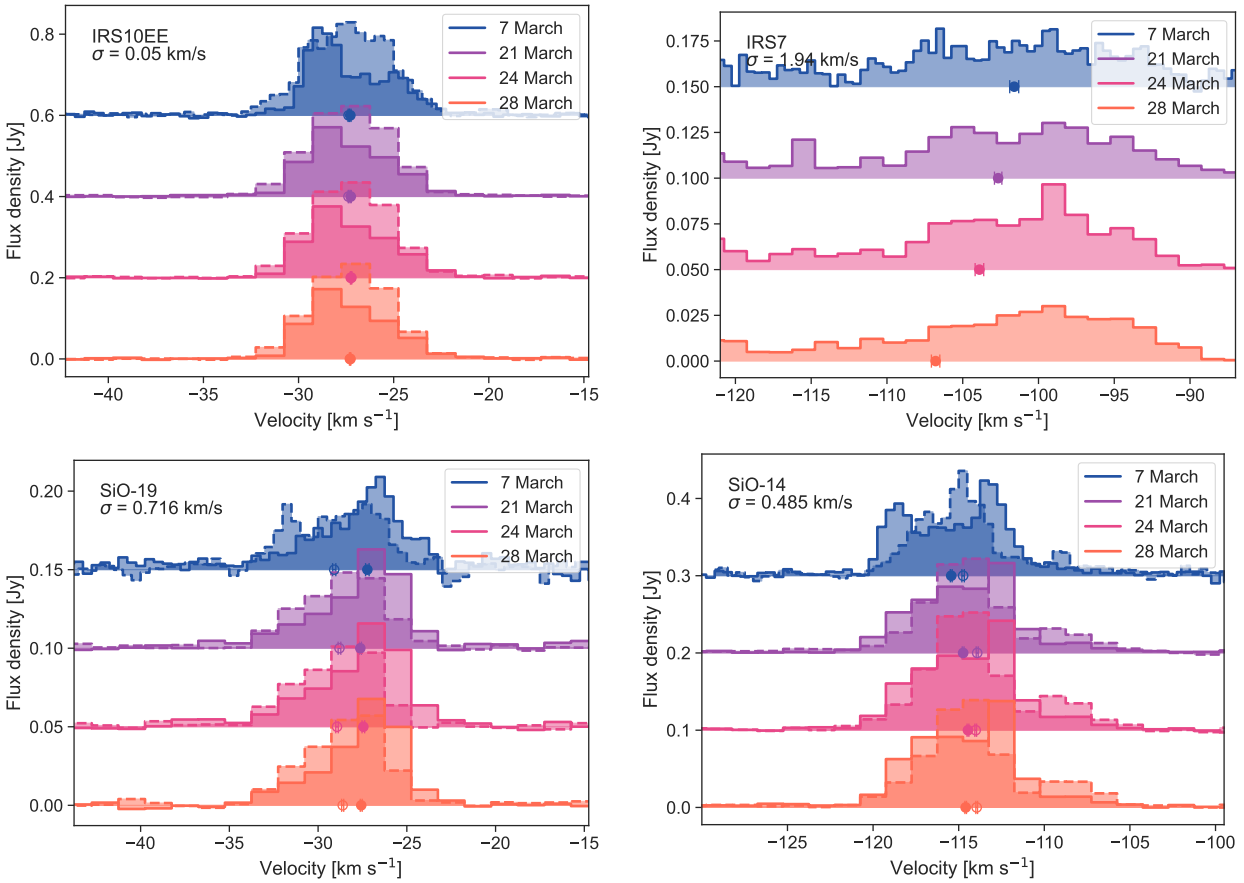

Figure 5.1: Examples of the March 2022 VLA spectra from 22A-202 (7 March) and 22A-328 (21, 24, and 28 March). Error bars indicate the velocity centroid of each spectrum. Solid lines and filled circles indicate the $v = 1$ $J = 1 - 0$ line; dashed lines and open circles indicate the $v = 2$ $J = 1 - 0$ line. The examples shown are the maser with the smallest standard deviation of the velocities (IRS 10EE, upper left), the largest standard deviation (IRS 7, upper right), the next largest standard deviation (SiO-19, lower left), and a more representative example of the typical spread in velocities (SiO-14, lower right).

IRS 7, however, requires separate analysis of the 43 and 86 GHz maser spectra due to the significant offset in the velocities of the lines, shown in Figure E.1. For this maser we adopt a larger systematic uncertainty of 2 km s^{-1}, following the standard deviation in velocities from the various March 2022 VLA observations described above. Then we fit an acceleration to the 43 GHz and 86 GHz spectra separately. In each case we have three epochs of observations, the minimum needed statistically to fit a line. The acceleration of the 43 GHz and 86 GHz masers were 0.19 ± 0.46 km s^{-1} yr^{-1} and 0.26 ± 0.24 km s^{-1} yr^{-1}, respectively. Since both results are consistent with zero

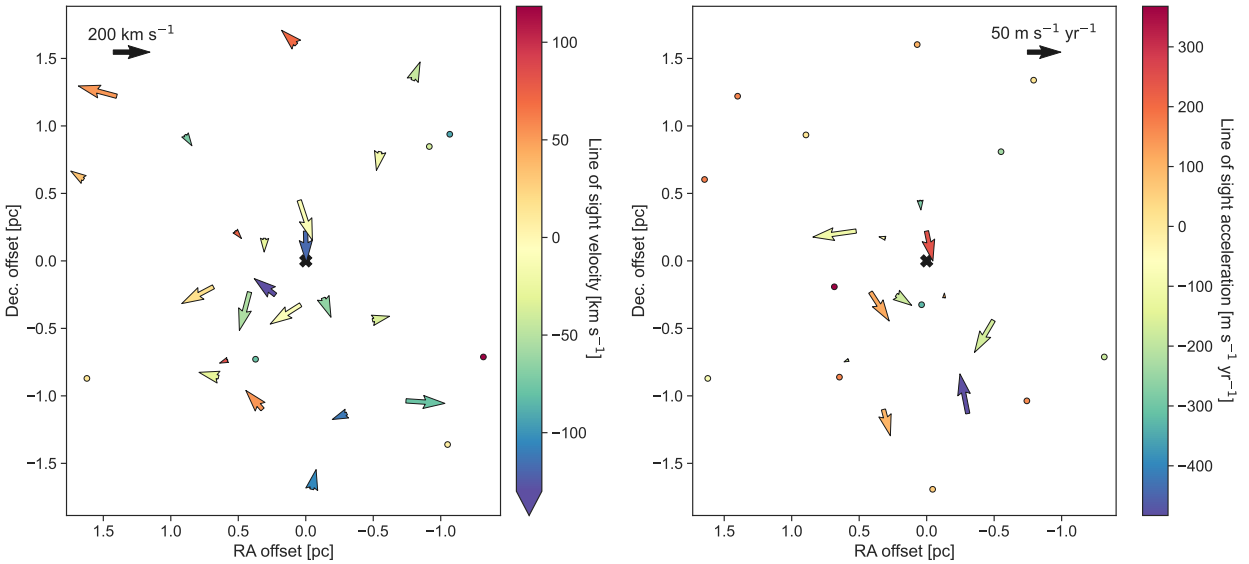

Figure 5.2: Stellar velocities (left) and accelerations (right) assuming a distance of 8.2 kpc to the GC. The 2D velocities of SiO-25, SiO-16, and SiO-21 are not displayed as they are potentially spurious (see Chapter 4). Otherwise, circles indicate stars without 2D velocity or acceleration measurements in Table 5.3. IRS 9 has a radial velocity of -340 km s^{-1}, which is below the range of the velocity color bar on the left.

acceleration, we take the error-weight mean of the two measurements as the radial acceleration of the star, which is 0.24 ± 0.21 km s^{-1} yr^{-1}. The error-weighted mean velocity is -118.2 ± 0.9 km s^{-1}, but in Table 5.3 we manually increase the uncertainty to 5 km s^{-1} due to the large spread in maser emission.

5.5 Results

5.5.1 3D Stellar Kinematics

The stellar kinematics listed in Table 5.3 are shown in Figure 5.2. We can assess the acceleration limits with respect to the orbital accelerations predicted for various realistic mass distributions in the Galactic Center (see Chapter 4 for details), displayed in Figure 5.3.

In cases where the acceleration upper limit falls below any model for the acceleration at the star's projected distance, we can obtain a more accurate lower limit on the star's distance from Sgr

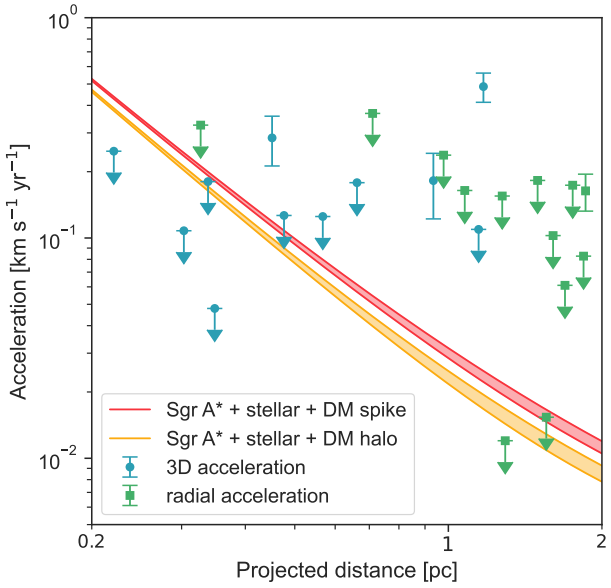

Figure 5.3: Acceleration upper limits compared to predicted accelerations for circular orbits in the GC (see Chapter 4 for details). Measurements including 2D acceleration from astrometry are indicated by blue circles, and measurements including only the radial acceleration component are indicated by green squares. Error bars indicate $> 3\sigma$ measurements of the acceleration.

A*. The minimum distance is simply found using the equation:

$$r_{min} = \sqrt{\frac{GM_{min}(r_{proj})}{a_{up}}}, \tag{5.3}$$

where $M_{min}(r_{proj})$ is the minimal total interior mass at the the star's projected distance, and a_{up} is the upper limit on the star's total acceleration. Three stars have 3D acceleration upper limits below the predicted value at their r_{proj}: IRS 7, IRS 12N, and IRS 10EE at r_{proj} of 0.22 pc, 0.30 pc, and 0.35 pc, respectively. We find minimum distances for these stars of $r_{min} = 0.27$ pc, 0.41 pc, and 0.62 pc. SiO-26 at $r_{proj} = 1.29$ pc has only a radial acceleration upper limit which falls below the prediction on Figure 5.3, so we do not calculate a minimum distance for that star. For randomly located stars about Sgr A*, the typical projected distance will be $r_{proj} \approx \sqrt{\frac{2}{3}}\,|\mathbf{r}|$, where $|\mathbf{r}|$ is the magnitude of the actual separation vector. In the cases of IRS 7, IRS 12N, and IRS 10EE, one might then expect their true separations to be around 0.27 pc, 0.37 pc, and 0.43 pc, respectively. The fact that these expectations are roughly in line with our acceleration-based r_{min} estimates (in fact, equivalent for IRS 7) indicate that the acceleration precision is approaching the

real accelerations of the stars.

Also indicated on Figure 5.3 are four stars with $> 3\sigma$ acceleration measurements. Three of these stars with 3D acceleration measurements are, in order of increasing projected distance, IRS 15NE, IRS 19NW, and SiO-14 with accelerations of 0.28 ± 0.07 km s^{-1} yr^{-1}, 0.18 ± 0.06 km s^{-1} yr^{-1}, and 0.49 ± 0.07 km s^{-1} yr^{-1}, respectively. In each case, the total acceleration is dominated by a large radial acceleration. Additionally, SiO-6 has a a radial acceleration measurement of 0.16 ± 0.03 km s^{-1} yr^{-1}. As discussed in Chapter 4, the accuracy of the radial accelerations of these stars may be impacted by the spectral variability of SiO masers. However, the accelerations are consistent with those found in the Chapter 4 even with two additional epochs of observations and our new method of estimating a systematic uncertainty to account for the spectral variability. In Section 5.6.1, we discuss one possible explanation of these accelerations, which is that the stars are in orbit about a binary center of mass and thus the galactocentric acceleration calculation is an underestimate of the real accelerations of the stars.

5.5.2 Galactic Center Mass Limits

In Figure 5.4, we present updated enclosed mass lower limits based on the 3D stellar velocities (see Chapter 4 for details). For IRS 7, IRS 12N, and IRS 10EE, we also plot the enclosed mass limit at the minimum distance for the star based on acceleration. In general, the new mass limits are not significantly different to those presented in Chapter 4, except for a couple of cases where the uncertainties in the proper motions were improved with the addition of the two new epochs. The largest outliers are the same stars identified in Chapter 4 as high velocity stars: SiO-25, SiO-16, and SiO-21. However, SiO-25 and SiO-16 were not detected in either ALMA 2021 or VLA 2022 and therefore the lower limits presented here are only distinct from the results of Chapter 4 due to changes in our proper motion fitting methods. SiO-21 has one additional epoch from ALMA 2021, and the proper motion is consistent with the result in Chapter 4.

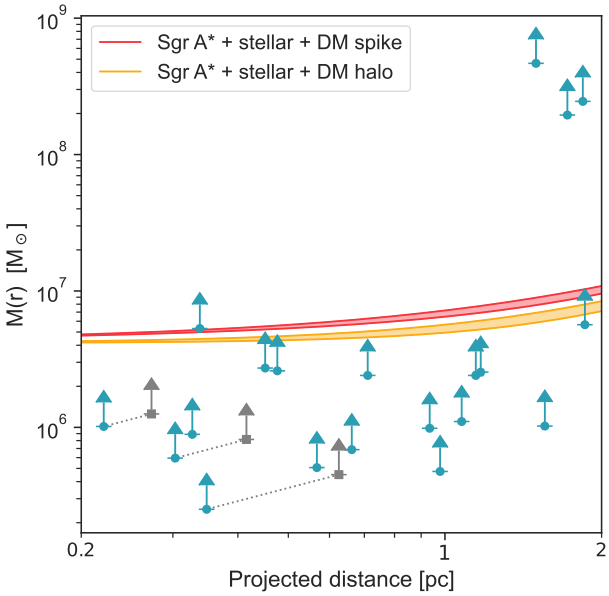

Figure 5.4: Lower limits on the enclosed mass at the projected distance of each maser derived from the 3D velocities (blue). In the case of three masers where an r_{min} was calculated using their acceleration limits, the enclosed mass lower limit at that r_{min} is also plotted (grey).

5.6 Discussion

5.6.1 Binaries and Anomalous Acceleration Measurements

In Section 5.3, we excluded 2D accelerations from proper accelerations for stars with < 15 years of astrometry due to the strong chance that outliers in the position time series would result in unrealistically large acceleration values. Additionally, we find several masers with significantly larger than expected radial acceleration measurements. However, these expectations are based purely on the acceleration of a star on a circular orbit about the GC. If a star in our sample were in a binary with an unseen companion, one would expect to observe astrometric and velocity outliers on shorter timescales than the trend due to the galactocentric orbits of these stars. Here we assess whether there is evidence that any of our high-acceleration stars are in binaries.

The acceleration of a star in a circular orbit about the binary's center of mass is given by

$$a_1 = G^{1/3} \left(\frac{2\pi}{P}\right)^{4/3} \frac{m_2}{(m_1 + m_2)^{2/3}}, \tag{5.4}$$

where P is the binary period, m_1 is the mass of the star, and m_2 is the mass of the companion.

The radius of the star's orbit about the center of mass will be

$$r_1 = G^{1/3} \left(\frac{P}{2\pi} \right)^{2/3} \frac{m_2}{(m_1 + m_2)^{2/3}}. \tag{5.5}$$

In each of the following case studies, we approximate a typical AGB mass of 3 $M_\odot$ and a companion with mass in the range of $1 - 10$ $M_\odot$.

SiO-14, IRS 15NE, and IRS 19NW have a radial accelerations of -0.483 ± 0.070 km s^{-1} yr^{-1}, 0.284 ± 0.072 km s^{-1} yr^{-1}, and 0.182 ± 0.060 km s^{-1} yr^{-1}. These accelerations, if caused by orbiting a binary center of mass with companion mass between $1 - 10$ $M_\odot$, would correspond to periods between approximately $40 - 130$ years, $60 - 190$ years, and $80 - 260$ years, respectively. The radii of the orbits about the center of mass would range from $5 - 47$ AU, $6 - 60$ AU, and $8 - 74$ AU. On the lower end, these radii are comparable to the size of the SiO maser emitting shell. On the higher end, the radii correspond to > 5 mas at a distance of 8.2 kpc, which would be resolvable with VLA and ALMA astrometry. The proper accelerations of these stars are not detected, but we would expect to see proper acceleration on the same timescale as the radial acceleration unless the orbit of the binary were edge on and nearly aligned with the direction of the proper motion of the system. We observe significant scatter about the proper motion trend, but for these to be caused by an astrometric binary would require periods on the order of 1 year as opposed to 100 years.

In the case of SiO-14, the radial velocity is approximately unchanged over the most recent three epochs. If the star were in a binary and recently passed the point in its orbit closest to the solar system, then a shift toward a less negative velocity may be observed in future observations. Using the observations presented here, however, we do not find sufficient evidence that the anomalously large radial accelerations are explained by binaries.

As listed in Table 5.2, we fit a statistically significant RA proper acceleration for IRS 14NE, which would correspond to approximately 25 km s^{-1} yr^{-1} acceleration along the RA coordinate direction. However, this measurement is based on only four data points, and we see no evidence for acceleration in the Dec or radial directions. A 25 km s^{-1} yr^{-1} acceleration would correspond to a binary period in the range of about $2 - 7$ years, so a more frequent cadence of observations

than presented here would be necessary to fit this hypothetical binary orbit.

We also note that IRS 10EE has been proposed to be in a binary system. Peeples et al. (2007) detected an X-ray source within $0.8''$ of IRS 10EE, and VLBA observations from Oyama et al. (2008) suggested that IRS 10EE is an astrometric binary with a black hole companion in a mass range of $13.1 - 16.2\ M_{\odot}$ based on apparently periodic deviations of the RA positions from the proper motion fit. They found a 5.65 ± 0.12 year orbit with semi-major and semi-minor axes diameters of 0.73 ± 0.41 mas and 0.35 ± 0.10 mas, respectively, by fitting binary orbital elements to their IRS 10EE astrometry. The largest significant residual of the RA proper motion fit presented here is about 0.6 mas to the west, so our astrometry is potentially consistent with this orbit. However, fitting the orbital elements of IRS 10EE would require a higher cadence of observations and therefore falls outside of the scope of this work.

In summary, our data do not present a conclusive case for binaries. The radial accelerations of SiO-14, IRS 15NE, and IRS 19NW may be consistent with binary star orbits, but we do not detect proper acceleration of these stars. An eccentric orbit could result in a small proper acceleration component, though, depending on the orientation of the orbit. The proper acceleration of IRS 14NE is more likely caused by insufficient data for an accurate fit, which is why this star and others with short time baselines do not have 2D acceleration measurements in Table 5.3. Finally, our data are roughly consistent with the proposed binary orbit of IRS 10EE (Oyama et al., 2008), but we do not find independent evidence that it is a binary.

5.6.2 Prospects for Future Maser Measurements

There are several notable limitations to the utility of the current maser observations for tracking stellar kinematics and studying the environment in the GC. These include the inherent spectral variability of SiO masers, the scatter seen in the maser astrometry over time, and the lack of known 3D distances of the stars. Here we discuss potential avenues to address these issues with future observations.

The accuracy of SiO maser spectra for measuring the instantaneous stellar velocity is depen-

dent on the distribution of SiO maser emission around the star, which is variable and unknown without VLBI observations which resolve the masers. However, AGB stars often also host OH masers at around 1612 MHz, which originate in the expanding circumstellar envelope. Stellar OH masers typically exhibit a characteristic double peaked spectral profile, where the strongest emission is originating directly in front of and behind the star along the line of sight (Reid et al. 1977; see also Habing 1996 for review). Thus the midpoint of the double peak feature is the systemic radial stellar velocity. By simultaneously detecting the OH and SiO masers, one may calibrate the SiO-based Doppler velocity measurements.

As discussed above, unseen binaries are a potential cause of both the spectral variations and astrometric scatter seen in the SiO masers time series, but it is outside of the scope of this work to confirm whether the most likely candidates are truly in binaries. We may also expect scatter in the astrometry due to the location of the strongest masers around the stars changing over time. At a distance of 8.2 kpc, a maser ring with diameter of 8 AU would correspond to approximately 1 mas. However, the maser astrometry frequently have significant outliers to the proper motion fits on the order of 10 mas or larger. We would expect to be able to partially resolve a maser ring of this angular size, but the sources in our sample are unresolved by both VLA and ALMA. VLBI observations which resolve the maser components could settle this issue and provide insight into the impact of maser variability on our measurements, but the advantage of relatively lower resolution observations from VLA and ALMA is to be able to simultaneously detect the entire sample of masers within 2 pc of Sgr A*.

Finally, the current analysis of the stellar kinematics is limited due to the unknown 3D distances of the stars from Sgr A*. As shown in Figure 5.4, the velocity-based enclosed mass limits are more constraining if one can better estimate a star's 3D distance using the acceleration measurements. More observations with VLA or ALMA will reduce acceleration uncertainties, especially if the above spectral and astrometric scatter issues are addressed, leading to better 3D distance estimates for a larger portion of the sample.

Another avenue to utilize the maser kinematics in the absence of full 3D distance estimates

would be to infer the underlying mass distribution using machine learning. Various methods to map the gravitational potential in the Milky Way with deep learning using large data sets of stellar kinematics, such as *Gaia*, have been developed (e.g. An et al. 2021; Green et al. 2023). Additionally, Nguyen et al. (2023) demonstrated that simulation-based inference and machine learning may accurately infer the dark matter profiles in dwarf galaxies using only projected distances and Doppler velocities of small samples of stars. In principle, similar methods could be applied to the 3D kinematics presented here to infer the mass density profile in the GC without measuring 3D distances of the stars.

5.7 Conclusions

In this chapter we have presented updated observations of the GC stellar SiO masers and refined 3D kinematics using new methods. 2D velocities and accelerations are measured with typically 10 km s^{-1} and 1 km s^{-1} yr^{-1} precision, respectively, but are as low as 0.6 km s^{-1} and 0.02 km s^{-1} yr^{-1} for stars in sample with the longest time baselines for astrometry. Radial velocities and accelerations are measured with 0.5 km s^{-1} and 0.1 km s^{-1} yr^{-1} precision. The radial velocity and acceleration fits include a conservative systematic uncertainty estimated from the variability of four different measurements of the 43 GHz spectra from March 2022.

We compared the stellar kinematics to models of the stellar and dark matter mass profiles in the GC. For IRS 7, IRS 12N, and IRS 10EE, their lack of acceleration detections translate to updated minimum distance estimates since the acceleration upper limits are lower than the what mass models predict. The accelerations of IRS 15NE, IRS 19NW, and SiO-14 are larger than expected for stars in orbit about the GC with at least 3σ significance. These accelerations may be caused by binary orbits, but we cannot conclusively constrain potential binary orbits with the current data and analysis.

We conclude that further observations are required to investigate the origins of these anomalous accelerations, and to resolve issues of spectral variability and astrometric scatter affecting the entire sample. These would include OH maser spectra measurements to calibrate the SiO maser

radial velocities, as well as continued high resolution astrometry and spectra of the SiO masers. Future observations will produce more precise accelerations, 3D distance estimates, and enclosed mass limits. In the near-term, the current kinematics may be reanalyzed using machine learning to infer the enclosed mass profile.

Acknowledgements

The authors acknowledge support from the NSF Graduate Research Fellowship Program under grant DGE-1650115 and the NSF grant AST-1908122. This paper makes use of the following ALMA data: ADS/JAO.ALMA#2019.1.00292.S. ALMA is a partnership of ESO (representing its member states), NSF (USA) and NINS (Japan), together with NRC (Canada), MOST and ASIAA (Taiwan), and KASI (Republic of Korea), in cooperation with the Republic of Chile. The Joint ALMA Observatory is operated by ESO, AUI/NRAO and NAOJ.

Software used in this research: Astropy (Astropy Collaboration et al., 2013, 2018, 2022), CASA (McMullin et al., 2007), numpy (Harris et al., 2020), matplotlib (Hunter, 2007), uvmultifit (Martí-Vidal et al., 2014)

Chapter 6

Conclusions

In Chapter 2, I created a catalog of over 500,000 mid-IR selected AGN in the first *Gaia* data release. Using these sources and their projected end-of-mission proper motion errors, I simulated the detection of the secular aberration drift dipole and the triaxial anisotropic expansion quadrupole. The former was predicted to be detectable with a high degree of significance (23σ). Since the publication of this chapter, the secular aberration drift has in fact been detected in *Gaia* DR3 proper motions of 1.2 million quasar-like sources (Gaia Collaboration et al., 2021b). The recovered dipole is 5.05 ± 0.35 μas yr^{-1}, corresponding to galactocentric acceleration of $(2.32 \pm 1.6) \times 10^{-10}$ m s^{-2}.

In Chapter 3, I presented a distinct sample of nearby galaxies in the *Gaia* catalog cross-matched with Cosmicflows-3. With this sample, I found the first observational limit on secular extragalactic parallax of 3500 μas yr^{-1} Mpc using *Gaia* DR2 (the already published result), and an improved limit of 980 μas yr^{-1} using *Gaia* DR3. The uncertainties on the new measurement are about a factor of 5 lower due to the increased sample size and more precise proper motion measurements of the latest data release. However, the current limits are potentially sensitive to large scale systematics in the *Gaia* astrometry as we find that the distance-independent dipole fits to the galaxy samples have consistent direction with the distance-dependent fits. A research note detailing the new result is in preparation to be submitted to the Research Notes of the AAS in 2023.

I also simulated end-of-mission proper motions of the *Gaia*-Cosmicflows galaxies under the

assumptions that the entire sample will have measured proper motions in the future, and that the precision will be similar to that of point sources. These simulations included the peculiar velocity field reconstructed from the Cosmicflows-3 catalog of line-of-sight peculiar velocities. I found that the peculiar velocity field offsets the direction and amplitude of the measured secular parallax dipole resulting in a 107 ± 12 μas yr^{-1} Mpc dipole toward ($195^\circ \pm 6^\circ$, $22^\circ \pm 7^\circ$) in RA and Dec, which is predicted to be detectable with $\sim 8\sigma$ significance.

Using the Cosmicflows peculiar velocity field, I investigated the simulated peculiar proper motions and their low-mulitpole correlated signals. The simulated peculiar proper motions are broadly consistent with predictions from LSS theory (Hall, 2019). However, the octopole power at relatively small distances is enhanced compared to theory predictions, which may be probing the deviation of the local matter power spectrum (i.e. due to the local super cluster) from cosmological simulations averaged over the universe. These simulated proper motions demonstrate how high precision extragalactic astrometry compliments work that is already underway mapping the local matter density. My simulations do not predict that *Gaia* will be able to detect the local peculiar proper motion field with fine enough distance binning to constrain these deviations from LSS theory. The peculiar motions also produce distance independent multipole signals that would be indistinguishable from 1% deviation from isotropic expansion and will likely dominate the E-modes of a primordial gravitational wave background.

These works forecasting *Gaia* extragalactic proper motions motivate further developments in the field of high precision extragalatic astrometry. For example, Ferree & Bunn (2022) predict that an optimal survey to measure H_0 would contain about 100 galaxies within a redshift range out to $z_{max} = 0.06$ and with individual proper motion uncertainties of about 0.5 μas yr^{-1}. The Vera C. Rubin Observatory's projected precision per object over a 10 year baseline is not this low (~ 1 mas yr^{-1} on the faint end; Ivezić et al. 2019), but it will detect objects 4 mag fainter than *Gaia* and will fit an extended source model to most sources. It will therefore most likely greatly enhance the proper motion measurements possible with the nearby sample of galaxies.

In Chapter 4, I presented five observations of stellar SiO masers in the GC using VLA and

ALMA, and used a novel approach to SiO maser astrometry of visibility fitting to achieve the highest precision measurements possible. Combined with extant maser astrometry, I measured 2D stellar maser kinematics with 0.5 km s^{-1} and 0.04 km s^{-1} yr^{-1} precision for velocities and accelerations, respectively. The radial velocities and accelerations are measured with 0.5 km s^{-1} and 0.1 km s^{-1} yr^{-1} precision, respectively. These measurements are the current benchmark for the published kinematics of these stars. By modeling the expected kinematics of stars in circular orbits about the GC, I identified several stars with anomalous velocity or acceleration measurements which are significantly higher than anticipated. I built upon this work in Chapter 5 with the inclusion of two additional epochs of observations, new methods for measuring proper motions and proper accelerations, and a more physically motivated estimate of the systematic uncertainty caused by spectral variability. The results of this work confirm several of the previously identified anomalous kinematic measurements.

Motivated by the persistent measurements of significantly larger than expected accelerations, I assessed the whether the underlying cause may be that the stars are in orbit about a binary center of mass. Assuming a relatively high mass companion, the observed radial accelerations correspond to binary orbital periods $\gtrsim$ 100 years, which are generally inconsistent with the lack of proper acceleration detections for these stars. However, immediate future work on this topic could include a more thorough investigation of the companion mass-period parameter space (i.e. the inferred orbital periods decrease for smaller companion mass). In the slightly longer-term, this work would benefit from continued observations on an approximately yearly basis — as we have done since 2020 — to constrain the possibility binary orbits with shorter periods.

The results of Chapters 4 and 5 demonstrate the applications of maser kinematics to probing the mass distribution on small scales in the GC. Many of the velocity-based enclosed mass lower limits are already approaching the expected masses at their projected distances. As the precision of the acceleration measurements improve, more accurate distance estimates will be possible for these stars which will increase the lower bound of the estimated mass range. In the near-term, I plan to implement a machine learning approach to infer the gravity profile, potentially borrowing

from methods developed for studies of dwarf galaxies using a small sample of stars. Even without the addition of 3D distance estimates, machine learning techniques may still extract estimates of the potential in the GC and therefore constrain the dark matter mass profile.

The primary limitation of SiO maser measurements of stellar kinematics is the confounding intrinsic maser variability. Unfortunately, without VLBI observations which resolve the maser emission, it is not possible to conclusively determine whether some of the outliers in the astrometric and velocity timeseries of these masers is due to changes in the maser structure. However, a promising avenue to calibrate this effect in the radial component is to simultaneously measure OH maser spectra from the same stars, which can be a more accurate estimate of the systemic stellar velocities. Such observations could be done with the VLA, and would not require observing in the most extended configuration if the goal is primarily to gather spectra. Another solution could be to simultaneously fit the maser spectra over time and model the acceleration of individual components, rather than measure a velocity via a centroid calculation for each spectrum independently. The feasibility of this technique depends on more measurements of the spectra so that one could fit each line independently.

Finally, it should be noted that many of the proper motion measurements explored in this dissertation work will benefit from the Next Generation Very Large Array (ngVLA), which will have 10 times the collecting area and 10 times better spatial resolution than the current VLA (Carilli et al., 2015). In terms of extragalactic proper motions, Bower et al. (2015) forecast that measurements of a sample of 10,000 sources with 10 μas yr^{-1} precision per object — which will be possible using ngVLA with VLBA baselines — will be sensitive to correlated proper motions down to ~ 0.1 μas yr^{-1}. If secular parallax can be disentangled from peculiar proper motions, this precision may enable parallax-based distance estimates out to about 8 Mpc. In terms of maser astrometry, ngVLA will operate from 1 – 115 GHz, detecting both the $J = 1 - 0$ and $J = 2 - 1$ transitions of SiO. The mas-resolution of ngVLA will be comparable to the size of the maser shell for stars in the GC, so utilizing the highest resolution capabilities may complicate the astrometry of stars with slightly resolved masers. The larger collecting area of ngVLA will enable fast detection

of fainter sources, increasing the maser sample size and thus improving mass profile mapping.

Bibliography

Abbott, B. P., Abbott, R., Abbott, T. D., et al. 2016, Phys. Rev. Lett., 116, 131102, doi: 10.1103/PhysRevLett.116.131102

Abbott, R., Abbott, T. D., Abraham, S., et al. 2021, Phys. Rev. D, 104, 022004, doi: 10.1103/PhysRevD.104.022004

Ahn, C. P., Alexandroff, R., Allende Prieto, C., et al. 2012, ApJS, 203, 21, doi: 10.1088/0067-0049/203/2/21

Alam, S., Albareti, F. D., Allende Prieto, C., et al. 2015, ApJS, 219, 12, doi: 10.1088/0067-0049/219/1/12

Amendola, L., Eggers Bjæ lde, O., Valkenburg, W., & Wong, Y. Y. Y. 2013, J. Cosmology Astropart. Phys., 2013, 042, doi: 10.1088/1475-7516/2013/12/042

An, J., Naik, A. P., Evans, N. W., & Burrage, C. 2021, MNRAS, 506, 5721, doi: 10.1093/mnras/stab2049

Angélil, R., & Saha, P. 2011, ApJ, 734, L19, doi: 10.1088/2041-8205/734/1/L19

Arzoumanian, Z., Baker, P. T., Blumer, H., et al. 2020, ApJ, 905, L34, doi: 10.3847/2041-8213/abd401

Assef, R. J., Stern, D., Kochanek, C. S., et al. 2013, ApJ, 772, 26, doi: 10.1088/0004-637X/772/1/26

Astropy Collaboration, Robitaille, T. P., Tollerud, E. J., et al. 2013, A&A, 558, A33, doi: 10.1051/0004-6361/201322068

Astropy Collaboration, Price-Whelan, A. M., Sipőcz, B. M., et al. 2018, AJ, 156, 123, doi: 10.3847/1538-3881/aabc4f

Astropy Collaboration, Price-Whelan, A. M., Lim, P. L., et al. 2022, ApJ, 935, 167, doi: 10.3847/1538-4357/ac7c74

Bachchan, R. K., Hobbs, D., & Lindegren, L. 2016, A&A, 589, A71, doi: 10.1051/0004-6361/201527935

Baumann, D., Jackson, M. G., Adshead, P., et al. 2009, in American Institute of Physics Conference Series, Vol. 1141, CMB Polarization Workshop: Theory and Foregrounds: CMBPol Mission Concept Study, ed. S. Dodelson, D. Baumann, A. Cooray, J. Dunkley, A. Fraisse, M. G. Jackson, A. Kogut, L. Krauss, M. Zaldarriaga, & K. Smith, 10–120, doi: 10.1063/1.3160885

Bengaly, C. A. P., J. 2016, J. Cosmology Astropart. Phys., 2016, 036, doi: 10.1088/1475-7516/2016/04/036

Biscoveanu, S., Talbot, C., Thrane, E., & Smith, R. 2020, Phys. Rev. Lett., 125, 241101, doi: 10.1103/PhysRevLett.125.241101

Boehle, A., Ghez, A. M., Schödel, R., et al. 2016, ApJ, 830, 17, doi: 10.3847/0004-637X/830/1/17

Book, L. G., & Flanagan, É. É. 2011, Phys. Rev. D, 83, 024024, doi: 10.1103/PhysRevD.83.024024

Borkar, A., Eckart, A., Straubmeier, C., et al. 2020, in Multifrequency Behaviour of High Energy Cosmic Sources - XIII. 3-8 June 2019. Palermo, 33, doi: 10.22323/1.362.0033

Bower, G. C., Demorest, P., Braatz, J., et al. 2015, arXiv e-prints, arXiv:1510.06432, doi: 10.48550/arXiv.1510.06432

Braginsky, V. B., Kardashev, N. S., Polnarev, A. G., & Novikov, I. D. 1990, Nuovo Cimento B Serie, 105, 1141, doi: 10.1007/BF02827323

Carilli, C. L., McKinnon, M., Ott, J., et al. 2015, arXiv e-prints, arXiv:1510.06438, doi: 10.48550/arXiv.1510.06438

Chang, Z., & Lin, H.-N. 2015, MNRAS, 446, 2952, doi: 10.1093/mnras/stu2349

Charlot, P., Jacobs, C. S., Gordon, D., et al. 2020, A&A, 644, A159, doi: 10.1051/0004-6361/202038368

Darling, J. 2014, MNRAS, 442, L66, doi: 10.1093/mnrasl/slu057

Darling, J., & Truebenbach, A. E. 2018, ApJ, 864, 37, doi: 10.3847/1538-4357/aad3d0

Darling, J., Truebenbach, A. E., & Paine, J. 2018, ApJ, 861, 113, doi: 10.3847/1538-4357/aac772

de Blok, W. J. G. 2010, Advances in Astronomy, 2010, 789293, doi: 10.1155/2010/789293

Di Valentino, E., Mena, O., Pan, S., et al. 2021, Classical and Quantum Gravity, 38, 153001, doi: 10.1088/1361-6382/ac086d

Ding, F., & Croft, R. A. C. 2009, MNRAS, 397, 1739, doi: 10.1111/j.1365-2966.2009.15111.x

Djorgovski, S., & Davis, M. 1987, ApJ, 313, 59, doi: 10.1086/164948

Do, T., Hees, A., Ghez, A., et al. 2019, Science, 365, 664, doi: 10.1126/science.aav8137

Doeleman, S. S., Weintroub, J., Rogers, A. E. E., et al. 2008, Nature, 455, 78, doi: 10.1038/nature07245

Dressler, A., Lynden-Bell, D., Burstein, D., et al. 1987, ApJ, 313, 42, doi: 10.1086/164947

Eisenhauer, F., Genzel, R., Alexander, T., et al. 2005, ApJ, 628, 246, doi: 10.1086/430667

Elitzur, M. 1992, Astronomical masers, Vol. 170, doi: 10.1007/978-94-011-2394-5

Ferree, N. C., & Bunn, E. F. 2022, MNRAS, 515, 4990, doi: 10.1093/mnras/stac1870

Fontanini, M., West, E. J., & Trodden, M. 2009, Phys. Rev. D, 80, 123515, doi: 10.1103/PhysRevD.80.123515

Gaia Collaboration, Prusti, T., de Bruijne, J. H. J., et al. 2016a, A&A, 595, A1, doi: 10.1051/0004-6361/201629272

Gaia Collaboration, Brown, A. G. A., Vallenari, A., et al. 2016b, A&A, 595, A2, doi: 10.1051/0004-6361/201629512

—. 2018a, A&A, 616, A1, doi: 10.1051/0004-6361/201833051

Gaia Collaboration, Mignard, F., Klioner, S. A., et al. 2018b, A&A, 616, A14, doi: 10.1051/0004-6361/201832916

Gaia Collaboration, Brown, A. G. A., Vallenari, A., et al. 2021a, A&A, 649, A1, doi: 10.1051/0004-6361/202039657

Gaia Collaboration, Klioner, S. A., Mignard, F., et al. 2021b, A&A, 649, A9, doi: 10.1051/0004-6361/202039734

Gaia Collaboration, Klioner, S. A., Lindegren, L., et al. 2022a, A&A, 667, A148, doi: 10.1051/0004-6361/202243483

Gaia Collaboration, Vallenari, A., Brown, A. G. A., et al. 2022b, arXiv e-prints, arXiv:2208.00211, doi: 10.48550/arXiv.2208.00211

Gaia Collaboration, Bailer-Jones, C. A. L., Teyssier, D., et al. 2022c, arXiv e-prints, arXiv:2206.05681, doi: 10.48550/arXiv.2206.05681

Genzel, R., Eisenhauer, F., & Gillessen, S. 2010, Reviews of Modern Physics, 82, 3121, doi: 10.1103/RevModPhys.82.3121

Ghez, A. M., Morris, M., Becklin, E. E., Tanner, A., & Kremenek, T. 2000, Nature, 407, 349, doi: 10.1038/35030032

Ghez, A. M., Salim, S., Hornstein, S. D., et al. 2005, ApJ, 620, 744, doi: 10.1086/427175

Ghez, A. M., Salim, S., Weinberg, N. N., et al. 2008, ApJ, 689, 1044, doi: 10.1086/592738

Gnedin, O. Y., & Primack, J. R. 2004, Phys. Rev. Lett., 93, 061302, doi: 10.1103/PhysRevLett.93.061302

Gondolo, P., & Silk, J. 1999, Phys. Rev. Lett., 83, 1719, doi: 10.1103/PhysRevLett.83.1719

Gonidakis, I., Diamond, P. J., & Kemball, A. J. 2010, MNRAS, 406, 395, doi: 10.1111/j.1365-2966.2010.16716.x

—. 2013, MNRAS, 433, 3133, doi: 10.1093/mnras/stt954

GRAVITY Collaboration, Abuter, R., Amorim, A., et al. 2018, A&A, 615, L15, doi: 10.1051/0004-6361/201833718

—. 2019, A&A, 625, L10, doi: 10.1051/0004-6361/201935656

—. 2020, A&A, 636, L5, doi: 10.1051/0004-6361/202037813

—. 2021, A&A, 647, A59, doi: 10.1051/0004-6361/202040208

Graziani, R., Courtois, H. M., Lavaux, G., et al. 2019, MNRAS, 488, 5438, doi: 10.1093/mnras/stz078

Green, G. M., Ting, Y.-S., & Kamdar, H. 2023, ApJ, 942, 26, doi: 10.3847/1538-4357/aca3a7

Gwinn, C. R., Eubanks, T. M., Pyne, T., Birkinshaw, M., & Matsakis, D. N. 1997, ApJ, 485, 87, doi: 10.1086/304424

Habibi, M., Gillessen, S., Pfuhl, O., et al. 2019, ApJ, 872, L15, doi: 10.3847/2041-8213/ab03cf

Habing, H. J. 1996, A&A Rev., 7, 97, doi: 10.1007/PL00013287

Hall, A. 2019, MNRAS, 486, 145, doi: 10.1093/mnras/stz648

Harris, C. R., Millman, K. J., van der Walt, S. J., et al. 2020, Nature, 585, 357, doi: 10.1038/s41586-020-2649-2

Hinshaw, G., Weiland, J. L., Hill, R. S., et al. 2009, ApJS, 180, 225, doi: 10.1088/0067-0049/180/2/225

Hogg, D. W. 1999, arXiv e-prints, astro, doi: 10.48550/arXiv.astro-ph/9905116

Hunter, J. D. 2007, Computing in Science and Engineering, 9, 90, doi: 10.1109/MCSE.2007.55

Ivezić, Ž., Kahn, S. M., Tyson, J. A., et al. 2019, ApJ, 873, 111, doi: 10.3847/1538-4357/ab042c

Jackson, T., Ivezić, Ž., & Knapp, G. R. 2002, MNRAS, 337, 749, doi: 10.1046/j.1365-8711.2002.05980.x

Jewell, P. R., Snyder, L. E., Walmsley, C. M., Wilson, T. L., & Gensheimer, P. D. 1991, A&A, 242, 211

Kardashev, N. S. 1986, AZh, 63, 845

Kemball, A. J. 2007, in Astrophysical Masers and their Environments, ed. J. M. Chapman & W. A. Baan, Vol. 242, 236–245, doi: 10.1017/S1743921307013063

Kirkpatrick, J. D., Cushing, M. C., Gelino, C. R., et al. 2011, ApJS, 197, 19, doi: 10.1088/0067-0049/197/2/19

Kovalevsky, J. 2003, A&A, 404, 743, doi: 10.1051/0004-6361:20030560

Lacroix, T. 2018, A&A, 619, A46, doi: 10.1051/0004-6361/201832652

Leung, H. W., Bovy, J., Mackereth, J. T., et al. 2023, MNRAS, 519, 948, doi: 10.1093/mnras/stac3529

Lewis, G. F., & Ibata, R. A. 1998, ApJ, 501, 478, doi: 10.1086/305860

Li, J., An, T., Shen, Z.-Q., & Miyazaki, A. 2010, ApJ, 720, L56, doi: 10.1088/2041-8205/720/1/L56

Lindegren, L., Hernández, J., Bombrun, A., et al. 2018, A&A, 616, A2, doi: 10.1051/0004-6361/201832727

Lindegren, L., Klioner, S. A., Hernández, J., et al. 2021, A&A, 649, A2, doi: 10.1051/0004-6361/202039709

Mainzer, A., Bauer, J., Grav, T., et al. 2011, ApJ, 731, 53, doi: 10.1088/0004-637X/731/1/53

Marrese, P. M., Marinoni, S., Fabrizio, M., & Giuffrida, G. 2017, A&A, 607, A105, doi: 10.1051/0004-6361/201730965

Martí-Vidal, I., Pérez-Torres, M. A., & Lobanov, A. P. 2012, A&A, 541, A135, doi: 10.1051/0004-6361/201118334

Martí-Vidal, I., Vlemmings, W. H. T., Muller, S., & Casey, S. 2014, A&A, 563, A136, doi: 10.1051/0004-6361/201322633

Mateos, S., Alonso-Herrero, A., Carrera, F. J., et al. 2012, MNRAS, 426, 3271, doi: 10.1111/j.1365-2966.2012.21843.x

McMillan, P. J. 2017, MNRAS, 465, 76, doi: 10.1093/mnras/stw2759

McMullin, J. P., Waters, B., Schiebel, D., Young, W., & Golap, K. 2007, in Astronomical Society of the Pacific Conference Series, Vol. 376, Astronomical Data Analysis Software and Systems XVI, ed. R. A. Shaw, F. Hill, & D. J. Bell, 127

Menten, K. M., Reid, M. J., Eckart, A., & Genzel, R. 1997, ApJ, 475, L111, doi: 10.1086/310472

Merritt, D. 2004, Phys. Rev. Lett., 92, 201304, doi: 10.1103/PhysRevLett.92.201304

Mignard, F. 2012, Mem. Soc. Astron. Italiana, 83, 918

Mignard, F., & Klioner, S. 2012, A&A, 547, A59, doi: 10.1051/0004-6361/201219927

Nguyen, T., Mishra-Sharma, S., Williams, R., & Necib, L. 2023, Phys. Rev. D, 107, 043015, doi: 10.1103/PhysRevD.107.043015

Nikutta, R., Hunt-Walker, N., Nenkova, M., Ivezić, Ž., & Elitzur, M. 2014, MNRAS, 442, 3361, doi: 10.1093/mnras/stu1087

Nusser, A., Branchini, E., & Davis, M. 2012, ApJ, 755, 58, doi: 10.1088/0004-637X/755/1/58

Oyama, T., Miyoshi, M., Deguchi, S., Imai, H., & Shen, Z.-Q. 2008, PASJ, 60, 11, doi: 10.1093/pasj/60.1.11

Padovani, P., Alexander, D. M., Assef, R. J., et al. 2017, A&A Rev., 25, 2, doi: 10.1007/s00159-017-0102-9

Paine, J., & Darling, J. 2022, ApJ, 927, 181, doi: 10.3847/1538-4357/ac3a87

Paine, J., Darling, J., & Truebenbach, A. 2018, ApJS, 236, 37, doi: 10.3847/1538-4365/aabe2d

Pardo, J. R., Alcolea, J., Bujarrabal, V., et al. 2004, A&A, 424, 145, doi: 10.1051/0004-6361:20040309

Pâris, I., Petitjean, P., Ross, N. P., et al. 2017, A&A, 597, A79, doi: 10.1051/0004-6361/201527999

Pearson, T. J. 1995, in Astronomical Society of the Pacific Conference Series, Vol. 82, Very Long Baseline Interferometry and the VLBA, ed. J. A. Zensus, P. J. Diamond, & P. J. Napier, 267

Peeples, M. S., Stanek, K. Z., & Depoy, D. L. 2007, Acta Astron., 57, 173, doi: 10.48550/arXiv.astro-ph/0703769

Percival, W. J., & White, M. 2009, MNRAS, 393, 297, doi: 10.1111/j.1365-2966.2008.14211.x

Pesce, D. W., Braatz, J. A., Reid, M. J., et al. 2020, ApJ, 890, 118, doi: 10.3847/1538-4357/ab6bcd

Planck Collaboration, Ade, P. A. R., Aghanim, N., et al. 2016, A&A, 594, A16, doi: 10.1051/0004-6361/201526681

Planck Collaboration, Aghanim, N., Akrami, Y., et al. 2018, A&A, 617, A48, doi: 10.1051/0004-6361/201731489

Planck Collaboration, Akrami, Y., Ashdown, M., et al. 2020, A&A, 641, A7, doi: 10.1051/0004-6361/201935201

Plewa, P. M., Gillessen, S., Eisenhauer, F., et al. 2015, MNRAS, 453, 3234, doi: 10.1093/mnras/stv1910

Popović, L. Č., Jovanović, P., Stalevski, M., et al. 2012, A&A, 538, A107, doi: 10.1051/0004-6361/201117245

Popović, L. Č., & Simić, S. 2013, MNRAS, 432, 848, doi: 10.1093/mnras/stt498

Quercellini, C., Cabella, P., Amendola, L., Quartin, M., & Balbi, A. 2009, Phys. Rev. D, 80, 063527, doi: 10.1103/PhysRevD.80.063527

Reid, M. J. 2002, in Cosmic Masers: From Proto-Stars to Black Holes, ed. V. Migenes & M. J. Reid, Vol. 206, 506

Reid, M. J., Braatz, J. A., Condon, J. J., et al. 2013, ApJ, 767, 154, doi: 10.1088/0004-637X/767/2/154

Reid, M. J., Menten, K. M., Genzel, R., et al. 2003, ApJ, 587, 208, doi: 10.1086/368074

Reid, M. J., Menten, K. M., Trippe, S., Ott, T., & Genzel, R. 2007, ApJ, 659, 378, doi: 10.1086/511744

Reid, M. J., Muhleman, D. O., Moran, J. M., Johnston, K. J., & Schwartz, P. R. 1977, ApJ, 214, 60, doi: 10.1086/155230

Reid, M. J., Menten, K. M., Brunthaler, A., et al. 2014, ApJ, 783, 130, doi: 10.1088/0004-637X/783/2/130

—. 2019, ApJ, 885, 131, doi: 10.3847/1538-4357/ab4a11

Robin, A. C., Luri, X., Reylé, C., et al. 2012, A&A, 543, A100, doi: 10.1051/0004-6361/201118646

Sakai, S., Lu, J. R., Ghez, A., et al. 2019, ApJ, 873, 65, doi: 10.3847/1538-4357/ab0361

Schödel, R., Gallego-Cano, E., Dong, H., et al. 2018, A&A, 609, A27, doi: 10.1051/0004-6361/201730452

Schödel, R., Ott, T., Genzel, R., et al. 2002, Nature, 419, 694, doi: 10.1038/nature01121

Secrest, N. J., Dudik, R. P., Dorland, B. N., et al. 2015, ApJS, 221, 12, doi: 10.1088/0067-0049/221/1/12

Shapiro, S. L., & Heggie, D. C. 2022, Phys. Rev. D, 106, 043018, doi: 10.1103/PhysRevD.106.043018

Souchay, J., Andrei, A. H., Barache, C., et al. 2015, A&A, 583, A75, doi: 10.1051/0004-6361/201526092

Stern, D., Eisenhardt, P., Gorjian, V., et al. 2005, ApJ, 631, 163, doi: 10.1086/432523

Stern, D., Assef, R. J., Benford, D. J., et al. 2012, ApJ, 753, 30, doi: 10.1088/0004-637X/753/1/30

Taylor, M. B. 2005, in Astronomical Society of the Pacific Conference Series, Vol. 347, Astronomical Data Analysis Software and Systems XIV, ed. P. Shopbell, M. Britton, & R. Ebert, 29

Taylor, M. B. 2006, in Astronomical Society of the Pacific Conference Series, Vol. 351, Astronomical Data Analysis Software and Systems XV, ed. C. Gabriel, C. Arviset, D. Ponz, & S. Enrique, 666

Thompson, A. R., Moran, J. M., & Swenson, George W., J. 2017, Interferometry and Synthesis in Radio Astronomy, 3rd Edition, doi: 10.1007/978-3-319-44431-4

Titov, O., & Lambert, S. 2013, A&A, 559, A95, doi: 10.1051/0004-6361/201321806

Titov, O., Lambert, S. B., & Gontier, A. M. 2011, A&A, 529, A91, doi: 10.1051/0004-6361/201015718

Treyer, M., & Wambsganss, J. 2004, A&A, 416, 19, doi: 10.1051/0004-6361:20034284

Trippe, S., Gillessen, S., Gerhard, O. E., et al. 2008, A&A, 492, 419, doi: 10.1051/0004-6361:200810191

Truebenbach, A. E., & Darling, J. 2017a, MNRAS, 468, 196, doi: 10.1093/mnras/stx456

—. 2017b, ApJS, 233, 3, doi: 10.3847/1538-4365/aa9026

—. 2018, ApJ, 868, 69, doi: 10.3847/1538-4357/aae830

Tully, R. B., Courtois, H. M., & Sorce, J. G. 2016, AJ, 152, 50, doi: 10.3847/0004-6256/152/2/50

Tully, R. B., & Fisher, J. R. 1977, A&A, 54, 661

Véron-Cetty, M. P., & Véron, P. 2010, A&A, 518, A10, doi: 10.1051/0004-6361/201014188

Virtanen, P., Gommers, R., Oliphant, T. E., et al. 2020, Nature Methods, 17, 261, doi: 10.1038/s41592-019-0686-2

Williams, L. L. R., & Saha, P. 1995, AJ, 110, 1471, doi: 10.1086/117620

Wright, E. L., Eisenhardt, P. R. M., Mainzer, A. K., et al. 2010, AJ, 140, 1868, doi: 10.1088/0004-6256/140/6/1868

Xu, M. H., Wang, G. L., & Zhao, M. 2012, A&A, 544, A135, doi: 10.1051/0004-6361/201219593

Yelda, S., Lu, J. R., Ghez, A. M., et al. 2010, ApJ, 725, 331, doi: 10.1088/0004-637X/725/1/331

Appendix A

Gaia-WISE Catalog

Table A.1 lists the first ten rows of the *Gaia-WISE* extragalactic catalog. The full catalog containing 567,721 objects is available as a machine-readable table online and at `http://vizier.u-strasbg.fr/vizier/`.

Table **A.1**: *Gaia*-*WISE* Extragalactic Catalog

Gaia ID	RA J2000 (degrees)	σ_{RA} (mas)	Dec J2000 (degrees)	σ_{Dec} (mas)	G (mag)	*ALLWISE* ID	$W1$ (mag)	σ_{W1} (mag)	$W2$ (mag)	σ_{W2} (mag)	$W3$ (mag)	σ_{W3} (mag)	Redshift	Proper Motion Uncertainties[a] $\sigma_{\mu,RA}$ (μas yr^{-1})	Proper Motion Uncertainties[a] $\sigma_{\mu,Dec}$ (μas yr^{-1})
4990063153917291776	0.00026196	0.4	-47.64309208	0.4	18.637	J000000.06-473835.1	14.086	0.027	13.233	0.028	9.987	0.048		81	81
2875546163053982464	0.00062956	2.6	35.51784342	1.0	18.537	J000000.15+ 353104.1	14.522	0.030	13.372	0.031	10.663	0.102		108	108
2341836724939897216	0.00066058	0.3	-20.07434420	0.3	17.910	J000000.15-200427.7	13.548	0.026	12.539	0.025	9.727	0.053		85	85
4635686437412067840	0.00102928	1.2	-78.53449449	1.4	20.226	J000000.23-783204.1	15.212	0.031	13.694	0.028	10.388	0.055		336	336
2305851255551067776	0.00142474	3.9	-41.49299774	0.6	18.597	J000000.33-412934.9	15.083	0.033	13.881	0.035	10.396	0.060		93	93
2747188660230483712	0.00191760	0.4	9.38565564	0.2	18.234	J000000.46+ 092308.2	15.316	0.042	14.019	0.044	10.518	0.108		113	113
2420718231737082368	0.00308067	1.2	-13.95693841	1.0	19.833	J000000.73-135724.8	15.894	0.053	14.556	0.058	11.170	0.147		371	371
2341416058663072000	0.00345683	0.4	-21.29793756	0.4	18.551	J000000.82-211752.5	14.668	0.031	13.405	0.032	10.934	0.130		132	132
2744944385199380480	0.00408179	1.3	4.82979136	0.4	19.661	J000000.98+ 044947.1	15.503	0.044	13.987	0.044	10.764	0.112	1.62	338	338
2746747137592463872	0.00424303	1.8	8.07294561	0.7	20.003	J000001.02+ 080422.6	15.332	0.042	14.160	0.045	11.118	0.171		441	441

[a] *Gaia* expected end-of-mission proper motion uncertainty (see Section **2.3.5**).

Appendix B

Gaia DR2-Cosmicflows Galaxies

Galaxies in the *Gaia*-Cosmicflows crossmatch were each visually inspected for features that would indicate a poor *Gaia* fit, as discussed in Section 3.3.1.1. Figure B.1 shows images of the 232 galaxies used for the parallax limit in Section 3.3.2. SDSS g-band images are shown where available, otherwise the images are DSS2 red-band. Several galaxies are located near the edge of the SDSS plate, in which case we reviewed additional images in the literature, but we display the truncated SDSS images in Figure B.1

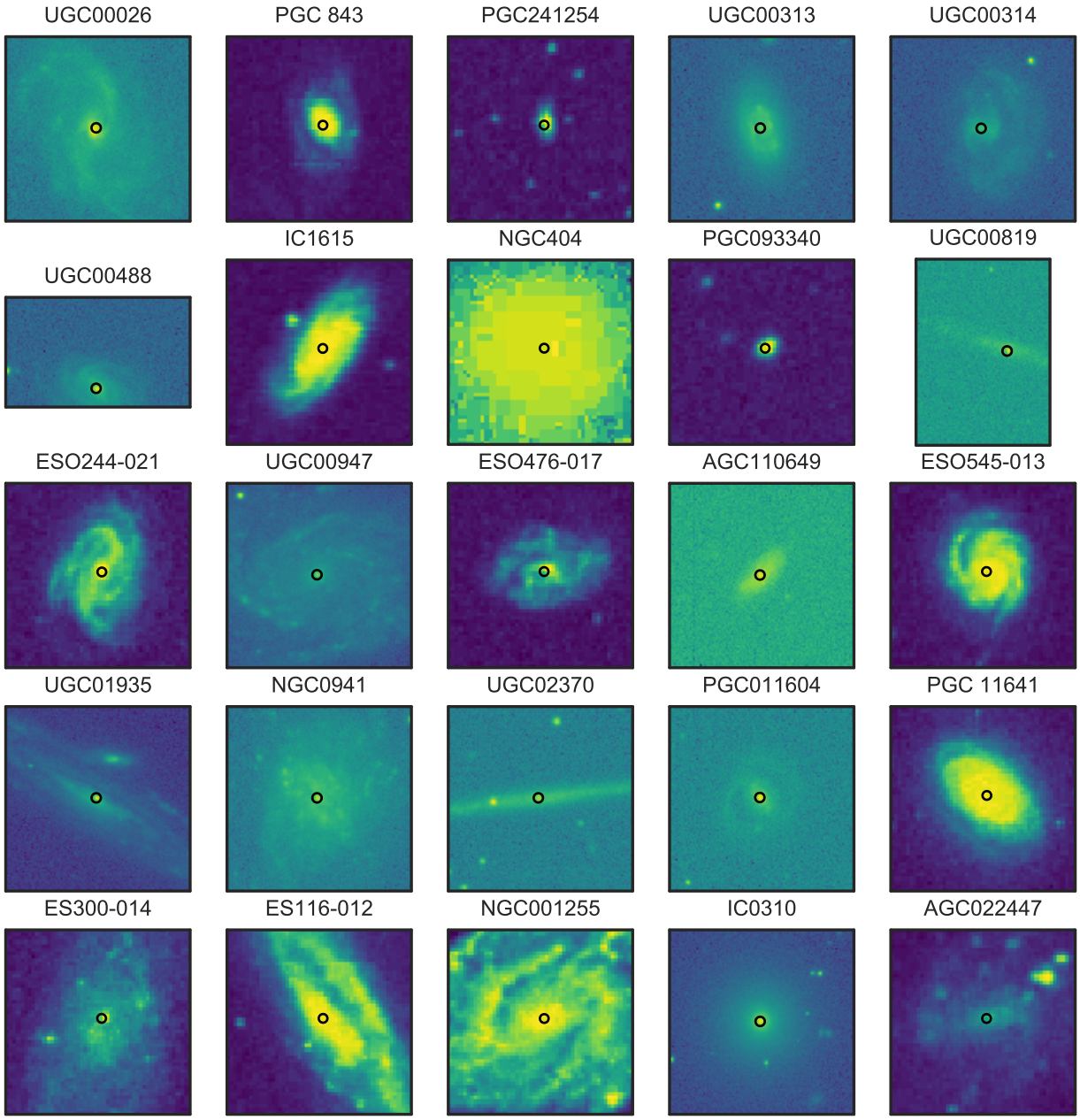

Figure B.1: SDSS g-band or DSS2 red-band imaging for galaxies selected to attempt detection of the secular parallax dipole.

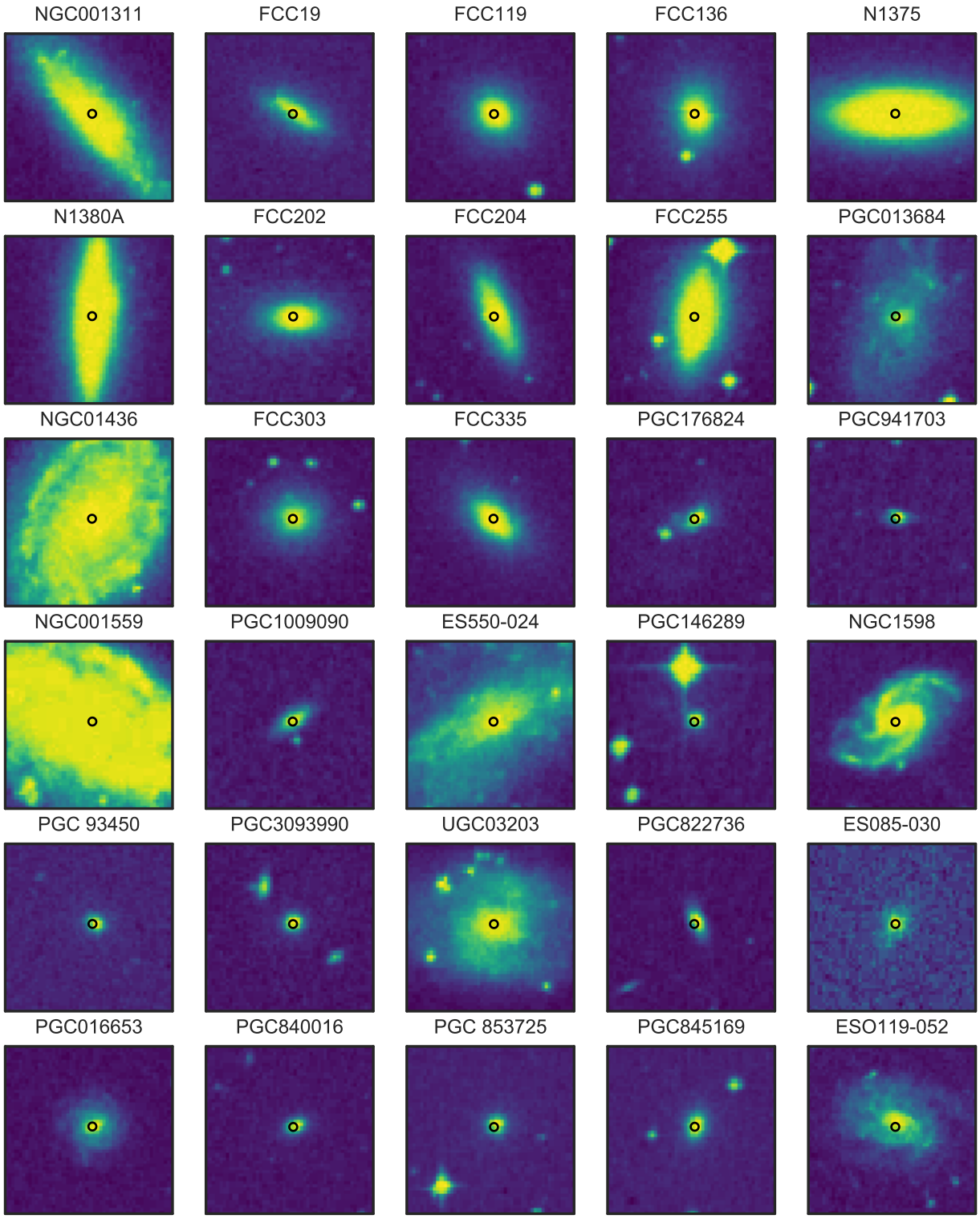
NGC001311
FCC19
FCC119
FCC136
N1375
N1380A
FCC202
FCC204
FCC255
PGC013684
NGC01436
FCC303
FCC335
PGC176824
PGC941703
NGC001559
PGC1009090
ES550-024
PGC146289
NGC1598
PGC 93450
PGC3093990
UGC03203
PGC822736
ES085-030
PGC016653
PGC840016
PGC 853725
PGC845169
ESO119-052

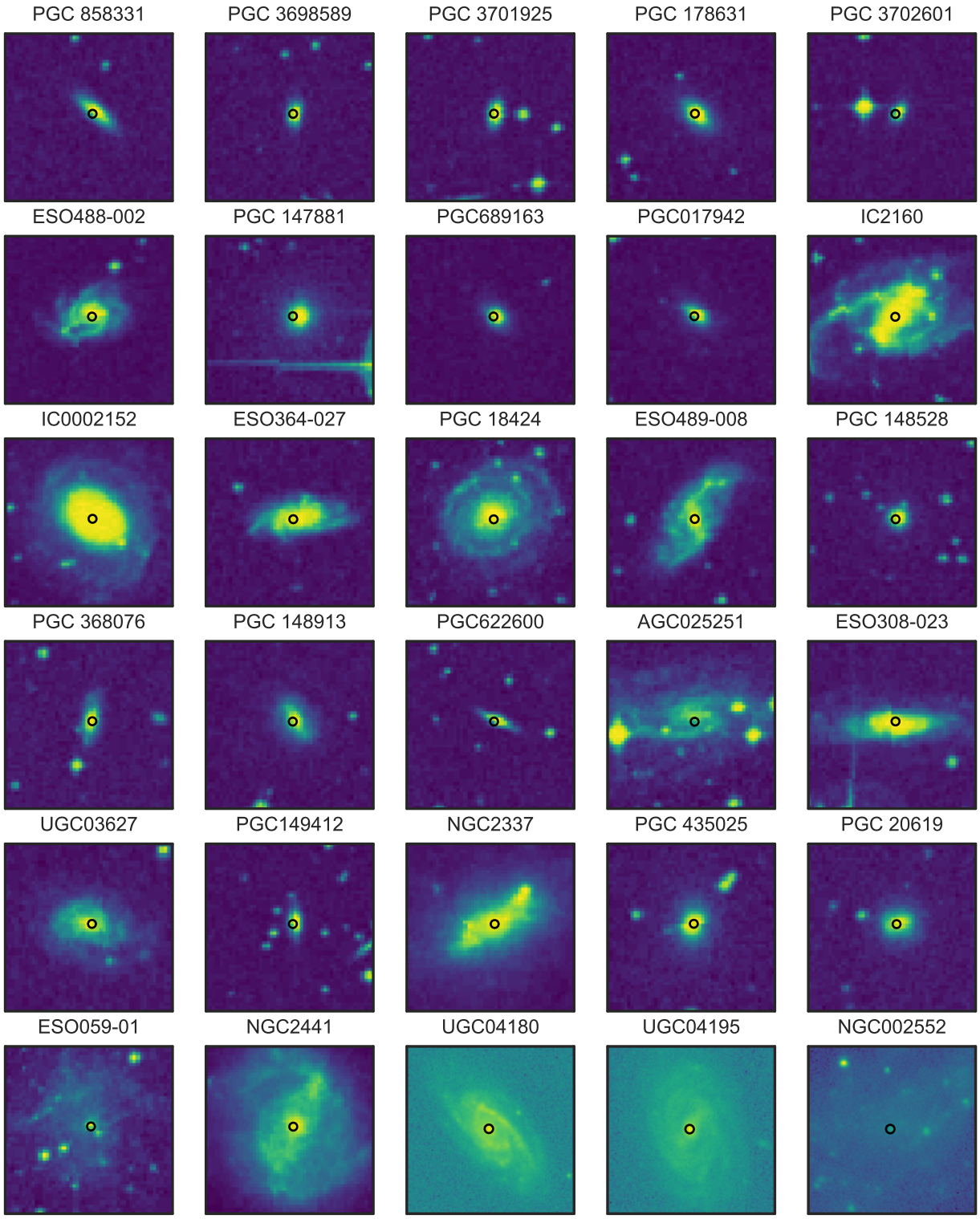
PGC 858331
PGC 3698589
PGC 3701925
PGC 178631
PGC 3702601
ESO488-002
PGC 147881
PGC689163
PGC017942
IC2160
IC0002152
ESO364-027
PGC 18424
ESO489-008
PGC 148528
PGC 368076
PGC 148913
PGC622600
AGC025251
ESO308-023
UGC03627
PGC149412
NGC2337
PGC 435025
PGC 20619
ESO059-01
NGC2441
UGC04180
UGC04195
NGC002552

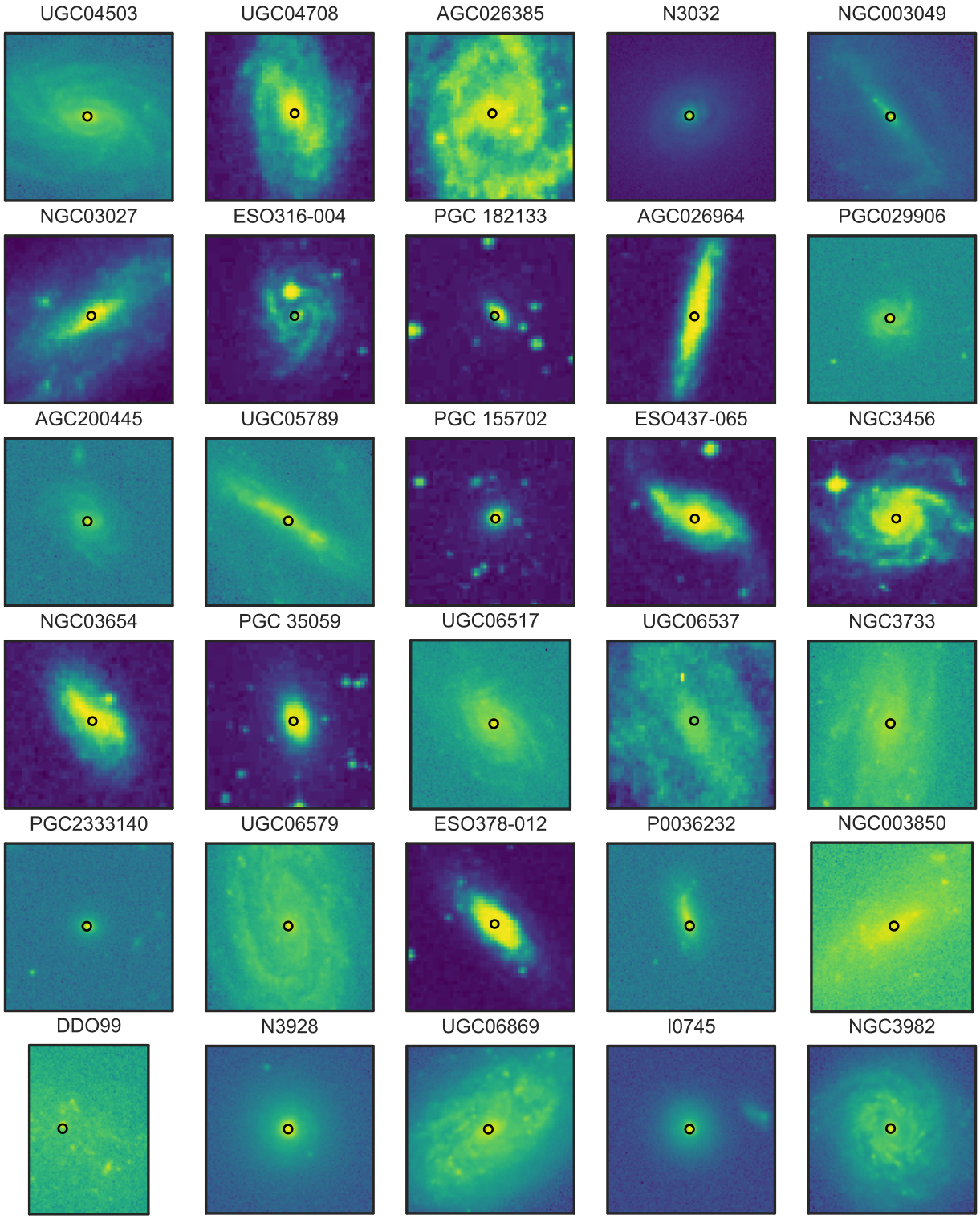
UGC04503
UGC04708
AGC026385
N3032
NGC003049
NGC03027
ESO316-004
PGC 182133
AGC026964
PGC029906
AGC200445
UGC05789
PGC 155702
ESO437-065
NGC3456
NGC03654
PGC 35059
UGC06517
UGC06537
NGC3733
PGC2333140
UGC06579
ESO378-012
P0036232
NGC003850
DDO99
N3928
UGC06869
I0745
NGC3982

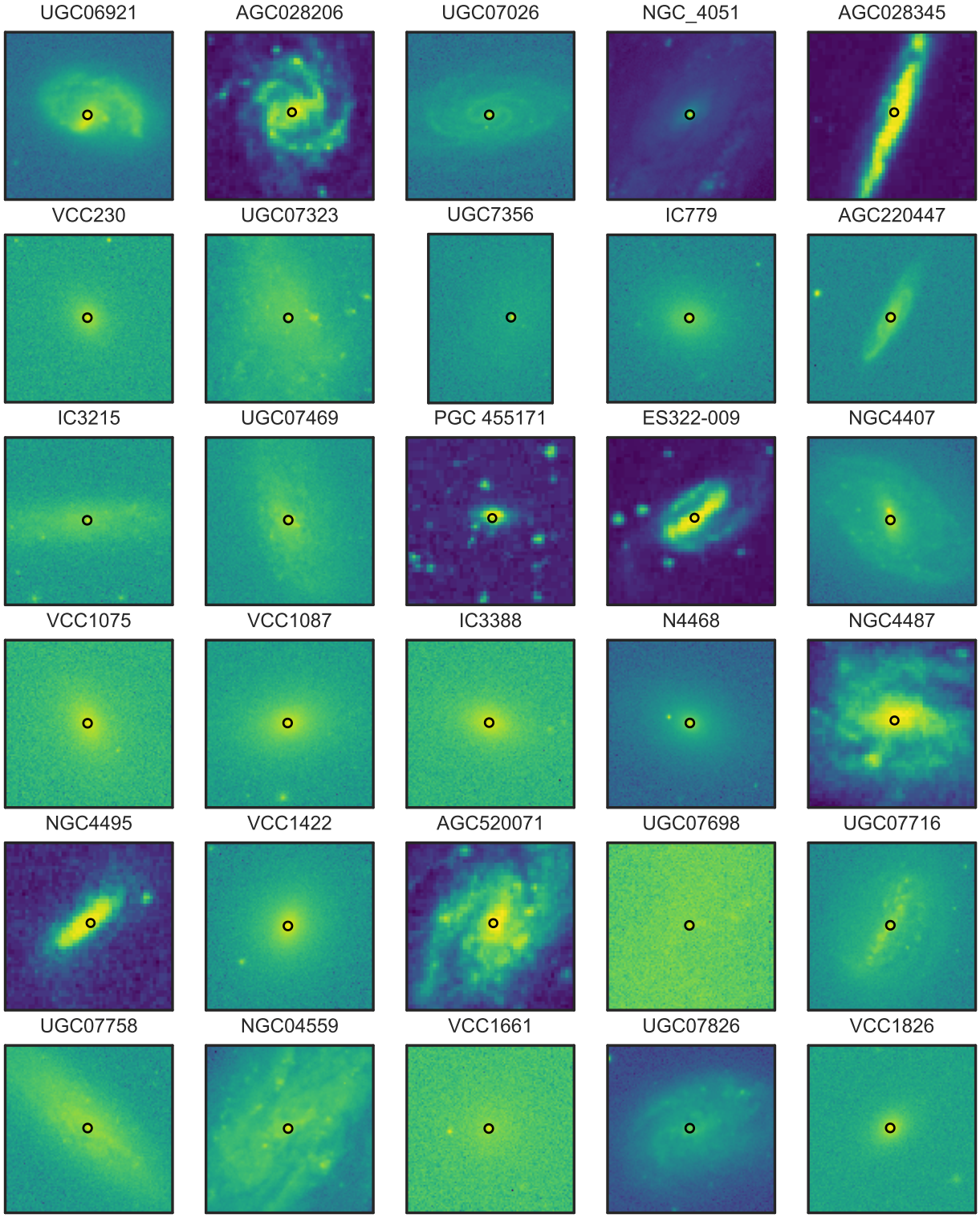
UGC06921
AGC028206
UGC07026
NGC_4051
AGC028345
VCC230
UGC07323
UGC7356
IC779
AGC220447
IC3215
UGC07469
PGC 455171
ES322-009
NGC4407
VCC1075
VCC1087
IC3388
N4468
NGC4487
NGC4495
VCC1422
AGC520071
UGC07698
UGC07716
UGC07758
NGC04559
VCC1661
UGC07826
VCC1826

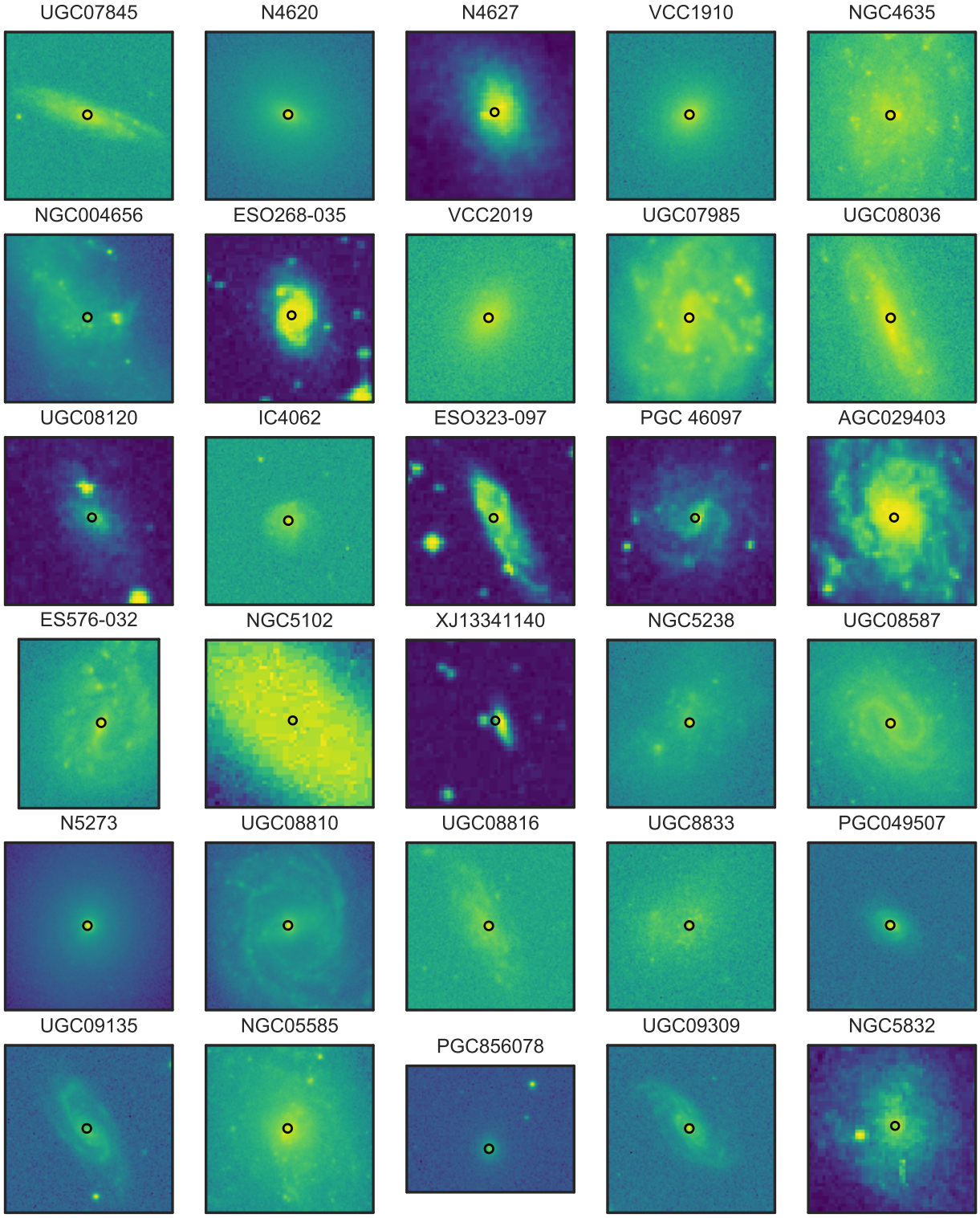
UGC07845
N4620
N4627
VCC1910
NGC4635
NGC004656
ESO268-035
VCC2019
UGC07985
UGC08036
UGC08120
IC4062
ESO323-097
PGC 46097
AGC029403
ES576-032
NGC5102
XJ13341140
NGC5238
UGC08587
N5273
UGC08810
UGC08816
UGC8833
PGC049507
UGC09135
NGC05585
PGC856078
UGC09309
NGC5832

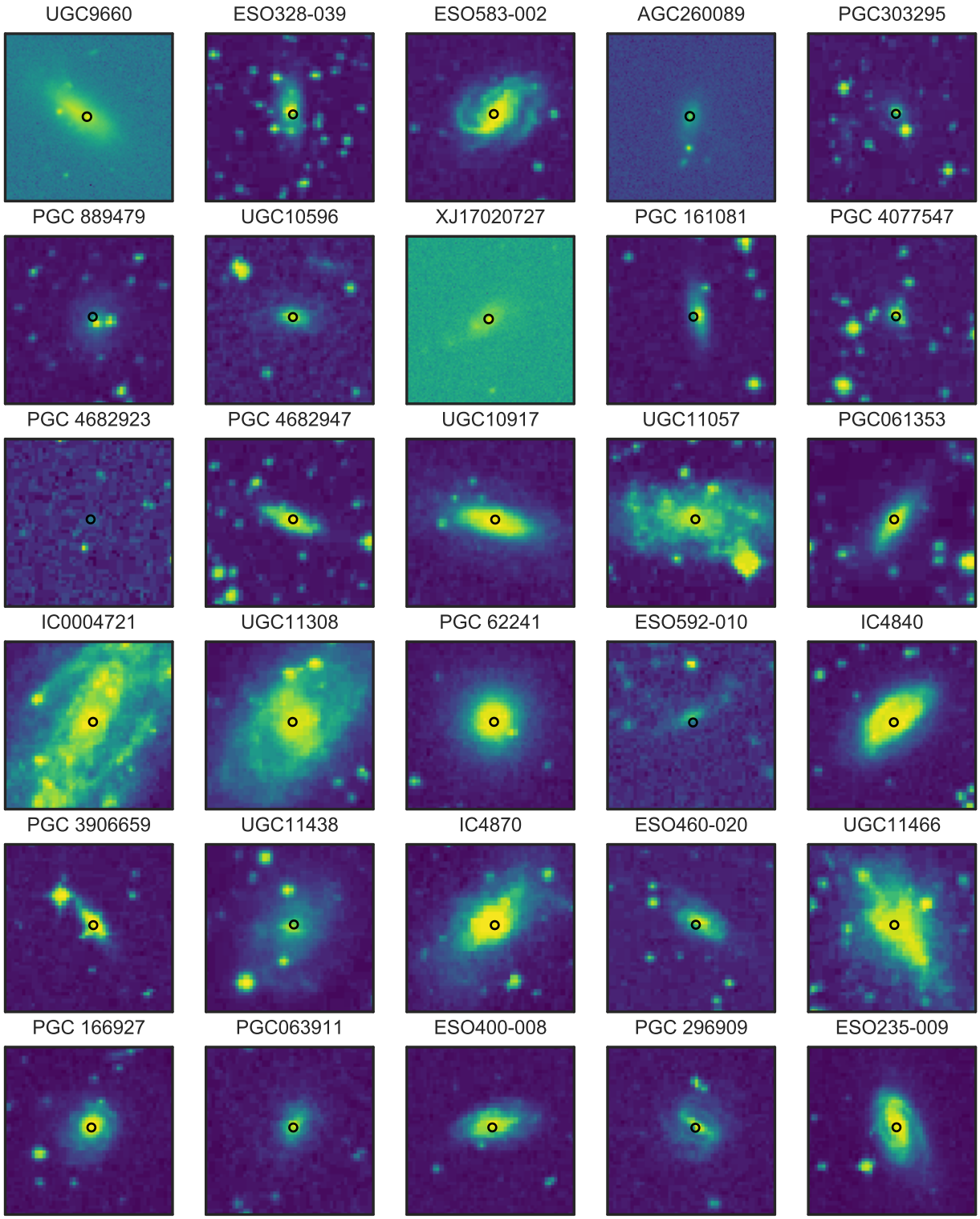
UGC9660
ESO328-039
ESO583-002
AGC260089
PGC303295
PGC 889479
UGC10596
XJ17020727
PGC 161081
PGC 4077547
PGC 4682923
PGC 4682947
UGC10917
UGC11057
PGC061353
IC0004721
UGC11308
PGC 62241
ESO592-010
IC4840
PGC 3906659
UGC11438
IC4870
ESO460-020
UGC11466
PGC 166927
PGC063911
ESO400-008
PGC 296909
ESO235-009

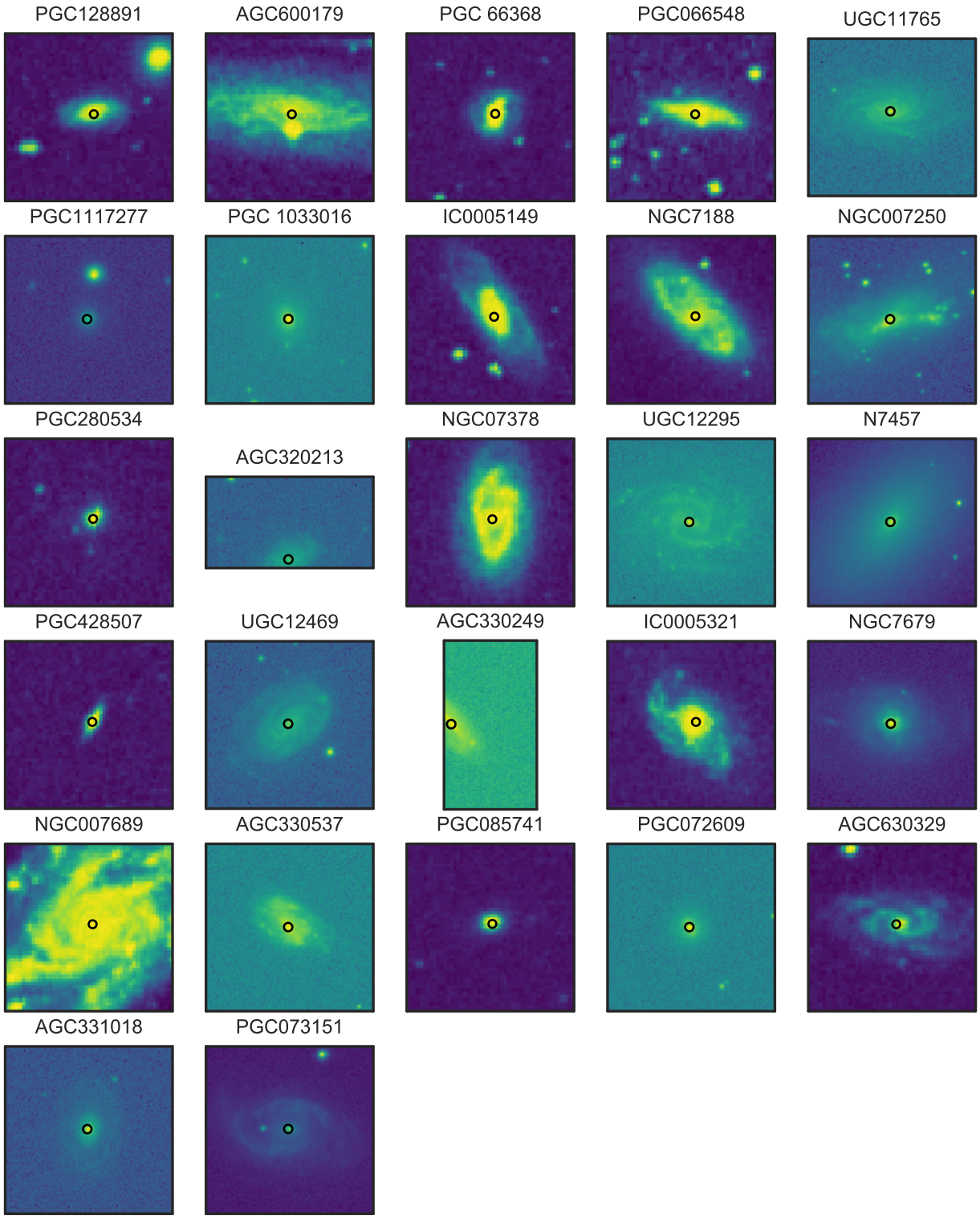
PGC128891
AGC600179
PGC 66368
PGC066548
UGC11765
PGC1117277
PGC 1033016
IC0005149
NGC7188
NGC007250
PGC280534
NGC07378
UGC12295
N7457
AGC320213
PGC428507
UGC12469
AGC330249
IC0005321
NGC7679
NGC007689
AGC330537
PGC085741
PGC072609
AGC630329
AGC331018
PGC073151

Appendix C

SiO maser spectra and Doppler fits

Figure C.1 shows maser spectra and radial velocity and radial acceleration fits described in Section 4.3.3.

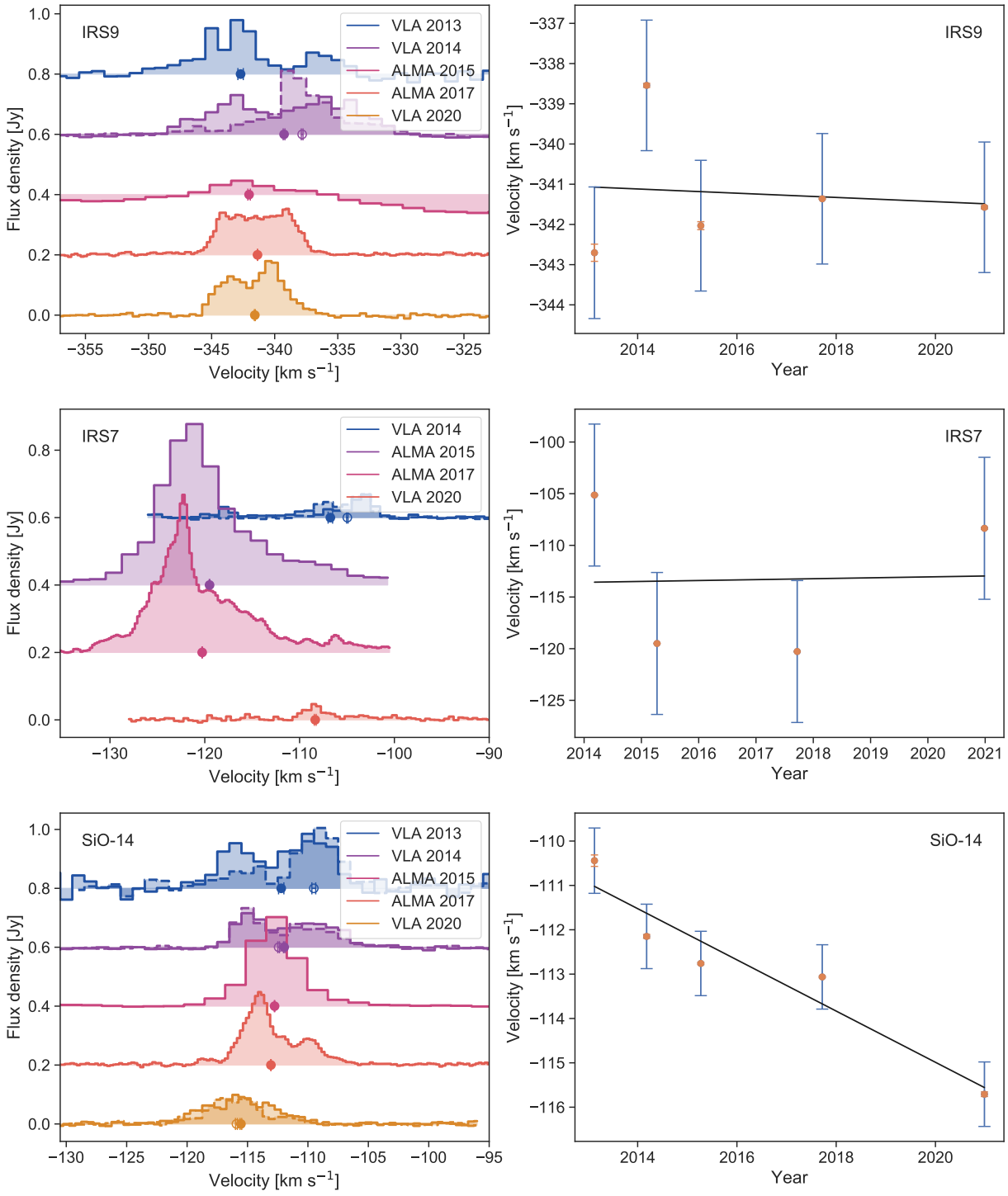

Figure C.1: Left: Maser spectra for each epoch when detected. For VLA epochs, solid lines indicate $J = 1 - 0$, $v = 1$ spectra and dashed lines are $J = 1 - 0$, $v = 2$ spectra. Error bars indicate the centroid velocity for each spectrum, with filled circles for $v = 1$ spectra and open circles for $v = 2$. Right: Velocity measurements as a function of time for each maser. Velocities have been averaged per epoch. Orange error bars show the statistical uncertainty on the velocity and blue error bars show the additional systematic uncertainty. Solid lines are the acceleration fits described in Section 4.3.3. Dotted lines are the error-weighted mean velocities for masers with too few data points for an acceleration fit.

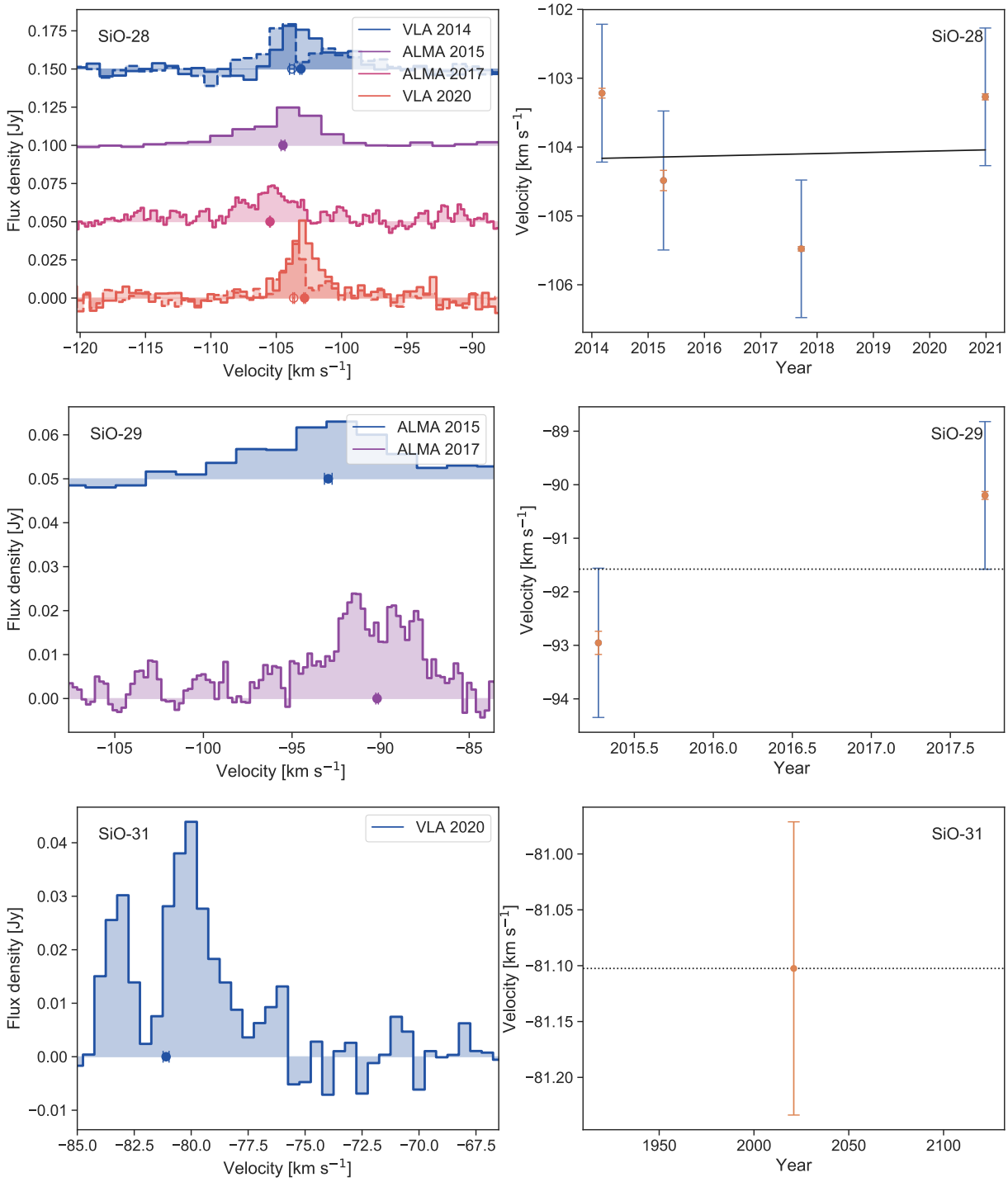
SiO-28
VLA 2014
ALMA 2015
ALMA 2017
VLA 2020
Flux density [Jy]
Velocity [km s^{-1}]
SiO-28
Velocity [km s^{-1}]
Year
SiO-29
ALMA 2015
ALMA 2017
Flux density [Jy]
Velocity [km s^{-1}]
SiO-29
Velocity [km s^{-1}]
Year
SiO-31
VLA 2020
Flux density [Jy]
Velocity [km s^{-1}]
SiO-31
Velocity [km s^{-1}]
Year

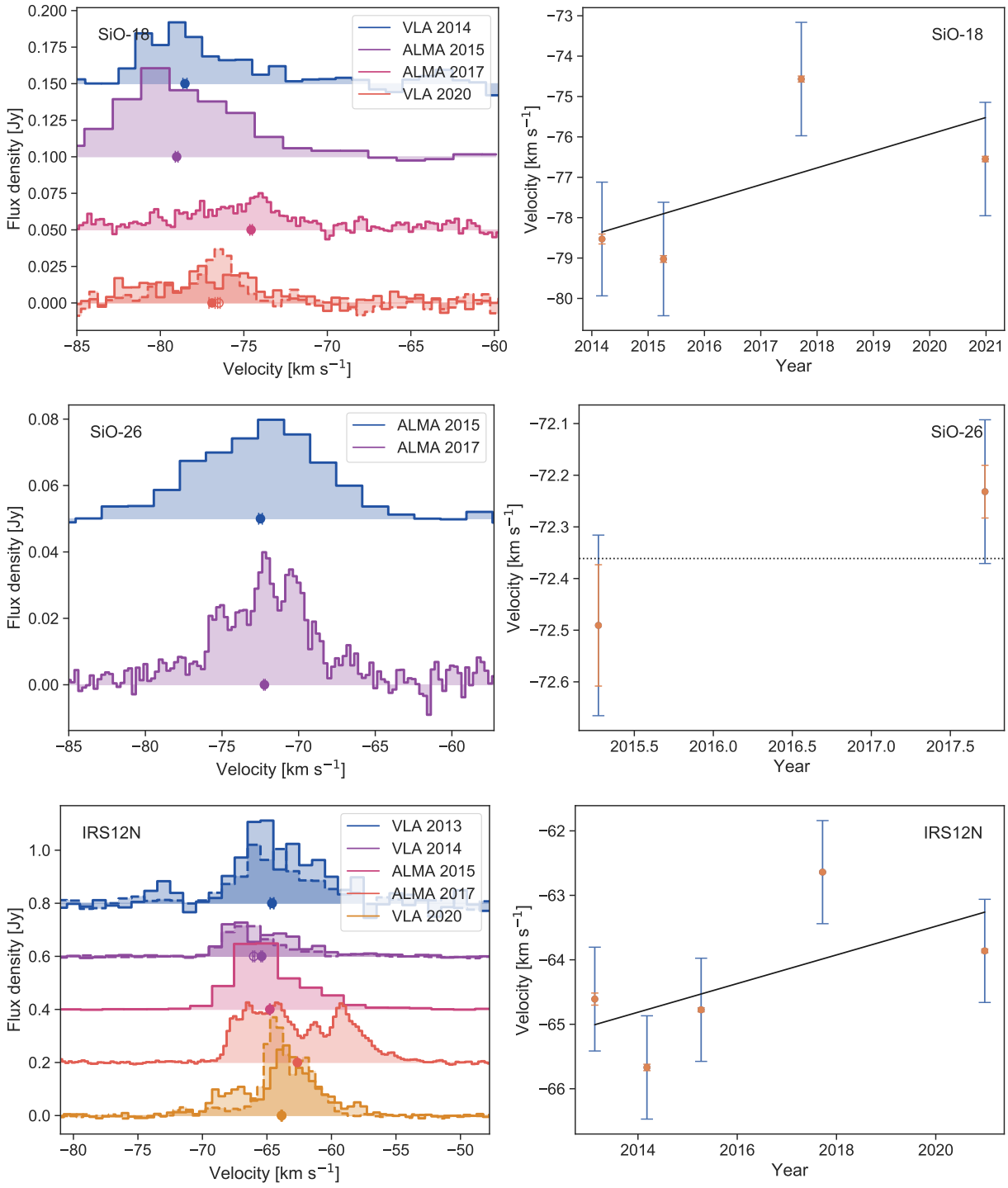
SiO-18
VLA 2014
ALMA 2015
ALMA 2017
VLA 2020
Flux density [Jy]
Velocity [km s^{-1}]
SiO-18
Velocity [km s^{-1}]
Year
SiO-26
ALMA 2015
ALMA 2017
Flux density [Jy]
Velocity [km s^{-1}]
SiO-26
Velocity [km s^{-1}]
Year
IRS12N
VLA 2013
VLA 2014
ALMA 2015
ALMA 2017
VLA 2020
Flux density [Jy]
Velocity [km s^{-1}]
IRS12N
Velocity [km s^{-1}]
Year

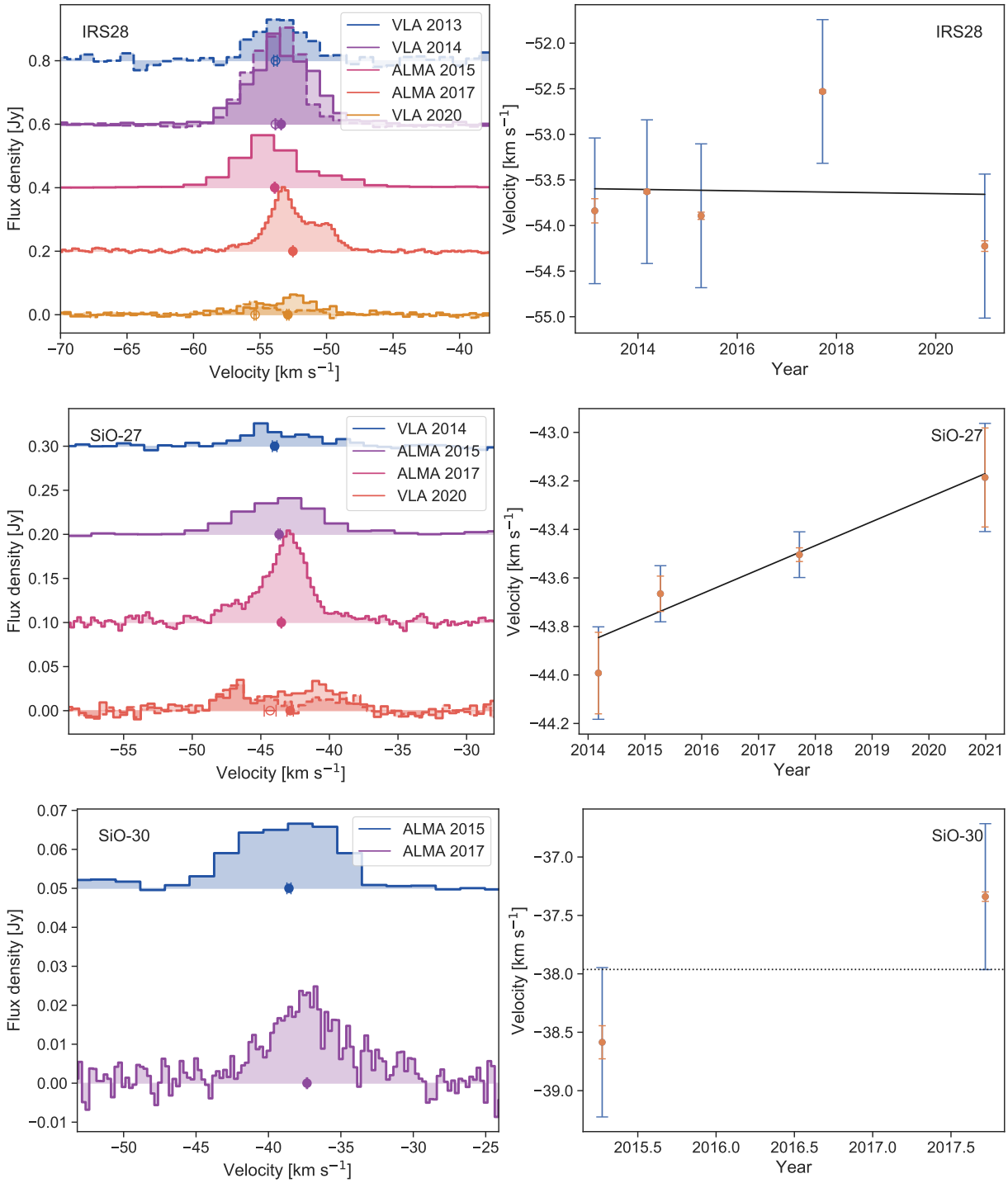
IRS28
VLA 2013
VLA 2014
ALMA 2015
ALMA 2017
VLA 2020
Flux density [Jy]
Velocity [km s^{-1}]
IRS28
Velocity [km s^{-1}]
Year
SiO-27
VLA 2014
ALMA 2015
ALMA 2017
VLA 2020
Flux density [Jy]
Velocity [km s^{-1}]
SiO-27
Velocity [km s^{-1}]
Year
SiO-30
ALMA 2015
ALMA 2017
Flux density [Jy]
Velocity [km s^{-1}]
SiO-30
Velocity [km s^{-1}]
Year

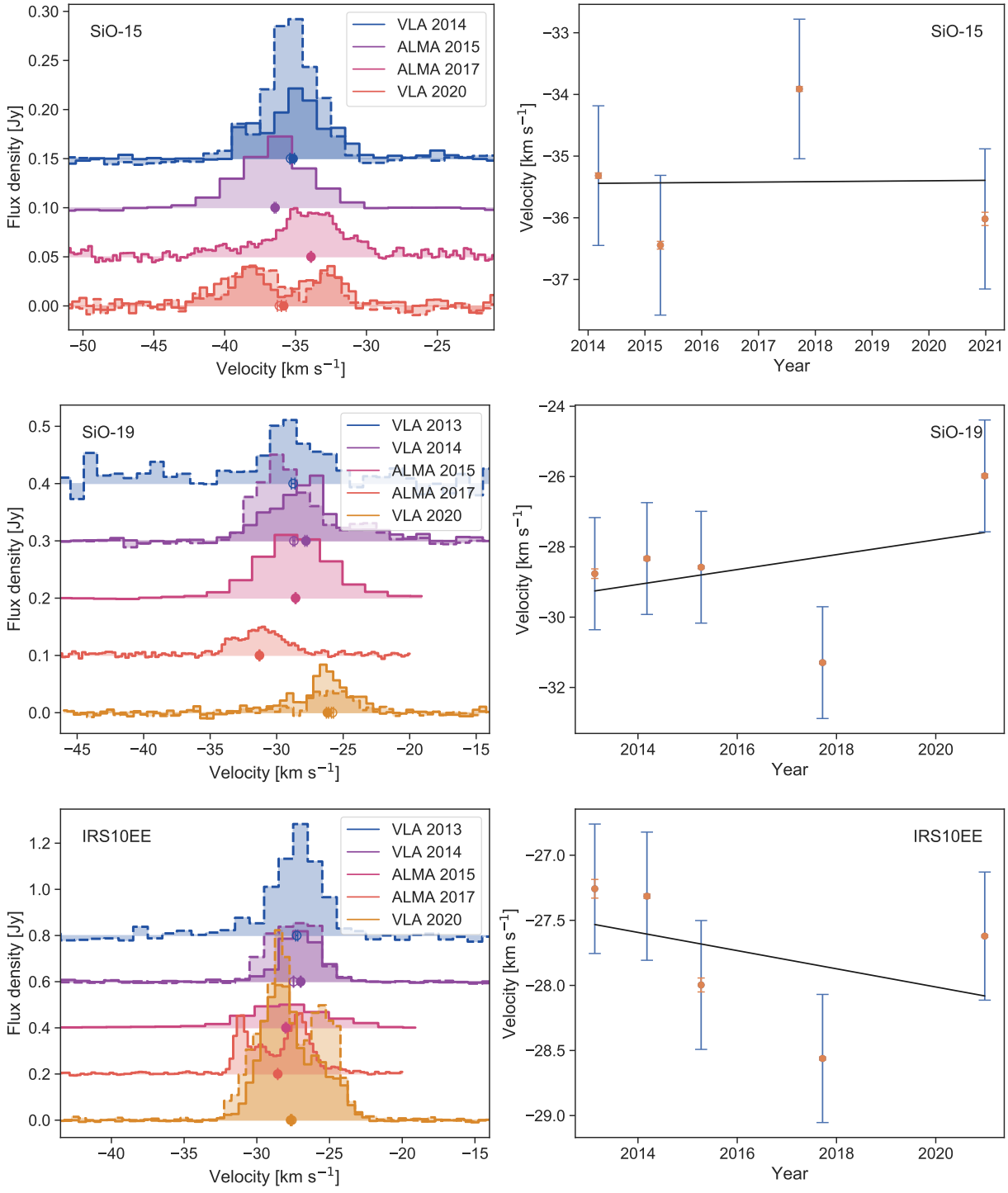
SiO-15
VLA 2014
ALMA 2015
ALMA 2017
VLA 2020
Flux density [Jy]
Velocity [km s^{-1}]
SiO-15
Velocity [km s^{-1}]
Year
SiO-19
VLA 2013
VLA 2014
ALMA 2015
ALMA 2017
VLA 2020
Flux density [Jy]
Velocity [km s^{-1}]
SiO-19
Velocity [km s^{-1}]
Year
IRS10EE
VLA 2013
VLA 2014
ALMA 2015
ALMA 2017
VLA 2020
Flux density [Jy]
Velocity [km s^{-1}]
IRS10EE
Velocity [km s^{-1}]
Year

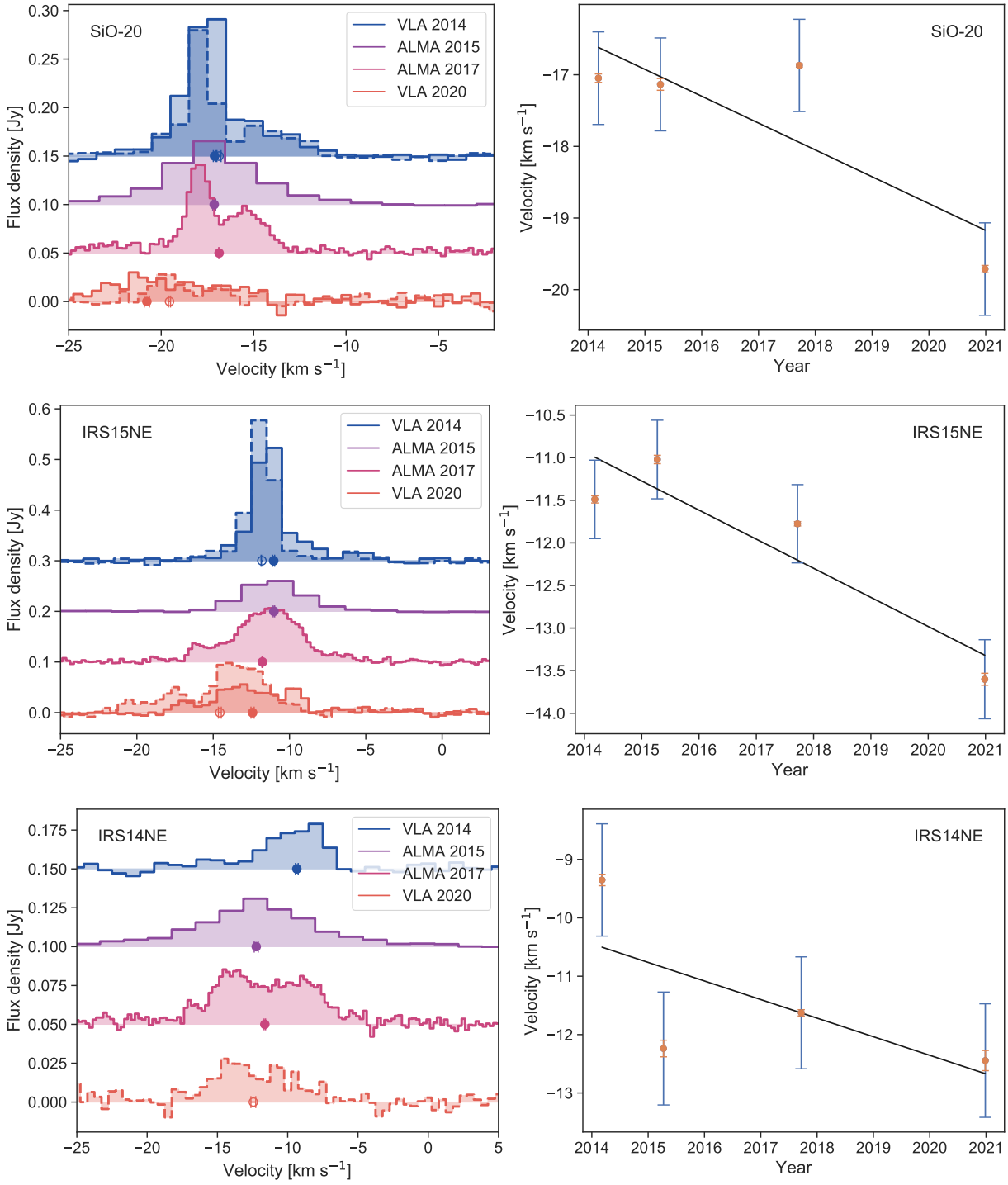
SiO-20
VLA 2014
ALMA 2015
ALMA 2017
VLA 2020
Flux density [Jy]
Velocity [km s^{-1}]
SiO-20
Velocity [km s^{-1}]
Year
IRS15NE
VLA 2014
ALMA 2015
ALMA 2017
VLA 2020
Flux density [Jy]
Velocity [km s^{-1}]
IRS15NE
Velocity [km s^{-1}]
Year
IRS14NE
VLA 2014
ALMA 2015
ALMA 2017
VLA 2020
Flux density [Jy]
Velocity [km s^{-1}]
IRS14NE
Velocity [km s^{-1}]
Year

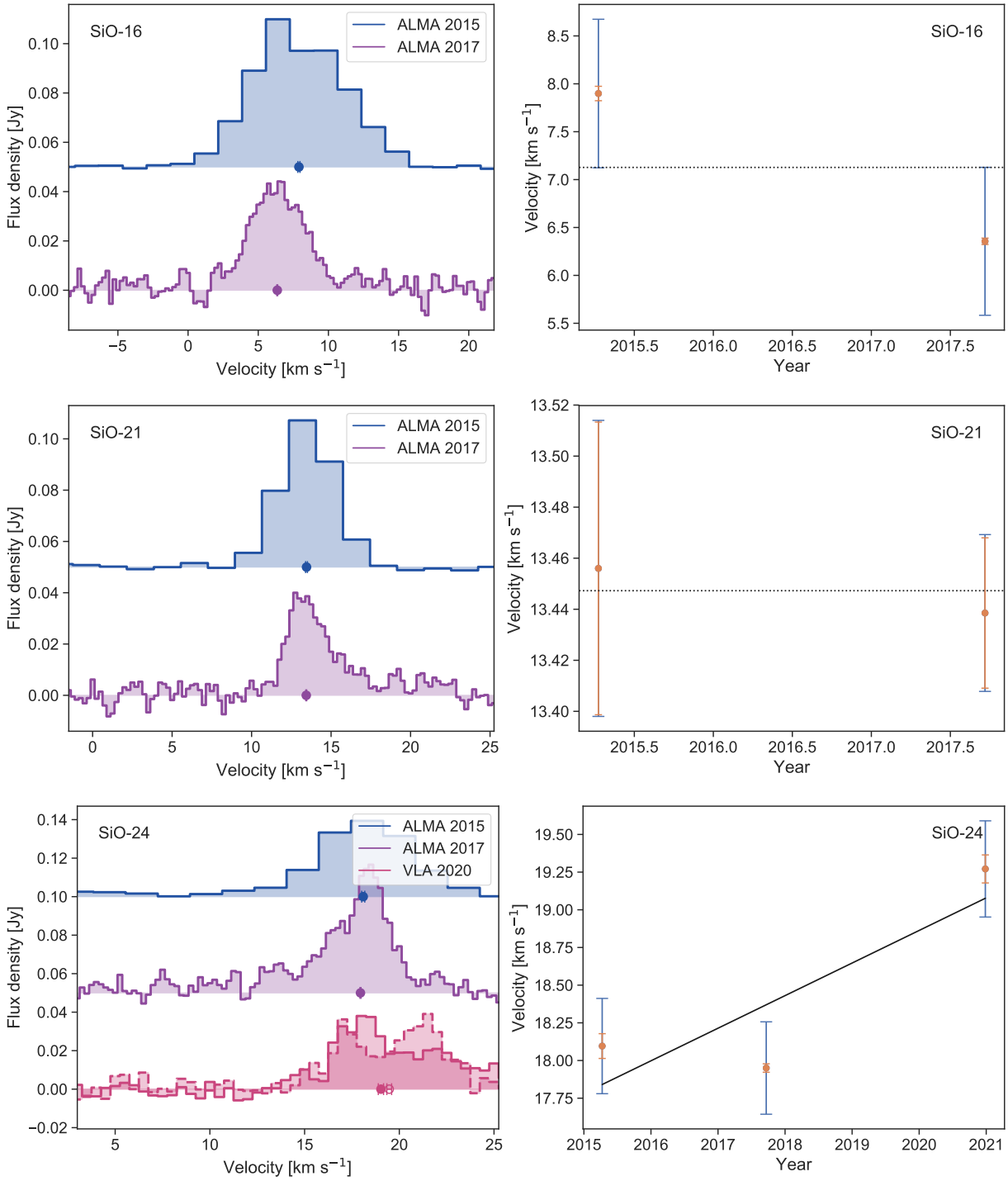
SiO-16
ALMA 2015
ALMA 2017
Flux density [Jy]
Velocity [km s^{-1}]
SiO-16
Velocity [km s^{-1}]
Year
SiO-21
ALMA 2015
ALMA 2017
Flux density [Jy]
Velocity [km s^{-1}]
SiO-21
Velocity [km s^{-1}]
Year
SiO-24
ALMA 2015
ALMA 2017
VLA 2020
Flux density [Jy]
Velocity [km s^{-1}]
SiO-24
Velocity [km s^{-1}]
Year

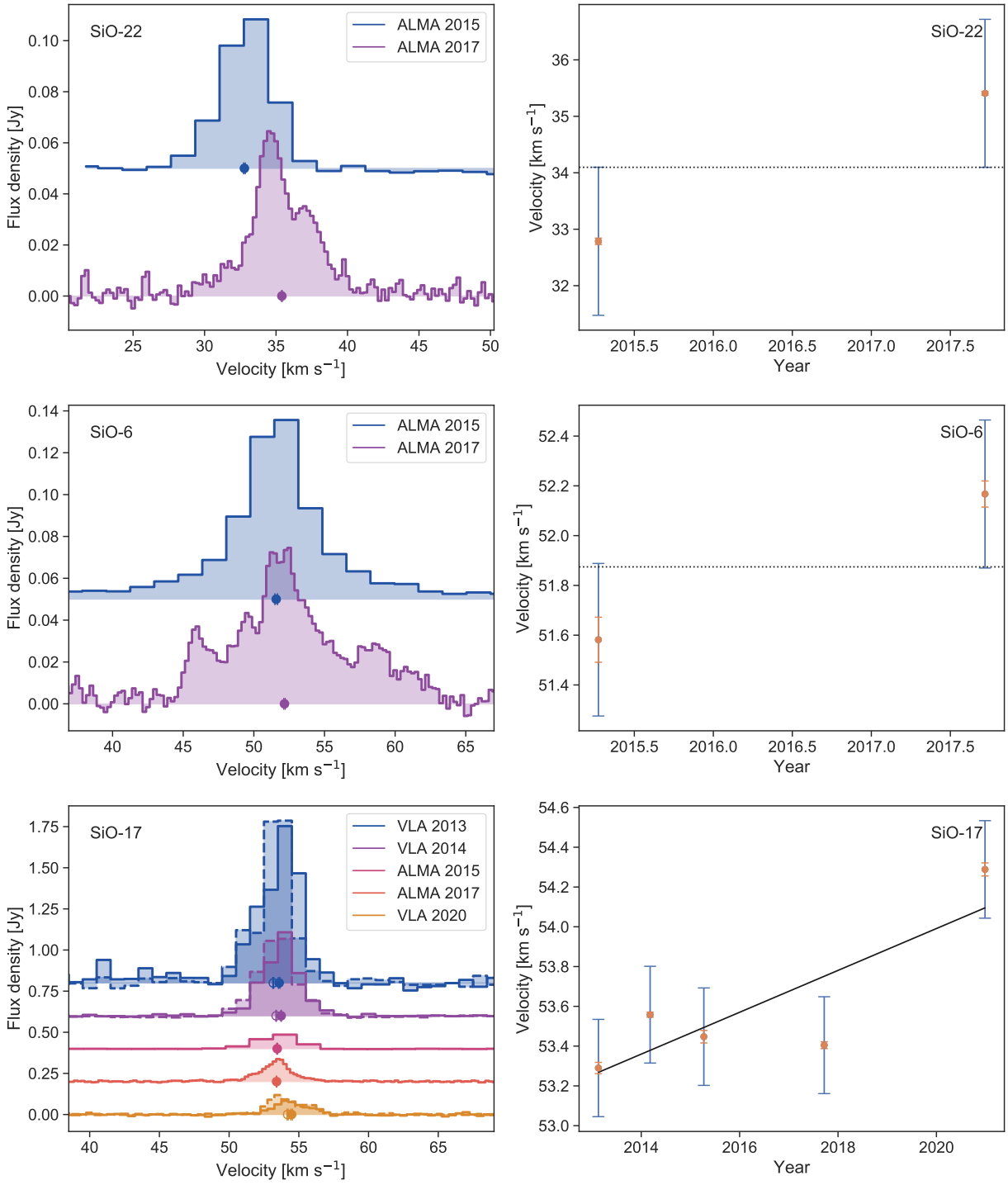
SiO-22
ALMA 2015
ALMA 2017
Flux density [Jy]
Velocity [km s^{-1}]
SiO-22
Velocity [km s^{-1}]
Year
SiO-6
ALMA 2015
ALMA 2017
Flux density [Jy]
Velocity [km s^{-1}]
SiO-6
Velocity [km s^{-1}]
Year
SiO-17
VLA 2013
VLA 2014
ALMA 2015
ALMA 2017
VLA 2020
Flux density [Jy]
Velocity [km s^{-1}]
SiO-17
Velocity [km s^{-1}]
Year

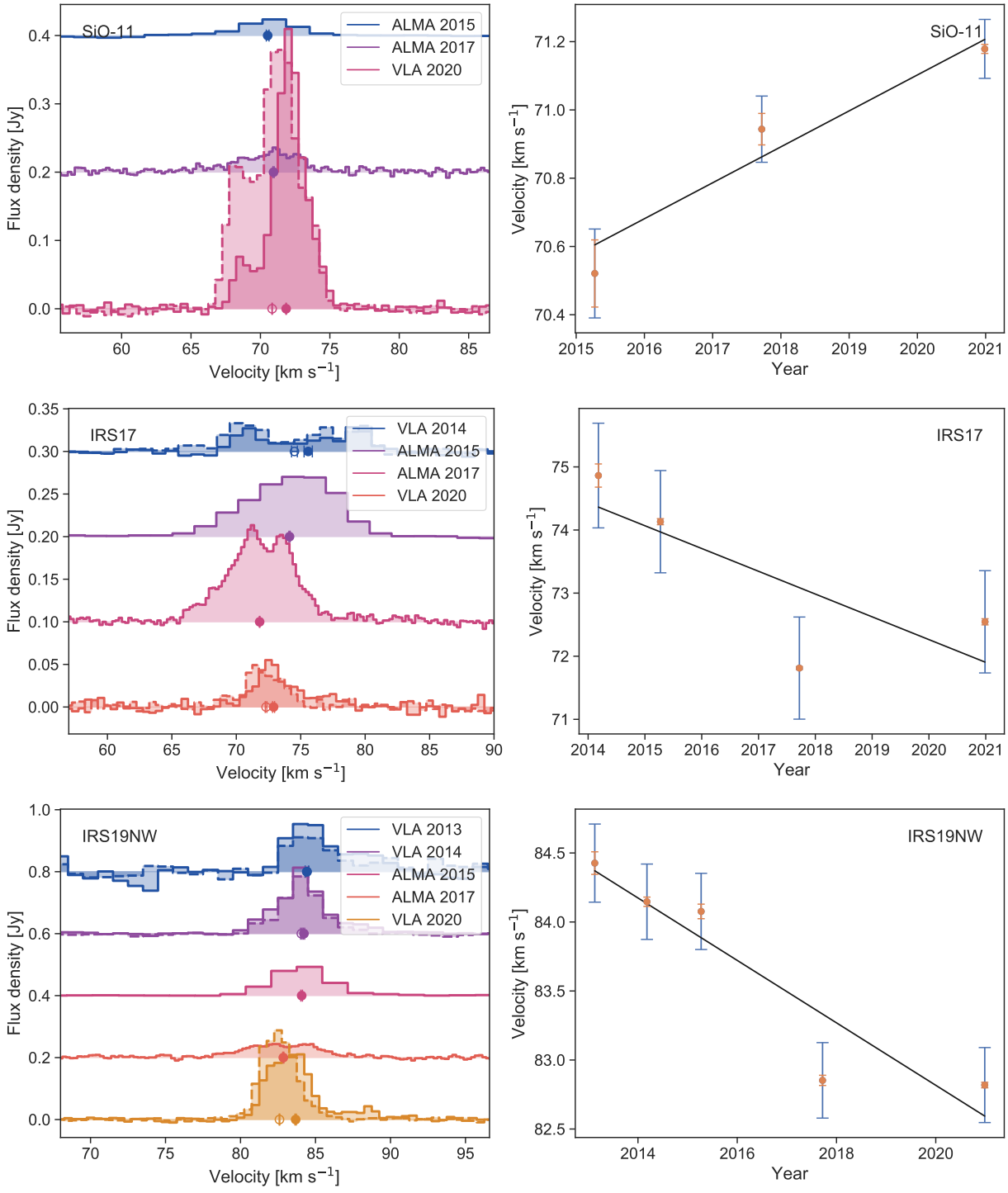
SiO-11
ALMA 2015
ALMA 2017
VLA 2020
Flux density [Jy]
Velocity [km s^{-1}]
SiO-11
Velocity [km s^{-1}]
Year
IRS17
VLA 2014
ALMA 2015
ALMA 2017
VLA 2020
Flux density [Jy]
Velocity [km s^{-1}]
IRS17
Velocity [km s^{-1}]
Year
IRS19NW
VLA 2013
VLA 2014
ALMA 2015
ALMA 2017
VLA 2020
Flux density [Jy]
Velocity [km s^{-1}]
IRS19NW
Velocity [km s^{-1}]
Year

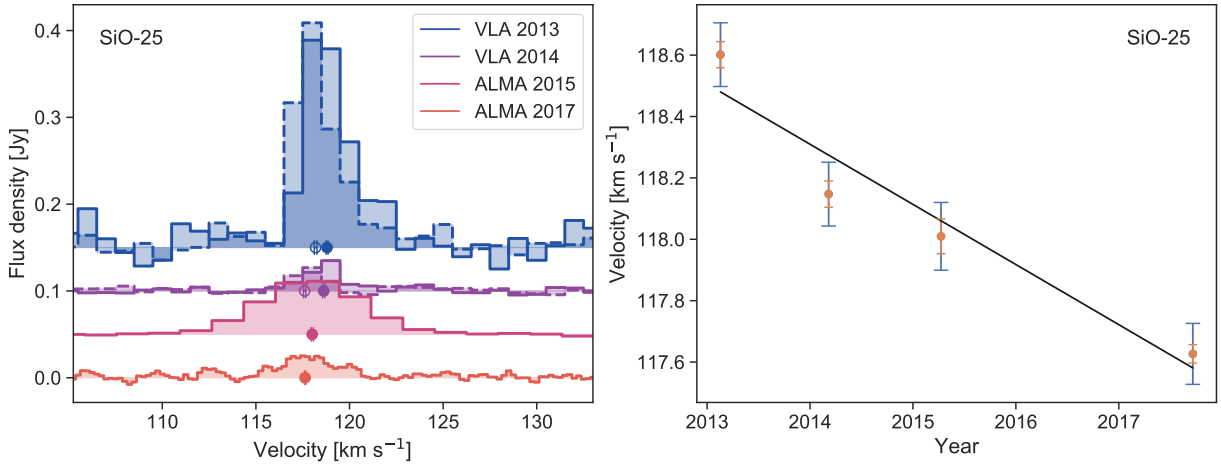
SiO-25
VLA 2013
VLA 2014
ALMA 2015
ALMA 2017
Flux density [Jy]
Velocity [km s^{-1}]
SiO-25
Velocity [km s^{-1}]
Year

Appendix D

SiO maser proper motion and proper acceleration fits

Figure D.1 shows proper motion and proper acceleration fits described in Section 4.3.1.

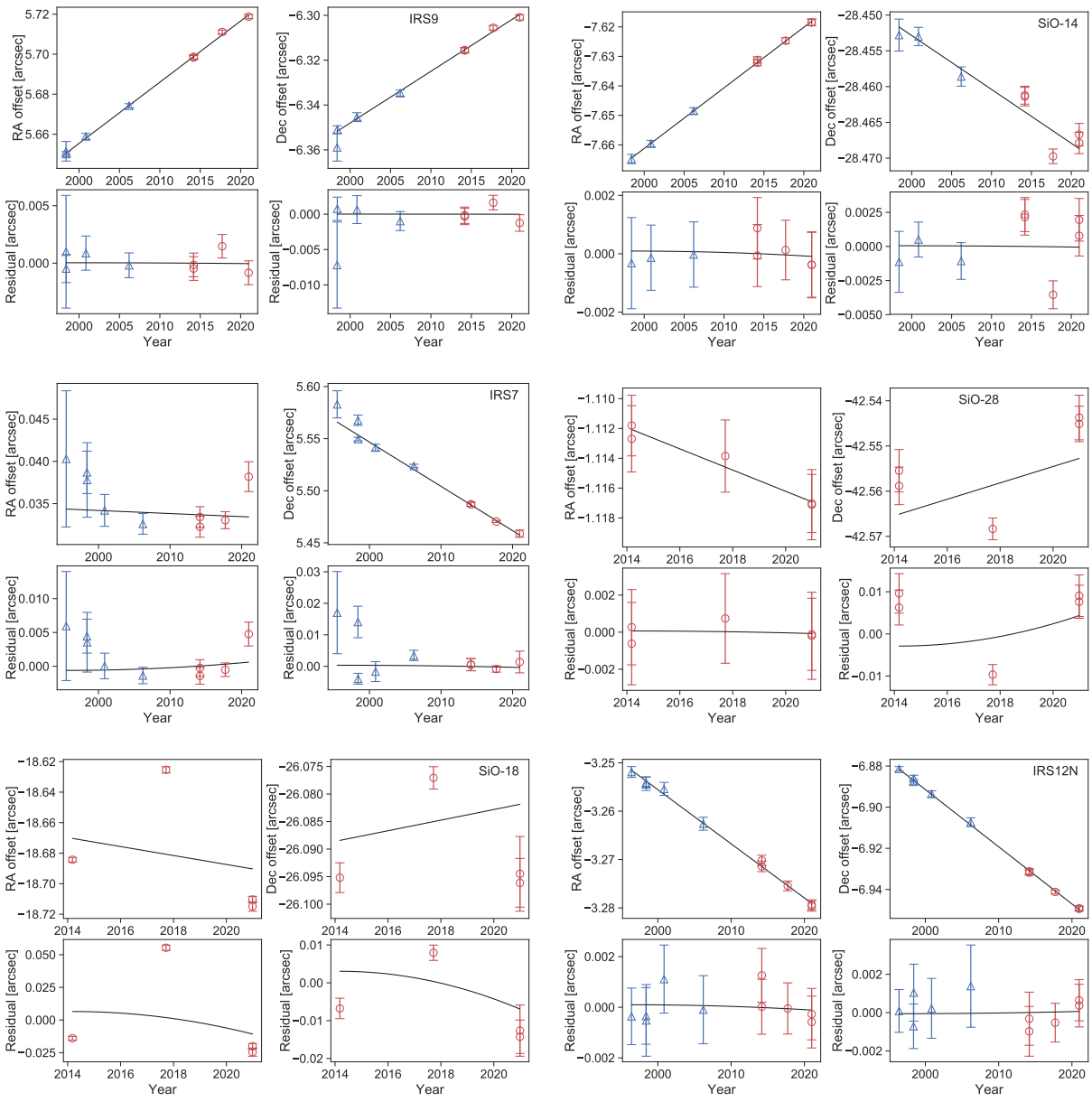

Figure D.1: Proper motion and proper acceleration fits for each maser described in Section 4.3.1. Maser positions are from Reid et al. (2007) (blue triangles), Li et al. (2010) (orange squares), and this work (red circles). The upper panels show linear fits to the position time series to obtain proper motions, and the bottom panels show quadratic fits to the residuals of the linear fits to obtain proper accelerations.

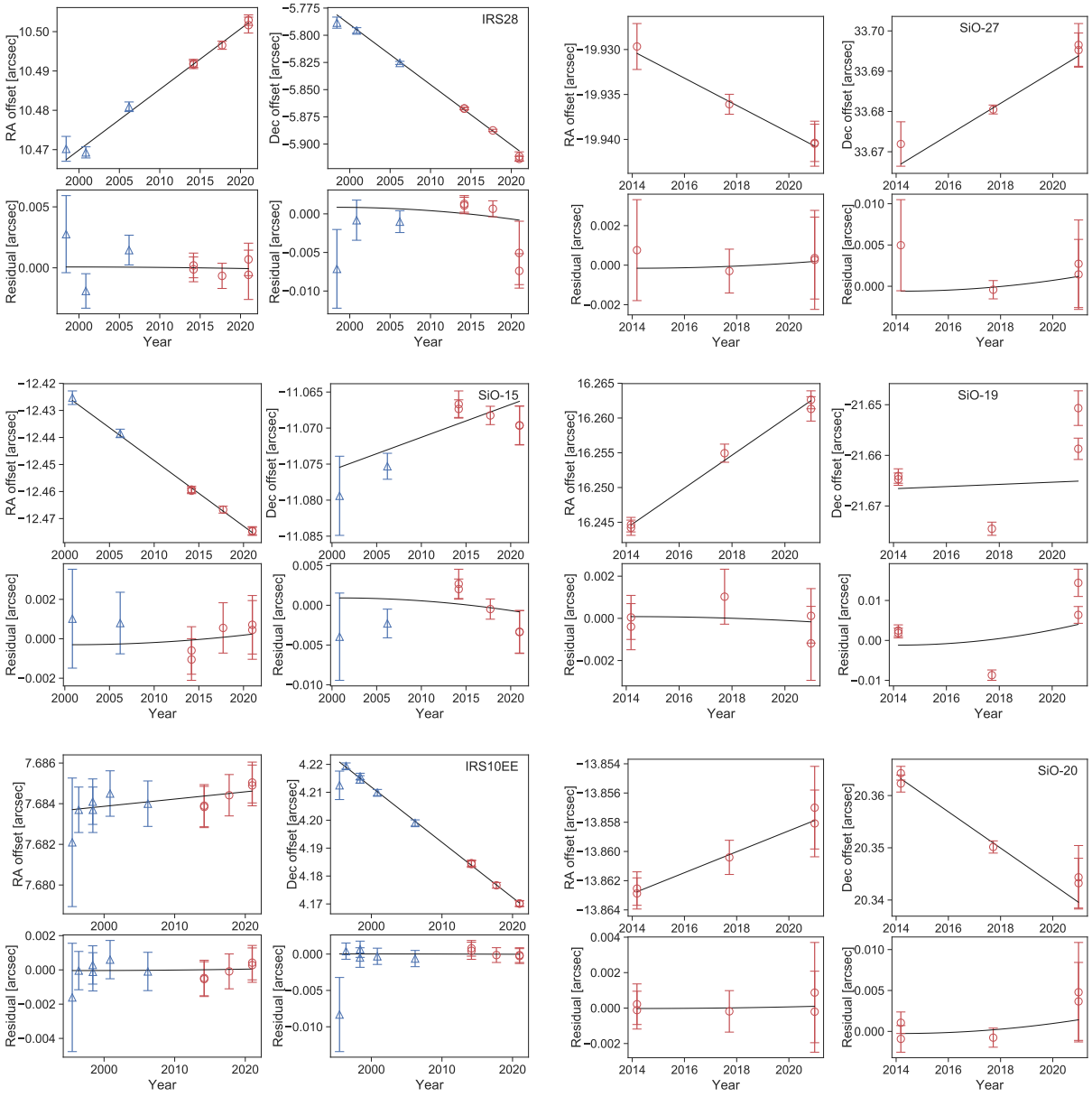
IRS28
SiO-27
SiO-15
SiO-19
IRS10EE
SiO-20
RA offset [arcsec]
Dec offset [arcsec]
Residual [arcsec]
Year

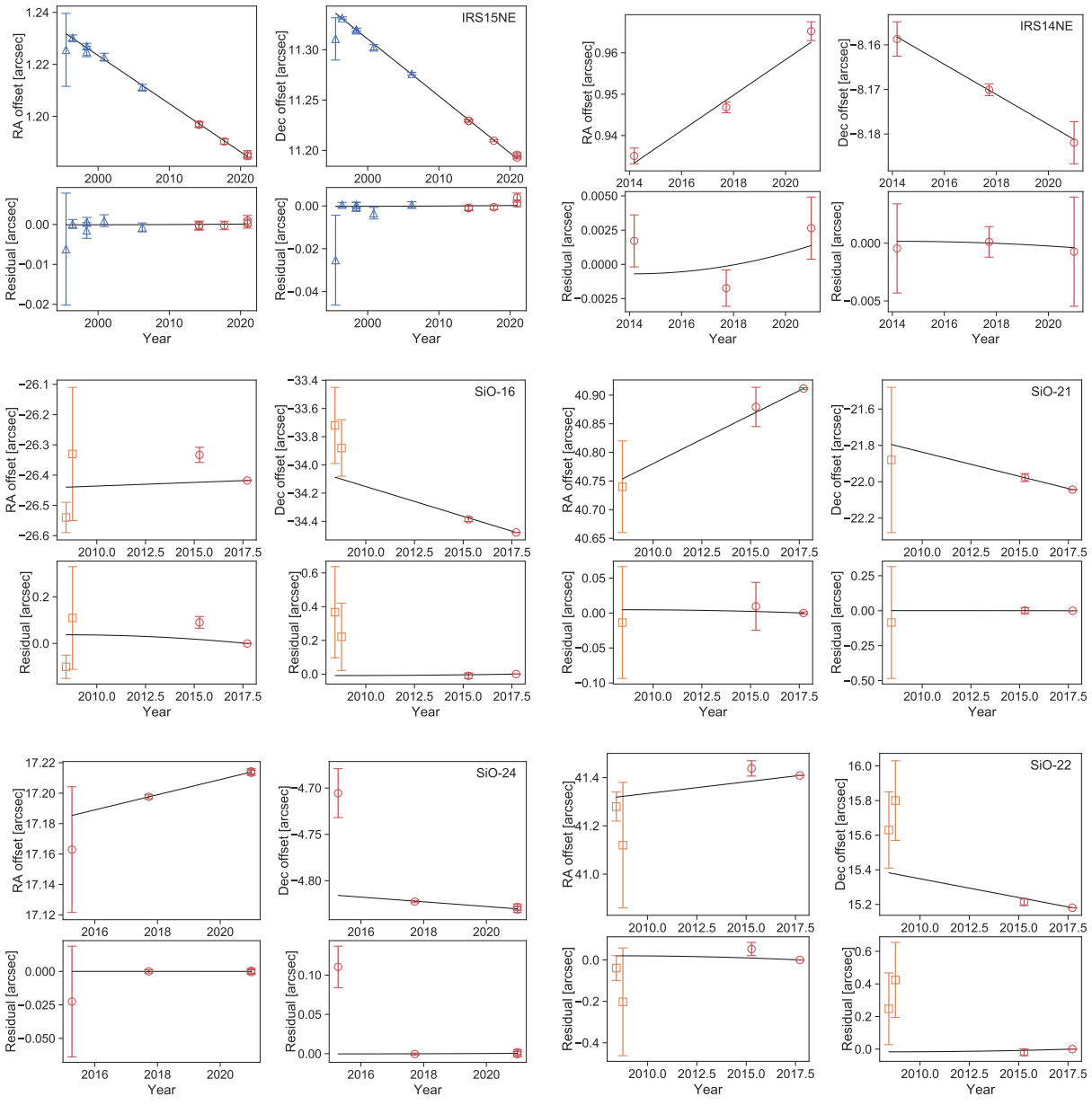
IRS15NE
IRS14NE
SiO-16
SiO-21
SiO-24
SiO-22
RA offset [arcsec]
Dec offset [arcsec]
Residual [arcsec]
Year

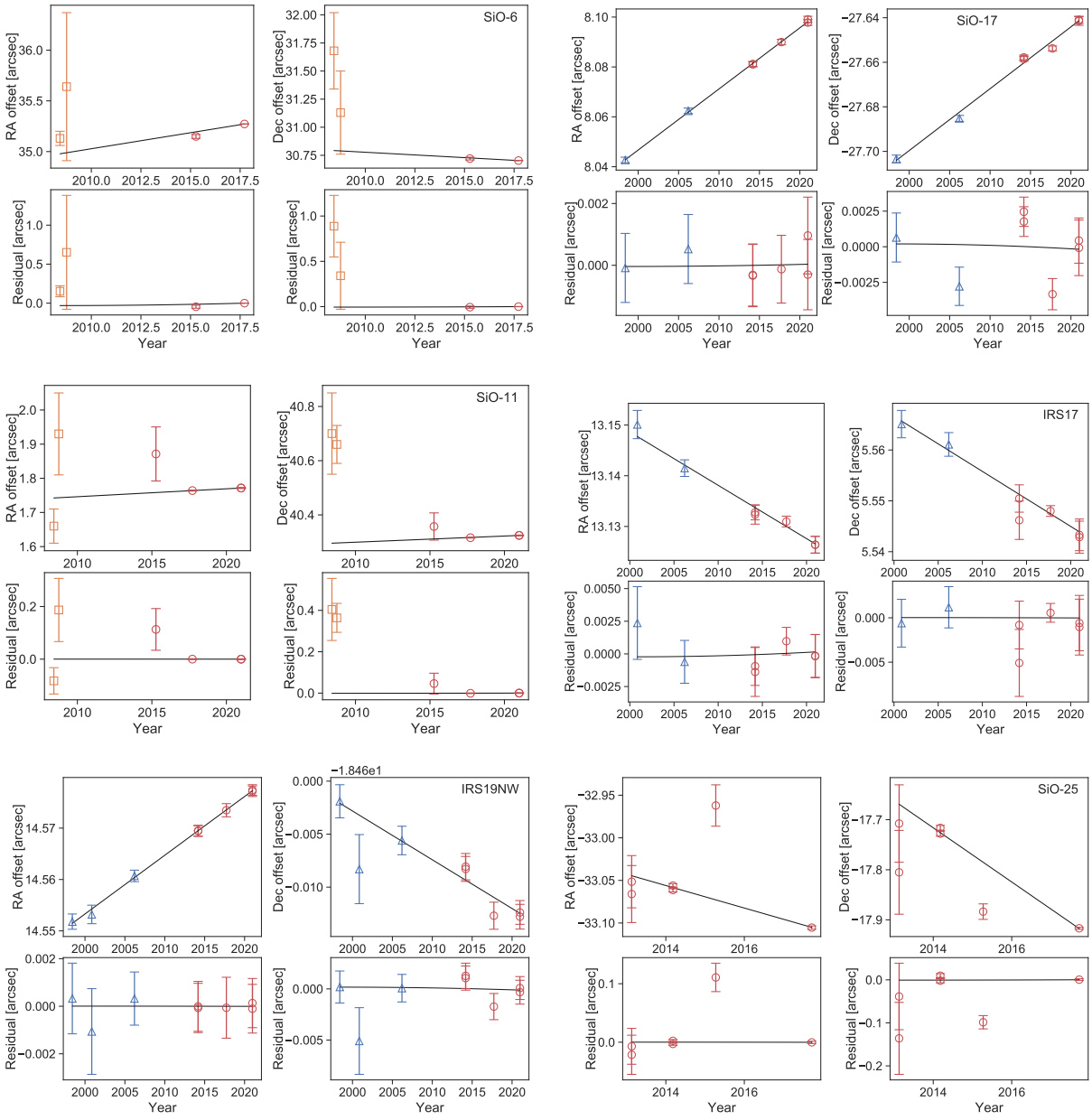
SiO-6
SiO-17
SiO-11
IRS17
IRS19NW
SiO-25
RA offset [arcsec]
Dec offset [arcsec]
Residual [arcsec]
Year
−1.846e1

Appendix E

Updated SiO Maser Spectra and Doppler Fits

Figure E.1 shows the SiO maser spectra measured between 2013 - 2022, velocity centroids for each spectrum, and acceleration fits described in Chapter 5.

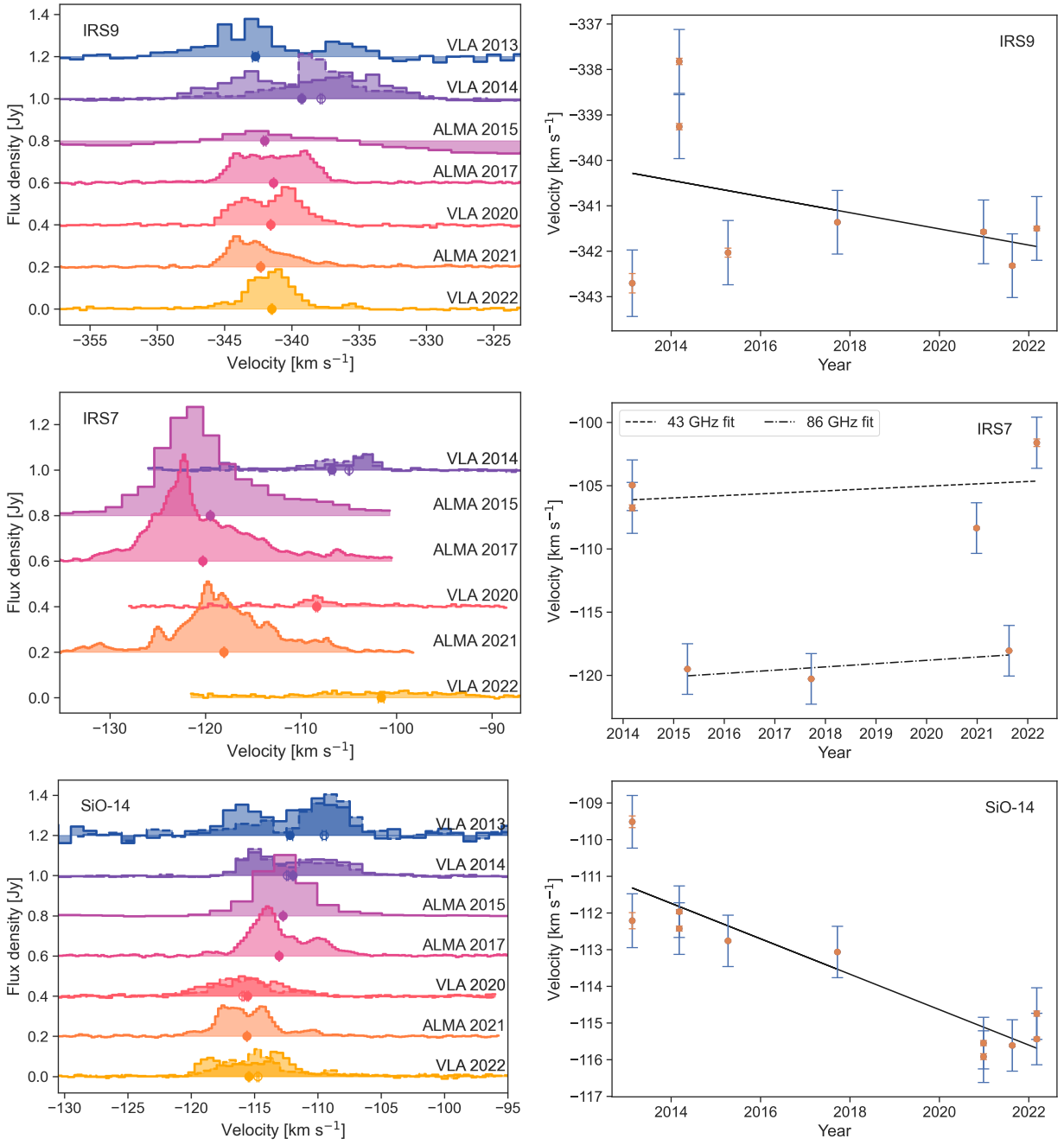

Figure E.1: Left: Maser spectra for each epoch when detected. For VLA epochs, solid lines indicate $J = 1 - 0$, $v = 1$ spectra and dashed lines are $J = 1 - 0$, $v = 2$ spectra. Error bars indicate the centroid velocity for each spectrum, with filled circles for $v = 1$ spectra and open circles for $v = 2$. Right: Acceleration fits to the maser velocities over time. Orange error bars indicate the statistical uncertainties, and blue show the total uncertainty including the systematic. Dotted lines are the error-weighted mean velocities for masers with too few data points for an acceleration fit. For IRS 7, both the fits to the 43 GHz and 86 GHz velocities are shown.

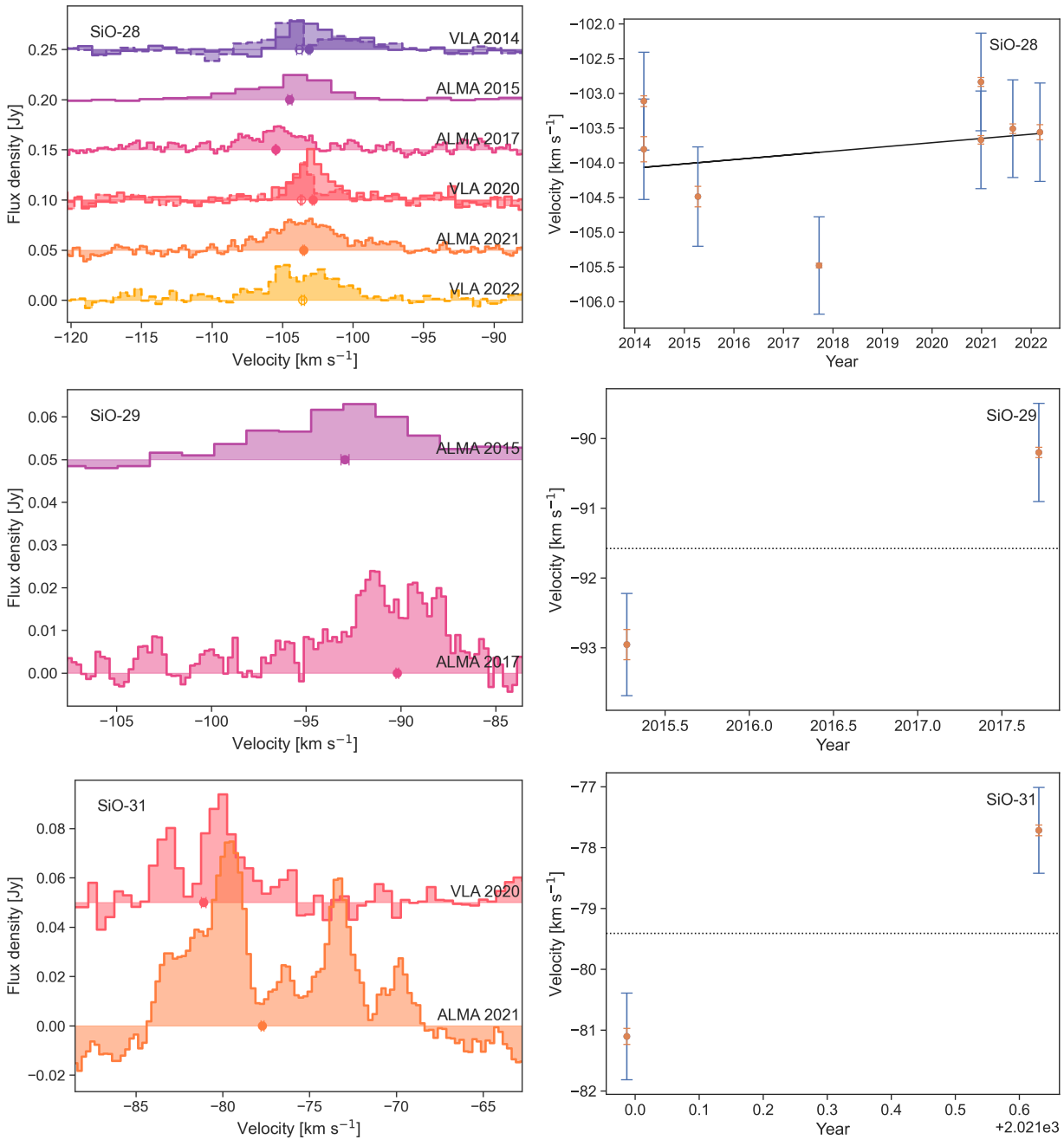
SiO-28
VLA 2014
ALMA 2015
ALMA 2017
VLA 2020
ALMA 2021
VLA 2022
Flux density [Jy]
Velocity [km s^{-1}]
SiO-28
Velocity [km s^{-1}]
Year
SiO-29
ALMA 2015
ALMA 2017
Flux density [Jy]
Velocity [km s^{-1}]
SiO-29
Velocity [km s^{-1}]
Year
SiO-31
VLA 2020
ALMA 2021
Flux density [Jy]
Velocity [km s^{-1}]
SiO-31
Velocity [km s^{-1}]
Year
+2.021e3

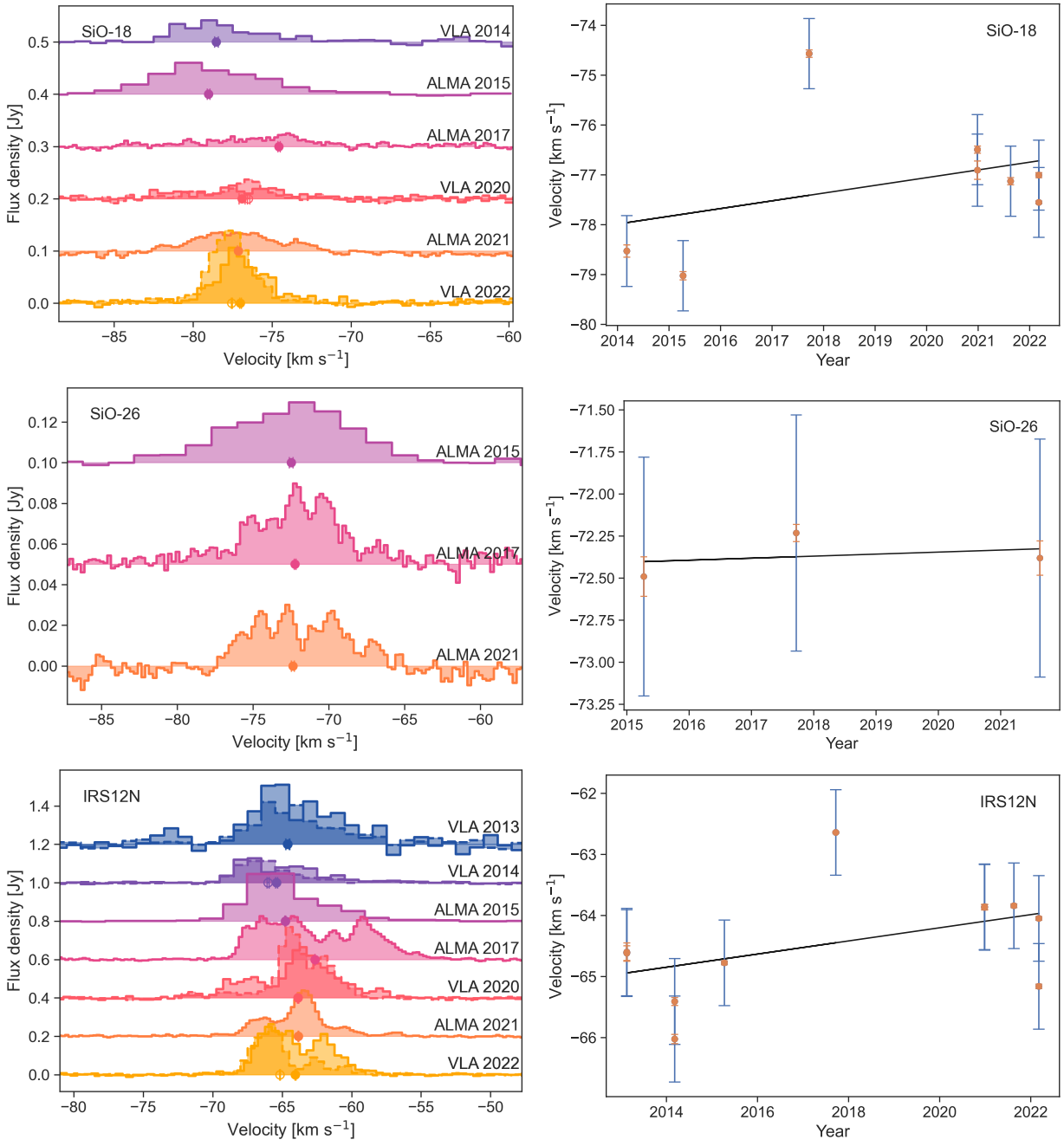
SiO-18
VLA 2014
ALMA 2015
ALMA 2017
VLA 2020
ALMA 2021
VLA 2022
Flux density [Jy]
Velocity [km s^{-1}]
SiO-18
Velocity [km s^{-1}]
Year
SiO-26
ALMA 2015
ALMA 2017
ALMA 2021
Flux density [Jy]
Velocity [km s^{-1}]
SiO-26
Velocity [km s^{-1}]
Year
IRS12N
VLA 2013
VLA 2014
ALMA 2015
ALMA 2017
VLA 2020
ALMA 2021
VLA 2022
Flux density [Jy]
Velocity [km s^{-1}]
IRS12N
Velocity [km s^{-1}]
Year

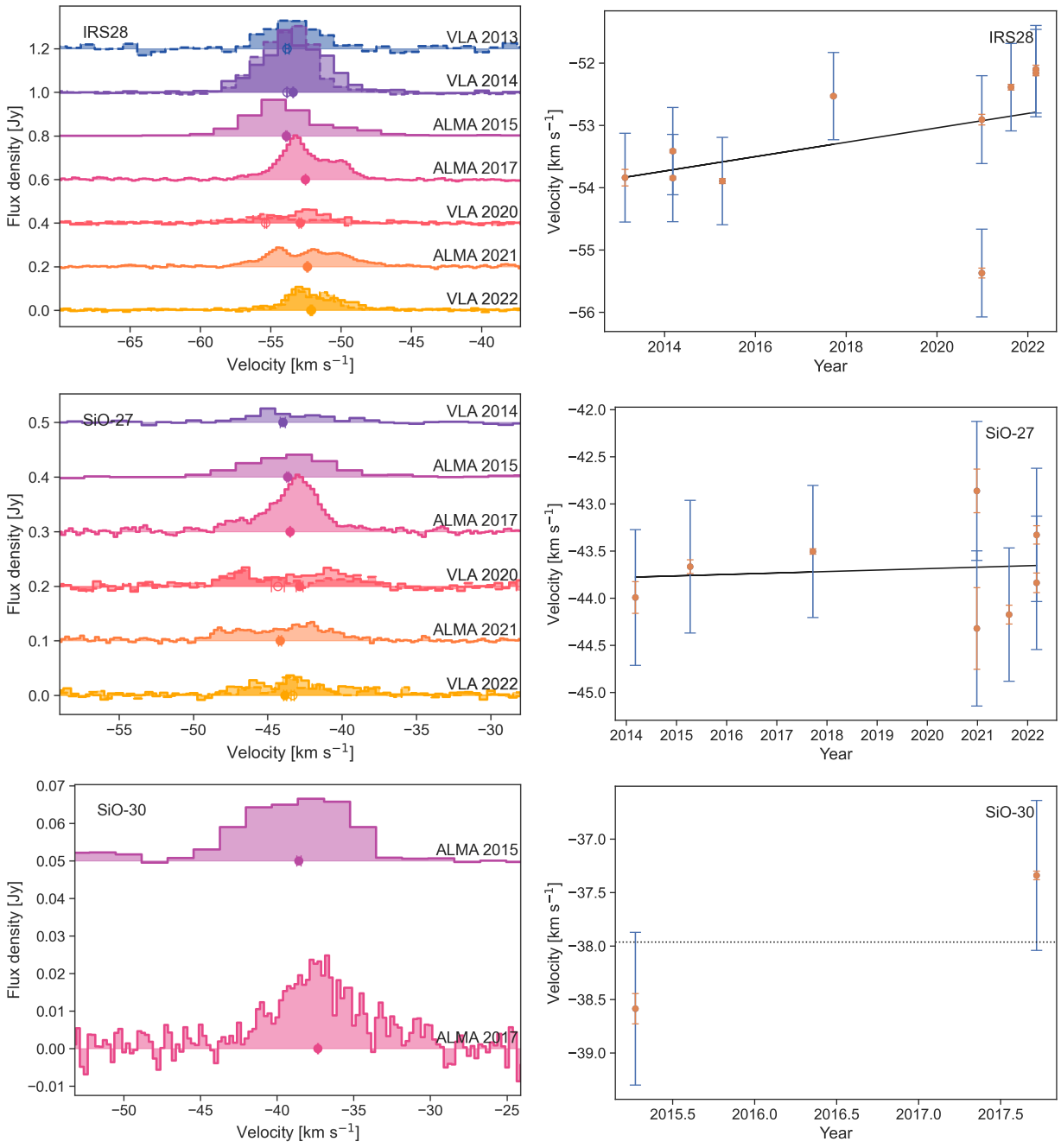
IRS28
VLA 2013
VLA 2014
ALMA 2015
ALMA 2017
VLA 2020
ALMA 2021
VLA 2022
Flux density [Jy]
Velocity [km s^{-1}]
IRS28
Velocity [km s^{-1}]
Year
SiO-27
VLA 2014
ALMA 2015
ALMA 2017
VLA 2020
ALMA 2021
VLA 2022
Flux density [Jy]
Velocity [km s^{-1}]
SiO-27
Velocity [km s^{-1}]
Year
SiO-30
ALMA 2015
ALMA 2017
Flux density [Jy]
Velocity [km s^{-1}]
SiO-30
Velocity [km s^{-1}]
Year

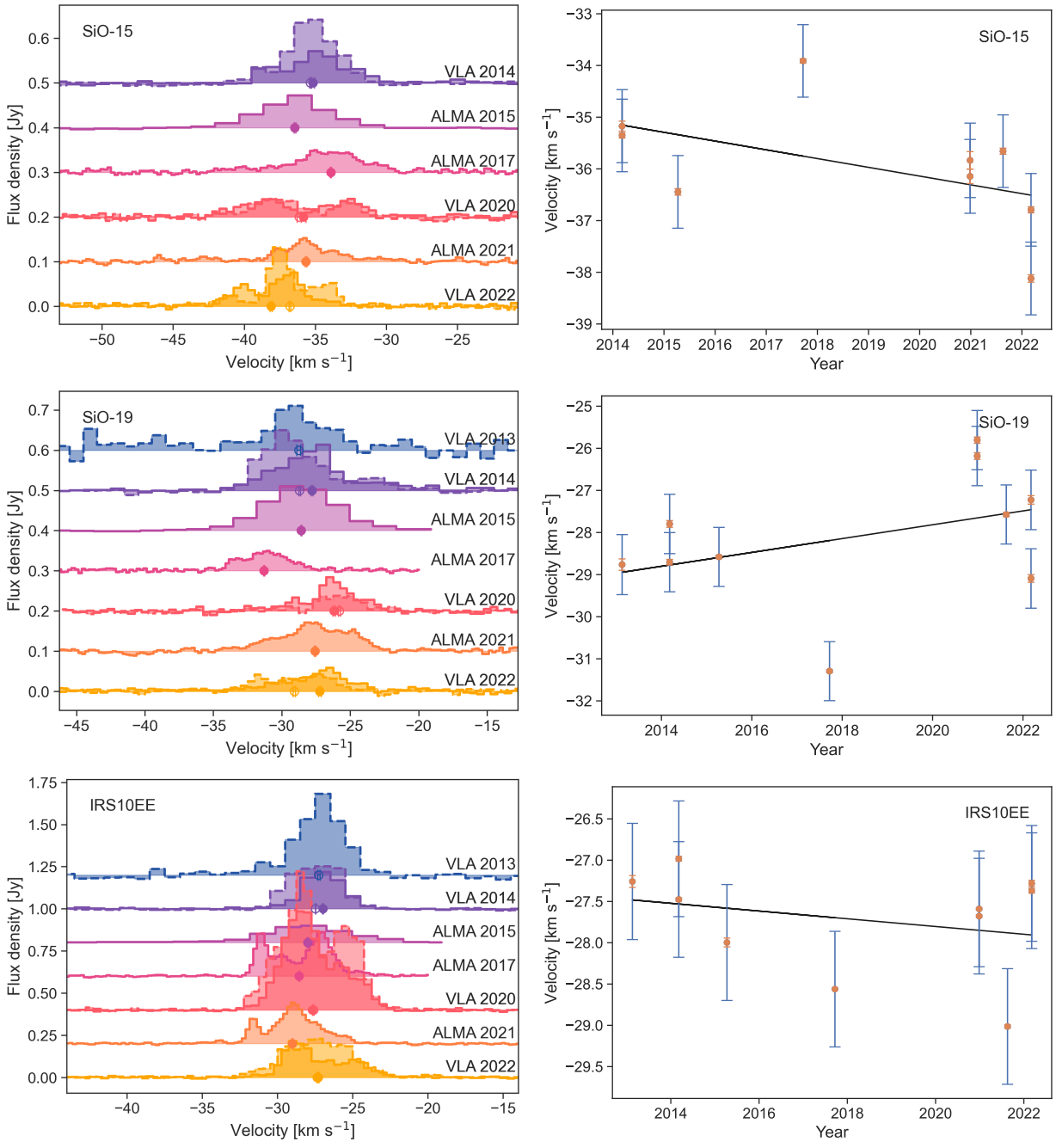
SiO-15
VLA 2014
ALMA 2015
ALMA 2017
VLA 2020
ALMA 2021
VLA 2022
Flux density [Jy]
Velocity [km s^{-1}]
SiO-15
Velocity [km s^{-1}]
Year
SiO-19
VLA 2013
VLA 2014
ALMA 2015
ALMA 2017
VLA 2020
ALMA 2021
VLA 2022
Flux density [Jy]
Velocity [km s^{-1}]
SiO-19
Velocity [km s^{-1}]
Year
IRS10EE
VLA 2013
VLA 2014
ALMA 2015
ALMA 2017
VLA 2020
ALMA 2021
VLA 2022
Flux density [Jy]
Velocity [km s^{-1}]
IRS10EE
Velocity [km s^{-1}]
Year

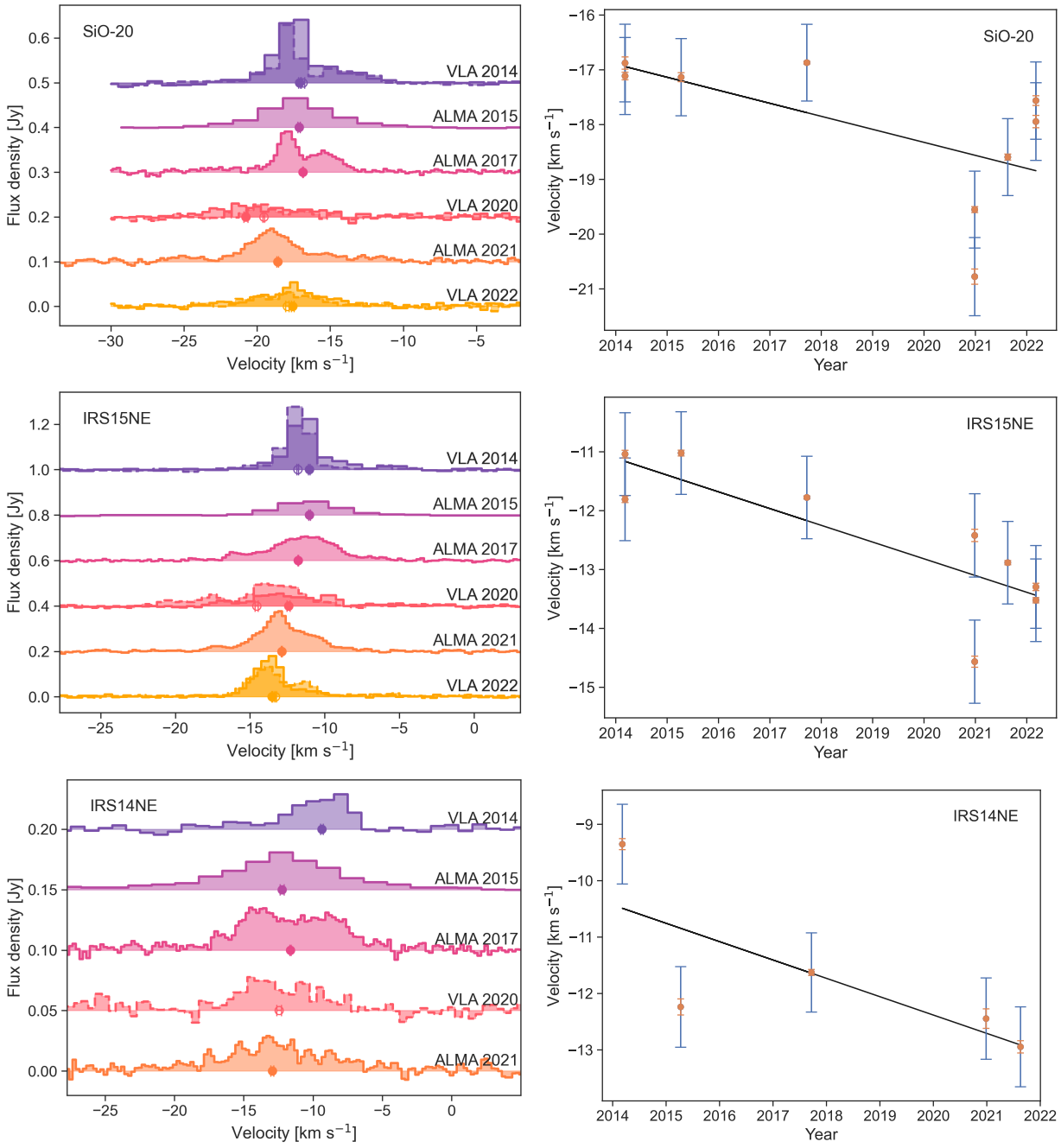
SiO-20
VLA 2014
ALMA 2015
ALMA 2017
VLA 2020
ALMA 2021
VLA 2022
Flux density [Jy]
Velocity [km s^{-1}]
SiO-20
Velocity [km s^{-1}]
Year
IRS15NE
VLA 2014
ALMA 2015
ALMA 2017
VLA 2020
ALMA 2021
VLA 2022
Flux density [Jy]
Velocity [km s^{-1}]
IRS15NE
Velocity [km s^{-1}]
Year
IRS14NE
VLA 2014
ALMA 2015
ALMA 2017
VLA 2020
ALMA 2021
Flux density [Jy]
Velocity [km s^{-1}]
IRS14NE
Velocity [km s^{-1}]
Year

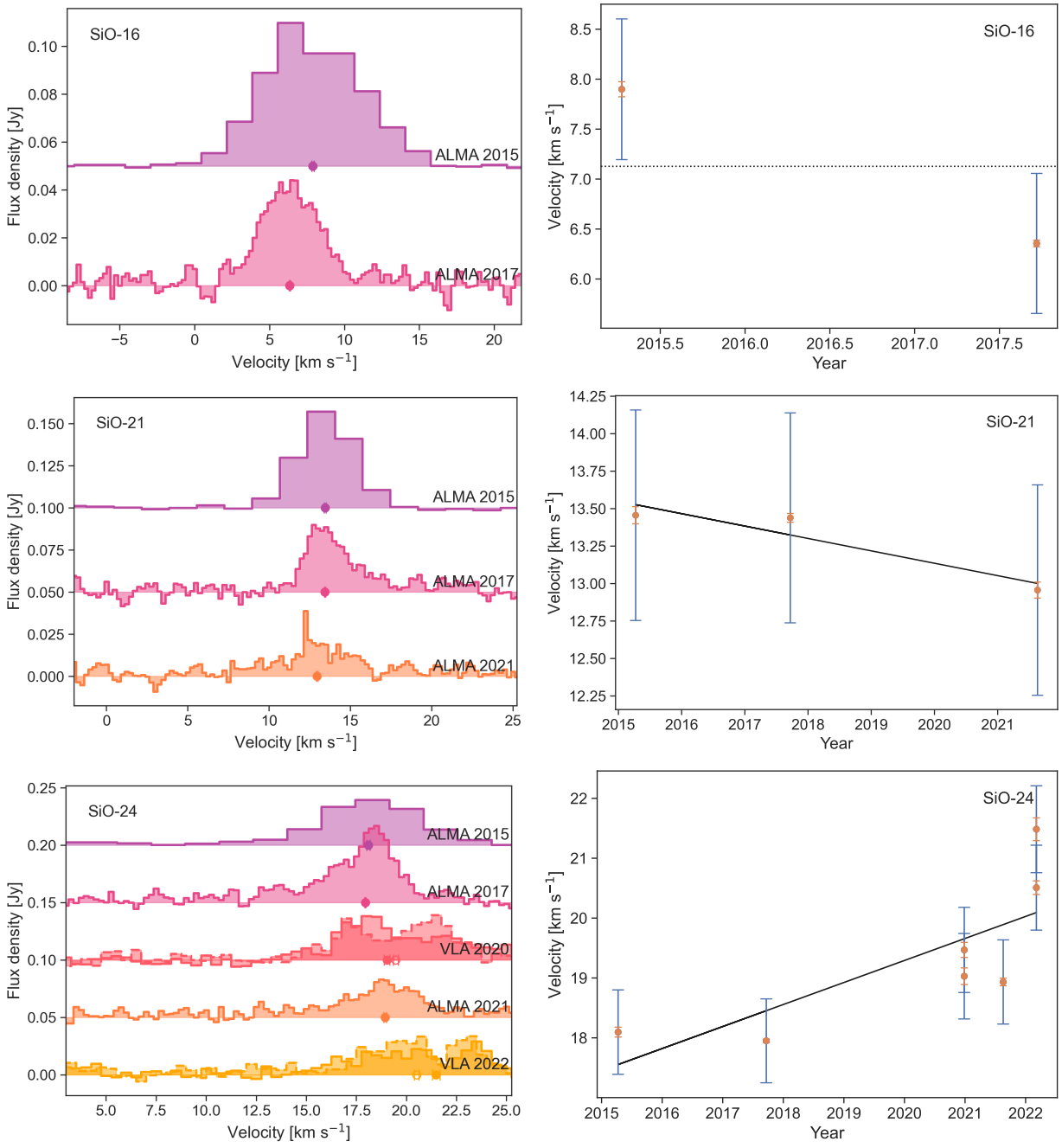
SiO-16
ALMA 2015
ALMA 2017
Flux density [Jy]
Velocity [km s^{-1}]
SiO-16
Velocity [km s^{-1}]
Year
SiO-21
ALMA 2015
ALMA 2017
ALMA 2021
Flux density [Jy]
Velocity [km s^{-1}]
SiO-21
Velocity [km s^{-1}]
Year
SiO-24
ALMA 2015
ALMA 2017
VLA 2020
ALMA 2021
VLA 2022
Flux density [Jy]
Velocity [km s^{-1}]
SiO-24
Velocity [km s^{-1}]
Year

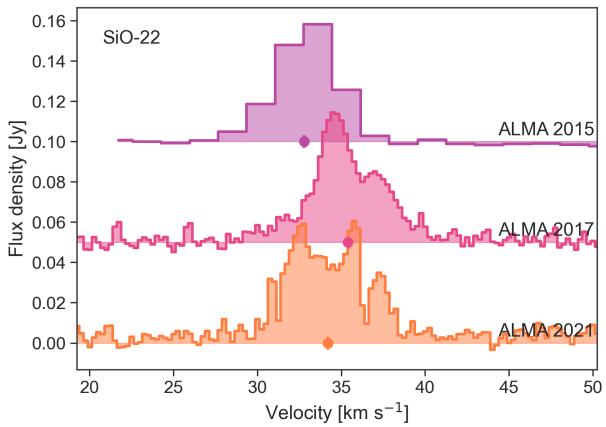
SiO-22
ALMA 2015
ALMA 2017
ALMA 2021
Flux density [Jy]
Velocity [km s^{-1}]

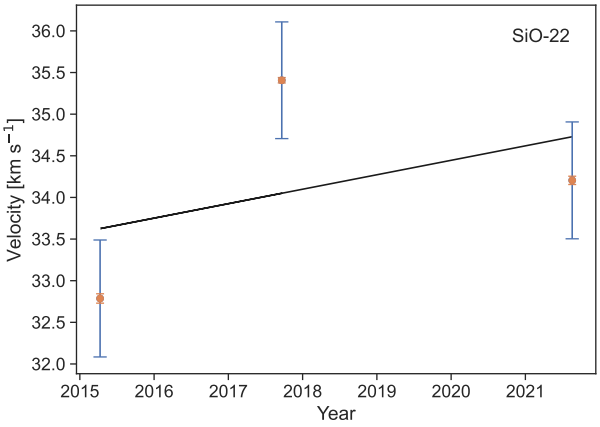
SiO-22
Velocity [km s^{-1}]
Year

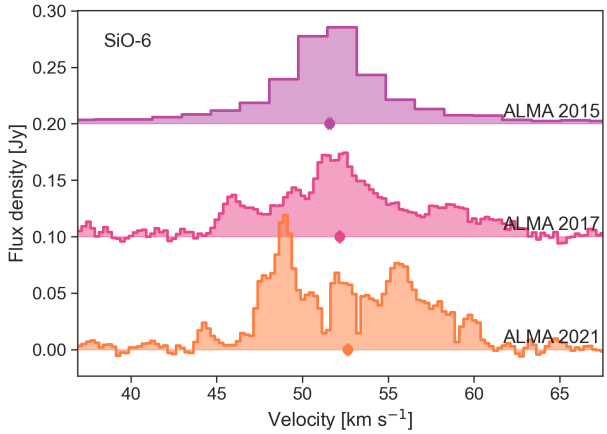
SiO-6
ALMA 2015
ALMA 2017
ALMA 2021
Flux density [Jy]
Velocity [km s^{-1}]

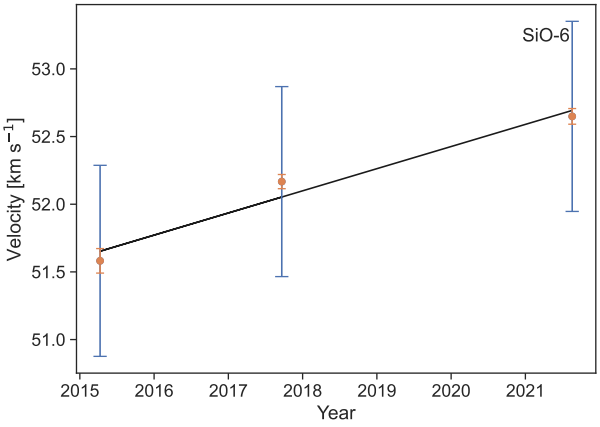
SiO-6
Velocity [km s^{-1}]
Year

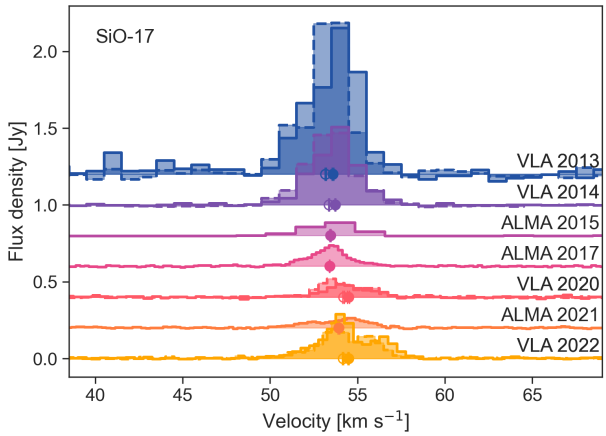
SiO-17
VLA 2013
VLA 2014
ALMA 2015
ALMA 2017
VLA 2020
ALMA 2021
VLA 2022
Flux density [Jy]
Velocity [km s^{-1}]

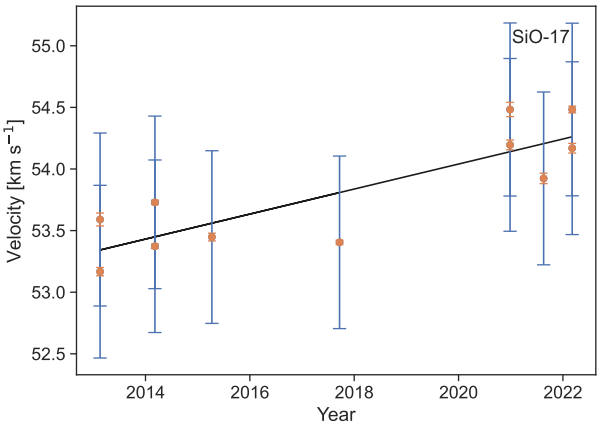
SiO-17
Velocity [km s^{-1}]
Year

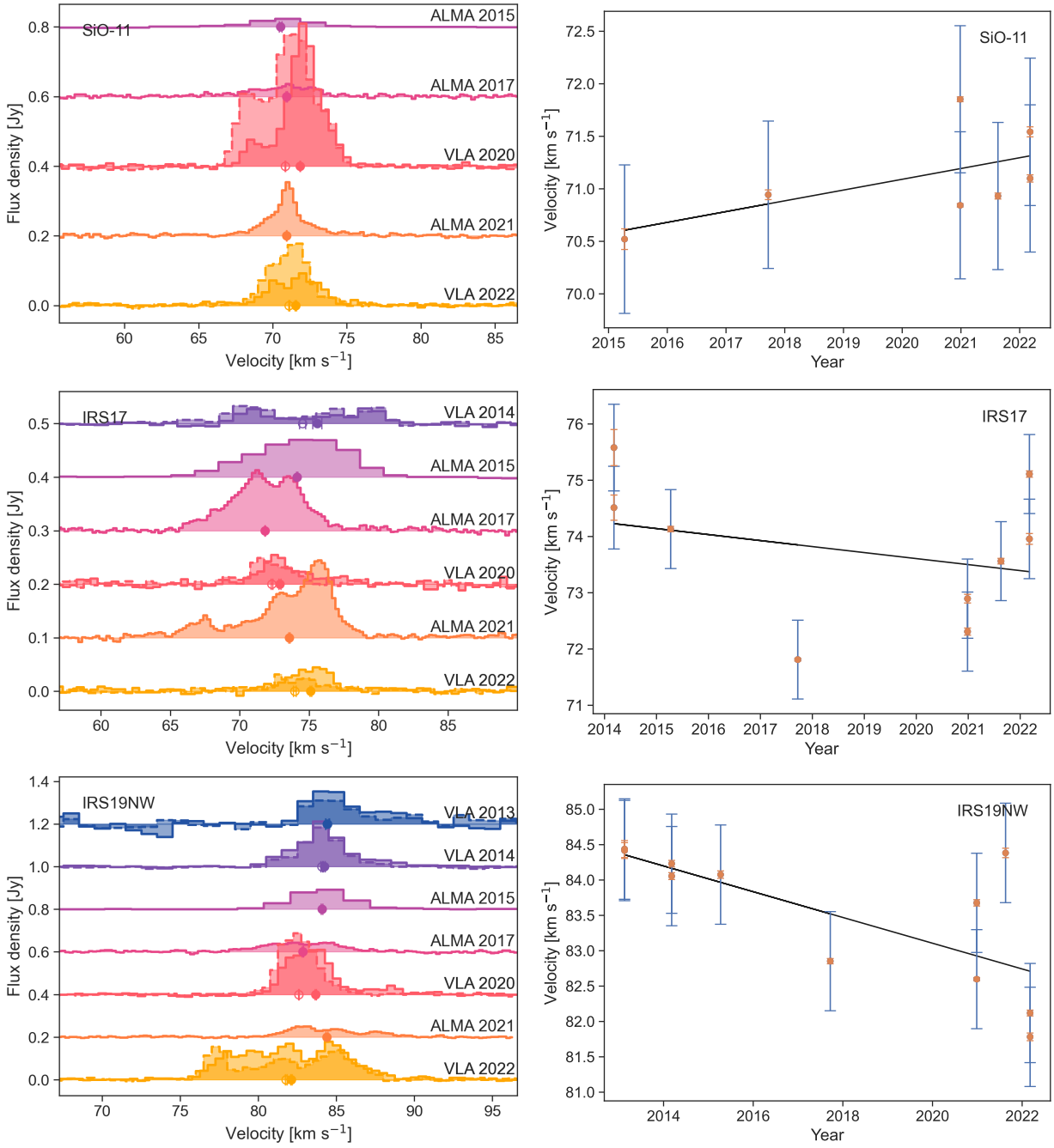
SiO-11
ALMA 2015
ALMA 2017
VLA 2020
ALMA 2021
VLA 2022
Flux density [Jy]
Velocity [km s^{-1}]
SiO-11
Velocity [km s^{-1}]
Year
IRS17
VLA 2014
ALMA 2015
ALMA 2017
VLA 2020
ALMA 2021
VLA 2022
Flux density [Jy]
Velocity [km s^{-1}]
IRS17
Velocity [km s^{-1}]
Year
IRS19NW
VLA 2013
VLA 2014
ALMA 2015
ALMA 2017
VLA 2020
ALMA 2021
VLA 2022
Flux density [Jy]
Velocity [km s^{-1}]
IRS19NW
Velocity [km s^{-1}]
Year

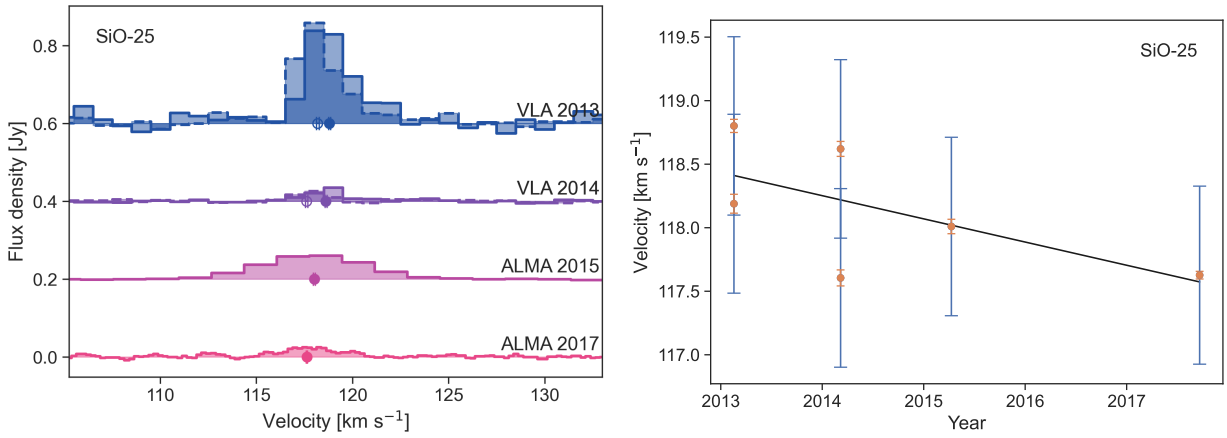
SiO-25
VLA 2013
VLA 2014
ALMA 2015
ALMA 2017
Flux density [Jy]
Velocity [km s^{-1}]
SiO-25
Velocity [km s^{-1}]
Year

Appendix F

Updated SiO Maser Proper Motion and Proper Acceleration Fits

Figure F.1 shows the proper motion fits and proper acceleration fits to the residuals for the SiO maser astrometry described in Chapter 5.

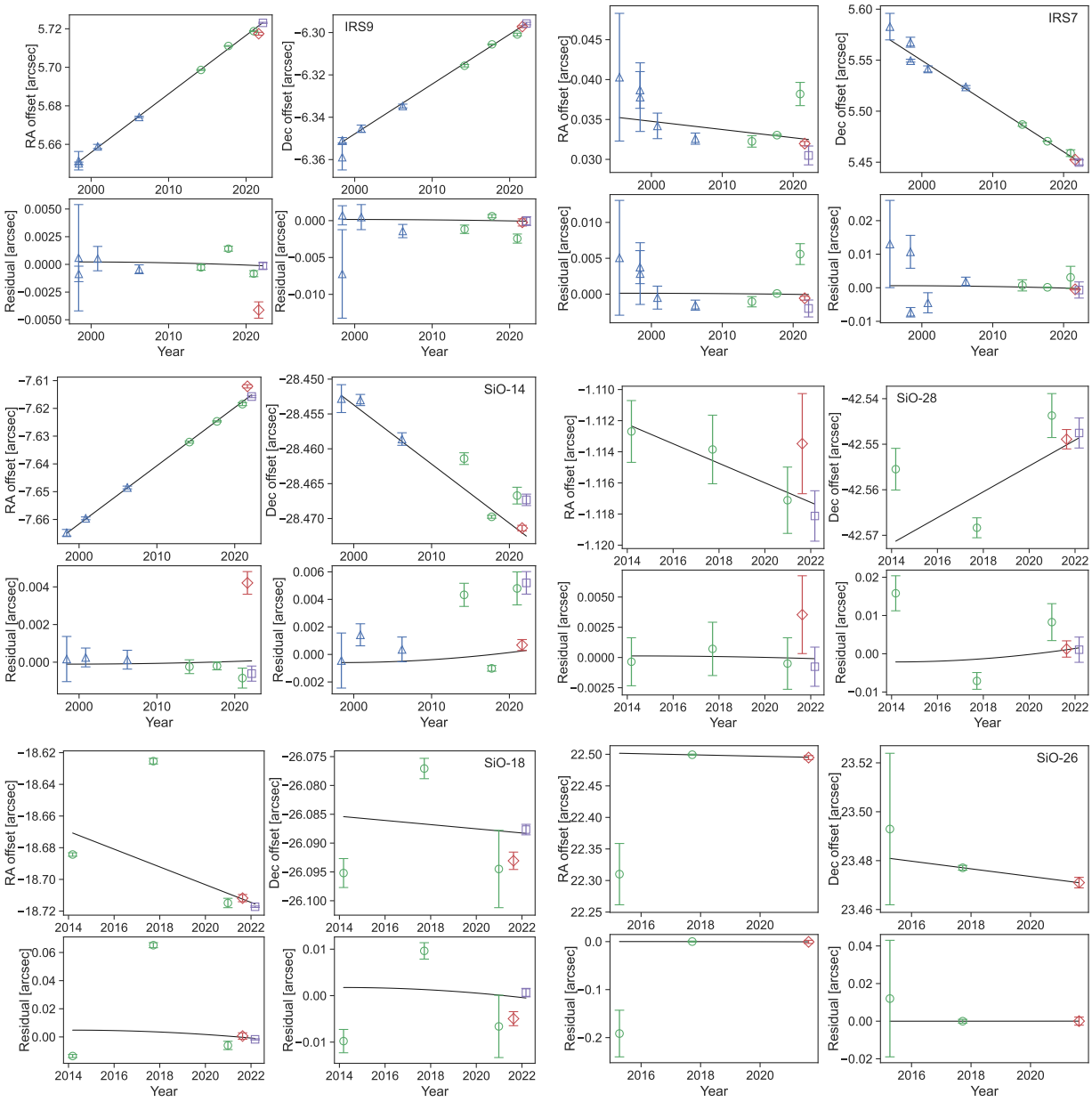

Figure F.1: Proper motion and proper acceleration fits described in Section 5.3. Positions are from Reid et al. (2007) (blue triangles), Li et al. (2010) (orange upside down trianges), Paine & Darling (2022) (green circles), VLA 2021 (red diamonds), and ALMA 2022 (purple squares).

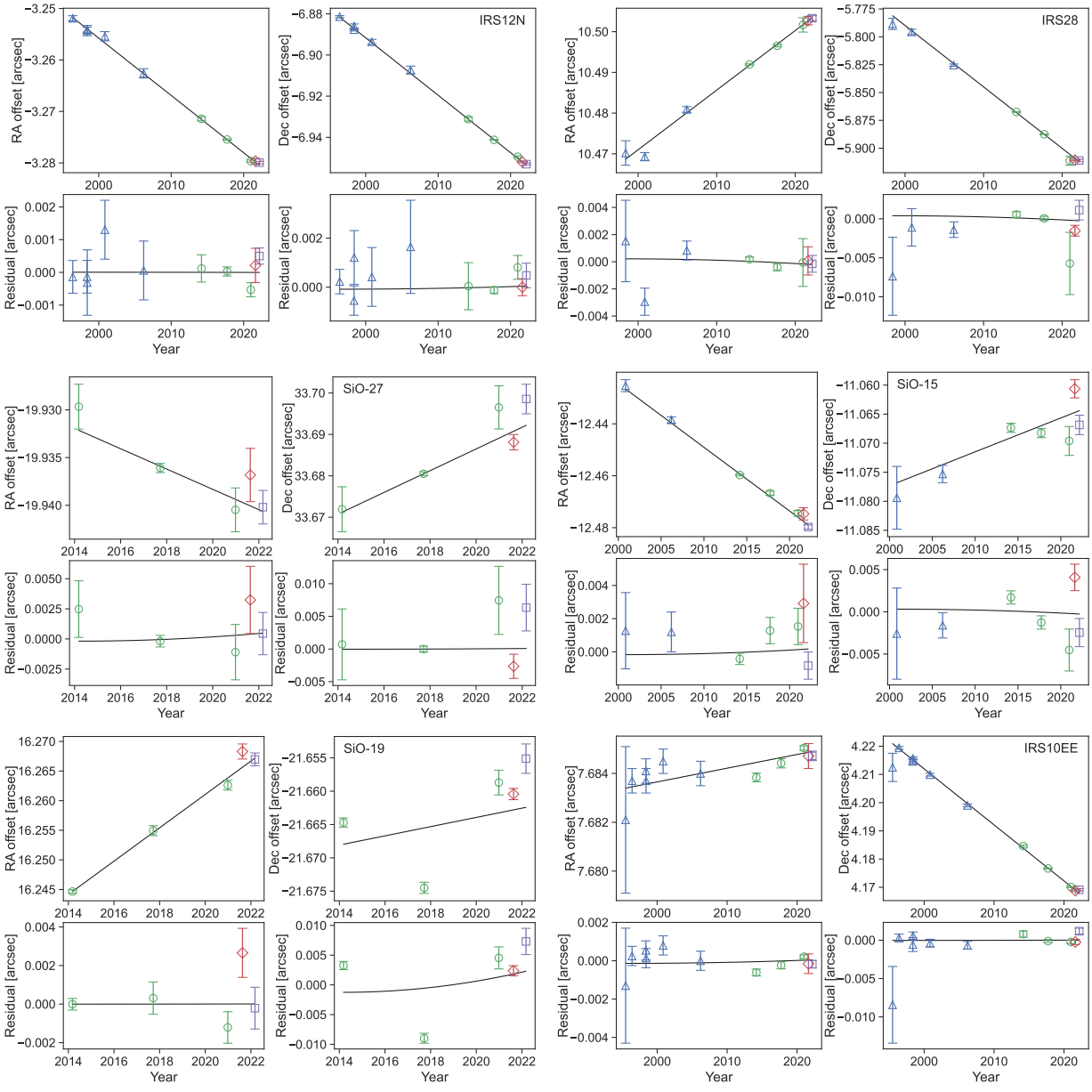
IRS12N
IRS28
SiO-27
SiO-15
SiO-19
IRS10EE
RA offset [arcsec]
Dec offset [arcsec]
Residual [arcsec]
Year

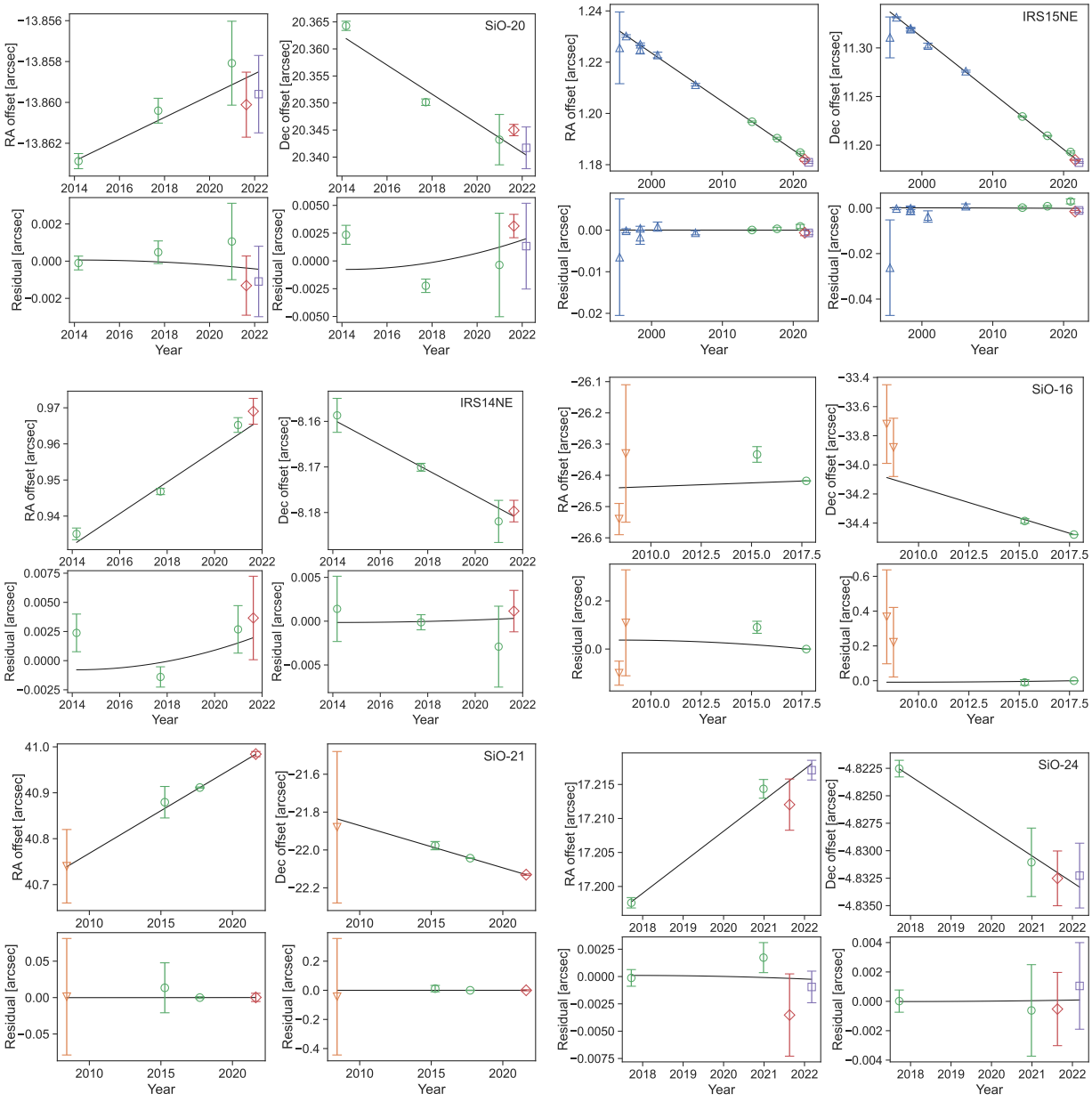
SiO-20
IRS15NE
IRS14NE
SiO-16
SiO-21
SiO-24
RA offset [arcsec]
Dec offset [arcsec]
Residual [arcsec]
Year

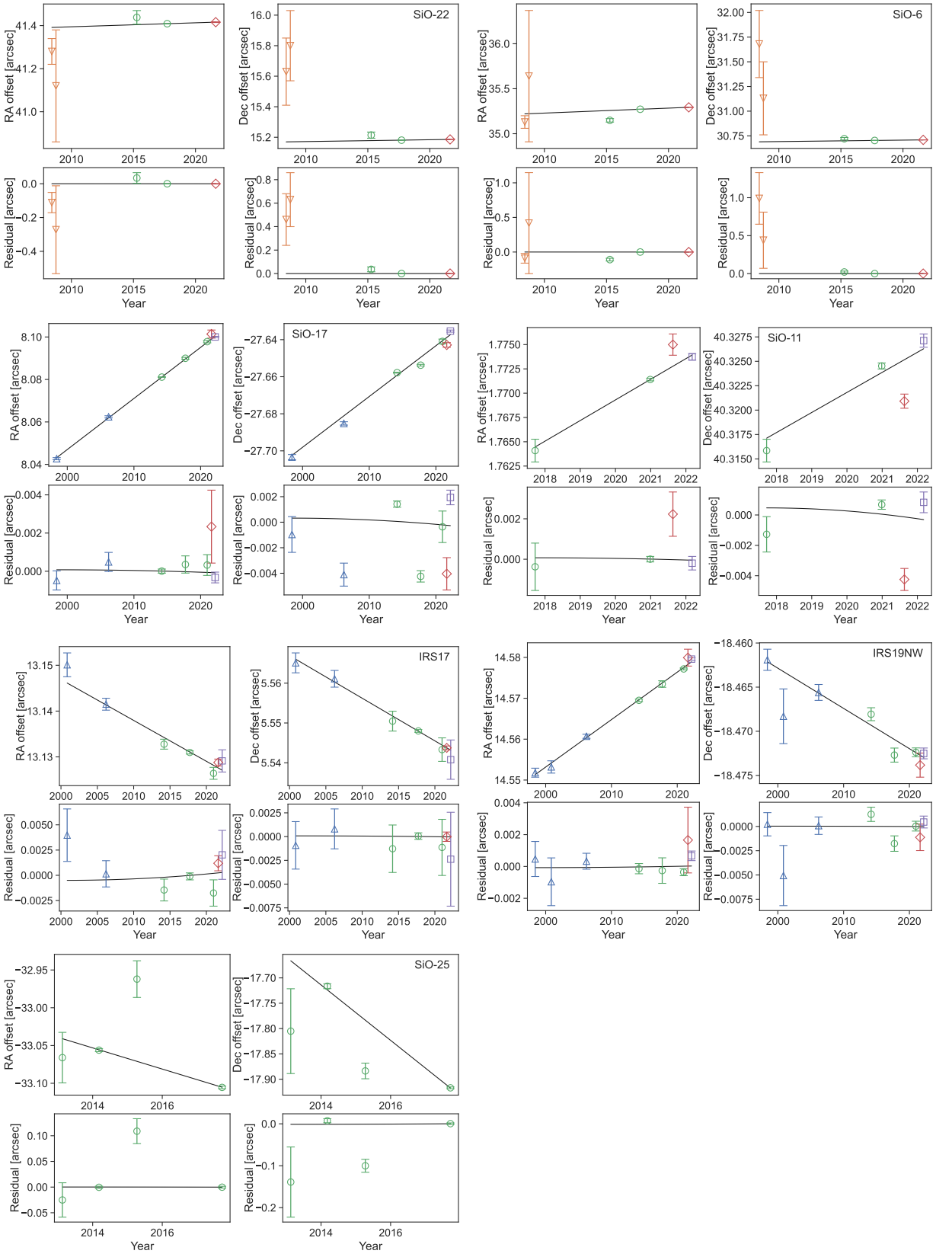
SiO-22
SiO-6
SiO-17
SiO-11
IRS17
IRS19NW
SiO-25
RA offset [arcsec]
Dec offset [arcsec]
Residual [arcsec]
Year